Analysis of geometrical nonlinearities with applications to timber structures

by

Lars Wollebæk

Dr.ing.-thesis

Trondheim, May 2005

Norwegian University of Science and Technology
Faculty of Engineering Science and Technology
Department of Structural Engineering

NTNU

To Elise, without whom this would not have been possible, and to the little lady who could not wait.

Abstract

A large part of the study is concerned with geometrical nonlinearities in structural systems, primarily 3D frame type structures. Parametrizations of finite rotations are studied, and geometric terms associated with transition from pseudo-vector representation to Euler angles are presented. The theories of Cosserat rods and the element independent co-rotational formulation, with emphasis on beam elements, are also presented and discussed. Furthermore, simplifications to the Cosserat rod theory, used in a co-rotational frame, is tested, as well as the use of *B*-spline basis functions for interpolating displacements and rotations. A consistent linearization of the internal forces, for the use in linearized buckling, is presented for this formulation.

A comprehensive finite element computer program has been developed and implemented, and numerical results obtained with this analysis tool are presented and discussed for some typical timber structures. Stability of glue laminated timber arches is the center of attention, but also modelling issues related to a timber footbridge as well as the effect of typical material properties, such as orthotropy and low shear modulus, are discussed.

Acknowledgements

I would like to express my gratitude to my advisor Professor Kolbein Bell for starting me on this journey, and for all the help along the way. I would also like to thank Bjørn Haugen, PhD, for giving of his time for much appreciated discussions and correspondence.

This work has been made possible by the financial support of the Norwegian University of Science and Technology. A travel scholarship, donated by Det Norske Veritas (DNV), enabling a one-year stay at UC Berkeley, has also been received. These contributions are gratefully acknowledged.

I would like thank Professor Filip C. Filippou for assisting me in my stay at UC Berkeley. In addition I would like to send a special thank you to Afsin and Prashanth for helping me in re-orienting my study, making the experience pivotal.

I am also grateful for the informal contributions from my close colleagues at the department.

Preface

At the start of this work, the tentative thesis title was: "*Computer aided analysis and design of 3D timber structures*". It was meant to be a natural continuation of the thesis by T. Eggen [10], completed just prior to the start of this project. Based on the theory described by Eggen, my objective was to develop a prototype computer program, based on advanced nonlinear finite element analysis, for practical design of large-scale timber structures by ordinary, but well qualified design engineers.

Current codes of practise treat the field of geometrically nonlinear analysis sparingly, and only to the extent of second order effects. Furthermore, (the very few) guidelines are generally formulated as principles that are difficult to apply in practise. Personal computers have had the computational capabilities needed to run sophisticated nonlinear analyses for some time now. The fact that this is not reflected in current codes of practice is partly due to the slow migration of 3D nonlinear analysis tools into engineering offices in general, and timber engineering in particular[1]. One reason for this may be the quality of the user interfaces, another costs in the creation and verification of the computer models.

An integral part of the safe use of complex analysis tools in design is the human-machine interaction aspect. How to assure that the model, as intended by the designer, is in fact correctly represented in the computer is an important issue. This is particularly true for nonlinear 3D analyses of framed structures, as opposed to 2D analyses. The amount of information needed increases significantly, and the representation of joints and supports is more complex. Current computer graphics is now at a level of speed and sophistication that life like images of complex models can be handled with ease. A secondary objective of the current work was to give some insight into the use of computer graphics for immediate and safe visual control of the computer model. Also, I wanted to develop methods to prevent common 'pitfalls' connected with the modeling and analysis of typical timber structures. This would reduce the cost of modeling, reduce modeling errors, and basically improve robustness.

1. Cause and effect is clearly open for debate.

In spite of these considerations, the present work deals primarily with aspects related to the theory of geometrically nonlinear analyses. Aspects related to design of timber structures are treated more sketchy. This apparent derailment is due to the occurrence of some unforeseen, but interesting theoretical questions, described in the introduction, which were considered too important to neglect. On account of this, and the time constraints placed on this study, the design aspect had to yield. For the reader interested in timber design, chapters 7 and 8 contain relevant material. While not a comprehensive study, the results presented in this part of the thesis may hopefully inspire and guide future developments.

Finally, I would like to mention that a significant amount of work has gone into in the development of a graphical user interface (GUI), a key element in model verification of intricate structures. A scientific treatment of questions related to GUI's was on the agenda, and I had hoped to take relevant courses to this effect during my one-year stay at UC Berkeley. These courses, however, were given exclusively to students enrolled at the university. Left with little more than qualified guessing and personal taste, a rigorous treatment of the GUI was abandoned.

Lars Wollebæk

Table of content

Notation, symbols and abbreviations

Vectors, tensors and matrices are denoted by boldface. When distinction between material and spatial objects is not needed, vectors are normally denoted by lower case letters, while matrices are upper case. When this distinction is needed, upper case letters are used to denote objects in the material (or intermediate) configuration, while lower case letters are used for spatial objects. It is assumed that the context will make it clear which convention is used. However, boldface letters with a single index is invariably a vectorial quantity. Unless otherwise stated, summation is taken over repeated indices. Lower case latin letters take on the values 1, 2 and 3, while greek letters are summed over the values 2 and 3. Upper case latin letters are used for summations exceeding three dimensions.

- **Symbols**

δ_{ij}	- Kronecker-delta $\delta_{ij} = \begin{cases} 1, & i = j \\ 0, & i \neq j \end{cases}$
$\mathbf{0}$	- Second order zero tensor $\mathbf{0}_{ij} = 0$
$\mathbf{1}$	- Second order identity tensor $\mathbf{1}_{ij} = \delta_{ij}$
A_α	- Reduced shear area in the direction of $\alpha = 2, 3$
A_s	- Reduced shear area (used if $A_2 = A_3$)
B_i	- Shape function
$\mathbf{C}$	- Constitutive tensor
$\{\mathbf{e}_i\}$	- Spatial basis ($\{\mathbf{e}_i\} = \{\mathbf{e}_1, \mathbf{e}_2, \mathbf{e}_3\}$)
$\{\mathbf{E}_i\}$	- Material basis
$\mathbf{F}$	- Deformation gradient
$\mathbf{G}$	- Matrix for extraction of rigid body rotations
$\mathbf{H}$	- Tangent vector space of rotations transformation matrix
$\{\mathbf{I}_i\}$	- Observer-attached (global) orthogonal reference frame ($\mathbf{I}_i = \left[\delta_{1i}\ \delta_{2i}\ \delta_{3i}\right]^T$)
N	- Number of nodes
$\mathbf{n}$	- Spatial nodal forces/unit direction vector
$\mathbf{N}$	- Material nodal forces
$\mathbf{m}$	- Spatial nodal moments
$\mathbf{M}$	- Material nodal moments/mass matrix

$\mathbf{P}$	-Projection matrix/First Piola-Kirchhoff stress tensor
$\mathbf{r}$	-Rigid body displacement
$\mathbf{R}$	-Rotation matrix
$\mathbb{R}$	-The set of all real numbers
$\mathbb{R}_+ \subset \mathbb{R}$	-The set of all real, positive numbers (not including zero)
$\mathbf{T}_i$	-Material tractions
$\mathbf{u}$	-Deformational displacement
$\mathbf{v}$	-Total nodal-displacements
$\mathbf{x}$	-Spatial coordinates
$\mathbf{X}$	-Material coordinates

- **Subscripts**

I	-Node-number, taking values from 1 to N
d	-Deformational measure
r	-Quantity associated with rigid body motion

- **Superscripts**

c	-quantity evaluated at element centroid
CR	-Co-rotational quantity
n	-quantity at configuration $n \geq 0$

- **Operators**

dyad ($\otimes$)

$$\mathbf{A} = \mathbf{a} \otimes \mathbf{b} \quad \Rightarrow A_{ij} = a_i b_j$$

dot-product ($\cdot$)

$$a = \mathbf{a} \cdot \mathbf{b} = \mathbf{a}_i \mathbf{b}_i$$

- **Diacriticals**

$\tilde{(\circ)}$	-Quantity with components in local reference frame
$\widehat{(\circ)}$	-Short-hand notation for Spin($\circ$)
$(\circ)'$	-derivative with respect to length-parameter
$\dot{(\circ)}$	-material time-derivative
$\overline{(\circ)}$	-Prescribed loads

- **Abbreviations**

$COPO_N^{gp}$	- N-node Cosserat element with polynomial interpolation of order N - 1. Numerically integrated with gp Gauss-Legendre integration points (if omitted $gp = N - 1$).
$COSP_N^{d,gp}$	- N-node Cosserat element with B-spline interpolation of polynomial order d. Numerically integrated with gp Gauss-Legendre integration points (if omitted $gp = d$).
EB	- Euler-Bernoulli beam element
EBT	- Euler-Bernoulli beam element with approximated shear deformations due to Timoshenko
EICR	- Element Independent Co-Rotational formulation
LRC	- Simplified (reduced) Cosserat element with linear interpolation
RM	- Reissner-Mindlin C^0 beam element with linear interpolation
TL	- Total Lagrangian formulation
UL	- Updated Lagrangian formulation

Chapter 1
Introduction

1.1 Analysis and design - current practice

The design of timber structures has traditionally been based on linear analyses of plane models. In order to account for nonlinear (2^{nd} order) effects, current European codes of practice dictate that the linear response is "corrected" by various (*k*-) factors. Some of these factors account for material properties, while others deal (primarily) with geometrical effects and stability. Concentrating on the geometrical effects, these factors are relatively easy to determine for individual members that are not part of a larger assembly. For complex structures, however, they are often difficult and sometimes very difficult to estimate. This is particularly true in situations where significant 3D effects, not captured by the plane models, are present. The underlying assumption of this design principle is that estimates should be on the conservative side. The fundamental question, however, is whether the difficulties experienced in estimating these factors will lead to designs that are excessively conservative, or even worse, unsafe.

1.2 Tomorrow's solution - capabilities and obstacles

Current commercial software packages have made sophisticated nonlinear analyses of structures available within the scientific community and at large or specialized engineering offices. The level of expertise needed and costs involved, however, are still too high for the use of these programs to be commonplace in everyday timber engineering and design. It is, however, only a question of time before the use of 'custom made' advanced nonlinear 3D analysis tools are made available for design purposes. In order for these tools

to become useful and safe, they need to address the fact that the skill and knowledge of the users may be variable. Hence, the program must be able to help and guide the user through the design process. Although the tool should ideally spur the novice's interest for the underlying theory, the user threshold must be relatively low: Only the understanding of some fundamental concepts and range of applicability should be required. This will inevitably put an great responsibility on the program design and implementation; it will require not only a solid theoretical knowledge, but also a thorough understanding of the design process as well as good insight into the many subtleties of GUI design. Furthermore, current computer graphics can significantly aid the user, but it can also mislead and instill false confidence.

Another obstacle in promoting the use of advanced nonlinear computational capabilities in the design process is the conservative view taken by most codes, and their lack of specifications for the use of such methods. One area in particular that is vital for nonlinear analysis concerns geometrical imperfections of the structural system.

1.3 Purpose and scope

In the field of computational mechanics of structures, two principal directions for the treatment of geometrically nonlinear behavior exist. The most prevalent and accepted direction is the one usually referred to as the Lagrangian methods (Total Lagrangian and Updated Lagrangian). Developing elements with these methods generally entails the establishment of a nonlinear relationship for the stresses and strains with respect to displacements. Subsequently, simplifying assumptions are often introduced by excluding unnecessary terms. The other, less favoured direction is the co-rotational formulations. The fundamental difference, compared to the Lagrangian methods, is that the co-rotational formulations focus only on the rigid body motion of the element. The assumption is that the principal source of nonlinearity is captured by the rigid body motion of the element. Even restricting the discussion to beam type elements, a multitude of formulations of both types exist. In this thesis, we will focus primarily on the Lagrangian beam element formulation due to Simo et. al. [35, 36 and 37] (Cosserat rod), and the element independent co-rotational formulation (EICR) of Nour-Omid, Rankin and Brogan [26, 32, 33]. While the

first is a beam element formulation, it should be stressed that the latter is a general formulation, independent of element type and geometric discretization (e.g. solid, shell or beam elements). Although exemplified by beam elements, this independence of geometry is also true for a large part of our discussion regarding this formulation. While several authors have claimed equivalence between Lagrangian and co-rotational beam elements, it will be shown in this thesis that this is due to simplifying assumptions and/or chance. In the view of the author such comparisons are somewhat artificial, since both formulations are based on different, but equally valid principles; thus the comparisons only add to the confusion. Furthermore, the mixing of these formulations does not pose a problem provided the rotational parameterization is consistent.

During a literature search on EICR some misconceptions were encountered, primarily due to unclear language and unnecessary simplifying assumptions. This thesis attempts to bring forth these assumptions and specify where they are needed. In so doing, it is hoped that the benefits and potential of this formulation will become more evident. The notation and symbolism presented differ to some extent from what is commonly used when describing the EICR. This was necessary in order to maintain a uniform use of symbols throughout the presentation. Furthermore, the separation of rotations into rigid body and deformational motion is done in the reverse order to what is commonly done. Although shown to be of no consequence to the formulation, the reader should be aware of this to avoid confusion. Also, it is shown that the measure of deformation can be formulated independently of the co-rotational description of motion used in the EICR.

Timber is a very orthotropic material, and this is particularly evident in the relationship between the modulus of elasticity parallel to grain and the modulus of shear. If the isotopic relationship is used (although an absurd notion), the Poisson's ratio would be in the order of 7. It is therefore of interest to study the influence that shear has on different element formulations. In order to compare the use of simple linear elements used in the EICR formulation with the Lagrangian elements (with internal geometric stiffness), the C^0 beam element formulation of Simo et. al. has been chosen. The presentation of this formulation closely follow the presentation given in [35, 36 and 37], with two exceptions: The consistent linearization of internal forces, to be used in a linearized buckling stiffness matrix, is believed to be novel. Also, the element formulation is tested and verified for interpolation in a B-spline basis. This has resulted in a family of highly accurate and stable elements.

The study of finite elements in combination with timber engineering design is driven primarily by the need for a more rational approach through the use of already available nonlinear formulations. However, timber structures are normally designed to behave reasonably linearly with respect to geometrical effects. For plane problems in particular, deformations usually lie well within the range of second order theory. It is therefore pertinent to ask why these rather sophisticated element formulations are considered. On the other hand, one may just as well ask whether one knows that the structures really behave according to second order theory if higher order terms are not considered. This is particularly true for problems relating to the stability of structures: *"Buckling is possible even with very small strains, so when buckling is a possibility, measures which can properly account for large deformations should be used",* Belytschko [6]. Although current design practice dictates that shape imperfections should be accounted for in the nonlinear analyses of structures, thus minimizing the danger of catastrophic collapse, the ability to detect singularities in the solution is crucial for several reasons. First and foremost, instabilities, both in terms of bifurcation points and limit points, may occur in spite of the design procedure. Secondly, linearized buckling analyses may give good indications as to where a solution lies in the nonlinear range[1]. This concept is illustrated in Figure 1.1. Finally, an

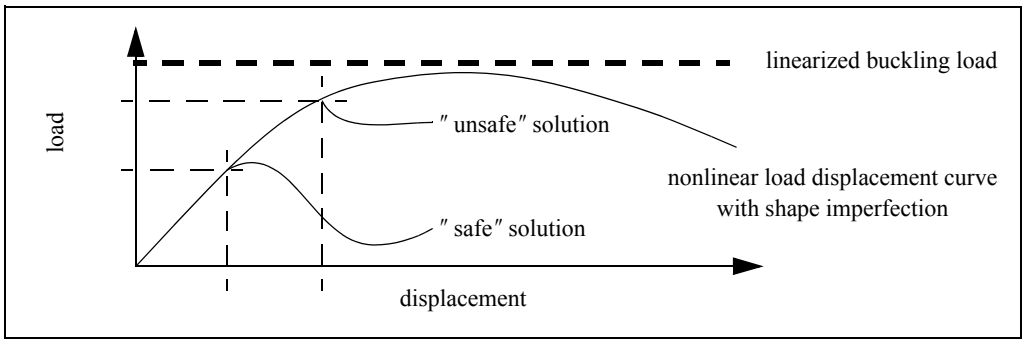

Figure 1.1 Typical load displacement curve and buckling load

important application of the method of linearized buckling is the use of the buckling modes for semi-automatic generation of shape imperfections. Testing and documenting

1. This use of linearized buckling loads is, however, associated with a large degree of uncertainty and should be used with caution.

adequate (robust) 3D beam element formulations for the use in timber design is therefore believed to be of some importance.

An important part of the analysis of a structure is the correct modeling of its boundary conditions and connections. Errors in this area are among the most subtle and difficult to assess. To a relative novice in the field of finite rotations, some rather surprising effects were observed in connection with the analysis of a problem where a single rotational degree of freedom at a node was constrained. When performing a nonlinear analysis of a simply supported beam, prevented from twisting at both ends, and subjected to a constant bending moment about the strong axis, the predicted buckling load did not correspond well to closed form solutions. This is a classical lateral torsional buckling problem with well established solutions. Furthermore, nonlinear analyses with initial shape imperfections, where the beam was first loaded followed by complete unloading, the final state of rotation at the ends did not match the prescribed boundary conditions. This led to a detailed study of finite rotations and boundary conditions, resulting in recommendations for an appropriate rotational representation for this particular boundary condition. A geometric stiffness term associated with the transition from the most prevalent parametrization of finite rotations to the parameterization used here has been developed. The result of using this parametrization in the case described above is demonstrated in Section 6.6.3.

1.4 Organization of thesis

The thesis is divided into two main parts:

“Part I - Theoretical background and finite element technology” deals primarily, as the name indicates with (nonlinear) element formulations. This constitutes the bulk of the work presented, starting with the fundamentals of finite rotations in Chapter 3. Different rotational parametrizations and representations are discussed, as well as boundary conditions and the transition from one rotational parameterization to another. Chapters 4 and 5 deal with the element formulations of Cosserat rods and EICR, respectively. Numerical verification and comparisons are made in Chapter 6.

"Part II - Numerical studies" contains some numerical studies of buckling of timber arches, as well as two examples of the use of a nonlinear 3D analysis tool for the design of real, complex timber structures.

A versatile computer program, including a comprehensive graphical presentation of model and results, has been developed, more or less from scratch. This effort, which account for a large part of the total work, is only indirectly documented in the thesis, through the many numerical results and a fair number of illustrations in the form of "screen-shots" from the program.

Part I
Theoretical basis and FEM technology

Chapter 2

Fundamentals of numerical analyses of structures

2.1 Static analysis

In the numerical analysis of static problems, be it linear or nonlinear, we are normally seeking to find a solution to a discrete version of the equilibrium equation:

$$\mathbf{r}(\varphi\,;\,\mathbf{p}) \;=\; \mathbf{f}(\varphi) - \mathbf{p}(t) \;=\; \mathbf{0} \tag{2.1}$$

where $\mathbf{f}$ is the vector of resisting nodal forces, $\mathbf{p}$ is a vector of applied nodal forces and $\mathbf{r}$ is the residual. φ is used to denote the current state of deformation or configuration. Note that this may or may not be a vectorial quantity. In general, this equation may be established on the basis of the *Principle of virtual work* (PVW):

$$G_{Stat}(\varphi,\ \eta\ ;\ \bar{\sigma}) \;=\; 0 \tag{2.2}$$

where G_{Stat} is an integral equation, $\bar{\sigma}$ is the internally applied stresses (or resultant forces and moments). η is a weight function, usually taken to be the tangent vector space of φ at the current state of deformation.

As indicated in Equation (2.1), the applied forces may be a function of time. Since no dynamic effects are considered in a static analysis, the forces may be arbitrarily parametrized. It is common practice to denote time with the pseudo-time variable λ, thus emphasizing the lack of dynamic effects. By defining successive *stages*, $\mathbf{p}(\lambda_k) \;=\; \mathbf{p}_k$, $k \;=\; 0,\ 1,\ \cdots,\ n$, the final solution is found as the progressive solution of Equation (2.1) from $\mathbf{p} \;=\; \mathbf{p}(\lambda_0)$ to $\mathbf{p} \;=\; \mathbf{p}(\lambda_n)$. In between two successive stages, the load is normally linearly interpolated:

$$\mathbf{p} = \frac{\lambda_k - \lambda}{\lambda_k - \lambda_{k-1}}\mathbf{p}_{k-1} + \frac{\lambda - \lambda_{k-1}}{\lambda_k - \lambda_{k-1}}\mathbf{p}_k, \quad \lambda_{k-1} \le \lambda \le \lambda_k \tag{2.3}$$

Progressing the solution from one stage to the next is conveniently done in a series of incremental steps $\lambda(t_i) = \lambda(t_{i-1}) + \Delta\lambda$, where $\Delta\lambda$ is an assigned or calculated *stepsize*. Solving for the principal unknowns with a truncated Taylor series, i.e. using the iterative Newton-Raphson method, results in the following set of linear equations

$$\begin{aligned} \mathbf{r}(\varphi_{i+1}\,;\,\mathbf{p}(\lambda)) &= \mathbf{r}(\varphi_i \oplus \Delta\varphi_i\,;\,\mathbf{p}) \cong L[\mathbf{r}(\Delta\varphi_i\,;\varphi_i,\,\mathbf{p})] \\ &= \mathbf{r}(\varphi_i\,;\,\mathbf{p}) + \frac{\partial \mathbf{f}}{\partial \varphi}\Delta\varphi_i - \frac{\partial \mathbf{p}}{\partial \varphi}\,\Delta\varphi_i \\ &= \mathbf{r}(\varphi_i\,;\,\mathbf{p}) + \mathbf{K}_T\Delta\varphi_i = \mathbf{0} \end{aligned} \tag{2.4}$$

The abstract addition operator $\oplus$ is used to indicate that the update from φ_i to φ_{i+1} does not necessarily follow the linear rules of vector addition. For a linear problem the procedure will converge in a single iteration. If we have a single load increment, the familiar equation of linear analysis presents itself:

$$\mathbf{f} = \mathbf{K}_T\Delta\varphi = \mathbf{p} \tag{2.5}$$

The procedure described here is the standard Newton-Raphson scheme with load control. This procedure has some serious drawbacks, among which can be mentioned the inability to follow the solution past a limit point in a stable and reliable manner. To solve this problem, a number of augmented versions of the basic Newton-Raphson scheme have been proposed. Collectively these methods are named “arch-length” methods and involve introducing the incremental load as a free parameter as well as some form of additional constraint. The study of these methods is beyond the scope of this work.

The convergence properties of the Newton-Raphson method are well documented, and for well behaved problems quadratic convergence is to be expected. However, as noted above, the algorithm is not guaranteed to converge and convergence is not a guarantee for the real solution being found. The latter problem is illustrated for a one-dimensional problem in Figure 2.1. For the target load p_{target}, the system has three solutions v_1, v_2 and v_3 for the displacement v. Applying the NR algorithm to this problem would produce the answer $v = v_2$ when starting at zero. This problem is commonly known as “overstepping” the solution. The problem is normally minimized by either reducing the stepsize directly or by

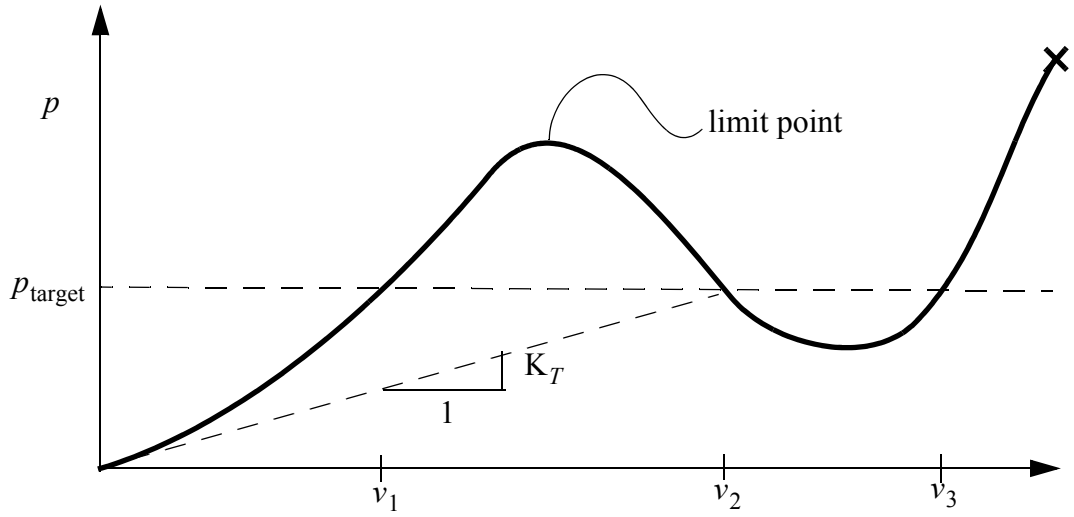

Figure 2.1 Load-displacement curve (overstepping)

modifying the arch-length constraints. Although the solution may seem simple, this will require some prior knowledge of the problem. From an algorithmic point of view, these "false" solutions have no characteristics that can be easily flagged.

A slightly less sever problem is the linear convergence rate near critical points such as limit and bifurcation points.

2.2 Linearized stability analysis

In the study of stability of structures, in the absence of follower loads, a commonly adopted approach is the *Linearized buckling* procedure. In a more general setting, this method is only a special case of *Lyapunov* (or *dynamic*) *stability,* reduced to account for symmetric stiffness matrices only. For static equilibrium, stability in the sense of Lyapunov is the study of the solution of a perturbed equilibrium position. If the configuration $\boldsymbol{\varphi}_{eq}(\mathbf{X},\ t_0)$ and velocity $\mathbf{V}(\mathbf{X},\ t_0) = \mathbb{0}$ is a known state of equilibrium, we can define a perturbed initial configuration $\boldsymbol{\varphi}(\mathbf{X},\ t_0)$ and $\mathbf{V}(\mathbf{X},\ t_0) = \mathbb{0}$ that in some sense is close to $\boldsymbol{\varphi}_{eq}(\mathbf{X},\ t_0)$, i.e. $\|\boldsymbol{\varphi}(\mathbf{X},\ t_0) - \boldsymbol{\varphi}_{eq}(\mathbf{X},\ t_0)\|$ is small in a given norm $\|\circ\|$. The solution is now considered stable if the nonlinear dynamic problem remains close to the equilibrium position $\boldsymbol{\varphi}_{eq}(\mathbf{X},\ t_0)$ for all times $t > t_0$:

$$\left\|\boldsymbol{\varphi}(\mathbf{X},\ t) - \boldsymbol{\varphi}_{eq}(\mathbf{X},\ t_0)\right\| = O(\left\|\boldsymbol{\varphi}(\mathbf{X},\ t_0) - \boldsymbol{\varphi}_{eq}(\mathbf{X},\ t_0)\right\|) \quad \|\mathbf{V}(\mathbf{X},\ t)\| \cong 0 \tag{2.6}$$

Solving this highly nonlinear problem is exceedingly difficult, and practically impossible for most cases. In the *linear stability analysis*, we linearize the dynamic equations at a given equilibrium position. If we by $\Delta\boldsymbol{\varphi} = \Delta\hat{\boldsymbol{\varphi}}\, e^{-i\omega t}$ denote an increment in the configuration, the acceleration becomes $\Delta\ddot{\boldsymbol{\varphi}} = -\omega^2 \Delta\hat{\boldsymbol{\varphi}}\, e^{-i\omega t}$. Using this in the linearized dynamic equations and neglecting damping, we get the general (not necessarily symmetric) eigenvalue problem:

$$(\mathbf{K}_T - \omega^2 \mathbf{M})\Delta\hat{\boldsymbol{\varphi}} = \mathbf{0} \tag{2.7}$$

In the preceding, ω is the frequency of the oscillation[1], $\mathbf{M}$ is the mass matrix and $\mathbf{K}_T$ is the tangent stiffness matrix. In the solution of Equation (2.7), there are fundamentally three different cases to consider. A so-called *stable* mode occurs when the imaginary part of ω is negative ($Im(\omega) < 0$). In this case the oscillations will decay in time as $\Delta\boldsymbol{\varphi} = \Delta\hat{\boldsymbol{\varphi}}\, e^{-iRe(\omega)t}\, e^{-Im(\omega)t}$. If $Im(\omega) > 0$, the motion will increase in time and the solution is unstable. The special case of $Im(\omega) = 0$ requires the consideration of higher order terms. One can show that a linear instable solution implies full nonlinear instability, the linear stable solution does not, however, guarantee nonlinear stability[2].

As stated in any textbook on linear algebra, the eigenvalues for any problem involving symmetric matrices are always real, $\omega^2 \in \mathbb{R}$. For conservative systems, the stiffness matrix is symmetric ($\mathbf{K}_T = \mathbf{K}_T^{\mathsf{T}}$), thus leaving the eigenfrequencies either strictly imaginary ($\omega^2 < 0$) or strictly real ($\omega^2 > 0$). As $\omega^2 < 0 \Rightarrow Im(\omega) > 0$, imaginary frequencies will necessarily imply instability. Contrary to the general case, the transition from real to imaginary frequencies can only occur via $\omega^2 = \omega = 0$ for symmetric matrices. The question of stability can now be posed as the problem of finding the points where the frequencies vanish, or equivalently the points of singularity of $\mathbf{K}_T$:

$$\mathbf{K}_T\Delta\hat{\boldsymbol{\varphi}} = \mathbf{0} \Rightarrow \left|\mathbf{K}_T\right| = 0 \tag{2.8}$$

1. Note that the motion is oscillatory only if $Re(\omega) \neq 0$
2. For a detailed account of the stability of functions, see for instance Marsden & Ratiu [24]

For conservative problems, Equation (2.8) can be shown to be a necessary condition for instability. The solution of Equation (2.8) can be found through the evolution of $\mathbf{K}$ in time. A Taylor series expansion of $\mathbf{K}$ up to linear terms in time results in:

$$\mathbf{K}_T(\varphi,\ \mathbf{p}) \cong \mathbf{K}_T(\varphi_{eq},\ \mathbf{p}_0) + \Delta t\dot{\mathbf{K}}_T \tag{2.9}$$

Although this looks like a simple general eigenvalue problem, it should be augmented with the requirement of $\mathbf{K}_T$ being evaluated at an equilibrium position. To circumvent this problem, the resisting forces are assumed to be a linear function of the internal stresses $\boldsymbol{\sigma}$ only. The internal stresses are then linearized with respect to the increment in applied external forces:

$$\dot{\mathbf{K}}_T = \frac{\partial \mathbf{K}_T}{\partial \boldsymbol{\sigma}}\dot{\boldsymbol{\sigma}}, \qquad \dot{\boldsymbol{\sigma}} = \frac{\partial \boldsymbol{\sigma}}{\partial \mathbf{p}}\ \dot{\mathbf{p}} \tag{2.10}$$

In static analysis, Δt is generally replaced with the pseudo-time, or load amplification factor, $\Delta\lambda$ as $\dot{\mathbf{p}} = \frac{\Delta\lambda}{\Delta t}\mathbf{p}_{ref}$, where $\mathbf{p}_{ref}$ is a reference load vector defined for the current load increment. For the sake of generality, this will not be pursued here. With these restrictions, the stability of a structure can thus be found by solving the following general eigenvalue problem:

$$\left(\mathbf{K}_T(\varphi_{eq},\ \mathbf{p}_0) + \Delta t\frac{\partial \mathbf{K}_T}{\partial \boldsymbol{\sigma}}\frac{\partial \boldsymbol{\sigma}}{\partial \mathbf{p}}\ \dot{\mathbf{p}}\right)\mathbf{x} = \mathbf{0} \tag{2.11}$$

This is a procedure commonly known as *linearized buckling* and is usually written as:

$$(\mathbf{K}_T(\varphi_{eq},\ \mathbf{p}_0) + \Delta\lambda\mathbf{K}_g(\Delta\boldsymbol{\sigma},\ \varphi_{eq},\ \mathbf{p}_0))\mathbf{x} = \mathbf{0} \tag{2.12}$$

where

$$\Delta\boldsymbol{\sigma} = \frac{\partial \boldsymbol{\sigma}}{\partial \varphi}\frac{\partial \varphi}{\partial \mathbf{p}}\ \mathbf{p}_{ref} \tag{2.13}$$

Linearized buckling is frequently performed for structures in its initial, undeformed, configuration ($\mathbf{p}_0 = \mathbf{0}$ and $\varphi_{eq} = \varphi_{undef}$). Equation (2.12) is, however, valid for any state of deformation and can be performed at any stage in a nonlinear analysis provided $\left|\mathbf{K}(\varphi_{eq},\ \mathbf{p}_0)\right| \geq 0$. This is particularly useful for problems with initially nonlinear, followed by linear behavior.

2.3 Symmetry of tangent operator in structural analyses

Symmetry of the tangent operator is an important property for several reasons. The first reason that is usually quoted is the simplifications this implies for solving systems of linear equations and eigenvalue problems. With this comes a significant decrease in cost of CPU-time and memory requirement. However, this is a minor inconvenience when compared to the implications of asymmetry in stability analysis. The methodology of using the singularity of the stiffness matrix to predict bifurcation points relies crucially on symmetry of the stiffness matrix (i.e. a conservative system). A common description of the element formulations that follow in subsequent chapters is that they are symmetrizable due to symmetry at an equilibrium state. This must be (and is often) followed by the condition of conservative forces and boundary conditions. When this is not the case, dynamic instabilities such as flutter are not detectable in the stiffness matrix. Furthermore, symmetrizing the stiffness matrix ($\mathbf{K}_T^{sym} = (\mathbf{K}_T + \mathbf{K}_T^{\mathsf{T}})/2$) may cause the prediction of "false" instabilities. This is a far more severe problem than the loss of consistency and subsequent reduced convergence rate. Most loads and boundary conditions used in structural analysis of timber structures are treated and modeled as conservative. Most non-conservative loads are easily identifiable. However, there is one non-conservative load that can easily be missed, namely the case of a moment about a fixed axis in space. For a short explanation, we start by presenting the stiffness matrix associated with load eccentricity, developed by Haugen and Felippa in [17]:

$$\mathbf{k}_{\mathrm{GE},I} = \mathbf{e}_I^n \otimes \mathbf{n}_I - (\mathbf{n}_I \cdot \mathbf{e}_I^n)\mathbb{1} \tag{2.14}$$

here $\otimes$ is the dyadic (outer product), and $\mathbb{1}$ is the 3×3 identity tensor. $\mathbf{e}_I^n$ is the current vector of eccentricity at node I and $\mathbf{n}_I$ is the eccentrically placed forces at node I. The matrix $\mathbf{k}_{\mathrm{GE},I}$ can be split into a symmetric and a skew symmetric part:

$$\mathrm{sym}(\mathbf{k}_{\mathrm{GE},I}) = \frac{1}{2}(\mathbf{e}_I^n \otimes \mathbf{n}_I + \mathbf{n}_I \otimes \mathbf{e}_I^n) - (\mathbf{n}_I \cdot \mathbf{e}_I^n)\mathbb{1} \tag{2.15}$$

$$\mathrm{skew}(\mathbf{k}_{\mathrm{GE},I}) = \frac{1}{2}(\mathbf{e}_I^n \otimes \mathbf{n}_I - \mathbf{n}_I \otimes \mathbf{e}_I^n) \tag{2.16}$$

From Equation (2.16) it can be seen that if $\mathbf{e}_I^n \,||\, \mathbf{n}_I$ (i.e. no eccentricity moments), the skew symmetric part vanishes. If we denote the eccentricity moment by $\mathbf{m}^e = \mathbf{n}_I \times \mathbf{e}_I^n$, it can be shown that:

$$\text{skew}(\mathbf{k}_{\text{GE},I}) = \frac{1}{2}\begin{bmatrix} 0 & -m_3^e & m_2^e \\ m_3^e & 0 & -m_1^e \\ -m_2^e & m_1^e & 0 \end{bmatrix} \tag{2.17}$$

Since the stiffness matrix is constructed on the basis of a conservative load, the total stiffness matrix after assembly should be symmetric. A skew symmetric term in the element formulation must therefore cancel Equation (2.17). The term (2.17) is missing for a moment with fixed axis, resulting in a skew symmetry equal to $-\text{skew}(\mathbf{k}_{\text{GE},I})$. For a detailed account of different descriptions of moments, as well as a different presentation of this case, the interested reader is referred to the work of Argyris et al. [1] and Bolotin [7]. We will restrict ourselves, and state that any moment, not being the result of a pair of conservative forces, will be non-conservative[1].

1. Note that moments, coupled with a single rotational degree of freedom (rotation in 2D), is conservative and symmetry is maintained.

Chapter 3
Finite rotations, restraints and parametrization

3.1 Introduction to finite rotations

In the following we will be interested in the effect of rotating a vector in space. This can be described as a rotation of a rigid body about a fixed point (i.e. spherical motion). By tracking the position of a vector attached to this rigid body during the motion we can deduce some basic relations.

We define $\mathbf{X}_p^\mathsf{T} = \left[\mathrm{X}_p^1\ \mathrm{X}_p^2\ \mathrm{X}_p^3\right]$ as the initial position of an arbitrary point in the rigid body, referred to a set of Cartesian base vectors $\mathbf{E}_1,\ \mathbf{E}_2,\ \mathbf{E}_3$ positioned at the center of rotation. The position of the same point after rotation is given by $\mathbf{x}_p^\mathsf{T} = \left[\mathrm{x}_p^1\ \mathrm{x}_p^2\ \mathrm{x}_p^3\right]$, also with components expressed in the base vectors $\mathbf{E}_i$. If this motion is a pure rotation, we can express the new position as a linear transformation of $\mathbf{X}_p$:

$$\mathbf{x}_p = \mathbf{R}\mathbf{X}_p \tag{3.1}$$

By observing that the transformation should preserve the length of the vector, the orthogonal property of $\mathbf{R}$ becomes apparent.

$$\mathbf{x}^\mathsf{T}\mathbf{x} = \mathbf{X}^\mathsf{T}\mathbf{R}^\mathsf{T}\mathbf{R}\mathbf{X} = \mathbf{X}^\mathsf{T}\mathbf{X} \Rightarrow \mathbf{R}^\mathsf{T}\mathbf{R} = \mathbb{1} \tag{3.2}$$

Likewise, we can define a set of rotated basis-vectors[1] $\mathbf{e}_1,\ \mathbf{e}_2,\ \mathbf{e}_3$, where $\mathbf{e}_i = \mathbf{R}\mathbf{E}_i$, and the basis-vector matrices:

1. In the following, only orthonormal basis-vectors are considered, so $\mathbf{E}_i \cdot \mathbf{E}_j = \delta_{ij}$.

$$\mathbf{T}_E^{\mathsf{T}} = \left[\mathbf{E}_1\ \mathbf{E}_2\ \mathbf{E}_3\right] = \mathbf{E}_i \otimes \mathbf{I}_i \quad \text{and} \quad \mathbf{T}_e^{\mathsf{T}} = \left[\mathbf{e}_1\ \mathbf{e}_2\ \mathbf{e}_3\right] = \mathbf{e}_i \otimes \mathbf{I}_i, \tag{3.3}$$

where $\otimes$ denotes the dyadic (outer) product, and the vectors $\{\mathbf{I}_i\}$ define the basis of the ambient space (global axes). By this definition, we have the following relationship:

$$\mathbf{T}_e^{\mathsf{T}} = \mathbf{R}\mathbf{T}_E^{\mathsf{T}} \tag{3.4}$$

Since $\mathbf{T}_E$ defines a right handed Cartesian system, so should $\mathbf{T}_e$, and the corresponding determinants evaluate to unity:

$$1 = \left|\mathbf{T}_e\right| = \left|\mathbf{T}_E\mathbf{R}^{\mathsf{T}}\right| = \left|\mathbf{T}_E\right|\left|\mathbf{R}^{\mathsf{T}}\right| = \left|\mathbf{R}\right| \tag{3.5}$$

As can be seen from relation (3.5), $\mathbf{R}$ is a proper orthogonal matrix. The set of all such matrices form a group under multiplication, which is denoted **SO**(n) (Special Orthogonal matrices defined in $\mathbb{R}^{n\times n}$). In the following, due to their physical interpretation, we will be working with the subgroups **SO**(2) and **SO**(3), which can be interpreted as rotations in the Euclidian spaces of two and three dimensions respectively.

Composition of rotations now becomes quite simple: Given an initial state of rotation defined by $\mathbf{R}_0$, and an increment in rotation $\mathbf{R}_\Delta$, we seek to rotate the initially rotated base-vectors $\mathbf{T}_e^{\mathsf{T}}$ such that $\mathbf{T}_{e'}^{\mathsf{T}} = \mathbf{R}_\Delta\mathbf{T}_e^{\mathsf{T}} = \mathbf{R}_\Delta\mathbf{R}_0\mathbf{T}_E^{\mathsf{T}} = \mathbf{R}_{0+\Delta}\mathbf{T}_E^{\mathsf{T}}$, and the total rotation is defined as $\mathbf{R}_{0+\Delta} = \mathbf{R}_\Delta\mathbf{R}_0$

As the base-vector matrices are orthogonal matrices, the relation (3.4) allows us to express $\mathbf{R}$ in terms of the initial and the updated basis.

$$\mathbf{R} = \mathbf{T}_e^{\mathsf{T}}\mathbf{T}_E = \mathbf{e}_i \otimes \mathbf{E}_i \tag{3.6}$$

Thus $\mathbf{R}$ merely transforms a vector with components $\left[\mathrm{X}_p^1\ \mathrm{X}_p^2\ \mathrm{X}_p^3\right]^{\mathsf{T}}$ in the basis $\mathbf{E}_i$ to a vector with the same components, but now in the basis $\mathbf{e}_i$.

3.2 Vectorial representation

The orthogonal property of the rotation matrix allows us to express it in terms of its invariants. A multitude of sets of parameters can be defined to describe these invariants, the most common of which are the Euler parameters (quaternion representation), pseudovec-

tor representation and the Rodriguez parameters (tangent-scaled pseudovector representation). The Euler-representation is a four-parameter representation whereas the pseudovector and Rodriguez-representation is a three parameter representation of the rotations. In this text, the pseudovector will be the parametrization of choice. However, as the Rodriguez-parameters frequently occur in the literature, a short account of the principal results is presented.

3.2.1 Pseudovector

A rotation in space can be defined by a vector containing the (unit) axis of rotation $\mathbf{n}$ and the magnitude θ of the rotation. By this definition the ordered pair $(\mathbf{n}, \theta)$ is a unique rep-

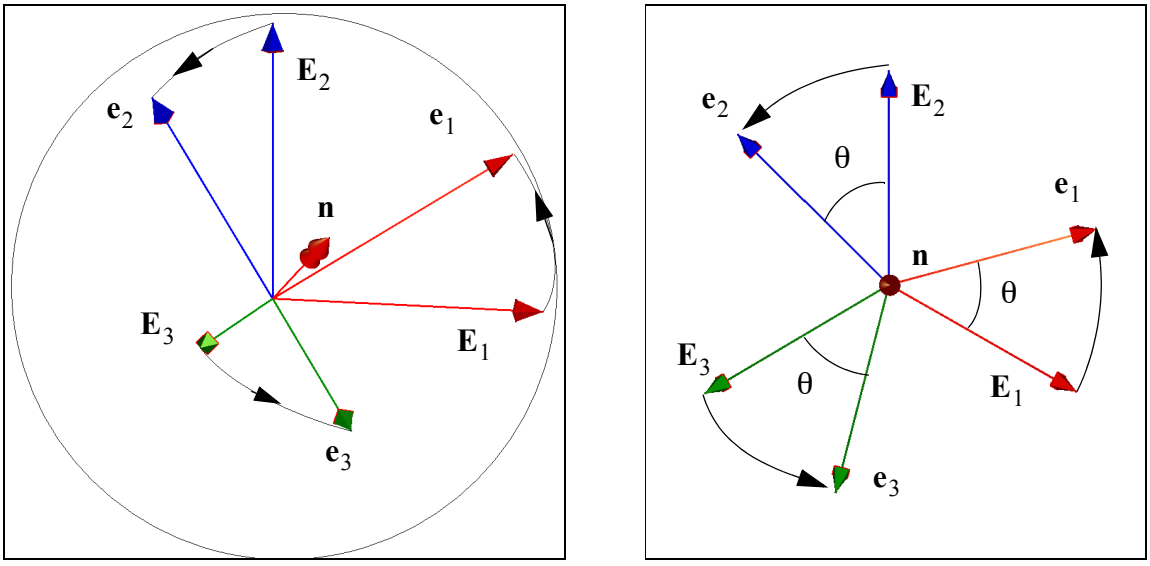

a) 3D view b) Rotation - plane view

Figure 3.1 Updated base-vectors

resentation of any finite rotation in $\mathbb{R}^3$ if $\theta \in \{0, \mathbb{R}_+\}$ and $\mathbf{n} \in \mathbb{R}^3$, where $\|\mathbf{n}\| = 1$. This is a set of only 3 free parameters, which is the minimum number of parameters needed for the definition to be unique. In Figure 3.1b, the motion of the base-vectors is depicted in the rotation-plane, defined by the normal $\mathbf{n}$. Here it is seen that any rotation in 3D can be thought of as a 2D rotation in a specific plane. An important property of the representation is that the rotation is defined to be non-negative. On account of this, no information is lost in the transition to the so-called pseudovector representation of rotations:

$$\boldsymbol{\theta} = \theta\mathbf{n} = \theta\begin{bmatrix} n_1 \\ n_2 \\ n_3 \end{bmatrix} = \begin{bmatrix} \theta_1 \\ \theta_2 \\ \theta_3 \end{bmatrix} \quad \text{and} \quad \theta = \|\boldsymbol{\theta}\| = \theta\|\mathbf{n}\| = \theta \tag{3.7}$$

The relationship between the pseudovector representation and the rotation matrix $\mathbf{R}$ is defined by the relation known as Rodriguez formula:

$$\mathbf{R}(\theta,\ \mathbf{n}) = \mathbb{1} + (1 - \cos(\theta))\mathrm{Spin}^2(\mathbf{n}) + \sin(\theta)\mathrm{Spin}(\mathbf{n}) \tag{3.8}$$

$\mathrm{Spin}(\mathbf{n})$ is a skew symmetric matrix, defined for any vector $\mathbf{w}$ as the matrix-representation of the cross product $\mathrm{Spin}(\mathbf{w})\mathbf{b} = \mathbf{w} \times \mathbf{b}$.

$$\mathrm{Spin}(\mathbf{n}) = \begin{bmatrix} 0 & -n_3 & n_2 \\ n_3 & 0 & -n_1 \\ -n_2 & n_1 & 0 \end{bmatrix} \tag{3.9}$$

The inverse of *Spin* is the operator *Axial* on the skew symmetric matrix $\mathbf{W}$ ($\mathbf{W} = \mathrm{Spin}(\mathbf{w})$, $\mathrm{Axial}(\mathbf{W}) = \mathbf{w}$).

As noted by several authors, among which can be mentioned the references [14,10,13,35], this relation can be derived from the exponential map of the spin of the pseudovector[1]. By using $\mathrm{Spin}^2(\mathbf{n}) = \mathbf{n} \otimes \mathbf{n} - \mathbb{1}$, an equivalent expression for Equation (3.8) is:

$$\mathbf{R}(\theta,\ \mathbf{n}) = \mathbb{1}\cos(\theta) + (1 - \cos(\theta))\mathbf{n} \otimes \mathbf{n} + \sin(\theta)\mathrm{Spin}(\mathbf{n}) \tag{3.10}$$

In the following, the short-hand notation $\widehat{(\circ)} = \mathrm{Spin}(\circ)$ will often be used in conjunction with individual vectors for compactness. The diacritical $(\frown)$ will not be used in any other context, thus minimizing the notational confusion.

It is rather straightforward to show that $\mathbf{R}(\mathbf{n},\ \theta) = \mathbf{R}(\mathbf{n},\ \theta + n2\pi) = \mathbf{R}(-\mathbf{n},\ 2\pi - \theta)$. Thus the matrix representation of rotations is not unique, but rather periodic in θ and with the symmetry $(\mathbf{n},\ \theta) = (-\mathbf{n},\ 2\pi - \theta)$. This result is not surprising as the rotation-matrix only contains information about the effect of rotations on vectors, and a vector rotated by an angle θ will have the same components as a vector rotated by $\theta + n \cdot 2\pi$. As such, $\mathbf{R}$ does not define the concept of a rotation, but rather the action of rotation on the compo-

1. See Appendix C for a geometric interpretation of the exponential map

nents of a vector (tensor). Special care will therefore have to be taken if this form is used as parametrization. Interpolation, for instance, will often be based on some form of heuristic, such as assuming that the rotation is limited to $0 \le \theta \le \pi$. In this range $\mathbf{R}$ is unique, and a unique function $\boldsymbol{\theta}(\mathbf{R})$, that extracts the pseudovector from a given proper orthogonal matrix $\mathbf{R}$, exists. In contrast, the pseudo-vector representation is complete, unique and singularity-free, regardless of the magnitude of θ. However, as no method exists for direct evaluation of compound pseudovectors, composition rules will either have singularities or be non-unique. One method, frequently adopted, is to make use of the composition rule for rotation matrices; given two successive pseudovector rotations, $\boldsymbol{\alpha}$ followed by $\boldsymbol{\beta}$, the rotation matrix $\mathbf{R}_{\alpha+\beta}$ of the total rotation can be expressed as:

$$\mathbf{R}_{\alpha+\beta} = \mathbf{R}(\boldsymbol{\beta})\mathbf{R}(\boldsymbol{\alpha}) = \mathbf{R}(\boldsymbol{\psi}) \tag{3.11}$$

The pseudovector $\boldsymbol{\psi} = \boldsymbol{\theta}(\mathbf{R}_{\alpha+\beta})$, is now the pseudovector of the compound rotation. To extract the components of $\boldsymbol{\psi}$, the method of *Spurrier's algorithm* (Appendix D) is generally the method of choice. In this way, singularities are avoided, although uniqueness is lost.

3.2.2 Rodriguez-parameters

In the previous section, the director $(\mathbf{n})$ was scaled by the magnitude of rotation. This is, however, an almost arbitrary choice. Another frequently used scaling is the tangent-scaled pseudovector, or Rodriguez-parameters:

$$\bar{\boldsymbol{\theta}} = \frac{\tan(\|\boldsymbol{\theta}\|/2)}{\|\boldsymbol{\theta}\|}\boldsymbol{\theta} = \tan(\|\boldsymbol{\theta}\|/2)\,\mathbf{n} \tag{3.12}$$

In (3.12), the superimposed bar is used to distinguish the Rodriguez-parameters from the pseudovector. This representation caters to a direct evaluation of compound rotations: Given two successive rotations, $\bar{\boldsymbol{\alpha}}$ followed by $\bar{\boldsymbol{\beta}}$, it can be shown that the total rotation $\bar{\boldsymbol{\psi}}$ can be expressed as:

$$\bar{\boldsymbol{\psi}} = \frac{1}{1-(\bar{\boldsymbol{\alpha}}\cdot\bar{\boldsymbol{\beta}})}[\bar{\boldsymbol{\alpha}}+\bar{\boldsymbol{\beta}}-\bar{\boldsymbol{\alpha}}\times\bar{\boldsymbol{\beta}}] \tag{3.13}$$

The principal disadvantage of the Rodriguez representation is that it becomes singular for rotations near $\pi \pm 2n\cdot\pi$, secondly we get $\bar{\boldsymbol{\psi}}(\mathbf{n},\ \theta) = \bar{\boldsymbol{\psi}}(\mathbf{n},\ \theta + 2n\cdot\pi)$. Neither will

usually constitute a problem, as most problems in the field of civil engineering does not involve rotations of this magnitude. However, a general purpose procedure should be able to handle these situations, if for no other reason, rotations during an incremental-iterative solution strategy may far exceed the possibly modest end-result. The benefit of the direct evaluation of compound rotations is therefore evaluated not to outweigh the danger of possible singularities. For a detailed account of the Rodriguez-parameters, see e.g. Géradin and Rixen [14].

3.3 Variation of rotations

A key point of any analysis involving large rotations is the variation of the rotation operator $\mathbf{R}$. Since **SO**(3) is a differentiable non-linear manifold and not a vector-space, some subtle differences appear compared with operating in $\mathbb{R}^3$. Operations such as interpolation, for instance, are not valid on manifolds. To overcome this difficulty, we typically do calculations in the tangent space of $\mathbf{R}$ (written $T_{\mathbf{R}(\boldsymbol{\theta}_0)}\mathbf{R}$), a strategy that works well with the finite element formulation. As there exists an isometry between $T_{\mathbf{R}(\boldsymbol{\theta}_0)}\mathbf{R}$ and $\mathbb{R}^3$, interpolation and other vector-operations are valid in this space. As indicated by $\mathbf{R}(\boldsymbol{\theta}_0)$, the tangent space changes continuously with position $\boldsymbol{\theta}_0$ and some initial choices will have to be made about in which space calculations are performed. First of all one has to be clear on which parameter is a free parameter and how it is updated. For completeness, we will elaborate in some detail, but the reader is referred to [14, 8, 9] for further details and a somewhat different approach.

In general, the rotation operator can be expressed as:

$$\mathbf{R} = \mathbf{R}(\boldsymbol{\theta}_n)\mathbf{R}(\boldsymbol{\theta}_{n-1})\cdots\mathbf{R}(\boldsymbol{\theta}_1)\mathbf{R}(\boldsymbol{\theta}_0) \tag{3.14}$$

where each $\boldsymbol{\theta}_i$, $i = 1..n$ can be a free parameter on which variation makes sense, $\boldsymbol{\theta}_0$ is denoted the identity and will thus be treated as a constant. Normally we will only be concerned with rotations with only one free parameter on the form $\mathbf{R} = \mathbf{R}(\boldsymbol{\theta})\mathbf{R}(\boldsymbol{\theta}_0)$.

Note: This is a so-called spatial form of rotations, where an already rotated state is further rotated by θ. *An equally valid form is the material description i.e.* $\mathbf{R} = \mathbf{R}(\boldsymbol{\theta}_0)\mathbf{R}(\boldsymbol{\Theta})$,

where Θ *is a material-vector and* $\mathbf{R}(\Theta) = \mathbf{R}^{\mathsf{T}}(\theta_0)\mathbf{R}(\theta)\mathbf{R}(\theta_0)$. *In the following we will continue to pursue the spatial description.*

Since the variation of the identity is zero, we start by taking the Frêchet-derivative of the incremental rotation with a perturbed θ:

$$\delta\mathbf{R}(\theta) = \mathrm{D}\mathbf{R}(\theta+\delta\theta)\cdot\delta\theta = \tag{3.15}$$

$$(\delta\theta\cdot\theta)\left[\frac{\sin(\|\theta\|)}{\|\theta\|}(\mathbf{n}\otimes\mathbf{n}-\mathbb{1})-\frac{\sin^2(\|\theta\|/2)}{(\|\theta\|/2)^2}\mathbf{n}\otimes\mathbf{n}+\left(\frac{\cos(\|\theta\|)}{\|\theta\|}-\frac{\sin(\|\theta\|)}{\|\theta\|^2}\right)\mathrm{Spin}(\mathbf{n})\right]$$

$$+\|\theta\|\frac{\sin^2(\|\theta\|/2)}{(\|\theta\|/2)^2}\mathrm{Sym}(\delta\theta\otimes\mathbf{n})+\frac{\sin(\|\theta\|)}{\|\theta\|}\mathrm{Spin}(\delta\theta)$$

where $\mathbf{n}$ is the unit director of θ.

After extensive algebraic manipulation we arrive at the result (see Appendix B)

$$T_{\mathbf{R}(\theta_0)}\mathbf{R} = \mathrm{D}\mathbf{R}\cdot\delta\theta = \mathrm{Spin}(\mathbf{H}^{-1}(\theta)\delta\theta)\mathbf{R} \tag{3.16}$$

where

$$\mathbf{H}^{-1}(\theta) = \mathbb{1}+\frac{2}{\|\theta\|}\sin^2\left(\frac{\|\theta\|}{2}\right)\widehat{\mathbf{n}}+\left(1-\frac{\sin(\|\theta\|)}{\|\theta\|}\right)\widehat{\mathbf{n}}^2 \tag{3.17}$$

If θ_0 is the pseudo-vector of the fully rotated state $\mathbf{R}$, such that $\theta = 0$, we get the variation expressed as the variation of the incremental rotation (instantaneous axis of rotation).

$$\mathbf{H}^{-1} = 1,\ T_{\mathbf{R}}\mathbf{R} = \mathrm{D}\mathbf{R}(\delta\omega)\mathbf{R}\cdot\delta\omega = \mathrm{Spin}(\delta\omega)\mathbf{R} \tag{3.18}$$

The shift in variable from θ to ω is motivated by the need to distinguish the additive increment $\Delta\theta$, $\mathbf{R} = \mathbf{R}(\theta+\Delta\theta)\mathbf{R}(\theta_0)$, from the multiplicative increment $\Delta\omega$, $\mathbf{R} = \mathbf{R}(\Delta\omega)\mathbf{R}(\theta)\mathbf{R}(\theta_0)$.

Since a perturbed θ should produce the same perturbed $\mathbf{R}$ as $\delta\omega$, we get the relation

$$\delta\theta = \mathbf{H}(\theta)\delta\omega \tag{3.19}$$

Following the notation of [16], $\mathbf{H}$ is a differential form that relates infinitesimal multiplicative rotation-increments to infinitesimal vectorial, additive, increments. It should be

noted that $\mathbf{H}^{-1}$ becomes singular when $\|\boldsymbol{\theta}\| = 2n\pi$ due to the fact that $\mathbf{R} = \mathbb{1}$ at these points. Since $\|\boldsymbol{\theta} + \delta\boldsymbol{\theta}\| = \|\boldsymbol{\theta}\|$ for $\delta\boldsymbol{\theta} \perp \boldsymbol{\theta}$, such a perturbation produce no change in $\mathbf{R}$ and thus $\delta\boldsymbol{\omega} = 0$.

$$\mathbf{H}(\boldsymbol{\theta}) = \mathbb{1} - \frac{\|\boldsymbol{\theta}\|}{2}\widehat{\mathbf{n}} + \left(1 - \frac{1}{2}\frac{\|\boldsymbol{\theta}\|}{\tan(\|\boldsymbol{\theta}\| / 2)}\right)\widehat{\mathbf{n}}^2 \tag{3.20}$$

In some texts the relation (3.19) is referred to as the relation between the infinitesimal (additive) rotations and the finite increments (multiplicative). To avoid confusion we stress that calculations in $T_1\mathbf{R}$ (i.e. $\theta_0 = 0$) are just as valid as in $T_{\mathbf{R}}\mathbf{R}$. Neither are restricted to infinitesimal rotations. While $T_1\mathbf{R}$ will yield additive increments, $T_{\mathbf{R}}\mathbf{R}$ produce multiplicative increments. As reported by Cardona and Géradin [8], operating in the vector-space of $T_1\mathbf{R}$ also makes it possible to derive a symmetric stiffness matrix in a consistent manner, even at a non-equilibrium state. This is not the case for operations in $T_{\mathbf{R}}\mathbf{R}$. The principal objection to $T_1\mathbf{R}$ lies in the fact that the space is a function of the rotational state. As will be shown later, the co-rotational formulation at the element-level will produce different measures of deformational rotation in a single node for neighboring elements. Thus, $T_1\mathbf{R}$ will be specific for each element and a transformation of the form (3.19) must be performed regardless.

3.4 Incremental/iterative solution strategy

In solving a non-linear set of equations, a commonly adopted strategy is to formulate the problem as the solution of a vanishing residual after incrementing the independent variables (such as external loading). By applying the Newton-Raphson algorithm we then seek to eliminate this residual by iterating until an accepted solution is found. In the following we will study the effect of this strategy when large rotations are part of the unknowns. Although not discussed here, it can easily be argued that the same effects will occur when a purely incremental algorithm is adopted, as the increments will behave in much the same manner as the iterations. The consequences are however quite different as will be noted at the end of this section.

To simplify the analysis, the problem can be stated as:

$$\mathbf{r} = \mathbf{f}(\boldsymbol{\theta}) - \mathbf{f}_e = 0 \tag{3.21}$$

where $\mathbf{f}(\theta)$ is a general (non-linear) vector-function of the rotational state at a single point and $\mathbf{f}_e$ is a vector of corresponding independent variables to be considered as constants. After employing the Newton-Raphson strategy, we can solve for the incremental (multiplicative) rotations until the residual vanishes (or an accepted solution is achieved).

$$\Delta\boldsymbol{\omega}_{i+1} = -\mathbf{K}_T^{-1}(\mathbf{f}(\boldsymbol{\theta}_i) - \mathbf{f}_e) = -\mathbf{K}_T^{-1}\mathbf{r}_i \tag{3.22}$$

$$\boldsymbol{\theta}_{i+1} = \Delta\boldsymbol{\omega}_{i+1} \oplus \boldsymbol{\theta}_i \tag{3.23}$$

$$\mathbf{R}(\boldsymbol{\theta}_{i+1}) = \mathbf{R}(\Delta\boldsymbol{\omega}_{i+1})\mathbf{R}(\boldsymbol{\theta}_i) \tag{3.24}$$

Where the pseudovector $\Delta\boldsymbol{\omega}_{i+1}$ is the instantaneous rotation and $\mathbf{K}_T$ is the jacobian matrix. In Equation (3.23) we have introduced the binary operator $\oplus$ to represent the updating procedure (composition). As the pseudovectors are not true vectorial quantities they do not add as vectors, rather the update must be performed by pre-multiplication as shown in Equation (3.24). The underlying assumption in this strategy is that the update brings us from one allowable state of rotation to another. If we denote the set of all permissible states as $\mathbb{S}_\theta$ and the set of all permissible increments as $\mathbb{S}_{\Delta\omega}$, the update is a mapping f such that

$$f : \mathbb{S}_{\Delta\omega} \times \mathbb{S}_\theta \rightarrow \mathbb{S}_\theta \tag{3.25}$$

As the identity element must be part of $\mathbb{S}_\theta$ [1], the set $\mathbb{S}_{\Delta\omega}$ must be fully contained within $\mathbb{S}_\theta$ and a common strategy is to set $\mathbb{S}_{\Delta\omega} = \mathbb{S}_\theta$. To assure convergence, for each element in the set there must also be an inverse element. Provided the function f is associative, we have now defined a group under the operation of f. To clarify we can make an example where Equation (3.21) is a function of vectorial quantities rather than pseudovectors.

$$\Delta\mathbf{v}_{i+1} = -\mathbf{K}_T^{-1}(\mathbf{f}(\mathbf{v}_i) - \mathbf{f}_e) = -\mathbf{K}_T^{-1}\mathbf{r}_i \tag{3.26}$$

$$\mathbf{v}_{i+1} = \Delta\mathbf{v}_{i+1} + \mathbf{v}_i, \qquad \mathbf{v}_0 = \mathbf{0} \tag{3.27}$$

1. The initial state will in general be the identity element. If an alternate state is defined as the initial state, the initial state can be defined as the identity element referred to this state.

If $\Delta\mathbf{v}_i \in \mathbb{R}^n$, then it follows naturally that this also applies for $\mathbf{v}_i$ for i = 1,2, …,n. If, on the other hand, the components of $\mathbf{v}_i$ and $\Delta\mathbf{v}_i$ are defined to be elements in $\{0, \mathbb{R}_+\}$ (0 is needed to provide the identity element), the procedure is only guaranteed to find solutions for a residual-norm described by a convex function. The set of positive real values, including zero, lacks the fundamental group property of containing the inverse element under the operation of addition.

In light of these considerations, we can proceed to investigate whether the procedure is computationally sound for solving functions involving finite rotations under the assumption that $\mathbb{S}_{\Delta\omega} = \mathbb{S}_\theta$. If we start by defining

$$\mathbb{S}_\theta^{(j,\ k)} = \{\boldsymbol{\theta} = (\theta_1, \theta_2, \theta_3) \,|\, \theta_i \in \mathbb{R},\ \theta_j = \theta_k = 0 \text{ and } i, j, k \text{ is a permutation of } 1, 2, 3\} \quad (3.28)$$

which is equivalent to restricting all rotations to be defined by a single axis, we can easily show that this is **SO**(2), thus having the discussed group properties under the operation of (3.23). Likewise, if we define

$$\mathbb{S}_\theta^0 = \{\boldsymbol{\theta} = (\theta_1, \theta_2, \theta_3) \,|\, \theta_i, \theta_j, \theta_k \in \mathbb{R} \text{ and } i, j, k \text{ is a permutation of } 1, 2, 3\} = \mathbb{R}^3 \quad [1] \quad (3.29)$$

that is setting all rotations in space as permissible, we can show equivalence with **SO**(3). In a typical finite element code, these cases will define cases of full rotational freedom in two and three dimensions respectively. If, on the other hand, we want to define the permissible states as the intermediate state, we loose the equivalence with **SO**(n).

We start by defining the set of permissible states as;

$$\mathbb{S}_\theta^k = \{\boldsymbol{\theta} = (\theta_1, \theta_2, \theta_3) \,|\, \theta_i, \theta_j \in \mathbb{R},\ \theta_k = 0 \text{ and } i, j, k \text{ is a permutation of } 1, 2, 3\} \quad (3.30)$$

which implies restraining the rotation about a one axis, while leaving the others free. In the following we will show that this set is not closed under addition as defined in Equations (3.23) and (3.24). Assume that $k = 1$, that is we want to restrain the rotation so that it contains no component in the direction of $\mathbf{E}_1$. The general form of a rotation-matrix obtained from $\theta\mathbf{n} \in \mathbb{S}_\theta^x$ can be written as:

1. This is a slight abuse of notation, and it is important to keep in mind that the arithmetic rules in $\mathbb{R}^3$ does not in general apply in $\mathbb{S}_\theta$. By $\mathbb{R}^3$ we denote the set, not the vector space.

$$\mathbf{R}(\theta\mathbf{n}) = \begin{bmatrix} \cos(\theta) & 0 & 0 \\ & n_y^2+n_z^2\cos(\theta) & (1-\cos(\theta))n_y n_z \\ sym & & n_z^2+n_y^2\cos(\theta) \end{bmatrix} + \begin{bmatrix} 0 & -n_z\sin(\theta) & n_y\sin(\theta) \\ & 0 & 0 \\ skew & & 0 \end{bmatrix} \tag{3.31}$$

where the matrix is split into a symmetric and a skew symmetric part for clarity.

Let $\boldsymbol{\alpha} = \begin{bmatrix} 0 & \alpha & 0 \end{bmatrix}^T$, $\boldsymbol{\beta} = \begin{bmatrix} 0 & 0 & \beta \end{bmatrix}^T$ and $\|\boldsymbol{\alpha}\| + \|\boldsymbol{\beta}\| < \pi$ be two successive rotations. Since both $\boldsymbol{\alpha}, \boldsymbol{\beta} \in \mathbb{S}^1_\theta$, the composition of these should result in a matrix of the form (3.31) if the set is closed under (3.24). Particularizing for $\boldsymbol{\alpha}$ and $\boldsymbol{\beta}$ we get:

$$\mathbf{R}(\boldsymbol{\alpha}) = \begin{bmatrix} \cos(\alpha) & 0 & \sin(\alpha) \\ 0 & 1 & 0 \\ -\sin(\alpha) & 0 & \cos(\alpha) \end{bmatrix}, \qquad \mathbf{R}(\boldsymbol{\beta}) = \begin{bmatrix} \cos(\beta) & -\sin(\beta) & 0 \\ \sin(\beta) & \cos(\beta) & 0 \\ 0 & 0 & 1 \end{bmatrix} \tag{3.32}$$

and the composition of $\boldsymbol{\alpha}$ followed by $\boldsymbol{\beta}$ results in:

$$\mathbf{R}^{sym} = \frac{1}{2}\begin{bmatrix} 2\cos(\alpha)\cos(\beta) & (\cos(\alpha)-1)\sin(\beta) & (\cos(\beta)-1)\sin(\alpha) \\ & 2\cos(\beta) & \sin(\alpha)\sin(\beta) \\ sym & & 2\cos(\alpha) \end{bmatrix} \text{ and} \tag{3.33}$$

$$\mathbf{R}^{skew} = \frac{1}{2}\begin{bmatrix} 0 & -(1+\cos(\alpha))\sin(\beta) & (1+\cos(\beta))\sin(\alpha) \\ & 0 & \sin(\alpha)\sin(\beta) \\ skew & & 0 \end{bmatrix} \tag{3.34}$$

It is easily verified that this is not the general form for arbitrary α and β [1], and composition will bring us from $\mathbb{S}^1_\theta$ to $\mathbb{R}^3$. In formal notation:

$$f : \mathbb{S}^1_\theta \times \mathbb{S}^1_\theta \rightarrow \mathbb{R}^3 \supseteq \mathbb{S}^1_\theta \tag{3.35}$$

This shows that the restriction (3.30) only restricts the incremental motion and not the total motion. A physical interpretation of this constraint could be a ball of radius r rolling without spinning on a table-top. Consider the effect on a body-attached coordinate-system when the ball first rolls πr in one direction followed by rolling a distance πr in a direction normal to the first direction. The body-attached coordinate-system will now have

1. For instance, in (3.31) $\mathbf{R}^{skew}_{2,3} = 0$, whereas $\mathbf{R}^{skew}_{2,3} = \sin(\alpha)\sin(\beta)$ in (3.34).

experienced spinning 90◦ normal to the plane. This fact will in general restrict the practical use of this form to explicit time-integration schemes or other purely incremental algorithms.

3.5 Alternative parametrization

In order to investigate the possibility of imposing other boundary-conditions than those applying to **SO**(2), it is of interest to formulate alternative rotational parametrizations. One such parametrization with an intuitive physical interpretation is the so-called Euler-angles[1]. This is a parametrization commonly used in aviation, where the quantities *roll, pitch and yaw* are three successive rotations about three distinct axes. This can be formally written as:

$$\mathbf{R} = \mathbf{R}(\phi_3\mathbf{E}_3)\mathbf{R}(\phi_2\mathbf{E}_2)\mathbf{R}(\phi_1\mathbf{E}_1) \tag{3.36}$$

where *roll* = ϕ_1 , *pitch* = ϕ_2 and *yaw* = ϕ_3 .

Usually, our equations are given as functions of the pseudovector and not the Euler-angles. In order to transform these, we need a differential form that relates rotational increments to increments in the Euler-angles. By equating the two and taking the variation we obtain:

$$\mathbf{R} = \mathbf{R}(\theta\mathbf{n}) = \mathbf{R}_3\mathbf{R}_2\mathbf{R}_1\,, \qquad \mathbf{R}_i = \mathbf{R}(\phi_i\mathbf{E}_i) \tag{3.37}$$

$$\delta\mathbf{R} = \delta\widehat{\boldsymbol{\omega}}\mathbf{R} = \delta\phi_3\,\widehat{\mathbf{E}}_3\,\mathbf{R} + \delta\phi_2\mathbf{R}_3\,\widehat{\mathbf{E}}_2\,\mathbf{R}_2\mathbf{R}_1 + \delta\phi_1\mathbf{R}_3\mathbf{R}_2\,\widehat{\mathbf{E}}_1\,\mathbf{R}_1 \tag{3.38}$$

$$\delta\widehat{\boldsymbol{\omega}} = \delta\phi_3\,\widehat{\mathbf{E}}_3 + \delta\phi_2\mathbf{R}_3\,\widehat{\mathbf{E}}_2\,\mathbf{R}_3^{\mathsf{T}} + \delta\phi_1\mathbf{R}_3\mathbf{R}_2\,\widehat{\mathbf{E}}_1\,\mathbf{R}_2^{\mathsf{T}}\mathbf{R}_3^{\mathsf{T}} \tag{3.39}$$

Extracting the axial-vector of (3.39) leads to:

$$\delta\boldsymbol{\omega} = \delta\phi_3\mathbf{E}_3 + \delta\phi_2\mathbf{R}_3\mathbf{E}_2 + \delta\phi_1\mathbf{R}_3\mathbf{R}_2\mathbf{E}_1 = \begin{bmatrix}\mathbf{R}_3\mathbf{R}_2\mathbf{E}_1 & \mathbf{R}_3\mathbf{E}_2 & \mathbf{E}_3\end{bmatrix}\begin{bmatrix}\delta\phi_1\\ \delta\phi_2\\ \delta\phi_3\end{bmatrix} = \boldsymbol{\Phi}\delta\boldsymbol{\phi} \tag{3.40}$$

1. The parametrization described here is strictly speaking known as *Bryant angles*. By setting $\phi_2 = \frac{\pi}{2} + \alpha_2$, the true Euler-angles are obtained.

where the matrix $\mathbf{\Phi}$ is defined by:

$$\begin{aligned}\mathbf{\Phi} &= \begin{bmatrix}\mathbf{R}_3\mathbf{R}_2\mathbf{E}_1 & \mathbf{R}_3\mathbf{E}_2 & \mathbf{E}_3\end{bmatrix} = \begin{bmatrix}\mathbf{R}_3\mathbf{R}_2\mathbf{E}_1 & \mathbf{R}_3\mathbf{E}_2 & \mathbf{R}_3\mathbf{E}_3\end{bmatrix} \\ &= \mathbf{R}_3\begin{bmatrix}\mathbf{R}_2\mathbf{E}_1 & \mathbf{E}_2 & \mathbf{E}_3\end{bmatrix}\end{aligned} \tag{3.41}$$

When particularizing for $\mathbf{E}_i = \mathbf{I}_i$:

$$\mathbf{\Phi} = \begin{bmatrix}\cos(\phi_3)\cos(\phi_2) & -\sin(\phi_3) & 0 \\ \sin(\phi_3)\cos(\phi_2) & \cos(\phi_3) & 0 \\ -\sin(\phi_2) & 0 & 1\end{bmatrix} \tag{3.42}$$

Since the physical moments are conjugate to the variation of the instantaneous axis of rotation in a virtual work sense, we can use this relation to re-express the virtual work of the unbalanced forces and moments in terms of the variations of the Euler-angles. This is a critical step in constructing a consistent formulation, as the varied parameters should be the same as the principal unknowns (see for instance [20]).

$$\delta W = \begin{bmatrix}\delta\mathbf{v} \\ \delta\boldsymbol{\omega}\end{bmatrix}\cdot\mathbf{f}_{\text{unb}} = \begin{bmatrix}\mathbf{1} & \mathbf{0} \\ \mathbf{0} & \mathbf{\Phi}\end{bmatrix}\begin{bmatrix}\delta\mathbf{v} \\ \delta\boldsymbol{\phi}\end{bmatrix}\cdot\mathbf{f}_{\text{unb}} = \begin{bmatrix}\delta\mathbf{v} \\ \delta\boldsymbol{\phi}\end{bmatrix}\cdot\begin{bmatrix}\mathbf{1} & \mathbf{0} \\ \mathbf{0} & \mathbf{\Phi}^{\mathsf{T}}\end{bmatrix}\mathbf{f}_{\text{unb}}\ , \tag{3.43}$$

where $\mathbf{f}_{\text{unb}} = \begin{bmatrix}\mathbf{n}_{\text{unb}}^{\mathsf{T}} & \mathbf{m}_{\text{unb}}^{\mathsf{T}}\end{bmatrix}^{\mathsf{T}}$ are the unbalanced residual forces. The Jacobian of (3.43), considering only the rotational terms, becomes:

$$\mathbf{K}_{T,\,\phi} = \frac{\partial}{\partial\boldsymbol{\phi}}\left(\begin{bmatrix}\mathbf{1} & \mathbf{0} \\ \mathbf{0} & \mathbf{\Phi}^{\mathsf{T}}\end{bmatrix}\mathbf{f}_{\text{unb}}\right) = \begin{bmatrix}\mathbf{0} & \mathbf{0} \\ \mathbf{0} & \mathbf{m}_{\text{unb}}\cdot\dfrac{\partial}{\partial\boldsymbol{\phi}}\mathbf{\Phi}\end{bmatrix} + \begin{bmatrix}\mathbf{1} & \mathbf{0} \\ \mathbf{0} & \mathbf{\Phi}^{\mathsf{T}}\end{bmatrix}\frac{\partial\mathbf{f}_{\text{unb}}}{\partial\boldsymbol{\phi}} \tag{3.44}$$

The second term evaluates to the stiffness matrix congruently transformed with respect to the pseudo-vector representation, and it can be denoted the material part in this context. It is important to note that the congruent form does not change positive semi-definiteness in the transformed matrix.

$$\mathbf{K}_{M\phi} = \begin{bmatrix}\mathbf{1} & \mathbf{0} \\ \mathbf{0} & \mathbf{\Phi}^{\mathsf{T}}\end{bmatrix}\frac{\partial\mathbf{f}_{\text{unb}}}{\partial\boldsymbol{\phi}} = \begin{bmatrix}\mathbf{1} & \mathbf{0} \\ \mathbf{0} & \mathbf{\Phi}^{\mathsf{T}}\end{bmatrix}\frac{\partial\mathbf{f}_{\text{unb}}}{\partial\boldsymbol{\omega}}\frac{\partial\boldsymbol{\omega}}{\partial\boldsymbol{\phi}} = \begin{bmatrix}\mathbf{1} & \mathbf{0} \\ \mathbf{0} & \mathbf{\Phi}^{\mathsf{T}}\end{bmatrix}\mathbf{K}(\boldsymbol{\omega})\mathbf{\Phi} \tag{3.45}$$

The first term constitute the geometric part in the transition from pseudovectors to Euler-angles, and written out column by column becomes (subscripts on the unbalanced moments are omitted to reduce clutter):

$$\mathbf{m} \cdot \frac{\partial}{\partial \phi_1} \mathbf{\Phi} = \begin{bmatrix} 0 \\ 0 \\ 0 \end{bmatrix} \tag{3.46}$$

$$\mathbf{m} \cdot \frac{\partial}{\partial \phi_2} \mathbf{\Phi} = \begin{bmatrix} (\mathbf{R}_3 \widehat{\mathbf{E}}_2 \mathbf{R}_2 \mathbf{E}_1)^{\mathsf{T}} \\ 0 \\ 0 \end{bmatrix} \mathbf{m} = \begin{bmatrix} \mathbf{R}_3 \mathbf{R}_2 \widehat{\mathbf{E}}_2 \mathbf{E}_1 \cdot \mathbf{m} \\ 0 \\ 0 \end{bmatrix} = - \begin{bmatrix} \mathbf{R}_3 \mathbf{R}_2 \mathbf{E}_3 \cdot \mathbf{m} \\ 0 \\ 0 \end{bmatrix} \tag{3.47}$$

$$\mathbf{m} \cdot \frac{\partial}{\partial \phi_3} \mathbf{\Phi} = \begin{bmatrix} (\widehat{\mathbf{E}}_3 \mathbf{R}_3 \mathbf{R}_2 \mathbf{E}_1)^{\mathsf{T}} \\ (\widehat{\mathbf{E}}_3 \mathbf{R}_3 \mathbf{E}_2)^{\mathsf{T}} \\ 0 \end{bmatrix} \mathbf{m} = \begin{bmatrix} \widehat{\mathbf{E}}_3 \mathbf{R}_3 \mathbf{R}_2 \mathbf{E}_1 \cdot \mathbf{m} \\ \mathbf{R}_3 \widehat{\mathbf{E}}_3 \mathbf{E}_2 \cdot \mathbf{m} \\ 0 \end{bmatrix} = - \begin{bmatrix} \mathbf{R}_3 \mathbf{R}_2 \mathbf{E}_1 \cdot (\mathbf{E}_3 \times \mathbf{m}) \\ \mathbf{R}_3 \mathbf{E}_1 \cdot \mathbf{m} \\ 0 \end{bmatrix} \tag{3.48}$$

$$\mathbf{K}_{G\phi} = - \begin{bmatrix} 0 & \mathbf{R}_3 \mathbf{R}_2 \mathbf{E}_3 \cdot \mathbf{m} & \mathbf{R}_3 \mathbf{R}_2 \mathbf{E}_1 \cdot (\mathbf{E}_3 \times \mathbf{m}) \\ 0 & 0 & \mathbf{R}_3 \mathbf{E}_1 \cdot \mathbf{m} \\ 0 & 0 & 0 \end{bmatrix} \tag{3.49}$$

[1]

If $\mathbf{E}_i = \mathbf{I}_i$, then

$$\mathbf{K}_{G\phi}(1,\ 2) = -\mathrm{m}_1 \cos(\phi_3) \sin(\phi_2) - \mathrm{m}_2 \sin(\phi_3) \sin(\phi_2) - \mathrm{m}_3 \cos(\phi_2)$$

$$\mathbf{K}_{G\phi}(1,\ 3) = -\mathrm{m}_1 \sin(\phi_3) \cos(\phi_2) + \mathrm{m}_2 \cos(\phi_3) \cos(\phi_2)$$

$$\mathbf{K}_{G\phi}(2,\ 3) = -\mathrm{m}_1 \cos(\phi_3) - \mathrm{m}_2 \sin(\phi_3)$$

at the identity we get

1. In the last steps of this derivation, the fact that $\widehat{\mathbf{E}}_2 \mathbf{E}_1 = -\mathbf{E}_3$ and $\widehat{\mathbf{E}}_3 \mathbf{E}_2 = -\mathbf{E}_1$ has been used in (3.47) and (3.48). By omitting this assumption, an expression of the form (3.49) can be obtained for any $\mathbf{E}_i$'s, not necessarily defining a full basis. This will, however, invalidate the following discussion of the properties of $\mathbf{\Phi}$.

$$\mathbf{K}^0_{G\phi} = -\begin{bmatrix} 0 & \mathbf{m}_3 & \mathbf{E}_1 \cdot (\mathbf{E}_3 \times \mathbf{m}) \\ 0 & 0 & \mathbf{m}_1 \\ 0 & 0 & 0 \end{bmatrix} = -\begin{bmatrix} 0 & \mathbf{m}_3 & -\mathbf{m}_2 \\ 0 & 0 & \mathbf{m}_1 \\ 0 & 0 & 0 \end{bmatrix} \tag{3.50}$$

Upon closer investigation of the matrix $\mathbf{\Phi}$, we see that

$$\mathbf{\Phi}^\mathsf{T}\mathbf{\Phi} = \begin{bmatrix} (\mathbf{R}_3\mathbf{R}_2\mathbf{E}_1)^\mathsf{T} \\ (\mathbf{R}_3\mathbf{E}_2)^\mathsf{T} \\ \mathbf{E}_3^\mathsf{T} \end{bmatrix} \begin{bmatrix} \mathbf{R}_3\mathbf{R}_2\mathbf{E}_1 & \mathbf{R}_3\mathbf{E}_2 & \mathbf{E}_3 \end{bmatrix} = \begin{bmatrix} 1 & 0 & \mathbf{E}_1^\mathsf{T}\mathbf{R}_2^\mathsf{T}\mathbf{E}_3 \\ 0 & 1 & 0 \\ \mathbf{E}_3^\mathsf{T}\mathbf{R}_2\mathbf{E}_1 & 0 & 1 \end{bmatrix}, \tag{3.51}$$

thus $\mathbf{\Phi}$ is orthogonal for $\phi_2 = n \cdot \pi$, and the transformation (3.45) does not change the eigenvalues of the original stiffness. The determinant of $\mathbf{\Phi}$ is $|\mathbf{\Phi}| = \pm\sqrt{1-(\mathbf{E}_1^\mathsf{T}\mathbf{R}_2^\mathsf{T}\mathbf{E}_3)^2} = \mathbf{E}_1 \cdot \mathbf{R}_2\mathbf{E}_1$, and because $0 \le |\mathbf{\Phi}|^2 \le 1$ the transformation will have a softening effect on the stiffness matrix away from the discrete points of orthogonality. Also, a point worth noting is that $2 \le rank(\mathbf{\Phi}) \le 3$. Singularities occur if and only if $\phi_2 = \pi/2 \pm n \cdot \pi$, in these cases the geometric contribution becomes:

$$\mathbf{K}_{G\phi} = -\begin{bmatrix} 0 & \pm\mathbf{R}_3\mathbf{E}_1 \cdot \mathbf{m} & \mp\mathbf{E}_3 \cdot (\mathbf{E}_3 \times \mathbf{m}) \\ 0 & 0 & \mathbf{R}_3\mathbf{E}_1 \cdot \mathbf{m} \\ 0 & 0 & 0 \end{bmatrix} = -\begin{bmatrix} 0 & \pm\mathbf{R}_3\mathbf{E}_1 \cdot \mathbf{m} & 0 \\ 0 & 0 & \mathbf{R}_3\mathbf{E}_1 \cdot \mathbf{m} \\ 0 & 0 & 0 \end{bmatrix} \tag{3.52}$$

This singularity arise naturally as the parametrization itself becomes singular at these points e.g. at $\phi_2 = \pi/2 \pm n \cdot \pi$ where the 3rd and updated 1st axes become co-linear.

$$\begin{aligned} \mathbf{R} &= \mathbf{R}(\phi_3\mathbf{E}_3)\mathbf{R}(\phi_2\mathbf{E}_2)\mathbf{R}(\phi_1\mathbf{E}_1) \\ &= \mathbf{R}(\phi_1\mathbf{e}_1)\mathbf{R}(\phi_3\mathbf{E}_3)\mathbf{R}(\phi_2\mathbf{E}_2) \\ &= \mathbf{R}((\phi_3+\phi_1)\mathbf{E}_3)\mathbf{R}(\phi_2\mathbf{E}_2) \end{aligned} \tag{3.53}$$

where $\mathbf{e}_1 = \mathbf{R}_3\mathbf{R}_2\mathbf{R}_1\mathbf{E}_1 = \mathbf{R}_3\mathbf{R}_2\mathbf{E}_1$ and the fact that $\mathbf{E}_3 \,||\, \mathbf{e}_1$ is used in the last step. If ϕ_2 is kept fixed at $\phi_2 = \pi/2 \pm n \cdot \pi$, both ϕ_1 and ϕ_3 will contribute to the single rotation about $\mathbf{E}_3$.

It may sometimes be necessary to have the inverse of relation (3.40). As this is not occurring in the current derivation, only the expression of $\mathbf{\Phi}^{-1}$ is given here. The points of sin-

gularity can easily be observed as the points where the denominators approach zero, that is when $\phi_2 \rightarrow \pi/2 \pm n \cdot \pi$.

$$\mathbf{\Phi}^{-1} = \begin{bmatrix} \mathbf{E}_1^\mathsf{T}\mathbf{R}_2^\mathsf{T} - \dfrac{(\mathbf{E}_1^\mathsf{T}\mathbf{R}_2^\mathsf{T}\mathbf{E}_3)}{(\mathbf{E}_3^\mathsf{T}\mathbf{R}_2^\mathsf{T}\mathbf{E}_3)}\mathbf{E}_3^\mathsf{T}\mathbf{R}_2^\mathsf{T} \\ \mathbf{E}_2^\mathsf{T} \\ \mathbf{E}_3^\mathsf{T} - \dfrac{(\mathbf{E}_3^\mathsf{T}\mathbf{R}_2\mathbf{E}_1)}{(\mathbf{E}_1^\mathsf{T}\mathbf{R}_2\mathbf{E}_1)}\mathbf{E}_1^\mathsf{T} \end{bmatrix} \mathbf{R}_3^\mathsf{T} \tag{3.54}$$

Comment on notation: In the preceding section capital **K** is used for the stiffnesses to emphasize that the relations are expressed at the system-level. It then becomes obvious that the geometric contribution evaluates to zero in an equilibrium configuration.

A peculiarity of the parametrization is that the order of rotation is interchangeable when updated axes are used, such that

$$\begin{aligned} \mathbf{R} &= \mathbf{R}(\phi_3\mathbf{E}_3)\mathbf{R}(\phi_2\mathbf{E}_2)\mathbf{R}(\phi_1\mathbf{E}_1) \\ &= \mathbf{R}(\phi_3\mathbf{E}_3)\mathbf{R}(\phi_1\mathbf{R}_2\mathbf{E}_1)\mathbf{R}(\phi_2\mathbf{E}_2) \\ &= \mathbf{R}(\phi_1\mathbf{R}_3\mathbf{R}_2\mathbf{R}_1\mathbf{E}_1)\mathbf{R}(\phi_2\mathbf{R}_3\mathbf{R}_2\mathbf{E}_2)\mathbf{R}(\phi_3\mathbf{E}_3) \end{aligned} \tag{3.55}$$

For our purpose, the principal reason for this parametrization is to constrain one of the axes, as this will have a well defined physical significance. As the $\mathbf{E}_i$'s are, as of yet, undefined, the formulation should produce comparable matrices irrespective of which axis is constrained. By setting each $\phi_i = 0$ in turn, we obtain:

$$\mathbf{K}^1_{G\phi} = -\begin{bmatrix} 0 & \mathbf{R}_3\mathbf{E}_1 \cdot \mathbf{m} \\ 0 & 0 \end{bmatrix} \tag{3.56}$$

$$\mathbf{K}^2_{G\phi} = -\begin{bmatrix} 0 & \mathbf{R}_3\mathbf{R}_2\mathbf{E}_1 \cdot (\mathbf{E}_3 \times \mathbf{m}) \\ 0 & 0 \end{bmatrix} = -\begin{bmatrix} 0 & -\mathbf{R}_3\widehat{\mathbf{E}}_3\mathbf{E}_1 \cdot \mathbf{m} \\ 0 & 0 \end{bmatrix} = \begin{bmatrix} 0 & \mathbf{R}_3\mathbf{E}_2 \cdot \mathbf{m} \\ 0 & 0 \end{bmatrix} \tag{3.57}$$

$$\mathbf{K}^3_{G\phi} = -\begin{bmatrix} 0 & \mathbf{R}_3\mathbf{R}_2\mathbf{E}_3 \cdot \mathbf{m} \\ 0 & 0 \end{bmatrix} = -\begin{bmatrix} 0 & \mathbf{R}_2\mathbf{E}_3 \cdot \mathbf{m} \\ 0 & 0 \end{bmatrix} \tag{3.58}$$

Similar results can be obtained for the material part of the stiffness matrix. In the further study of the matrices, choosing $\phi_2 = 0$ becomes convenient, as then $\mathbf{\Phi} = \mathbf{R}_3$, and thus $|\mathbf{\Phi}| = 1$. Based on this, the transformation does not change the eigenvalues of the material part of the stiffness, so no softening occurs, only rotation of the eigenvectors. The geometric stiffness matrix will, however, contribute even at a state of equilibrium. By observing that in general, the reaction force $\mathbf{R}_3\mathbf{E}_2 \cdot \mathbf{m} \neq 0$, the boundary-condition itself might "buckle" provided there exist some form of coupling between the force associated with the second dof and a change in the first dof. The following example will demonstrate this point.

Consider the mechanical system depicted in Figure 3.2, where the joints A and B are connected to rotational springs. By modelling the rigid beam as an eccentricity, we can easily capture the behavior of the system through the rotational degrees of freedom at the base of the beam. The initial rotational state is chosen to be $\phi_1 = 0$, $\phi_2 = \pi/2$ and $\phi_3 = 0$, and the fixed axis of rotation is ϕ_1. As noted earlier, this will lead to a singular transformation $\mathbf{\Phi}$. However, as long as one of the two co-linear axes is fixed, the singularity will not be a problem.

The stiffnesses of the springs yield the following stiffness matrix;

$$\mathbf{K}_S = \begin{bmatrix} \infty & 0 & 0 \\ 0 & k_2 & 0 \\ 0 & 0 & k_3 \end{bmatrix}, \tag{3.59}$$

or in the reduced system ($\hat{}$):

$$\hat{\mathbf{K}}_S = \begin{bmatrix} k_2 & 0 \\ 0 & k_3 \end{bmatrix} \tag{3.60}$$

$\hat{\mathbf{K}}_S$ is already expressed with respect to the variables $\boldsymbol{\phi}$, so no transformation is needed.

The eccentricity $\mathbf{e} = \begin{bmatrix} 0 & 0 & \mathrm{L} \end{bmatrix}^\mathsf{T}$ along with the forces $\mathbf{n} = \begin{bmatrix} 0 & -\mathrm{F} & 0 \end{bmatrix}^\mathsf{T}$ contribute to the eccentricity geometric stiffness $\mathbf{K}_{GE}$, where the variables are referred to the instantaneous rotations.

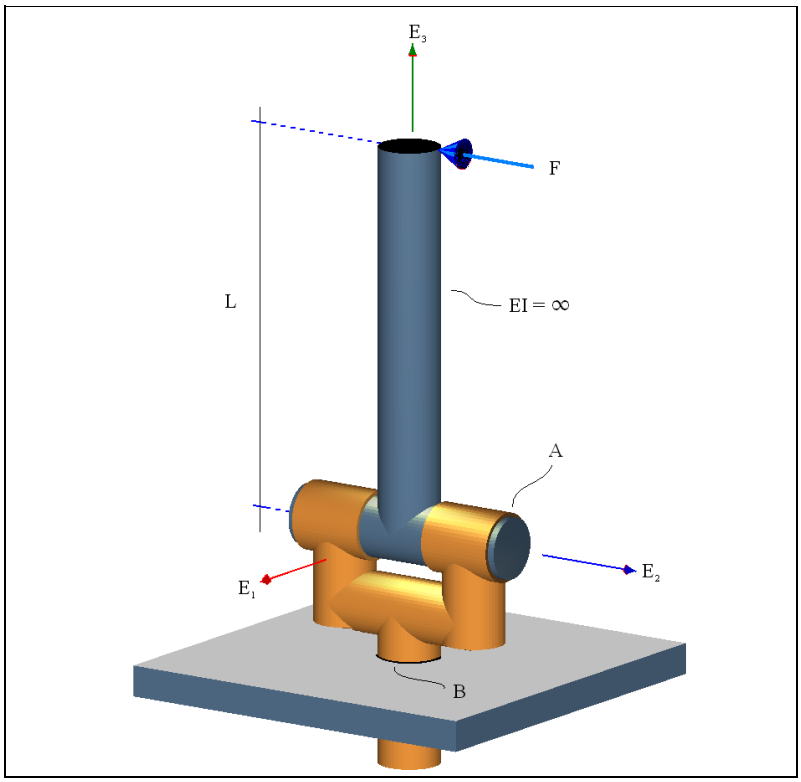

Figure 3.2 Model

$$\mathbf{K}_{GE} = \widehat{\mathbf{n}}\,\widehat{\mathbf{e}} = \begin{bmatrix} 0 & 0 & -F \\ 0 & 0 & 0 \\ F & 0 & 0 \end{bmatrix} \begin{bmatrix} 0 & -L & 0 \\ L & 0 & 0 \\ 0 & 0 & 0 \end{bmatrix} = \begin{bmatrix} 0 & 0 & 0 \\ 0 & 0 & 0 \\ 0 & -FL & 0 \end{bmatrix} \tag{3.61}$$

After realizing that $\mathbf{R}_3 = \mathbb{1}$, and $\mathbf{R}_2\mathbf{E}_1 = \mathbf{E}_3$ the transformation to ϕ's results in:

$$\mathbf{\Phi}^{\mathsf{T}}\mathbf{K}_{GE}\mathbf{\Phi} = \begin{bmatrix}\mathbf{E}_3 & \mathbf{E}_2 & \mathbf{E}_3\end{bmatrix}^{\mathsf{T}}\mathbf{K}_{GE}\begin{bmatrix}\mathbf{E}_3 & \mathbf{E}_2 & \mathbf{E}_3\end{bmatrix} = \begin{bmatrix} 0 & -FL & 0 \\ 0 & 0 & 0 \\ 0 & -FL & 0 \end{bmatrix} \quad \text{and} \quad \hat{\mathbf{K}}_{GE} = \begin{bmatrix} 0 & 0 \\ -FL & 0 \end{bmatrix} \tag{3.62}$$

If no other terms were present, the system would now be stable for any force F as the determinant of the stiffness matrix is simply $k_2 k_3$. The inclusion of (3.49) will reveal the necessary contribution:

$$\mathbf{K}^1_{G\phi} = -\begin{bmatrix} 0 & \mathbf{R}_3\mathbf{E}_1 \cdot \mathbf{m} \\ 0 & 0 \end{bmatrix} = -\begin{bmatrix} 0 & FL \\ 0 & 0 \end{bmatrix} \tag{3.63}$$

Obviously, this term alone is not sufficient to achieve the desired effect, rather the combination of $\mathbf{K}_{GE}$ and $\mathbf{K}_{G\phi}$ will provide the necessary coupling:

$$\left|\hat{\mathbf{K}}\right| = \left|\begin{bmatrix} k_2 & -\mathrm{FL} \\ -\mathrm{FL} & k_3 \end{bmatrix}\right| = k_2 k_3 - \mathrm{F}^2\mathrm{L}^2 \tag{3.64}$$

It is now a simple matter to evaluate the critical load:

$$\left|\hat{\mathbf{K}}\right| = 0 \Rightarrow \mathrm{F}_{\mathrm{cr}} = \pm\frac{\sqrt{k_2 k_3}}{\mathrm{L}} \tag{3.65}$$

With the corresponding eigenvectors:

$$\mathbf{x} = \begin{bmatrix} \pm\frac{\sqrt{k_2 k_3}}{k_2} \\ 1 \end{bmatrix} \tag{3.66}$$

A commonly adopted procedure in the estimation of critical points is to use the symmetrized stiffness. Thus, to compare the previous result to the result obtained when the term (3.63) is omitted, we set:

$$\hat{\mathbf{K}}_G = \frac{1}{2}(\hat{\mathbf{K}}_{GE} + \hat{\mathbf{K}}_{GE}^{\mathsf{T}}) = \frac{1}{2}\begin{bmatrix} 0 & -\mathrm{FL} \\ -\mathrm{FL} & 0 \end{bmatrix} \tag{3.67}$$

$$\left|\hat{\mathbf{K}}\right| = 0 \Rightarrow \mathrm{F}_{\mathrm{cr}} = \pm 2\frac{\sqrt{k_2 k_3}}{\mathrm{L}} \tag{3.68}$$

The predicted buckling load is now doubled, although the eigenvectors are identical to those found in (3.66). It should be stressed that this solution is inherently erroneous as the non-infinite eigenvalues are introduced by the symmetrization-process.

In order to verify the developed geometric terms, the discussed problem has been modeled using beam elements representing both the joints and the rigid bar. The boundary-condition is now enforced by linear couplings of selected degrees of freedom, so that the model has the ability to correctly describe the motion of the bar. For the example the following parameters are chosen:

$$L = 5{,}0m\,,\; k_2 = k_3 = 315{,}0\frac{\mathrm{kN}m}{rad}$$

$$\Rightarrow \mathrm{F}_{\mathrm{cr}}^{0} = \pm 63{,}0\mathrm{kN}$$

The stiffness-parameters of the rigid bar and joints are somewhat arbitrary, as long as they are not too rigid, so as to cause numerical difficulties, or too soft, so that the solution is polluted. The point of singularity for the model is determined in two ways; a) linearized buckling analysis with symmetrized matrices, and b) non-linear static analysis with a bisection algorithm for the unsymmetric matrices. As can be seen from Table 3.1, the buckling load corresponds well with the value predicted by the simple 2×2 system in (3.63).

Table 3.1 Buckling of full model

	Linearized buckling	**Bisection**
F_{cr} [kNm]	62,99	62,97
$(\mathrm{F}_{\mathrm{cr}} - \mathrm{F}_{\mathrm{cr}}^{0})/\mathrm{F}_{\mathrm{cr}}^{0}$ [%]	-0,02	-0,05

To verify both the numerical accuracy and the current implementation, analyses of a simplified model were carried out. This model consist of only a single beam of length L (modelled without eccentricities), free at the loaded end, and with the described boundary-condition at the other. As the eigenvalue-analyses were performed with symmetrized matrices, the result of enforcing the boundary condition on the pseudo-vector is also presented.

Table 3.2 Linearized buckling of simplified model (single beam)

	Euler-angles	**Pseudovector**
F_{cr} [kNm]	62,99	125,95
$(\mathrm{F}_{\mathrm{cr}} - \mathrm{F}_{\mathrm{cr}}^{0})/\mathrm{F}_{\mathrm{cr}}^{0}$ [%]	-0,02	99,9

For illustration purposes, Figure 3.3 shows the motion of the bar in the post-buckling range. The analysis is performed by perturbing the model in the direction of the first buckling mode with an amplitude of 10 mm, followed by a non-linear static analysis. As expected, the model seemed stationary until the load reached approximately 95% of the critical load, followed by an abrupt motion into the final and stable position depicted in Figure 3.3c.

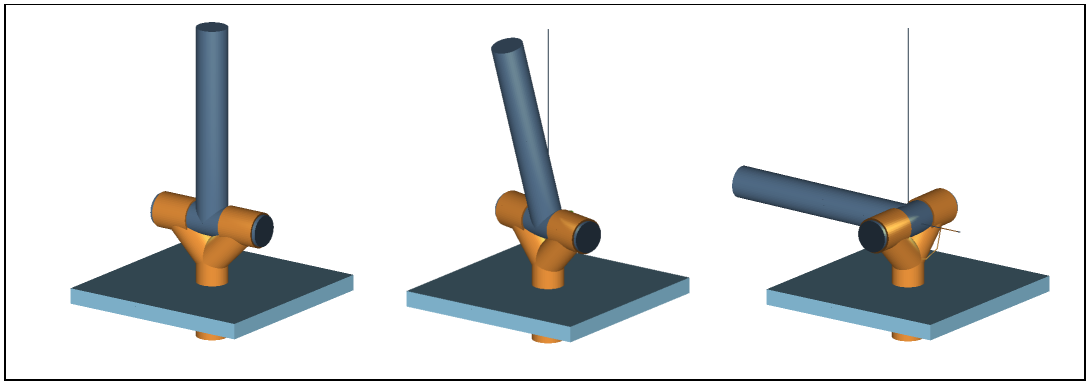

a) F = 0 b) F = 95% F_{cr} c) F = 110% F_{cr}

Figure 3.3 Post-buckling behavior

The previous example illustrates some of the complexities in the modelling of discrete rotational boundary-conditions. For many practical problems, the pseudovector-representation will be adequate in modelling singly restrained rotational degrees of freedom. In fact, the results of a linear static analyses is component for component equivalent to the results obtained from the Euler-angles, the physical interpretation is quite different though. In linearized buckling analyses, the difference is seldom as great as the one presented here.

Chapter 4
Cosserat rods

4.1 Introduction

In the following chapter, the Cosserat rod theory as described by J.C. Simo et al. [35, 36, 37] will be presented with emphasis on the governing equations of the weak form. Contrary to classical structural theories, this is a fully frame indifferent formulation emanating from the theory by the French Cosserat brothers in the beginning of the twentieth century. The theory uses finite strains, without any assumptions introduced on the magnitude of displacements and rotations, and it is therefore often called the *geometrically exact* approach. For a full account, the interested reader should confer with the mentioned papers by Simo and coworkers. It should be noted that the ordering of axes and the use of some symbols have been changed so as to correspond with notation used in previous and following chapters.

4.2 Geometric description and kinematic assumptions

Using common nomenclature in continuum mechanics, the *material* or *reference configuration* is taken as the straight line in the direction of the material vector $\mathbf{E}_1$ *(material beam axis)* on the interval $S \in [0,\ L]$. L is thus the generalized (constant) undeformed arch-length of the beam, and S is the arch-length parameter. The extent of the beam orthogonally to $\mathbf{E}_1$ is defined through the vector $\boldsymbol{\xi} = \xi_2\mathbf{E}_2 + \xi_3\mathbf{E}_3$, where $(\xi_2,\ \xi_3) \in \mathbb{A}(S)$ and $\mathbb{A}(S) \subset \mathbb{R}^2$ is a position vector inside the cross-section. $\mathbb{A}(S)$ must be a continuous function, defined for all positions S along the beam axis. With reference to Figure 4.1, the position of $\mathbf{E}_1$ relative to the cross-section is taken to be at the E_1 -

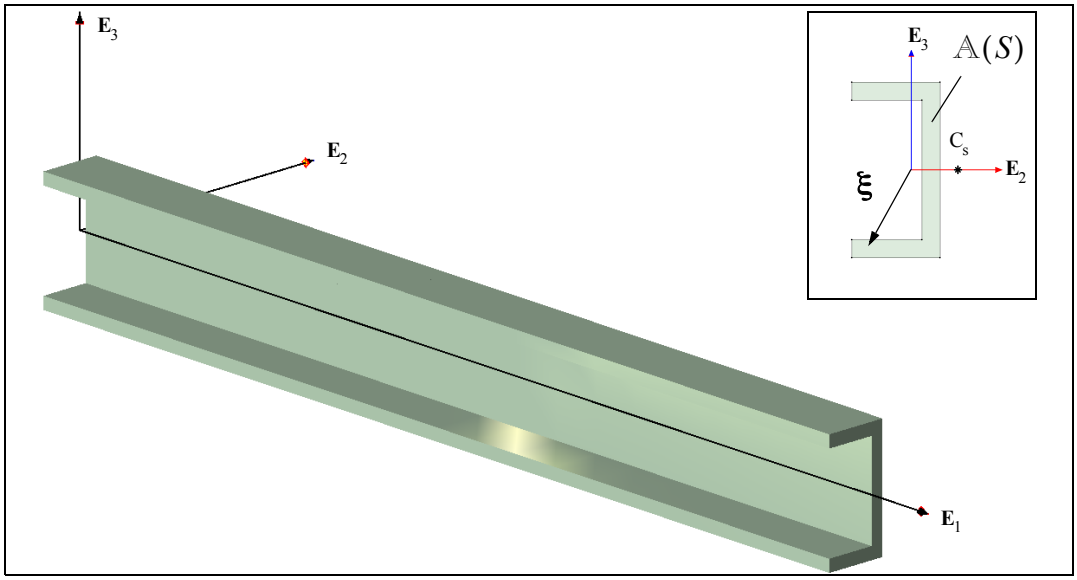

Figure 4.1 Material configuration

weighted centroid of the cross-section, where E_1 is the modulus of elasticity in the direction of $\mathbf{E}_1$ ($\boldsymbol{\xi} = \mathbf{0}$, is not necessarily $\in \mathbb{A}(S)$). The point $C_s = (\xi_2^s,\ \xi_3^s)$ is the shear center of the cross-section. For simplicity, $\mathbf{E}_2$ and $\mathbf{E}_3$ are oriented in the directions of the principal axes of the cross-section. The reference configuration of the beam, $\mathscr{B}_{Ref} \subset \mathbb{R}^3$, is thus :

$$\mathscr{B}_{Ref} = \left\{ \mathbf{X} = S\mathbf{E}_1 + \boldsymbol{\xi} \;\middle|\; S \in [0,\ L],\ \boldsymbol{\xi} \in \mathbb{A}(S),\ \int_{\mathbb{A}(S)} \mathrm{E}_1 \boldsymbol{\xi} dA = \mathbf{0} \right\} \tag{4.1}$$

$$\partial\mathscr{B} = \{0,\ L\} \tag{4.2}$$

where $\mathbf{X}$ is a *material point* within the beam.

The *current configuration* of the beam is a time-dependent configuration in the fixed spatial basis $\{\mathbf{e}_1,\ \mathbf{e}_2,\ \mathbf{e}_3\}$. For simplicity, this basis is taken to coincide with the material basis for initially straight members. The basic kinematic assumption introduced is that *plane sections, normal to the beam axis, remain plane but not necessarily normal to the beam axis*. By this assumption, the spatial position $\mathbf{x}$ of the material point $\mathbf{X}$ at time t may be given by the map $\varphi : [\,[0,\ L] \times \mathbb{A} \times \mathbb{R}_+\,] \rightarrow \mathbb{R}^3$:

$$\begin{aligned}\mathbf{x} = \boldsymbol{\varphi}(S,\ \xi_2,\ \xi_3,\ t) &= \boldsymbol{\varphi}_0(S,\ t) + \mathbf{R}(S,\ t)\boldsymbol{\xi} \\ &= \boldsymbol{\varphi}_0(S,\ t) + \boldsymbol{\varphi}_0(S,\ 0) + \mathbf{R}(S,\ t)\mathbf{R}(S,\ 0)\boldsymbol{\xi} \\ &= \boldsymbol{\varphi}_0^t(S) + \boldsymbol{\varphi}_0^0(S) + \mathbf{R}^t(S)\mathbf{R}^0(S)\boldsymbol{\xi}\end{aligned} \tag{4.3}$$

The position of the center line, $\boldsymbol{\varphi}_0(S,\ t) = \varphi_{0i}(S,\ t)\mathbf{e}_i \in \mathbb{R}^3$, is an ordinary vectorial function of S. To accommodate a general parametrization of the initial geometry, $\boldsymbol{\varphi}_0$ is additively decomposed into the initial map $\boldsymbol{\varphi}_0^0(S)$ and the time-dependent map $\boldsymbol{\varphi}_0^t(S)$. The spatial orientation of the cross-section is defined by the orthogonal matrix $\mathbf{R}(S,\ t) = r_{ij}(S,\ t)\mathbf{e}_i \otimes \mathbf{E}_j \in \mathbf{SO}(3)$. Since orthogonal matrices obey a multiplicative decomposition rule, the matrix is obtained as the product of the matrix $\mathbf{R}^0$, that defines the initial orientation, and the time-varying $\mathbf{R}^t$. By defining an orthonormal, moving basis $\mathbf{t}_i(S,\ t) = \mathbf{R}\mathbf{E}_i = r_{ji}(S,\ t)\mathbf{e}_j$, the rotation matrix can be recast as

$$\mathbf{R}(S,\ t) = r_{ij}(S,\ t)\mathbf{e}_i \otimes \mathbf{E}_j = \mathbf{t}_i(S,\ t) \otimes \mathbf{E}_i \tag{4.4}$$

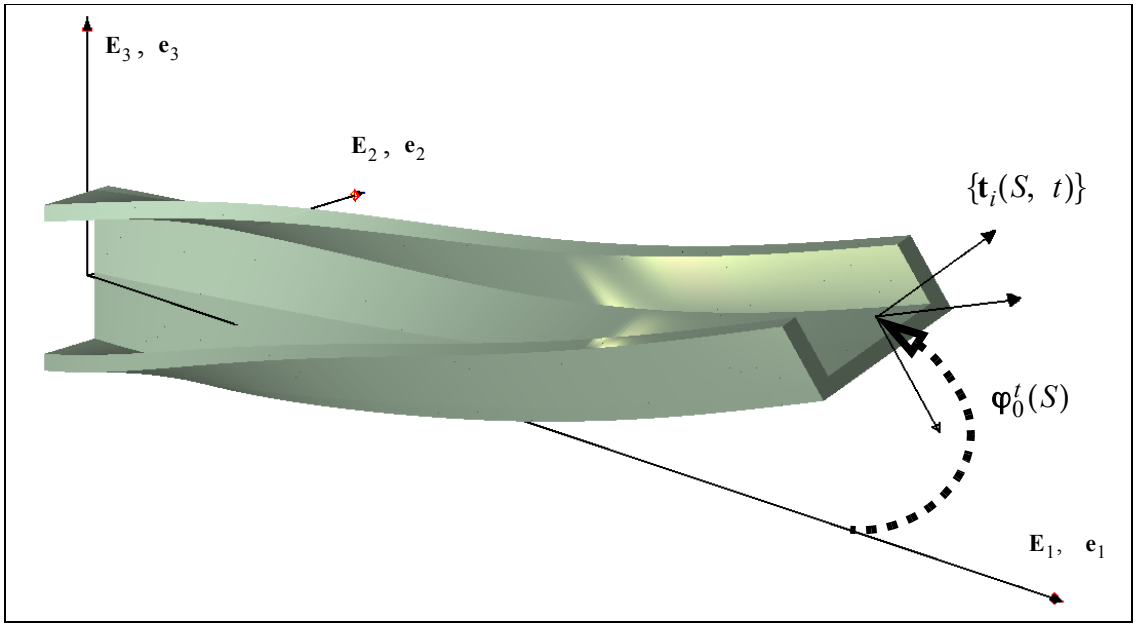

Figure 4.2 Current configuration (of initially straight member)

The initial parametrization is chosen so that $d\boldsymbol{\varphi}_0^0 / dS = \mathbf{R}^0\mathbf{E}_i = \mathbf{t}_1$. As shown in Figure 4.2, the basis $\{\mathbf{t}_i\}$ is an orthogonal basis in the current configuration that follows the principal axes of the deformed cross-section. Note that in general $d\boldsymbol{\varphi}_0 / dS = \mathbf{t}_1$ only at $t = 0$, since the formulation accounts for shear deformation of the beam, as depicted in

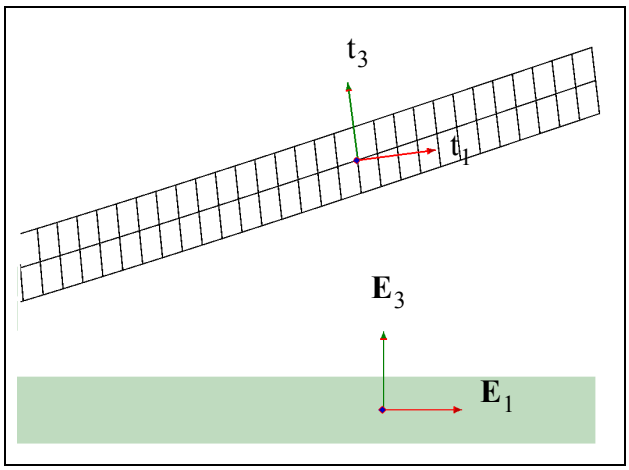

Figure 4.3 Orientation of $\{\mathbf{t}_i\}$ after deformation (planar motion)

Figure 4.3. For an initially straight and unstressed member, the initial maps simply become $\boldsymbol{\varphi}_0^0(S) = S\mathbf{e}_1$ and $\mathbf{R}^0 = \mathbf{e}_i \otimes \mathbf{E}_i \ (=\mathbb{1})$ (see Figure 4.2).

4.3 Internal forces and strain measure

With the definitions of Section 3.2 at our disposal, we start by deriving the deformation gradient $\mathbf{F}$. Using the notation

$$(\circ)' = \frac{\partial}{\partial S}(\circ) \tag{4.5}$$

we get:

$$\begin{aligned}\mathbf{F} = \frac{\partial \mathbf{x}}{\partial \mathbf{X}} &= \frac{\partial \boldsymbol{\varphi}_0}{\partial \mathbf{X}} + \frac{\partial}{\partial \mathbf{X}}(\mathbf{R}\boldsymbol{\xi}) = \left(\boldsymbol{\varphi}_0' + \frac{\partial \mathbf{R}}{\partial S}\mathbf{R}^T\mathbf{R}\boldsymbol{\xi}\right) \otimes \mathbf{E}_1 + \sum_{\alpha=2,\ 3} \mathbf{R}\mathbf{E}_\alpha \otimes \mathbf{E}_\alpha \\ &= (\boldsymbol{\varphi}_0' + \widehat{\boldsymbol{\kappa}}(\mathbf{x} - \boldsymbol{\varphi}_0)) \otimes \mathbf{E}_1 + \sum_{\alpha=2,\ 3} \mathbf{t}_\alpha \otimes \mathbf{E}_\alpha\end{aligned} \tag{4.6}$$

In Equation (4.6), the symbol $\boldsymbol{\kappa}$ is used to indicate the property of curvature. A detailed account of the derivation of $\boldsymbol{\kappa}$ for both initially straight and curved members is given in [36]. The complete derivation is quite involved, and it is therefore not included. As is common practice in continuum mechanics, upper case letters is used to indicate material tensors and vectors, while lower case letters is used for the corresponding spatial objects.

Thus, the material vector of curvature is denoted $\mathbf{K}$. The *pull-back* and *push-forward* operations are performed via the rotation tensor.

$$\frac{\partial \mathbf{R}}{\partial S}\,\mathbf{R}^{\mathsf{T}} = \widehat{\boldsymbol{\kappa}} = \mathbf{R}\,\widehat{\mathbf{K}}\,\mathbf{R}^{\mathsf{T}} \tag{4.7}$$

$$\boldsymbol{\kappa} = \mathrm{Axial}\left(\frac{\partial \mathbf{R}}{\partial S}\,\mathbf{R}^{\mathsf{T}}\right) = \kappa_i \mathbf{e}_i = K_i \mathbf{t}_i = K_i \mathbf{R}\mathbf{E}_i \tag{4.8}$$

$$\mathbf{K} = \mathrm{Axial}\left(\mathbf{R}^{\mathsf{T}}\frac{\partial \mathbf{R}}{\partial S}\right) = K_i \mathbf{E}_i = \mathbf{R}^{\mathsf{T}}\boldsymbol{\kappa} \tag{4.9}$$

In order to derive the conjugate measures of integrated stress and strain we use the equivalence of internal power:

$$W = \int_{\mathscr{B}_{Ref}} \mathbf{P}:\dot{\mathbf{F}}\,dV \tag{4.10}$$

where $\mathbf{P}$ is the unsymmetric first Piola-Kirchhoff (nominal) stress tensor:

$$\mathbf{P} = \mathbf{T}_i \otimes \mathbf{E}_i \tag{4.11}$$

As usual, a superimposed dot denotes the material time derivative. The rate of change of the deformation gradient now becomes:

$$\begin{aligned}
\dot{\mathbf{F}} &= \left(\dot{\boldsymbol{\varphi}}_0' + \dot{\widehat{\boldsymbol{\kappa}}}\,(\mathbf{x}-\boldsymbol{\varphi}_0) + \widehat{\boldsymbol{\kappa}}\,(\dot{\mathbf{x}}-\dot{\boldsymbol{\varphi}}_0)\right) \otimes \mathbf{E}_1 + \sum_{\alpha=2,\ 3} \widehat{\boldsymbol{\omega}}\,\mathbf{t}_\alpha \otimes \mathbf{E}_\alpha \\
&= \left(\dot{\boldsymbol{\varphi}}_0' + \dot{\widehat{\boldsymbol{\kappa}}}\,(\mathbf{x}-\boldsymbol{\varphi}_0) + \widehat{\boldsymbol{\kappa}}\,\dot{\mathbf{R}}\boldsymbol{\xi}\right) \otimes \mathbf{E}_1 + \sum_{\alpha=2,\ 3} \widehat{\boldsymbol{\omega}}\,\mathbf{t}_\alpha \otimes \mathbf{E}_\alpha \\
&= \left(\dot{\boldsymbol{\varphi}}_0' + \dot{\widehat{\boldsymbol{\kappa}}}\,(\mathbf{x}-\boldsymbol{\varphi}_0) + \widehat{\boldsymbol{\kappa}}\,\widehat{\boldsymbol{\omega}}\,(\mathbf{x}-\boldsymbol{\varphi}_0)\right) \otimes \mathbf{E}_1 + \sum_{\alpha=2,\ 3} \widehat{\boldsymbol{\omega}}\,\mathbf{t}_\alpha \otimes \mathbf{E}_\alpha
\end{aligned} \tag{4.12}$$

where $\boldsymbol{\omega}$ is the angular velocity and $\dot{\mathbf{t}}_\alpha = \dot{\mathbf{R}}\mathbf{E}_\alpha = \widehat{\boldsymbol{\omega}}\,\mathbf{R}\mathbf{E}_\alpha = \widehat{\boldsymbol{\omega}}\,\mathbf{t}_\alpha$.

From the balance of angular momentum $\mathbf{F}\mathbf{P}^T = \mathbf{P}\mathbf{F}^T$ we obtain;

$$\text{Spin}\left(\frac{\partial \mathbf{x}}{\partial \xi_I}\right)\mathbf{T}_I = 0 \Rightarrow \sum_{\alpha = 2,\ 3} \boldsymbol{\omega} \cdot \widehat{\mathbf{t}_\alpha}\mathbf{T}_\alpha = -\boldsymbol{\omega} \cdot \widehat{\frac{\partial \mathbf{x}}{\partial S}}\,\mathbf{T}_1 = -\mathbf{T}_1 \cdot \widehat{\boldsymbol{\omega}}\frac{\partial \mathbf{x}}{\partial S} \tag{4.13}$$

$$= -\mathbf{T}_1 \cdot \widehat{\boldsymbol{\omega}}(\boldsymbol{\varphi}_0' + \widehat{\boldsymbol{\kappa}}(\mathbf{x} - \boldsymbol{\varphi}_0))$$

Inserting equations (4.11, 4.12 and 4.13) into (4.10), results in:

$$\begin{aligned}
\mathbf{P}:\dot{\mathbf{F}} &= \mathbf{T}_1 \cdot \left(\dot{\boldsymbol{\varphi}}_0' + \widehat{\dot{\boldsymbol{\kappa}}}(\mathbf{x} - \boldsymbol{\varphi}_0) + \widehat{\boldsymbol{\kappa}}\,\widehat{\boldsymbol{\omega}}(\mathbf{x} - \boldsymbol{\varphi}_0)\right) + \sum_{\alpha = 2,\ 3} \mathbf{T}_\alpha \cdot \widehat{\boldsymbol{\omega}}\mathbf{t}_\alpha \\
&= \mathbf{T}_1 \cdot \dot{\boldsymbol{\varphi}}_0' + \dot{\boldsymbol{\kappa}} \cdot \text{Spin}(\mathbf{x} - \boldsymbol{\varphi}_0)\mathbf{T}_1 + \mathbf{T}_1 \cdot (\widehat{\boldsymbol{\kappa}}\,\widehat{\boldsymbol{\omega}}(\mathbf{x} - \boldsymbol{\varphi}_0)) + \sum_{\alpha = 2,\ 3} \boldsymbol{\omega} \cdot \widehat{\mathbf{t}_\alpha}\mathbf{T}_\alpha \\
&= \mathbf{T}_1 \cdot (\dot{\boldsymbol{\varphi}}_0' - \widehat{\boldsymbol{\omega}}\boldsymbol{\varphi}_0') + \dot{\boldsymbol{\kappa}} \cdot \text{Spin}(\mathbf{x} - \boldsymbol{\varphi}_0)\mathbf{T}_1 + \mathbf{T}_1 \cdot [\widehat{\boldsymbol{\kappa}}\,\widehat{\boldsymbol{\omega}} - \widehat{\boldsymbol{\omega}}\,\widehat{\boldsymbol{\kappa}}](\mathbf{x} - \boldsymbol{\varphi}_0) \\
&= \mathbf{T}_1 \cdot (\dot{\boldsymbol{\varphi}}_0' - \widehat{\boldsymbol{\omega}}\boldsymbol{\varphi}_0') + (\dot{\boldsymbol{\kappa}} - \widehat{\boldsymbol{\omega}}\boldsymbol{\kappa}) \cdot \text{Spin}(\mathbf{x} - \boldsymbol{\varphi}_0)\mathbf{T}_1 \\
&= \overset{\nabla}{\boldsymbol{\varphi}}_0' \cdot \mathbf{T}_1 + \overset{\nabla}{\boldsymbol{\kappa}} \cdot \text{Spin}(\mathbf{x} - \boldsymbol{\varphi}_0)\mathbf{T}_1
\end{aligned} \tag{4.14}$$

Here, the objective, *co-rotated rate* $\overset{\nabla}{(\circ)}$ has been introduced. This is the rate measured by an observer attached to the moving basis $\{\mathbf{t}_i\}$:

$$\overset{\nabla}{(\circ)} = \dot{(\circ)} - \boldsymbol{\omega} \times (\circ) \tag{4.15}$$

Integrating over the reference area we get the spatial cross-sectional stress resultant vectors $\mathbf{n}$ and $\mathbf{m}$ (forces and moments), conjugate to the spatial rate of change of deformation:

$$\int_A \mathbf{T}_1 \cdot \overset{\nabla}{\boldsymbol{\varphi}}_0' \, dA = \overset{\nabla}{\boldsymbol{\varphi}}_0' \cdot \int_A \mathbf{T}_1 \, dA = \overset{\nabla}{\boldsymbol{\varphi}}_0' \cdot \mathbf{n} \tag{4.16}$$

$$\int_A \overset{\nabla}{\boldsymbol{\kappa}} \cdot \text{Spin}(\mathbf{x} - \boldsymbol{\varphi}_0)\mathbf{T}_1 \, dA = \overset{\nabla}{\boldsymbol{\kappa}} \cdot \int_A \text{Spin}(\mathbf{x} - \boldsymbol{\varphi}_0)\mathbf{T}_1 \, dA = \overset{\nabla}{\boldsymbol{\kappa}} \cdot \mathbf{m} \tag{4.17}$$

$$\mathbf{n} := \int_A \mathbf{T}_1 dA\,,\ \mathbf{m} := \int_A \text{Spin}(\mathbf{x} - \boldsymbol{\varphi}_0)\mathbf{T}_1 dA \tag{4.18}$$

Since $\boldsymbol{\varphi}_0'$ is nonzero when the body is undeformed, it is an improper measure of strain. Again, noting that $\boldsymbol{\varphi}_0' = \mathbf{t}_1$ at $t = 0$, we introduce the spatial strain measure $\boldsymbol{\gamma}$:

$$\boldsymbol{\gamma} = \boldsymbol{\varphi}_0' - \mathbf{t}_1 \Rightarrow \quad \overset{\nabla}{\boldsymbol{\gamma}} = \dot{\boldsymbol{\varphi}}_0' - \widehat{\boldsymbol{\omega}}\boldsymbol{\varphi}_0' - \widehat{\boldsymbol{\omega}}\mathbf{t}_1 + \widehat{\boldsymbol{\omega}}\mathbf{t}_1 = \dot{\boldsymbol{\varphi}}_0' - \widehat{\boldsymbol{\omega}}\boldsymbol{\varphi}_0' = \overset{\nabla}{\boldsymbol{\varphi}}_0' \tag{4.19}$$

Using Equations (4.18) and (4.19) in (4.14) results in the following expression for the internal power:

$$\begin{aligned} \int_A \mathbf{P}:\dot{\mathbf{F}}\, dA &= \overset{\nabla}{\boldsymbol{\varphi}}_0' \cdot \mathbf{n} + \overset{\nabla}{\boldsymbol{\kappa}} \cdot \mathbf{m} \\ &= \overset{\nabla}{\boldsymbol{\gamma}} \cdot \mathbf{n} + \overset{\nabla}{\boldsymbol{\kappa}} \cdot \mathbf{m} \end{aligned} \tag{4.20}$$

If we introduce the *current arch-length s,* we observe that the measure $\boldsymbol{\gamma}$ results in no straining when the beam is undeformed:

$$s(S) = \int_{[0,\ S]} \left\| \frac{\partial}{\partial \mu} \boldsymbol{\varphi}_0(\mu,\ t) \right\| d\mu \tag{4.21}$$

For the special case of no shear deformation, we have:

$$\frac{\partial \boldsymbol{\varphi}_0}{\partial S} = \frac{\partial s}{\partial S}\mathbf{t}_1 \quad \Rightarrow \boldsymbol{\gamma} = \frac{\partial \boldsymbol{\varphi}_0}{\partial S} - \mathbf{t}_1 = \left(\frac{\partial s}{\partial S} - 1\right)\mathbf{t}_1 \tag{4.22}$$

4.4 Admissible variations and beam configuration

From the kinematic assumption (4.3), any configuration of the beam is described by the following non-linear differentiable manifold

$$\mathbb{C} = \{\, \boldsymbol{\varphi} = (\boldsymbol{\varphi}_0,\ \mathbf{R}) \,|\ \boldsymbol{\varphi}_0 : [0,\ L] \to \mathbb{R}^3,\ \mathbf{R} : [0,\ L] \to \mathbf{SO}(3) \,\} \tag{4.23}$$

where $(\boldsymbol{\varphi}_0, \mathbf{R})$ satisfies the essential boundary conditions. Composition of $\boldsymbol{\varphi}^1 = (\boldsymbol{\varphi}_0^1, \mathbf{R}^1) \in \mathbb{C}$ followed by $\boldsymbol{\varphi}^2 = (\boldsymbol{\varphi}_0^2, \mathbf{R}^2) \in \mathbb{C}$ now obeys the rule:

$$\boldsymbol{\varphi}^2 \oplus \boldsymbol{\varphi}^1 = (\boldsymbol{\varphi}_0^1 + \boldsymbol{\varphi}_0^2,\ \mathbf{R}^2\mathbf{R}^1) \notin \mathbb{C} \tag{4.24}$$

If instead, we only use the subset of $\mathbb{C}$ that satisfies the homogeneous part of the essential boundary conditions, we get the space of perturbed configurations $\mathbb{C}_\varepsilon$:

$$\mathbb{C}_\varepsilon = \left\{ \boldsymbol{\varphi} = (\boldsymbol{\varphi}_0^0 + \varepsilon \boldsymbol{\eta}_0,\ \mathbf{R}(\varepsilon \boldsymbol{\psi})\mathbf{R}^0) \middle| \boldsymbol{\varphi},\ \boldsymbol{\varphi}^0 \in \mathbb{C},\ \eta_{0i}\big|_{\partial \mathscr{B}_{ui}} = \psi_i\big|_{\partial \mathscr{B}_{ri}} = 0 \right\} \tag{4.25}$$

with the corresponding tangent space:

$$T_{\boldsymbol{\varphi}}\mathbb{C} = \left\{ \boldsymbol{\eta}_T = (\boldsymbol{\eta}_0,\ \widehat{\boldsymbol{\psi}}\mathbf{R}) \middle| \eta_{0i}\big|_{\partial \mathscr{B}_{ui}} = \psi_i\big|_{\partial \mathscr{B}_{ri}} = 0 \right\} \tag{4.26}$$

$\partial \mathscr{B}_u$ is the part of the boundary with prescribed displacements, whereas rotations are prescribed on $\partial \mathscr{B}_r$. With a slight abuse of notation, we will in the following say that $(\boldsymbol{\eta}_0, \widehat{\boldsymbol{\psi}})$ lie in the tangent space of $\mathbb{C}$. Due to the isometry between the skew symmetric matrices in $\mathbb{R}^{3x3}$ and $\mathbb{R}^3$ ($\boldsymbol{\psi} \sim \widehat{\boldsymbol{\psi}}$), the ordered vectors $\boldsymbol{\eta} = (\boldsymbol{\eta}_0, \boldsymbol{\psi})$ also lie in this space. It should be noted that this is a vector space, where interpolation is valid.

The local balance laws now takes on the forms

$$\frac{\partial \mathbf{n}}{\partial S} + \bar{\mathbf{n}} = \rho A \ddot{\boldsymbol{\varphi}}_0 \tag{4.27}$$

and

$$\frac{\partial \mathbf{m}}{\partial S} + \frac{\partial \boldsymbol{\varphi}_0}{\partial S} \times \mathbf{n} + \bar{\mathbf{m}} = \rho \boldsymbol{I} \dot{\boldsymbol{\omega}} + \boldsymbol{\omega} \times (\rho \boldsymbol{I} \boldsymbol{\omega}) \tag{4.28}$$

where $\boldsymbol{I}$ is the *spatial* inertia tensor and ρ is the mass density in the current configuration. Superimposed bars are used to indicate applied forces and moments.

Neglecting the dynamic contributions, we can, in classical fashion, formulate the functional G of the static part of the local balance equations:

$$\begin{aligned} G_{Stat}(\boldsymbol{\varphi},\ \boldsymbol{\eta}) &= \int_{[0,\ L]} \left[\left(\frac{\partial \mathbf{n}}{\partial S} + \bar{\mathbf{n}} \right) \cdot \boldsymbol{\eta}_0 + \left(\frac{\partial \mathbf{m}}{\partial S} + \frac{\partial \boldsymbol{\varphi}_0}{\partial S} \times \mathbf{n} + \bar{\mathbf{m}} \right) \cdot \boldsymbol{\psi} \right] dS \\ &= \int_{[0,\ L]} \left[\left(\frac{\partial \boldsymbol{\eta}_0}{\partial S} - \boldsymbol{\psi} \times \frac{\partial \boldsymbol{\varphi}_0}{\partial S} \right) \cdot \mathbf{n} + \frac{\partial \boldsymbol{\psi}}{\partial S} \cdot \mathbf{m} \right] dS \\ &\quad - \int_{[0,\ L]} [\boldsymbol{\eta}_0 \cdot \bar{\mathbf{n}} + \boldsymbol{\psi} \cdot \bar{\mathbf{m}}] dS \end{aligned} \tag{4.29}$$

Introducing the following vectors of integrated stresses

$$\boldsymbol{\Sigma} = \begin{bmatrix} \mathbf{N} \\ \mathbf{M} \end{bmatrix}, \boldsymbol{\sigma} = \begin{bmatrix} \mathbf{n} \\ \mathbf{m} \end{bmatrix} = \boldsymbol{\Pi}\boldsymbol{\Sigma}, \boldsymbol{\Pi} = \begin{bmatrix} \mathbf{R} & \mathbf{0} \\ \mathbf{0} & \mathbf{R} \end{bmatrix} \tag{4.30}$$

and the differential operator

$$\boldsymbol{\Xi} = \begin{bmatrix} \frac{d}{dS}\mathbf{1} & \mathbf{0} \\ -\widehat{\boldsymbol{\varphi}_0'} & \frac{d}{dS}\mathbf{1} \end{bmatrix} \tag{4.31}$$

G can be recast in the more compact form

$$G_{Stat}(\boldsymbol{\varphi}, \boldsymbol{\eta}) = \int_{[0,\ L]} [\ \boldsymbol{\Xi}^{\mathsf{T}}\boldsymbol{\eta} \cdot \boldsymbol{\Pi}\boldsymbol{\Sigma} - \boldsymbol{\eta} \cdot \bar{\boldsymbol{\sigma}}\ ] dS \tag{4.32}$$

In the incremental iterative solution process of this non-linear functional, we need to extract the linear part of (4.32), $L[G_{Stat}(\boldsymbol{\varphi}, \boldsymbol{\eta})]$. Only the principal steps will be presented here, as the details of the derivation are reported in [36]. In the following, $(\hat{\circ})$ is used to indicate a quantity evaluated at the current state of deformation. The linear part can be expressed as:

$$L[G_{Stat}(\hat{\boldsymbol{\varphi}}, \boldsymbol{\eta})] = G_{Stat}(\hat{\boldsymbol{\varphi}}, \boldsymbol{\eta}) + DG_{Stat}(\hat{\boldsymbol{\varphi}}, \boldsymbol{\eta}) \cdot \Delta\boldsymbol{\varphi} \tag{4.33}$$

Use has been made of the directional derivative

$$DG_{Stat}(\hat{\boldsymbol{\varphi}}, \boldsymbol{\eta}) \cdot \Delta\boldsymbol{\varphi} = \frac{d}{d\varepsilon} G_{Stat}(\hat{\boldsymbol{\varphi}}_{\varepsilon}, \boldsymbol{\eta})\Big|_{\varepsilon = 0} \tag{4.34}$$

where the increment $\Delta\boldsymbol{\varphi} = (\Delta\boldsymbol{\varphi}_0, \Delta\boldsymbol{\theta})$ is assumed to lie in the tangent space at $\hat{\boldsymbol{\varphi}}$.

By splitting DG_{Stat} into two parts, where DG^m_{Stat} and DG^g_{Stat} are the result of linearizing the stress-state $\boldsymbol{\Sigma}$ and the configuration $\boldsymbol{\Xi}\boldsymbol{\Pi}^{\mathsf{T}}$ separately. DG^m_{Stat} gives rise to the material stiffness, whereas DG^g_{Stat} contains the geometric contribution.

$$DG_{Stat}(\hat{\boldsymbol{\varphi}}, \boldsymbol{\eta}) \cdot \Delta\boldsymbol{\varphi} = DG^m_{Stat}(\hat{\boldsymbol{\varphi}}, \boldsymbol{\eta}) \cdot \Delta\boldsymbol{\varphi} + DG^g_{Stat}(\hat{\boldsymbol{\varphi}}, \boldsymbol{\eta}) \cdot \Delta\boldsymbol{\varphi} \tag{4.35}$$

Assuming hyperelastic material properties, in which case $D\boldsymbol{\Sigma} \cdot \Delta\boldsymbol{\varphi} = \hat{\mathbf{C}}\hat{\boldsymbol{\Pi}}^{\mathsf{T}}\hat{\boldsymbol{\Xi}}^{\mathsf{T}}\Delta\boldsymbol{\varphi}$, DG^{m}_{Stat} becomes:

$$DG^{m}_{Stat}(\hat{\boldsymbol{\varphi}},\ \boldsymbol{\eta}) \cdot\ \Delta\boldsymbol{\varphi} = \int_{[0,\ L]} \hat{\boldsymbol{\Xi}}^{\mathsf{T}}\boldsymbol{\eta} \cdot \hat{\boldsymbol{\Pi}}\hat{\mathbf{C}}\hat{\boldsymbol{\Pi}}^{\mathsf{T}}\hat{\boldsymbol{\Xi}}^{\mathsf{T}}\Delta\boldsymbol{\varphi}\ dS \tag{4.36}$$

In this equation, $\hat{\mathbf{C}}$ is the material elasticity tensor of the cross-section. For linear elastic materials the elasticity tensor is constant, and for symmetric cross-sections it simply becomes the diagonal matrix $\mathbf{C} = \text{Diag}\left[EA\ \ GA_2\ \ GA_3\ \ GI_t\ \ EI_2\ \ EI_3\right]$. As usual, A_α refers to the reduced shear area in the direction of $\mathbf{E}_\alpha$, $\alpha = 2,\ 3$. For rectangular cross-sections, the well known relationship $A_\alpha = A/1{,}2$ applies (for Poisson's ratio equal to zero). The simple extension to unsymmetric cross-sections reveal the more general form:

$$\mathbf{C} = \begin{bmatrix} EA & 0 & 0 & 0 & 0 & 0 \\ & GA_2 & 0 & -\xi^s_3 GA_2 & 0 & 0 \\ & & GA_3 & \xi^s_2 GA_3 & 0 & 0 \\ & & & GI_t + (\xi^s_3)^2 GA_2 + (\xi^s_2)^2 GA_3 & 0 & 0 \\ & \text{Sym} & & & EI_2 & 0 \\ & & & & & EI_3 \end{bmatrix} \tag{4.37}$$

Linearization of the change in the configuration results in:

$$DG^{g}_{Stat}(\hat{\boldsymbol{\varphi}},\ \boldsymbol{\eta}) \cdot \Delta\boldsymbol{\varphi}\ = \int_{[0,\ L]} \boldsymbol{\Psi}^{\mathsf{T}}\boldsymbol{\eta} \cdot \hat{\mathbf{A}}\boldsymbol{\Psi}^{\mathsf{T}}\Delta\boldsymbol{\varphi}\ dS, \tag{4.38}$$

where

$$\boldsymbol{\Psi} = \begin{bmatrix} \frac{d}{dS}\mathbf{1} & \mathbf{0} & \mathbf{0} \\ \mathbf{0} & \frac{d}{dS}\mathbf{1} & \mathbf{1} \end{bmatrix} \text{ and } \mathbf{A} = \begin{bmatrix} \mathbf{0} & \mathbf{0} & -\widehat{\mathbf{n}} \\ \mathbf{0} & \mathbf{0} & -\widehat{\mathbf{m}} \\ \widehat{\mathbf{n}} & \mathbf{0} & \mathbf{n} \otimes \boldsymbol{\varphi}_0' - (\mathbf{n} \cdot \boldsymbol{\varphi}_0')\mathbf{1} \end{bmatrix} \tag{4.39}$$

The key features derived in this section are summarized in Table 4.1.

Table 4.1 Strain measures and integrated stresses

	Spatial configuration	**Material configuration**
Strains	$\boldsymbol{\gamma} = \boldsymbol{\varphi}_0' - \mathbf{t}_1$ $\widehat{\boldsymbol{\kappa}} = \dfrac{\partial \mathbf{R}}{\partial S}\mathbf{R}^{\mathsf{T}} = K_i \widehat{\mathbf{t}_i}$	$\boldsymbol{\Gamma} = \mathbf{R}^{\mathsf{T}}\boldsymbol{\varphi}_0' - \mathbf{E}_1$ $\widehat{\mathbf{K}} = \mathbf{R}^{\mathsf{T}}\dfrac{\partial \mathbf{R}}{\partial S} = K_i \widehat{\mathbf{E}_i} = \mathbf{R}^{\mathsf{T}}\widehat{\boldsymbol{\kappa}}\mathbf{R}$
Forces	$\mathbf{n} = \int_{\mathrm{A}} \mathbf{T}_1 dA$ $\mathbf{m} = \int_{\mathrm{A}} \mathrm{Spin}(\mathbf{x} - \boldsymbol{\varphi}_0)\mathbf{T}_1 dA$	$\mathbf{N} = \mathbf{R}^{\mathsf{T}}\mathbf{n}$ $\mathbf{M} = \mathbf{R}^{\mathsf{T}}\mathbf{m}$

4.5 Finite element discretization

Having established the governing equations for the linearized weak form, we can proceed with the finite element approximation of Equation (4.33). First, the infinite-dimensional configuration space is approximated by the finite subspace $\mathbb{C}^h \subset \mathbb{C}$, where $\boldsymbol{\varphi}^h \in \mathbb{C}^h$ is defined by the approximating basis functions $\mathrm{B}_I(\mathrm{S})$, $I = 1, N$, subject to the usual completeness and continuity conditions.

$$\boldsymbol{\varphi} \cong \boldsymbol{\varphi}^h = (\boldsymbol{\varphi}_0^h,\ \mathbf{R}^h) \in \mathbb{C}^h \tag{4.40}$$

Introducing the displacement weights $w_I^j(t)$ and the position weights p_I^j (initial configuration), where subscripts refer to the associated function, and superscripts to the spatial direction, the position of the beam axis in the current configuration is defined as follows:

$$\begin{aligned} \boldsymbol{\varphi}_0^h(\mathrm{S},\ t) &= \sum_I [w_I^j(t) + \mathrm{p}_I^j]\,\mathbf{e}_j \mathrm{B}_I(S) \\ &= \boldsymbol{w}^{\mathsf{T}}\mathbf{B}(S) + \mathbf{p}^{\mathsf{T}}\mathbf{B}(S) \end{aligned} \tag{4.41}$$

$$\boldsymbol{w}^{\mathsf{T}} = \left[w_1^j \mathbf{e}_j \cdots w_N^j \mathbf{e}_j\right],\ \mathbf{p}^{\mathsf{T}} = \left[\mathrm{p}_1^j \mathbf{e}_j \cdots \mathrm{p}_N^j \mathbf{e}_j\right],\ \mathbf{B}(S) = \left[\mathrm{B}_1 \cdots \mathrm{B}_N\right]^{\mathsf{T}} \tag{4.42}$$

It should be noted that both the displacement and the position weights are not necessarily physical displacements and positions. In the papers by Simo et al. [35,36] the basis func-

tions were tacitly assumed to be interpolating polynomials. This was, however, never posed as a restriction on the formulation, and the assumption will not be made in this presentation.

Due to the manner in which the rotations are parametrized, the definition of the rotation field becomes somewhat more involved. Since composition of rotations follow a multiplicative rule when incremental rotations are used, we start by dividing the continuous time domain into discrete points. If we denote $r(t_n)$ the total number of rotational increments at time t_n, the rotation then becomes:

$$\mathbf{R}^h(S,\ t_n) = \prod_{k=r(t_n)}^{0} \Delta\mathbf{R}_k(S) \tag{4.43}$$

Introducing the approximating functions in the incremental pseudovectors, and with some loss of generality using the same basis functions as for the displacements, we get:

$$\Delta\mathbf{R}_k(\mathrm{S}) = \mathbf{R}\left(\sum_I {}_k\Delta\phi_I^j \mathbf{e}_j \mathrm{B}_I(S)\right) = \mathbf{R}(\ \Delta\boldsymbol{\phi}_k^{\mathsf{T}}\mathbf{B}(S)\ ) \tag{4.44}$$

$$\Delta\boldsymbol{\phi}_k^{\mathsf{T}} = \left[{}_k\Delta\phi_1^j \mathbf{e}_j \ \cdots {}_k\Delta\phi_N^j \mathbf{e}_j\right] \tag{4.45}$$

From Equation (4.43) it is apparent that, given rotational increments of polynomial order p, the rotation vector of $\mathbf{R}^h$ is not of the same polynomial order[1]. This entails that the rotational state must be stored separately for each integration point in a numerical integration scheme.

In the same manner as for the configuration space, the increments and trial functions are approximated by a finite dimensional space $T_{\boldsymbol{\varphi}}\mathbb{C}^h \subset T_{\boldsymbol{\varphi}}\mathbb{C}$:

$$\boldsymbol{\eta} \cong \boldsymbol{\eta}^h = (\boldsymbol{\eta}_0^h,\ \boldsymbol{\psi}^h) \tag{4.46}$$

$$\boldsymbol{\eta}_0^h = \sum_I \eta_I^j \mathbf{e}_j \mathrm{B}_I(S), \qquad \boldsymbol{\psi}^h = \sum_I \psi_I^j \mathbf{e}_j \mathrm{B}_I(S) \tag{4.47}$$

1. For colinear increments this will not be true as the rotations then will be additive, e.g. 2D rotation.

$$\Delta\boldsymbol{\varphi} \cong \Delta\boldsymbol{\varphi}^h = (\Delta\mathbf{u}^h,\ \Delta\boldsymbol{\theta}^h) \tag{4.48}$$

$$\Delta\mathbf{u}^h = \sum_I \Delta w_I^j \mathbf{e}_j \mathrm{B}_I(S), \qquad \Delta\boldsymbol{\theta}^h = \sum_I \Delta\phi_I^j \mathbf{e}_j \mathrm{B}_I(S) \tag{4.49}$$

To simplify the derivation, the following intermediate steps are taken:

$$\begin{aligned}\hat{\boldsymbol{\Xi}}^{\mathsf{T}}\boldsymbol{\eta}^h &= \begin{bmatrix} \frac{d}{dS}\mathbb{1} & \mathbf{0} \\ -\widehat{\boldsymbol{\varphi}_0'} & \frac{d}{dS}\mathbb{1} \end{bmatrix}^{\mathsf{T}} \sum_I \begin{bmatrix} \eta_I^j \mathbf{e}_j \mathrm{B}_I(S) \\ \vartheta_I^j \mathbf{e}_j \mathrm{B}_I(S) \end{bmatrix} = \sum_I \begin{bmatrix} \mathbb{1}\frac{d}{dS}\mathrm{B}_I(S) & \widehat{\boldsymbol{\varphi}_0'} \\ \mathbf{0} & \mathbb{1}\frac{d}{dS}\mathrm{B}_I(S) \end{bmatrix} \begin{bmatrix} \eta_I^j \mathbf{e}_j \\ \vartheta_I^j \mathbf{e}_j \end{bmatrix} \\ &= \sum_I \hat{\boldsymbol{\Xi}}_{hI}^{\mathsf{T}} \boldsymbol{\eta}_I^h \end{aligned} \tag{4.50}$$

$$\hat{\boldsymbol{\Xi}}^{\mathsf{T}}\Delta\boldsymbol{\varphi}^h = \sum_I \hat{\boldsymbol{\Xi}}_{hI}^{\mathsf{T}} \Delta\boldsymbol{\varphi}_I^h \tag{4.51}$$

In Equations (4.50) and (4.51), the discrete version $\hat{\boldsymbol{\Xi}}_{hI}^{\mathsf{T}}$ of the differential operator (4.31) has been introduced. This is a 6×6 matrix defined for each weighting function I as:

$$\hat{\boldsymbol{\Xi}}_{hI} = \begin{bmatrix} \mathbb{1}\frac{d}{dS}\mathrm{B}_I(S) & \mathbf{0} \\ -\widehat{\boldsymbol{\varphi}_0'}\,\mathrm{B}_I(S) & \mathbb{1}\frac{d}{dS}\mathrm{B}_I(S) \end{bmatrix} \tag{4.52}$$

The unbalanced force vector associated with node I is now evaluated as:

$$\mathbf{f}_I = \int_{[0,\ L]} \left[\hat{\boldsymbol{\Xi}}_{hI} \boldsymbol{\Pi}\boldsymbol{\Sigma} - \begin{bmatrix} \mathbb{1}\mathrm{B}_I(S) & \mathbf{0} \\ \mathbf{0} & \mathbb{1}\mathrm{B}_I(S) \end{bmatrix} \bar{\boldsymbol{\sigma}} \right] dS \tag{4.53}$$

The "material" part of the stiffness matrix (4.55), expressed as the matrix connecting node I and node J is found from Equation (4.36):

$$\begin{aligned} DG_{Stat}^m(\hat{\boldsymbol{\varphi}},\ \boldsymbol{\eta}) \cdot\ \Delta\boldsymbol{\varphi} &\cong \int_{[0,\ L]} \sum_I \hat{\boldsymbol{\Xi}}_{hI}^{\mathsf{T}} \boldsymbol{\eta}_I^h \cdot \hat{\boldsymbol{\Pi}}\hat{\mathbf{C}}\hat{\boldsymbol{\Pi}}^{\mathsf{T}} \sum_J \hat{\boldsymbol{\Xi}}_{hJ}^{\mathsf{T}} \Delta\boldsymbol{\varphi}_J^h\, dS \\ &= \sum_{I,\ J} \boldsymbol{\eta}_I^{h\mathsf{T}} \left(\int_{[0,\ L]} \hat{\boldsymbol{\Xi}}_{hI} \hat{\boldsymbol{\Pi}}\hat{\mathbf{C}}\hat{\boldsymbol{\Pi}}^{\mathsf{T}} \hat{\boldsymbol{\Xi}}_{hJ}^{\mathsf{T}} dS \right) \Delta\boldsymbol{\varphi}_J^h = \sum_{I,\ J} \boldsymbol{\eta}_I^{h\mathsf{T}} \mathbf{S}_{IJ} \Delta\boldsymbol{\varphi}_J^h \end{aligned} \tag{4.54}$$

$$\mathbf{S}_{IJ} = \int_{[0,\ L]} \hat{\boldsymbol{\Xi}}_{hI} \hat{\boldsymbol{\Pi}} \hat{\mathbf{C}} \hat{\boldsymbol{\Pi}}^{\mathsf{T}} \hat{\boldsymbol{\Xi}}_{hJ}^{\mathsf{T}} dS \tag{4.55}$$

Following the same procedure as in (4.50), we obtain:

$$\boldsymbol{\Psi}^{\mathsf{T}} \boldsymbol{\eta}^h = \sum_I \boldsymbol{\Psi}_{hI}^{\mathsf{T}} \boldsymbol{\eta}_I^h, \qquad \boldsymbol{\Psi}^{\mathsf{T}} \Delta\boldsymbol{\varphi}^h = \sum_I \boldsymbol{\Psi}_{hI}^{\mathsf{T}} \Delta\boldsymbol{\varphi}_I^h \tag{4.56}$$

$$\boldsymbol{\Psi}_{hI}^{\mathsf{T}} = \begin{bmatrix} \mathbb{1}\dfrac{d}{dS}\mathrm{B}_I(S) & \mathbf{0} \\ \mathbf{0} & \mathbb{1}\dfrac{d}{dS}\mathrm{B}_I(S) \\ \mathbf{0} & \mathbb{1}\mathrm{B}_I(S) \end{bmatrix} \tag{4.57}$$

Thus the "geometric" stiffness matrix becomes:

$$\begin{aligned} DG_{Stat}^{g}(\hat{\boldsymbol{\varphi}}, \boldsymbol{\eta}) \cdot \Delta\boldsymbol{\varphi} &\cong \int_{[0,\ L]} \sum_I \boldsymbol{\Psi}_{hI}^{\mathsf{T}} \boldsymbol{\eta}_I^h \cdot \hat{\mathbf{A}} \sum_J \boldsymbol{\Psi}_{hJ}^{\mathsf{T}} \Delta\boldsymbol{\varphi}_J^h \, dS \\ &= \sum_{I,\ J} \left[(\boldsymbol{\eta}_I^h)^{\mathsf{T}} \int_{[0,\ L]} \boldsymbol{\Psi}_{hI} \hat{\mathbf{A}} \boldsymbol{\Psi}_{hJ}^{\mathsf{T}} dS \Delta\boldsymbol{\varphi}_J^h \right] = \sum_{I,\ J} (\boldsymbol{\eta}_I^h)^{\mathsf{T}} \mathbf{T}_{IJ} \Delta\boldsymbol{\varphi}_J^h \end{aligned} \tag{4.58}$$

$$\mathbf{T}_{IJ} = \int_{[0,\ L]} \boldsymbol{\Psi}_{hI} \hat{\mathbf{A}} \boldsymbol{\Psi}_{hJ}^{\mathsf{T}} dS \tag{4.59}$$

As mentioned previously, this formulation require storing some variables at the element level. This is due to the fact that the rotations, incremented in this way, cannot be expressed by the same interpolation scheme as the increments. This fact is illustrated in Figure 4.4, where linear interpolation of incremental rotations has been used over the element. In this example, 5 randomized incremental rotations, with a mean value of $\overline{\|\boldsymbol{\theta}\|} = 0{,}14\pi$ at the nodes is presented. Clearly, the total rotation cannot be represented by linear interpolating functions. As the rotations are stored at the integration points and not interpolated, so is the curvature. After each increment, the configuration of the beam must be updated by the procedure described in Box 4.1 before evaluation of the internal forces. It should be noted that this update procedure differs slightly in the way curvatures are updated from the procedure described in [36]. There, $\boldsymbol{\beta}$ was the incremental spatial curvature at step *n*, whereas in the current presentation, $\boldsymbol{\beta}$ is the incremental curvature at step *n*,

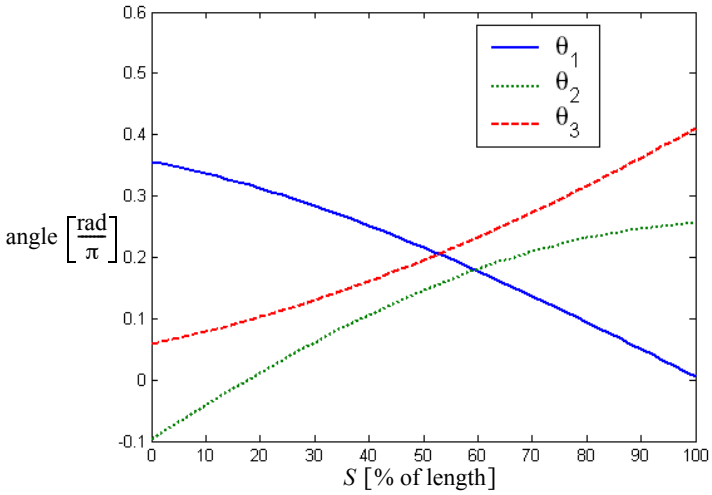

Figure 4.4 Components of rotation-vector along the length of a beam

referred to the spatial configuration at step *n-1*. This effect is obtained by simply changing the sign of the last term in the expression for $\boldsymbol{\beta}$. The motivation for this form is that when $\mathbf{R}_{n-1}(S_i) = \mathbb{1}$, the material curvature increment, $\Delta\mathbf{K}$, is calculated directly.

Box 4.1 Configuration update algorithm

Given nodal increments $\Delta \boldsymbol{w}$ and $\Delta \boldsymbol{\phi}$:

Update displacement-weights:

- $\boldsymbol{w}_n = \boldsymbol{w}_{n-1} + \Delta \boldsymbol{w}$

For each integration point *i:*

Compute:

- $\boldsymbol{\varphi}_0^h{}'(S_i) = \boldsymbol{w}_n^{\mathsf{T}} \mathbf{B}'(S_i) + \mathbf{p}^{\mathsf{T}} \mathbf{B}'(S_i)$
- $\Delta \boldsymbol{\theta}(S_i) = \Delta \boldsymbol{\phi}^{\mathsf{T}} \mathbf{B}(S_i)$, $\Delta \boldsymbol{\theta}'(S_i) = \Delta \boldsymbol{\phi}^{\mathsf{T}} \mathbf{B}'(S_i)$
- $\boldsymbol{\beta} = \text{Axial}\left(\Delta \mathbf{R}^{\mathsf{T}}(S_i) \frac{d}{dS} \Delta \mathbf{R}(S_i) \right)$

$$= \frac{\sin(\|\Delta\boldsymbol{\theta}\|)}{\|\Delta\boldsymbol{\theta}\|} \Delta\boldsymbol{\theta}' + \left(1 - \frac{\sin(\|\Delta\boldsymbol{\theta}\|)}{\|\Delta\boldsymbol{\theta}\|}\right) \frac{\Delta\boldsymbol{\theta} \cdot \Delta\boldsymbol{\theta}'}{\|\Delta\boldsymbol{\theta}\|^2} \Delta\boldsymbol{\theta} + \frac{1}{2} \left(\frac{\sin\left(\frac{\|\Delta\boldsymbol{\theta}\|}{2}\right)}{\frac{\|\Delta\boldsymbol{\theta}\|}{2}} \right)^2 \widehat{\Delta\boldsymbol{\theta}'} \Delta\boldsymbol{\theta}$$

- $\Delta \mathbf{K} = \mathbf{R}_{n-1}^{\mathsf{T}}(S_i) \boldsymbol{\beta}$
- $\Delta \mathbf{R}(S_i) = \mathbf{R}(\Delta \boldsymbol{\theta}(S_i))$

Update rotations and strains

- $\mathbf{R}_n(S_i) = \Delta \mathbf{R}(S_i) \mathbf{R}_{n-1}(S_i)$
- $\mathbf{K}_n = \mathbf{K}_{n-1} + \Delta \mathbf{K}$
- $\boldsymbol{\Gamma}_n = \mathbf{R}_n^{\mathsf{T}}(S_i) \boldsymbol{\varphi}_0^h{}' - \mathbf{E}_1$

4.6 Linearized buckling

In the preceding sections, emphasis has been on the kinematical description and the solution of the non-linear problem. Incorporation of this formulation in a linearized buckling analysis may, however, not be self-evident. To the author's knowledge, this has not previously been presented for this particular family of elements. The current section is therefore dedicated to the development of the necessary equations.

The problem of linearized buckling involves solving the following generalized eigenvalue problem

$$\left|\mathbf{K}_0 + \Delta\lambda\mathbf{K}_g\right| = \left|\mathbf{K}(\hat{\boldsymbol{\varphi}}, \hat{\boldsymbol{\sigma}}) + \Delta\lambda\mathbf{K}_g\left(\hat{\boldsymbol{\varphi}}, \mathrm{D}\boldsymbol{\sigma}\cdot\frac{d\boldsymbol{\varphi}}{d\lambda}\right)\right| = 0 \tag{4.60}$$

In this equation, $\Delta\lambda\mathbf{K}_g$ is the change in geometric stiffness as a consequence of the change in internal forces and moments, due to a change in applied loads. The term $\mathrm{D}\boldsymbol{\sigma}\cdot\frac{d\boldsymbol{\varphi}}{d\lambda}$ is the incremental internal force due to a change in the applied loads:

$$\mathrm{D}\boldsymbol{\sigma}\cdot\frac{d\boldsymbol{\varphi}}{d\lambda} = \Delta\boldsymbol{\sigma} = \begin{bmatrix}\Delta\mathbf{n}\\ \Delta\mathbf{m}\end{bmatrix} = \begin{bmatrix}\mathrm{D}\mathbf{n}\cdot\Delta\boldsymbol{\varphi}\\ \mathrm{D}\mathbf{m}\cdot\Delta\boldsymbol{\varphi}\end{bmatrix} \tag{4.61}$$

As the "material" term $\mathbf{S}$ is independent of the internal forces, the geometric stiffness matrix becomes $\mathbf{K}_g = \mathbf{T}(\hat{\boldsymbol{\varphi}}, \Delta\boldsymbol{\sigma}) = \underset{e=1,NEL}{Assem}(\mathbf{T}_e(\hat{\boldsymbol{\varphi}}, \Delta\boldsymbol{\sigma}_e))$. Since the assembly operator is a linear operator, the subscript *e* will be omitted in the following, focusing on the relations at the element level.

The derivation of the incremental forces is quite similar to the derivation of the stiffness matrix. Assuming that a linear increment in the configuration, $\Delta\boldsymbol{\varphi} = d\boldsymbol{\varphi}/d\lambda$, has been found, the linear increment in forces can readily be obtained as the linear increment of Equation (4.62a).

$$\boldsymbol{\sigma} = \boldsymbol{\Pi}\boldsymbol{\Sigma} \quad \Rightarrow \quad \mathrm{D}\boldsymbol{\sigma}\cdot\Delta\boldsymbol{\varphi} = (\mathrm{D}\boldsymbol{\Pi}\cdot\Delta\boldsymbol{\varphi})\hat{\boldsymbol{\Sigma}} + \hat{\boldsymbol{\Pi}}(\mathrm{D}\boldsymbol{\Sigma}\cdot\Delta\boldsymbol{\varphi}) \tag{4.62}$$

Keeping with the assumption of hyperelastic materials, the incremental internal material forces can be expressed as:

$$\mathrm{D}\boldsymbol{\Sigma}\cdot\Delta\boldsymbol{\varphi} \;=\; \hat{\mathbf{C}}\hat{\boldsymbol{\Pi}}^{\mathsf{T}}\hat{\boldsymbol{\Xi}}^{\mathsf{T}}\Delta\boldsymbol{\varphi} \tag{4.63}$$

Premultiplication with $\hat{\boldsymbol{\Pi}}$, results in the "material" contribution of the incremental spatial force

$$\Delta\boldsymbol{\sigma}_m \;=\; \hat{\boldsymbol{\Pi}}(\mathrm{D}\boldsymbol{\Sigma}\cdot\;\Delta\boldsymbol{\varphi}\,) \;=\; \hat{\boldsymbol{\Pi}}\hat{\mathbf{C}}\hat{\boldsymbol{\Pi}}^{\mathsf{T}}\hat{\boldsymbol{\Xi}}^{\mathsf{T}}\Delta\boldsymbol{\varphi} \;=\; \hat{\mathbf{c}}\,\hat{\boldsymbol{\Xi}}^{\mathsf{T}}\Delta\boldsymbol{\varphi} \tag{4.64}$$

In Equation (4.64) the spatial version $\hat{\mathbf{c}} \;=\; \hat{\boldsymbol{\Pi}}\hat{\mathbf{C}}\hat{\boldsymbol{\Pi}}^{\mathsf{T}}$ of the elasticity tensor of the cross-section is used for compactness.

The "geometric" contribution $(\,\mathrm{D}\boldsymbol{\Pi}\cdot\Delta\boldsymbol{\varphi}\,)\hat{\boldsymbol{\Sigma}}$ follows immediately when realizing that $\mathrm{D}\mathbf{R}\cdot\Delta\boldsymbol{\varphi} \;=\; \widehat{\Delta\boldsymbol{\theta}}\,\mathbf{R}$:

$$(\,\mathrm{D}\boldsymbol{\Pi}\cdot\Delta\boldsymbol{\varphi}\,)\hat{\boldsymbol{\Sigma}} \;=\; -\begin{bmatrix}\mathbf{0} & \widehat{\mathbf{n}}\\ \mathbf{0} & \widehat{\mathbf{m}}\end{bmatrix}\Delta\boldsymbol{\varphi} \tag{4.65}$$

Summarizing and collecting terms, we get

$$\begin{aligned}\begin{bmatrix}\Delta\mathbf{n}\\ \Delta\mathbf{m}\end{bmatrix} \;&=\; \left\{\hat{\mathbf{c}}\,\hat{\boldsymbol{\Xi}}^{\mathsf{T}} - \begin{bmatrix}\mathbf{0} & \widehat{\mathbf{n}}\\ \mathbf{0} & \widehat{\mathbf{m}}\end{bmatrix}\right\}\begin{bmatrix}\Delta\boldsymbol{\varphi}_0\\ \Delta\boldsymbol{\theta}\end{bmatrix}\\ &=\; \hat{\mathbf{c}}\begin{bmatrix}\Delta\boldsymbol{\varphi}_0' + \widehat{\boldsymbol{\varphi}_0'}\,\Delta\boldsymbol{\theta}\\ \Delta\boldsymbol{\theta}'\end{bmatrix} - \begin{bmatrix}\widehat{\mathbf{n}}\,\Delta\boldsymbol{\theta}\\ \widehat{\mathbf{m}}\,\Delta\boldsymbol{\theta}\end{bmatrix}\end{aligned} \tag{4.66}$$

When written out for the forces and moments separately we have:

$$\Delta\mathbf{n} \;=\; \left(\hat{\mathbf{c}}_{11}\widehat{\boldsymbol{\varphi}_0'} - \widehat{\mathbf{n}}\right)\Delta\boldsymbol{\theta} + \hat{\mathbf{c}}_{11}\Delta\boldsymbol{\varphi}_0' + \hat{\mathbf{c}}_{12}\Delta\boldsymbol{\theta}' \tag{4.67}$$

$$\Delta\mathbf{m} \;=\; \left(\hat{\mathbf{c}}_{21}\widehat{\boldsymbol{\varphi}_0'} - \widehat{\mathbf{m}}\right)\Delta\boldsymbol{\theta} + \hat{\mathbf{c}}_{21}\Delta\boldsymbol{\varphi}_0' + \hat{\mathbf{c}}_{22}\Delta\boldsymbol{\theta}' \tag{4.68}$$

If the linearized buckling analysis is performed from an unstressed and undeformed state, the incremental forces for an initially straight element reduce to:

$$\Delta \mathbf{n} = \hat{\mathbf{C}}_{11}\widehat{\mathbf{E}}_1 \Delta\boldsymbol{\theta} + \hat{\mathbf{C}}_{11}\Delta\boldsymbol{\varphi}_0' + \hat{\mathbf{C}}_{12}\Delta\boldsymbol{\theta}' \tag{4.69}$$

$$\Delta \mathbf{m} = \hat{\mathbf{C}}_{21}\widehat{\mathbf{E}}_1 \Delta\boldsymbol{\theta} + \hat{\mathbf{C}}_{21}\Delta\boldsymbol{\varphi}_0' + \hat{\mathbf{C}}_{22}\Delta\boldsymbol{\theta}' \tag{4.70}$$

When establishing the geometric stiffness matrix, Equation (4.59) is valid provided $\hat{\mathbf{A}}$ is replaced with $\Delta\hat{\mathbf{A}}$:

$$\Delta\hat{\mathbf{A}} = \begin{bmatrix} \mathbf{0} & \mathbf{0} & -\widehat{\Delta\mathbf{n}} \\ \mathbf{0} & \mathbf{0} & -\widehat{\Delta\mathbf{m}} \\ \widehat{\Delta\mathbf{n}} & \mathbf{0} & \Delta\mathbf{n} \otimes \hat{\boldsymbol{\varphi}}_0' - (\Delta\mathbf{n} \cdot \hat{\boldsymbol{\varphi}}_0')\mathbf{1} \end{bmatrix} \tag{4.71}$$

4.7 Element implementations

In the program implementation, different versions of this formulation has been tested. Although they are all based on the same principles, the differences between them need some explanation.

- *Cosserat Polynomial* ($COPO_N^{gp}$)

  The $COPO_N^{gp}$ element is a generalized implementation of the elements presented by Simo et al. It is based on a general Lagrange polynomial basis, with N weights (nodes) and polynomial degree $N-1$. The integration is taken over gp Gauss-Legendre integration points. Although the current implementation can handle any order polynomial, the formulation is in practice limited by; a) the well known instability of high order polynomials, and b) the excessive bandwidth that is the consequence of the non-local support of the basis.

- *Cosserat Spline* ($COSP_N^{d,gp}$)

  The $COSP_N^{d,gp}$ elements are basically the same elements as the $COPO$ elements, only with a *B-spline basis* for the approximating functions. In addition to the many desirable properties of splines, such as stability and local support, these functions also open the door to some interesting possibilities. First of all, it is fairly easy and inexpensive to implement the element in a generic fashion, so that all polynomial elements is implemented in a single set of subroutines. Secondly, the richness of splines is greater

than the polynomials, as the space of polynomials (and Bézier curves) is only a subset of the spline space. Furthermore, splines are piecewise smooth polynomials, so integration schemes developed for polynomials can easily be adopted for splines. Finally it should be noted that splines are often used in computer aided design, thus allowing for isoparametric formulation of geometry and displacements. This latter benefit has not been investigated in this work. Among the drawbacks are the fact that the nodal weights will in general not be physical. Calculation of convergence norms, and the determination of reasonable convergence criteria thus become obscured. What complicates this issue, is that as the nodal weights are in general larger than the physical values. The effect this will have on convergence rates need to be investigated. Fortunately, the *energy norm* is not affected, on account of weights and unbalanced forces being work-conjugate. Another solution is to statically condense internal nodes, using only displacements or forces at the end-nodes in the convergence criteria. The weights at these nodes will *always* be physical.

Since this implementation contain an infinite number of elements, the elements based on the current kinematic description and B-spline basis functions with a uniform knot sequence will be denoted $COSP_N^{d,gp}$, where d is the degree of spline, gp is the number of integration points within each knot sequence, and N is the number of nodes in the element. Any element $COSP_N^{N-1}$ will thus correspond to a polynomial element of degree $N-1$. Examples of basis functions for two element instances are shown in Fig-

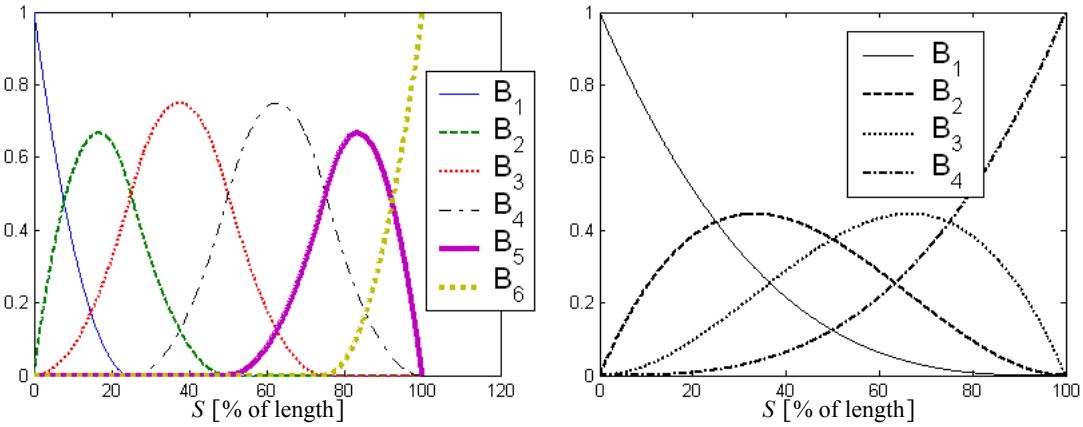

$COSP_6^2$ $COSP_4^3$

Figure 4.5 Examples of basis functions for $COSP_N^d$-elements

ure 4.5. The particular element $COSP_N^1$ will be a super-element, consisting of $N-1$ $COPO_1$-elements (see Figure 4.6). Similar superelements of higher order polynomials can be constructed by not restricting the knot sequence to be uniform.

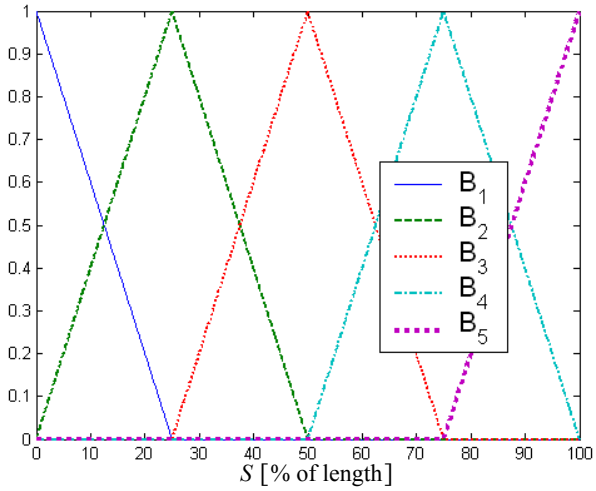

Figure 4.6 Basis functions for $COSP_5^1$

- *Linear, reduced Cosserat rod*

  The principal disadvantage of the formulation, as presented in the previous section, is the need for local element variables. Storing both the rotation and curvatures at integration points is inconvenient for two reasons; a) the memory requirement will increase, and b) the element will need a special update procedure when incrementing nodal values even for linear elastic materials. In addition, for rotations in 2D, the update procedure is unnecessary as the rotations become additive. To circumvent these problems, an element with linear interpolation of the total rotational state, $\mathbf{R}(S)$, is considered.

$$\boldsymbol{\theta}(S) = \sum_{i=1,2} \boldsymbol{\theta}_i \mathrm{B}_i(S) \quad , \qquad \mathbf{R}(S) = \mathbf{R}(\boldsymbol{\theta}(S)) \tag{4.72}$$

  By discarding the previous rotations, this element becomes slightly inconsistent as interpolation of the total pseudovectors is *not* the same as interpolating the incremental pseudovectors (see e.g. Cardona and Géradin [8]). This element is a good candidate to further illustrate the problem associated with the interpolation of rotations: Imagine an element, rotated rigidly π radians in the beam plane ($\mathbf{E}_1$, $\mathbf{E}_3$), followed by a deformational rotation, applied as a twist of $\pi/2$ at one node as shown in Figure 4.7. The twist

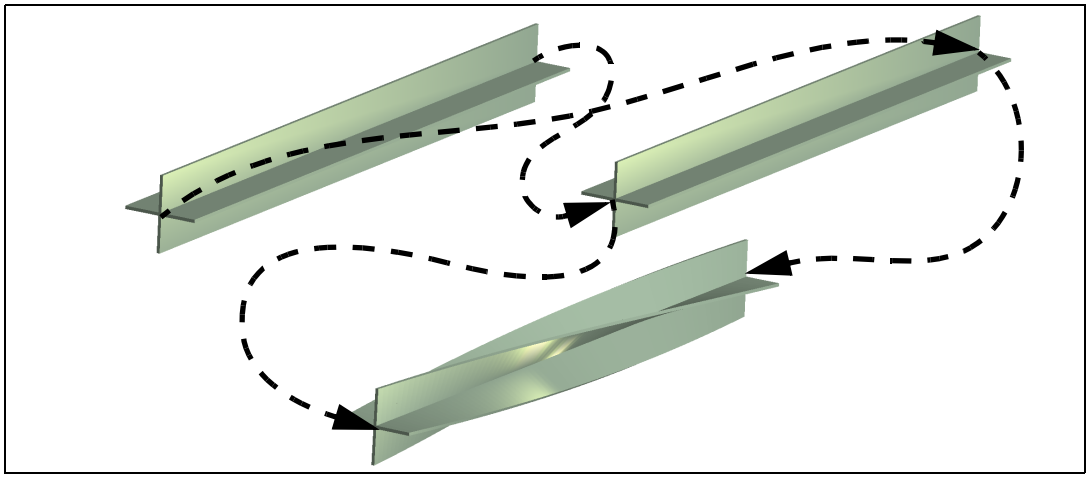

Figure 4.7 Element motion

is assumed to vary linearly along the length of the beam in the spatial configuration. The total rotations at the nodes now become: $\boldsymbol{\theta}_1 = \pi/\sqrt{2}\left[0\ 1\ 1\right]^{\mathsf{T}}$, and $\boldsymbol{\theta}_2 = \pi\left[0\ 1\ 0\right]^{\mathsf{T}}$. Using this to calculate the material curvature results in:

$$\mathbf{K} = \frac{\pi}{2L}\left[1.0398 \quad 0.0478 \quad -0.1154\right]^{\mathsf{T}} \tag{4.73}$$

Intuitively, this cannot be the correct curvature since the element is only in a state of twist, not bending. It should be noted that this would be the resulting curvature for a $COPO_1$-element, if this configuration was achieved in one step by an applied boundary condition. If, in stead of the total state, only the deformational rotations are interpolated, we get the following relationships:

$$\mathbf{R}(S) = \mathbf{R}_r\mathbf{R}(\boldsymbol{\theta}_d(S)), \quad \boldsymbol{\theta}_d(S) = \sum_{i=1,2} \boldsymbol{\theta}_{di}\mathrm{B}_i(S) \tag{4.74}$$

The curvature from this kinematic description is

$$\begin{aligned}
\mathbf{K} &= \mathrm{Axial}\left(\mathbf{R}^{\mathsf{T}}(S)\frac{d}{dS}\mathbf{R}(S)\right) = \mathrm{Axial}\left(\mathbf{R}_d^{\mathsf{T}}(S)\mathbf{R}_r^{\mathsf{T}}\frac{d}{dS}\mathbf{R}_r\mathbf{R}_d(S)\right) \\
&= \mathrm{Axial}\left(\mathbf{R}_d^{\mathsf{T}}(S)\mathbf{R}_r^{\mathsf{T}}\mathbf{R}_r\frac{d}{dS}\mathbf{R}_d(S)\right) = \mathrm{Axial}\left(\mathbf{R}_d^{\mathsf{T}}(S)\frac{d}{dS}\mathbf{R}_d(S)\right) \\
&= \frac{\sin(\|\boldsymbol{\theta}_d\|)}{\|\boldsymbol{\theta}_d\|}\boldsymbol{\theta}_d' + \left(1 - \frac{\sin(\|\boldsymbol{\theta}_d\|)}{\|\boldsymbol{\theta}_d\|}\right)\frac{\boldsymbol{\theta}_d \cdot \boldsymbol{\theta}_d'}{\|\boldsymbol{\theta}_d\|^2}\boldsymbol{\theta}_d + \frac{1}{2}\left(\frac{\sin\left(\frac{\|\boldsymbol{\theta}_d\|}{2}\right)}{\frac{\|\boldsymbol{\theta}_d\|}{2}}\right)^2 \widehat{\boldsymbol{\theta}}_d'\boldsymbol{\theta}_d
\end{aligned} \tag{4.75}$$

As expected, the rigid body rotation is removed from the curvature, and only the interpolated, deformational, pseudovector is needed.

In our example, setting the rigid body rotation to $\mathbf{R}_r = \mathbf{R}(\begin{bmatrix}\pi/4 & 0 & 0\end{bmatrix}^T)\mathbf{R}(\begin{bmatrix}0 & \pi & 0\end{bmatrix}^T)$, results in the following deformational nodal rotations: $\boldsymbol{\theta}_{d1} = -\boldsymbol{\theta}_{d2} = -\begin{bmatrix}\pi/4 & 0 & 0\end{bmatrix}^T$. Since this is the actual 2D rotation, the interpolation is exact, and the correct curvature is obtained:

$$\mathbf{K} = \frac{\pi}{2L}\begin{bmatrix}1 & 0 & 0\end{bmatrix}^T \tag{4.76}$$

In Figure 4.8, the resulting components of the pseudovectors of these descriptions are plotted. Here, $\boldsymbol{\theta}$ denotes the rotational pseudovector obtained for the linear interpolation of the total rotation, and $\boldsymbol{\phi} = \boldsymbol{\theta}(\mathbf{R}_r\mathbf{R}_d(S))$ is the pseudovector of the total rotation obtained when only the deformations are interpolated.

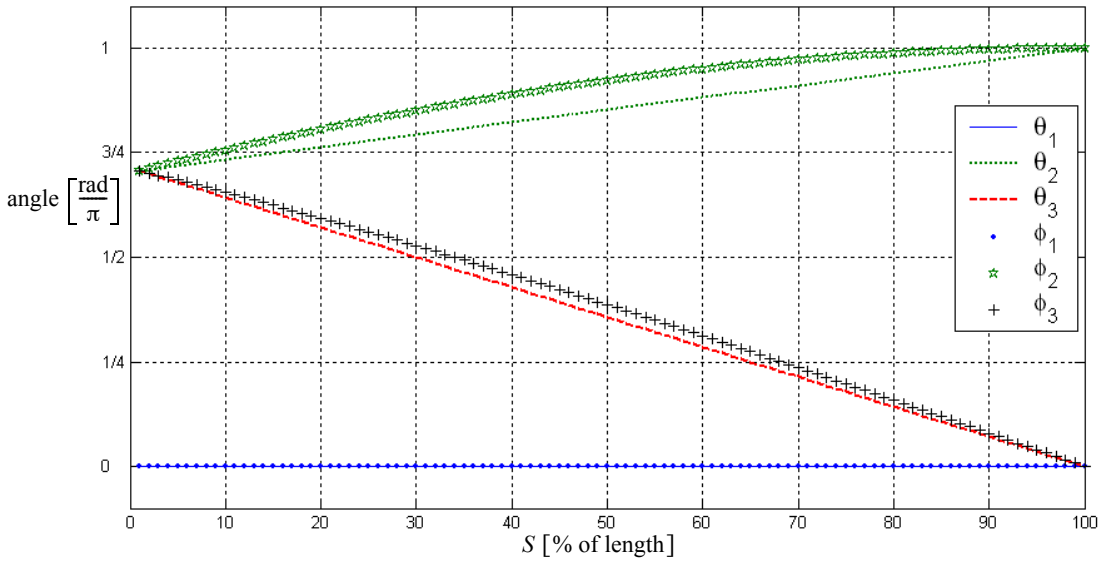

Figure 4.8 Components of the pseudovectors along the length of the beam

By this rationale, the actual element is implemented in conjunction with the co-rotational procedure presented in Section 4.1. When used within the co-rotational framework, average rigid body rotations are extracted from the nodal values. If we then assume small rotations within the element, the interpolation becomes reasonable. If the rotations are within $30°$, it is safe to assume that $\sin(\|\boldsymbol{\theta}_d\|)/\|\boldsymbol{\theta}_d\| \cong 1$, and a simplified expression for the curvature may be adopted:

$$\mathbf{K} = \Delta\mathbf{K} = \boldsymbol{\beta} \cong \boldsymbol{\theta}'_d + \frac{1}{2}\widehat{\boldsymbol{\theta}}'_d\,\boldsymbol{\theta}_d \tag{4.77}$$

It should be noted that even for reasonably small deformational rotations, the coupling term $\frac{1}{2}\widehat{\boldsymbol{\theta}}'_d\,\boldsymbol{\theta}_d$ may contribute, since, for short elements, $\boldsymbol{\theta}'_d$ may become large.

Similarly, the deformational rotation matrix along the length of the beam can safely be evaluated as the third, second or even first order approximation:

$$\mathbf{R}_d \cong \mathbb{1} + \left(1 - \frac{\|\boldsymbol{\theta}_d\|^2}{6}\right)\widehat{\boldsymbol{\theta}}_d + \frac{1}{2}\widehat{\boldsymbol{\theta}}_d^2 \cong \mathbb{1} + \widehat{\boldsymbol{\theta}}_d + \frac{1}{2}\widehat{\boldsymbol{\theta}}_d^2 \cong \mathbb{1} + \widehat{\boldsymbol{\theta}}_d \tag{4.78}$$

While this may seem like a small saving compared to the many operations needed to evaluate the stiffness matrix and the unbalanced forces, it should not be regarded as such. The calculation of the rotation matrix in a robust and accurate manner for small angles is actually a quite costly affair, involving both the evaluation of square roots as well as trigonometric functions.

Chapter 5
Element Independent Co-Rotational Formulation

The formulation of non-linear problems in structural mechanics is generally classified by the form of the governing equations and the stress and strain measures into three main groups:

- Total Lagrangian formulation (TL)
- Updated Lagrangian formulation (UL)
- Eulerian formulation (E)

In addition to these, we also have the co-rotational (CR) formulation. This is the most recent formulation and has, according to Felippa [13], yet to penetrate commercial software. This is not to say that CR does not have long historical roots, stretching back to the seminal work by de Veubeke published in 1976 (see Felippa [13] for an extensive historical review). The relatively moderate impact of CR may be explained by the many misconceptions surrounding the formulation. In fitting the formulation to the classical view of three principal forms, CR is frequently classified as an Eulerian description of motion. However, much work has been reported, in which equivalence with both the Total Lagrangian and Updated Lagrangian formulation has been demonstrated. Also, the formulation seems to spur developers to formulate their own version, leaving the core elements of the method rather obscured.

In this chapter, the Element Independent Co-Rotational formulation (EICR) will be discussed. The formulation presented here follows closely the important contributions by Brogan, Nour-Omid and Rankin [26,32,33], and the further elaboration by Haugen [16]. As the name indicates this is a formulation that operates independently of the elements, thus leaving the internal workings of the element open. Rather than a particular element

formulation, it can be interpreted as a *front-end filter* that is intended to improve the performance of a given element. A key point in the derivation that follows is that the rotational element degrees of freedom are the *incremental pseudovectors (instantaneous rotations)*; this means that the rotational increments are *not* additive, and require a special update procedure. If the element is developed using any other rotational parameters, which is the case for most linear elements, a shift of variables as described in Section 3.3, "Variation of rotations" should be applied in advance. This will assure that large rotations are handled in a consistent manner, and that moments are properly conjugate to the rotational parameters in a virtual work sense. For completeness, and to be in line with the afore-mentioned papers, the shift in variables is also presented.

In most texts on EICR, the deformations are assumed to be small. It should, however, be noted that nowhere in the derivations are any such assumptions introduced. It is still useful to keep in mind that the procedure was developed to improve the performance of simple linear elements that are not invariant to rigid body motion. Thus the primary advantage of the formulation is that one can easily include the principal sources of nonlinearity in large displacement[1]-small strain problems, using only standard (well proven) linear elements. By defining successive fixed (inertial) reference frames, to which deformations are measured, these elements will be valid even in problems involving large rotations as long as the deformations are moderate, or at least in the range that the element was originally developed to handle. Although EICR is founded on this idea, one is free to select any basis or configuration in which the deformations are actually measured. It is, however, convenient to take advantage of this 'rigid-body' free reference frame, in other words:

If one has chosen a method to extract rigid-body motion for the purpose of establishing the matrices in EICR, one also has a natural, but not necessary, choice of reference frame in which deformations are measured.

Based on this, the presentation is divided into two parts, one containing the core elements of the co-rotational procedure, and the other where the fundamentals of EICR is presented. In a later chapter it will be demonstrated that the efficiency of the formulation is governed

1. It should be noted that the actual displacement need not be large for the formulation to be warranted, e.g. in analyses where one wishes to determine possible critical points in the solution.

only by the element's capabilities to account for the deformations and the exactitude of the extracted rigid-body rotations.

5.1 Co-rotational procedure

5.1.1 Basic kinematic description

In the co-rotational process, we want to separate the motion of the body into two parts; the *deformational motion* and the *rigid-body motion*. In the following, we will be concerned only with a partition of the body, not the entire structure. In order to conform with standard notation and common practice in the finite-element literature, this part will be called an *element.* In spite of the name, this element can just as well be an assembly of finite elements, or even some other discretization of the domain. By denoting the mapping of rigid-body motion by $\boldsymbol{\varphi}_r(\mathbf{X})$, and the mapping of deformations by $\boldsymbol{\varphi}_d(\mathbf{X})$, the total map of the motion becomes in compact form:

$$\mathbf{x} = \boldsymbol{\varphi}(\mathbf{X}) = \boldsymbol{\varphi}_d \circ \boldsymbol{\varphi}_r = \boldsymbol{\varphi}_r \circ \boldsymbol{\varphi}_d^{CR} \tag{5.1}$$

Where $\circ$ is the symbol of composition of functions, so that $f_1 \circ f_2 = f_1(f_2)$. The significance of Equation (5.1) is that the map can either be obtained by a rigid-body motion followed by a deformation, or as a deformation followed by a rigid-body motion. Contrary to what is usual in the CR-literature, we will follow the latter approach in this presentation. It will then be shown that the basic results remain the same. These concepts are illustrated in Figure 5.1. The superscript *CR*, used to mark a co-rotated measure, might seem confusing when used in the context of the deformational map. The significance becomes clear, however, when one considers this to be a mapping within the co-rotating system $\{\mathbf{E}_i\}$. The first challenge is to define the mapping of the rigid-body. We start by defining the configuration $\mathbb{C}^0$ which is simply the initial spatial configuration, and the co-rotated configuration $\mathbb{C}^{0n}$ which is a virtual spatial configuration of the initial geometry, based on some form of 'best-fit' criterion of the deformed configuration $\mathbb{C}^n$. Exactly how $\mathbb{C}^{0n}$ is fitted to $\mathbb{C}^n$ depends primarily on the geometric properties of the element, e.g. a triangular shell element is fitted differently from that of a two-node beam. Even for a specific geometry, $\mathbb{C}^{0n}$ is not unique and several approaches have been used. Attached to the co-rotated con-

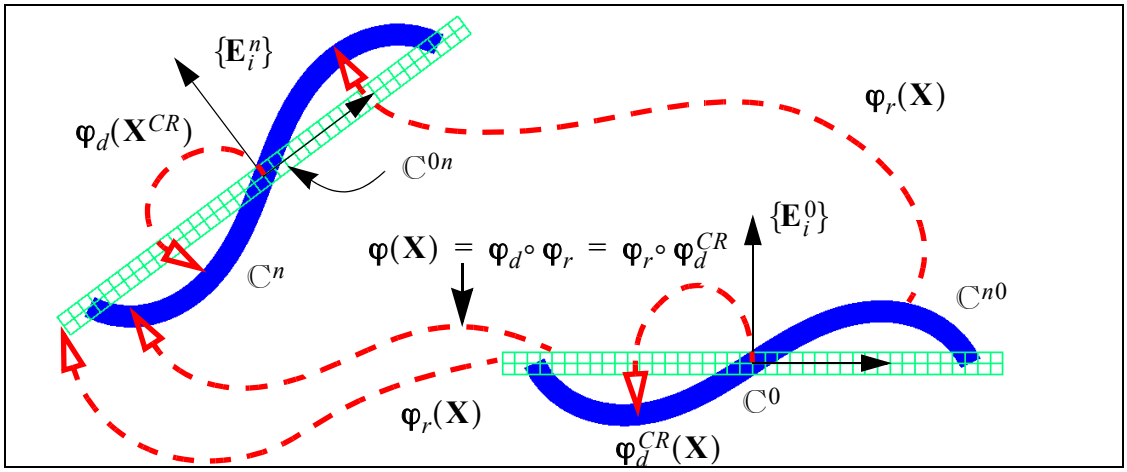

Figure 5.1 Mappings and configurations

figuration, is the co-rotated reference-frame, $\{\mathbf{x}_c^n,\ \mathbf{E}_i^n\}$, defined in a similar manner to the moving basis, $\{\mathbf{t}_i\}$, in the Cosserat rod theory. The significant difference between the moving basis and the co-rotated base-vectors is that the moving basis is continuously rotated and translated within the domain. The co-rotated basis, however, is constant and defined for the element as a whole. Leaving the $\mathbf{E}_i^n$'s unspecified, the general form of the rigid body map φ_r becomes:

$$\begin{aligned}\varphi_r(\mathbf{X}) &= \mathbf{x}_c^n + (\mathbf{E}_i^n \otimes \mathbf{I}_i)(\mathbf{I}_i \otimes \mathbf{E}_i^0)\mathbf{X} = \mathbf{x}_c^n + \mathbf{T}_n^{\mathsf{T}}\mathbf{T}_0\mathbf{X} \\ &= \mathbf{x}_c^n + \mathbf{T}_r^{\mathsf{T}}\mathbf{X} = \mathbf{x}_c^n + \mathbf{R}_r\mathbf{X}\end{aligned} \tag{5.2}$$

$$\mathbf{T}_n = \mathbf{I}_i \otimes \mathbf{E}_i^n,\ \mathbf{T}_0 = \mathbf{I}_i \otimes \mathbf{E}_i^0 \tag{5.3}$$

Here, the transformation-matrices $\mathbf{T}_n$ and $\mathbf{T}_0$ are introduced. They are the direction-cosine matrices relating the ambient space to the updated and original spatial basis respectively. The rotation matrix $\mathbf{R}_r = \mathbf{T}_n^{\mathsf{T}}\mathbf{T}_0$ defines the rigid body rotation of the configuration. This is a two-point tensor that is homogeneous within an element, and transforms objects in the basis $\{\mathbf{E}_i^0\}$ to objects in the basis $\{\mathbf{E}_i^n\}$. Inserting Equation (5.2) into (5.1) yields the following expression for the spatial position $\mathbf{x}$ of the material point $\mathbf{X}$:

$$\mathbf{x} = \varphi(\mathbf{X}) = \mathbf{x}_c^n + \mathbf{R}_r\varphi_d^{CR}(\mathbf{X}) \tag{5.4}$$

Here it is clear that only the deformational map, φ_d^{CR}, depend on the material position $\mathbf{X}$. Deriving the deformational gradient, we see the close relation to the polar decomposition theorem:

$$\mathbf{F} = \frac{\partial \mathbf{x}}{\partial \mathbf{X}} = \mathbf{R}_r \mathbf{F}_d(\mathbf{X}) = \mathbf{R}(\mathbf{X})\mathbf{U}(\mathbf{X}) = \mathbf{R}_r \tilde{\mathbf{R}}(\mathbf{X})\mathbf{U}(\mathbf{X}) \tag{5.5}$$

$$\mathbf{F}_d(\mathbf{X}) = \frac{\partial \varphi_d^{CR}}{\partial \mathbf{X}} = \tilde{\mathbf{R}}(\mathbf{X})\mathbf{U}(\mathbf{X}) \tag{5.6}$$

When the rigid-body rotation is the point-wise total rotation of the body, the deformation gradient of the deformational map, $\mathbf{F}_d$, reduces to the right stretch-tensor $\mathbf{U}$. A common assumption is that the additional rotation $\tilde{\mathbf{R}}$ is close to the identity. If the stretches are assumed to be close to the identity as well, deformations are small and a small-strain assumption can be adopted within the element. The primary observation is, however, that the principal source of non-linearity for slender structures such as beams and shells, namely rotations, are extracted for small elements:

$$V(\mathscr{B}_e) \to 0 \quad \Rightarrow \quad \mathbf{F}_d = \mathbf{U} \tag{5.7}$$

We now introduce the generalized Lagrangian strain tensor $\mathbf{E}^{(n)}$, defined for positive *n*. Obviously, these strains are unaffected by the rotations.

$$\mathbf{E}^{(n)} = \frac{1}{2n}[(\mathbf{F}^{\mathsf{T}}\mathbf{F})^n - \mathbb{1}] = \frac{1}{2n}[\mathbf{U}^{2n} - \mathbb{1}] \tag{5.8}$$

For the particular choice $n = 1/2$, we get the Biot-strain (5.9).

$$\mathbf{E}^{(\frac{1}{2})} = [\mathbf{U} - \mathbb{1}] = \mathbf{F}_d - \mathbb{1} = \frac{1}{2}(\mathbf{F}_d + \mathbf{F}_d^{\mathsf{T}}) - \mathbb{1} \tag{5.9}$$

Thus, the small strain tensor of the co-rotated element coincides with the Biot-strain when $\mathbf{F}_d = \mathbf{U}$. This is obviously subject to the condition that the rotations are correctly extracted, rendering $\mathbf{F}_d$ as a symmetric positive definite tensor.

Requiring the volume, $V(\mathscr{B}_e)$, of the element to vanish is an unnecessarily strong requirement, and may result in significant round-off errors. Most elements are quite accurate for moderate rotations, and usually the rigid-body rotations will rapidly dominate for reasonably fine meshes.

For continuum elements such as volume and membrane elements, these results are rather straightforward. The situation is somewhat more complicated in the case of structural elements such as shells and beams. These elements are based on some kinematical assump-

tions that inevitably introduce simplifications. Most of these simplifications are well founded, and the errors they introduce will vanish when the element size decrease, while others may not.

5.1.2 Linking the deformations to the global motion

In deriving the relationship between the deformational measures and the system level measures, it is convenient to do so only at N discrete points $\mathbf{X}_I$ in the domain. These points, called the 'visible' nodes, are chosen in such a manner that their displacement and rotation uniquely define the deformational state of the element. Based on the average

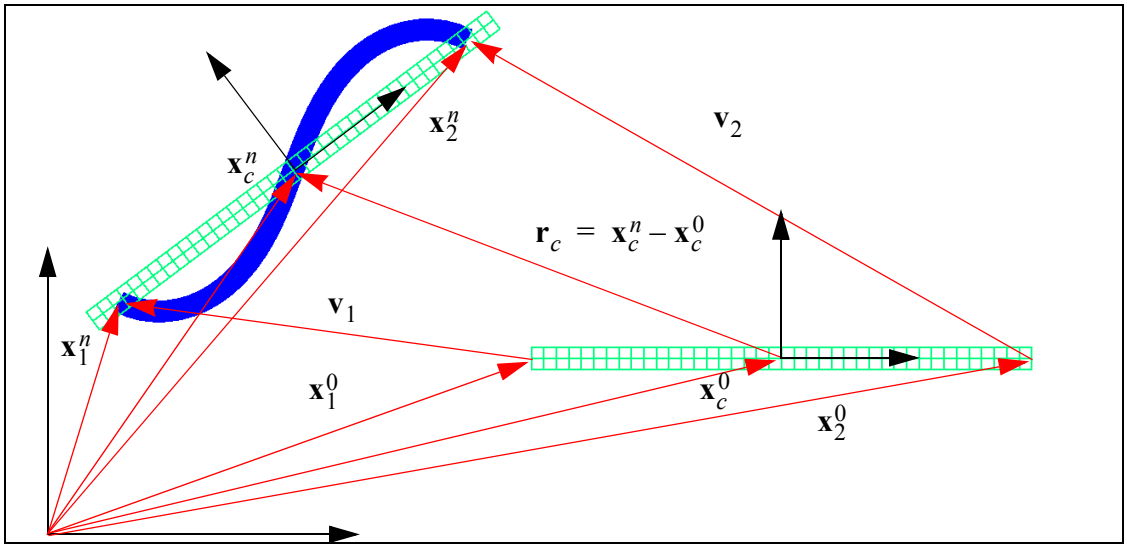

Figure 5.2 Global measures

nodal position, the origin $\mathbf{x}_c^n$ of the co-rotational basis is calculated for $n \in \mathbb{Z}$:

$$\mathbf{x}_c^n = \frac{1}{N} \sum_{I=1..N} \mathbf{x}_I^n \tag{5.10}$$

The global displacements at node I are collected in the vector $\mathbf{v}_I$ with components in the global spatial frame, see Figure 5.2:

$$\mathbf{x}_I^n = \mathbf{x}_I^0 + \mathbf{v}_I = \mathbf{x}_c^n + \mathbf{R}_r \boldsymbol{\varphi}_{dI}^{CR} = \mathbf{x}_c^n + \mathbf{R}_r(\boldsymbol{\varphi}_{0I}^{CR} + \mathbf{u}_{dI}^{CR}) \tag{5.11}$$

$$\mathbf{u}_{dI}^{CR} = \mathbf{R}_r^{\mathsf{T}}(\mathbf{x}_I^0 + \mathbf{v}_I - \mathbf{x}_c^n) - \boldsymbol{\varphi}_{0I}^{CR} \tag{5.12}$$

$\mathbf{u}_{dI}^{CR}$ is a vector of co-rotational displacements; it has components in the material frame (Although not strictly correct, in the following $\{\mathbf{E}_i^0\}$ will be denoted the *material basis* in order to reduce the number of configurations and bases needed). As usual, the derivations of the co-rotational rotations are a little more involved. For each node *I* in the element we define a set of spatial base-vectors $\{\mathbf{t}_I^i\}$, that is the rotated material basis $\mathbf{t}_I^i = \mathbf{R}_I \mathbf{E}_i^0$:

$$\mathbf{R}_I = \mathbf{t}_I^i \otimes \mathbf{E}_i^0 = \mathbf{R}_{dI}\mathbf{R}_r = (\mathbf{t}_I^i \otimes \mathbf{E}_i^n)(\mathbf{E}_j^n \otimes \mathbf{E}_j^0), \tag{5.13}$$

where $\mathbf{R}_I$ is the total rotation at node *I*, $\mathbf{R}_{dI}$ is the deformational rotation and $\mathbf{R}_r = \mathbf{T}_r^\mathsf{T}$ is the rigid body rotation of the element. Since the deformation $\mathbf{R}_{dI}$ is obtained as the remaining rotation of the node after the rigid body rotation of the *element* is extracted, this measure is element specific and will in general differ for neighboring elements. Also, we can observe that the relation (5.13) does not change if we perform a pull-back from the updated basis to the original coordinates:

$$\tilde{\mathbf{R}}_I = \mathbf{T}_r^\mathsf{T}\mathbf{R}_{dI}\mathbf{R}_r\mathbf{T}_r = \mathbf{R}_r\mathbf{R}_{dI} = \mathbf{R}_r\mathbf{T}_r\tilde{\mathbf{R}}_{dI}\mathbf{T}_r^\mathsf{T} = \tilde{\mathbf{R}}_{dI}\mathbf{R}_r \tag{5.14}$$

Neither Equation (5.13) nor (5.14) does, however, produce the required relation between the co-rotational and the nodal rotations. As a co-rotational measure should not change during rigid-body motion, the co-rotational, deformational rotations must be a material increment:

$$\begin{aligned}\mathbf{R}_I &= (\mathbf{t}_I^i \otimes \mathbf{E}_i^n)(\mathbf{E}_j^n \otimes \mathbf{E}_j^0)\\ &= (\mathbf{E}_k^n \otimes \mathbf{E}_k^0)(\mathbf{E}_l^0 \otimes \mathbf{E}_l^n)(\mathbf{t}_I^i \otimes \mathbf{E}_i^n)(\mathbf{E}_j^n \otimes \mathbf{E}_j^0)\\ &= (\mathbf{E}_i^n \otimes \mathbf{E}_i^0)(\mathbf{t}_j^{CR} \otimes \mathbf{E}_j^{CR})\\ &= \mathbf{R}_r\mathbf{R}_{dI}^{CR}\end{aligned} \tag{5.15}$$

$$\mathbf{t}_i^{CR} = (\mathbf{t}_I^i \cdot \mathbf{E}_j^n)\mathbf{E}_j^0, \quad \mathbf{E}_i^{CR} = (\mathbf{E}_i^n \cdot \mathbf{E}_j^n)\mathbf{E}_j^0 = \mathbf{E}_i^0 \tag{5.16}$$

Thus the co-rotated deformational rotations become a two-point tensor that brings a vector in the material configuration to the co-rotated spatial configuration:

$$\mathbf{R}_{dI}^{CR} = r_{dI}^{ij}(\mathbf{E}_i^0 \otimes \mathbf{E}_j^0) = \mathbf{t}_i^{CR} \otimes \mathbf{E}_i^0, \text{ where } r_{dI}^{ij} = \mathbf{E}_i^n \cdot \mathbf{t}_I^j \tag{5.17}$$

The general concepts in these relationships and transformations are collected and illustrated in Figure 5.3.

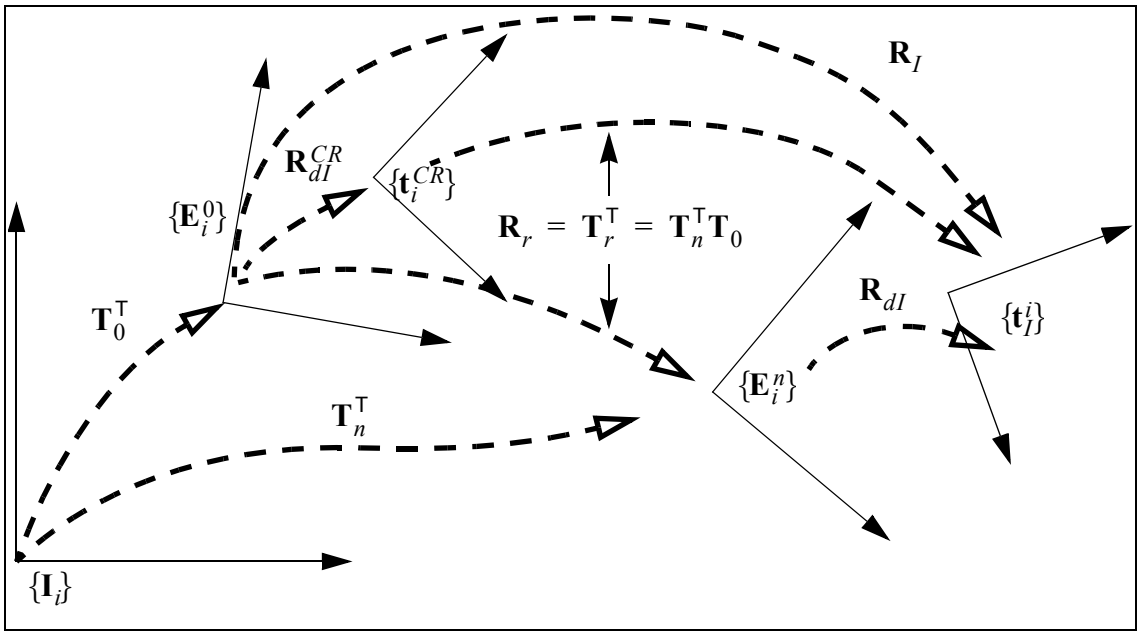

Figure 5.3 Chart of maps at node *I*

It should be noted that the components of the co-rotational deformations $\tilde{\mathbf{R}}_{dI}^{CR} = \mathbf{T}_0\mathbf{R}_{dI}^{CR}\mathbf{T}_0^\mathsf{T}$, expressed in the original basis, are identical to the components of $\tilde{\mathbf{R}}_{dI} = \mathbf{T}_n\mathbf{R}_{dI}\mathbf{T}_n^\mathsf{T}$, expressed in the updated basis. This is easily verified since

$$\tilde{\mathbf{R}}_{dI}^{CR} = \tilde{\mathbf{R}}_{dI} = \mathbf{T}_n\mathbf{R}_I\mathbf{T}_0^\mathsf{T} \tag{5.18}$$

If the deformational state of the element is given by the rotation pseudovector, it can generally be extracted from Equation (5.18) by means of algorithms such as *Spurrier's algorithm,* presented in Appendix D. In doing so, one should keep in mind the discussion on finite rotations in Chapter 2, where it was shown that while extracting the pseudovector from rotation-matrices is *one-to-one*, it is not *onto.* This means that some form of heuristic must be applied, generally by restricting the magnitude of rotations, i.e. letting the deformations be in the range $-\pi \le \theta \le \pi$.

$$\tilde{\boldsymbol{\theta}}_{dI}^{CR} = \boldsymbol{\theta}(\tilde{\mathbf{R}}_{dI}^{CR}),\ 0 \le \left\|\tilde{\boldsymbol{\theta}}_{dI}^{CR}\right\| \le \pi \tag{5.19}$$

Note that the transformation of co-rotational vectorial measures to local coordinates is given by $(\tilde{\circ})^{CR} = \mathbf{T}_0(\circ)^{CR}$, whereas global measures are transformed as $(\tilde{\circ}) = \mathbf{T}_n(\circ)$.

5.1.3 Differential relations

Having obtained the relationships between the co-rotated deformational measures and the global motions, we can proceed to find the corresponding relations of the differentials. Taking the variation of Equation (5.11), we get:

$$\delta\mathbf{x}_I^{\eta} = \delta\mathbf{v}_I = \delta\mathbf{x}_c + \delta\mathbf{R}_r\boldsymbol{\varphi}_{dI}^{CR} + \mathbf{R}_r\delta\mathbf{u}_{dI}^{CR} \tag{5.20}$$

$$\delta\mathbf{x}_c = \frac{1}{N}\sum_{I=1\ldots N}\delta\mathbf{x}_I = \frac{1}{N}\sum_{I=1\ldots N}\delta\mathbf{v}_I \tag{5.21}$$

$$\delta\mathbf{R}_r = (\delta\mathbf{T}_n^{\mathsf{T}})\mathbf{T}_0 = \mathrm{Spin}(\delta\boldsymbol{\omega}_r)\mathbf{T}_n^{\mathsf{T}}\mathbf{T}_0 = \mathbf{T}_n^{\mathsf{T}}\mathrm{Spin}(\delta\tilde{\boldsymbol{\omega}}_r)\mathbf{T}_0, \quad \delta\tilde{\boldsymbol{\omega}}_r = \mathbf{T}_n\delta\boldsymbol{\omega}_r \tag{5.22}$$

$$\begin{aligned}\delta\mathbf{v}_I &= \frac{1}{N}\sum_{J=1\ldots N}\delta\mathbf{v}_J + \mathbf{T}_n^{\mathsf{T}}\mathrm{Spin}(\delta\tilde{\boldsymbol{\omega}}_r)\mathbf{T}_0\boldsymbol{\varphi}_{dI}^{CR} + \mathbf{R}_r\delta\mathbf{u}_{dI}^{CR}\\ &= \frac{1}{N}\sum_{J=1\ldots N}\delta\mathbf{v}_J - \mathbf{T}_n^{\mathsf{T}}\mathrm{Spin}(\tilde{\boldsymbol{\varphi}}_{dI}^{CR})\delta\tilde{\boldsymbol{\omega}}_r + \mathbf{T}_n^{\mathsf{T}}\delta\tilde{\mathbf{u}}_{dI}^{CR}\\ \Rightarrow\delta\tilde{\mathbf{u}}_{dI}^{CR} &= \delta\tilde{\mathbf{v}}_I - \frac{1}{N}\sum_{J=1\ldots N}\delta\tilde{\mathbf{v}}_J + \mathrm{Spin}(\tilde{\boldsymbol{\varphi}}_{dI}^{CR})\delta\tilde{\boldsymbol{\omega}}_r\end{aligned} \tag{5.23}$$

By postulating the existence of a relation of the form

$$\delta\tilde{\boldsymbol{\omega}}_r = \tilde{\mathbf{G}}\delta\tilde{\mathbf{v}} \tag{5.24}$$

In which the rigid body rotations $\delta\tilde{\boldsymbol{\omega}}_r$ are extracted from the elements nodal displacements, we get a differential relation that links differentials in the visible dof's $\delta\tilde{\mathbf{v}}$ to the elements co-rotated translational dof's $\delta\tilde{\mathbf{u}}_{dI}^{CR}$:

$$(\delta\tilde{\mathbf{u}})_{CR} = \begin{bmatrix}\delta\tilde{\mathbf{u}}_{d1}^{CR}\\ \vdots\\ \delta\tilde{\mathbf{u}}_{dN}^{CR}\end{bmatrix} = \left(\begin{bmatrix}1&0&\ldots&0&0\\ \vdots&\vdots&\ddots&\vdots&\vdots\\ 0&0&\ldots&1&0\end{bmatrix} - \frac{1}{N}\begin{bmatrix}1&0&\ldots&1&0\\ \vdots&\vdots&\ddots&\vdots&\vdots\\ 1&0&\ldots&1&0\end{bmatrix} - \begin{bmatrix}\tilde{\mathbf{S}}_1\\ \vdots\\ \tilde{\mathbf{S}}_N\end{bmatrix}\tilde{\mathbf{G}}\right)\delta\tilde{\mathbf{v}}\ , \tag{5.25}$$

where

$$\tilde{\mathbf{S}}_I = -\mathrm{Spin}(\tilde{\boldsymbol{\varphi}}_{dI}^{CR}) \tag{5.26}$$

The matrix $\tilde{\mathbf{G}}$ is an element dependent matrix that depends on geometry and developer-choice, but not on the underlying element-formulation. In the special case of elements having the Kronecker delta property, that is

$$\delta\tilde{\mathbf{u}}_{dI}^{CR} = \delta\tilde{\mathbf{v}}_{dI}^{CR} \tag{5.27}$$

Equation (5.25) can be re-written in the form:

$$(\delta\tilde{\mathbf{v}})_{CR} = \begin{bmatrix} \delta\tilde{\mathbf{v}}_{d1}^{CR} \\ \vdots \\ \delta\tilde{\mathbf{v}}_{dN}^{CR} \end{bmatrix} = \left(\begin{bmatrix} 1 & 0 & \dots & 0 & 0 \\ \vdots & \vdots & \ddots & \vdots & \vdots \\ 0 & 0 & \dots & 1 & 0 \end{bmatrix} - \frac{1}{N} \begin{bmatrix} 1 & 0 & \dots & 1 & 0 \\ \vdots & \vdots & \ddots & \vdots & \vdots \\ 1 & 0 & \dots & 1 & 0 \end{bmatrix} - \begin{bmatrix} \tilde{\mathbf{S}}_1 \\ \vdots \\ \tilde{\mathbf{S}}_N \end{bmatrix} \tilde{\mathbf{G}} \right) \delta\tilde{\mathbf{v}} \tag{5.28}$$

In the following we will continue to use the notation $\tilde{\mathbf{u}}_{dI}^{CR}$, tacitly assuming that (5.27) holds for both displacements and incremental rotations. Using $\tilde{\mathbf{v}}_{dI}^{CR}$ is then superfluous, and will therefore be avoided.

In a manner similar to the displacements, we obtain by taking the variation of (5.15) with respect to the spatial increment the following differential relation:

$$\delta\mathbf{R}_I = \mathrm{Spin}(\delta\boldsymbol{\omega}_I)\mathbf{R}_I = \delta\mathbf{R}_r\mathbf{R}_{dI}^{CR} + \mathbf{R}_r\delta\mathbf{R}_{dI}^{CR} \tag{5.29}$$

$$\delta\mathbf{R}_r = \mathrm{Spin}(\delta\boldsymbol{\omega}_r)\mathbf{R}_r, \quad \delta\mathbf{R}_{dI}^{CR} = \mathrm{Spin}(\delta\boldsymbol{\omega}_{dI}^{CR})\mathbf{R}_{dI}^{CR} \tag{5.30}$$

$$\mathrm{Spin}(\delta\boldsymbol{\omega}_I) = \mathrm{Spin}(\delta\boldsymbol{\omega}_r) + \mathbf{R}_r\mathrm{Spin}(\delta\boldsymbol{\omega}_{dI}^{CR})\mathbf{R}_r^{\mathsf{T}} \tag{5.31}$$

$$\delta\boldsymbol{\omega}_{dI}^{CR} = \mathbf{R}_r^{\mathsf{T}}\delta\boldsymbol{\omega}_I - \mathbf{R}_r^{\mathsf{T}}\delta\boldsymbol{\omega}_r = \mathbf{T}_0^{\mathsf{T}}\delta\tilde{\boldsymbol{\omega}}_I - \mathbf{T}_0^{\mathsf{T}}\delta\tilde{\boldsymbol{\omega}}_r \tag{5.32}$$

$$\delta\tilde{\boldsymbol{\omega}}_{dI}^{CR} = \delta\tilde{\boldsymbol{\omega}}_I - \tilde{\mathbf{G}}\delta\tilde{\mathbf{v}} \tag{5.33}$$

$\delta\tilde{\boldsymbol{\omega}}_{dI}^{CR}$ is the vector of incremental rotational (co-rotated) deformations, which are the rotational dof's at element level, and $\delta\tilde{\boldsymbol{\omega}}_I$ contains the system-level dof's expressed in local coordinates. It is important to note that the variation of $\tilde{\boldsymbol{\omega}}_{dI}^{CR}$ is taken in the co-rotating frame, whereas $\delta\tilde{\boldsymbol{\omega}}_I$ and $\delta\tilde{\mathbf{v}}$ are vectors varied in a fixed (inertial) coordinate frame and expressed in a basis that instantaneously coincides with the co-rotating frame. Equation (5.32) verifies the expression reported by Nour-Omid and Rankin [26]. Rearranging Equation (5.33) in a manner similar to Equation (5.28) we get:

$$(\delta\tilde{\boldsymbol{\omega}})_{CR} = \begin{bmatrix} \delta\tilde{\boldsymbol{\omega}}_{d1}^{CR} \\ \vdots \\ \delta\tilde{\boldsymbol{\omega}}_{dN}^{CR} \end{bmatrix} = \left(\begin{bmatrix} \mathbf{0} & \mathbf{1} & \cdots & \mathbf{0} & \mathbf{0} \\ \vdots & \vdots & & \vdots & \vdots \\ \mathbf{0} & \mathbf{0} & \cdots & \mathbf{0} & \mathbf{1} \end{bmatrix} - \begin{bmatrix} \mathbf{1} \\ \vdots \\ \mathbf{1} \end{bmatrix} \tilde{\mathbf{G}} \right) \delta\tilde{\mathbf{v}} \tag{5.34}$$

Combining Equations (5.28) and (5.34) results in the final differential relationship between the co-rotated dof's and global, visible dof's:

$$\begin{aligned} (\delta\tilde{\mathbf{v}})_{CR} &= \begin{bmatrix} \delta\tilde{\mathbf{u}}_{d1}^{CR} \\ \delta\tilde{\boldsymbol{\omega}}_{d1}^{CR} \\ \vdots \\ \delta\tilde{\mathbf{u}}_{dN}^{CR} \\ \delta\tilde{\boldsymbol{\omega}}_{dN}^{CR} \end{bmatrix} = \left(\mathbf{1} - \frac{1}{N} \begin{bmatrix} \mathbf{1} & \mathbf{0} & \cdots & \mathbf{1} & \mathbf{0} \\ \mathbf{0} & \mathbf{0} & \cdots & \mathbf{0} & \mathbf{0} \\ \vdots & \vdots & & \vdots & \vdots \\ \mathbf{1} & \mathbf{0} & \cdots & \mathbf{1} & \mathbf{0} \\ \mathbf{0} & \mathbf{0} & \cdots & \mathbf{0} & \mathbf{0} \end{bmatrix} - \begin{bmatrix} \tilde{\mathbf{S}}_1 \\ \mathbf{1} \\ \vdots \\ \tilde{\mathbf{S}}_N \\ \mathbf{1} \end{bmatrix} \tilde{\mathbf{G}} \right) \mathbf{T}_{ne} \delta\mathbf{v} \\ &= \mathbf{P}\mathbf{T}_{ne}\mathbf{T}_{el}^{\mathsf{T}} \hat{\delta\mathbf{v}} = \mathbf{Q}\hat{\delta\mathbf{v}} \end{aligned} \tag{5.35}$$

$$\mathbf{T}_{ne} = \begin{bmatrix} \mathbf{T}_n & \mathbf{0} & \cdots & \mathbf{0} & \mathbf{0} \\ \mathbf{0} & \mathbf{T}_n & & \mathbf{0} & \mathbf{0} \\ \vdots & & \ddots & & \vdots \\ \mathbf{0} & \mathbf{0} & & \mathbf{T}_n & \mathbf{0} \\ \mathbf{0} & \mathbf{0} & \cdots & \mathbf{0} & \mathbf{T}_n \end{bmatrix}, \mathbf{T}_{el} = \begin{bmatrix} \mathbf{T}_{1t} & \mathbf{0} & \cdots & \mathbf{0} & \mathbf{0} \\ \mathbf{0} & \mathbf{T}_{1r} & & \mathbf{0} & \mathbf{0} \\ \vdots & & \ddots & & \vdots \\ \mathbf{0} & \mathbf{0} & & \mathbf{T}_{Nt} & \mathbf{0} \\ \mathbf{0} & \mathbf{0} & \cdots & \mathbf{0} & \mathbf{T}_{Nr} \end{bmatrix} \tag{5.36}$$

The matrix $\mathbf{T}_{ne} \in \mathbb{R}^{6N \times 6N}$ is a tri-diagonal matrix that collects the element transformation matrices for each node. In addition, each node is allowed to have different reference axes, where rotations and translations are treated separately in order to simplify the handling of different boundary conditions. These transformations are collected in the matrix $\mathbf{T}_{el} \in \mathbb{R}^{6N \times 6N}$. The diacritical $(\hat{\ })$ is used to indicate a property in local nodal-coordinates. As this only amounts to a transformation that is constant in time, this transformation will be omitted in the following.

Box 5.1 Co-rotational procedure

Given $\mathbf{x}_I^0$, $\mathbf{v}_I$, $\mathbf{R}_I$, **return** $\tilde{\theta}_{dI}^{CR}$ **and** $\tilde{\mathbf{u}}_{dI}^{CR}$, $I = 1 \ldots N$

- Establish $\mathbf{T}_0 = \mathbf{I}_i \otimes \mathbf{E}_i^0$ from $\mathbf{x}_I^0$
- Establish $\mathbf{T}_n = \mathbf{I}_i \otimes \mathbf{E}_i^n$ from $\mathbf{x}_I^n = \mathbf{v}_I + \mathbf{x}_I^0$ (and $\mathbf{R}_I$)
- Extract deformational rotations:

$$\tilde{\mathbf{R}}_{dI}^{CR} = \mathbf{T}_n \mathbf{R}_I \mathbf{T}_0^{\mathsf{T}}, \; \tilde{\theta}_{dI}^{CR} = \theta(\tilde{\mathbf{R}}_{dI}^{CR})$$

- Extract deformational displacements

$$\tilde{\mathbf{u}}_{dI}^{CR} = \mathbf{T}_n(\mathbf{x}_I^0 + \mathbf{v}_I - \mathbf{x}_c^n) - \tilde{\mathbf{X}}_I$$

5.2 Governing equations of EICR

Contrary to common practice in finite element formulations, the explicit form of the governing equations need not be formulated in the Element Independent Co-Rotational procedure. By definition, matters such as local equilibrium are the concern of the internal formulation of the element only. Instead, we assume that the virtual work of the structure can be captured using the discrete virtual work of the visible nodes. Hence, our principal concern is to investigate requirements and potential limitations imposed on the element by the formulation.

5.2.1 Frame invariance of strain energy

The fundament of the original development of EICR is the existence of a scalar strain-energy functional for an individual element. Due to the fundamental property of frame invariance of energy, the functional should be indifferent to rigid body motion:

$$U_e = U_e(\tilde{\varphi}_d, \; \tilde{\mathbf{R}}_d) = U_e(\varphi_d + \varphi_r, \; \mathbf{R}_d \mathbf{R}_r) \tag{5.37}$$

Where $(\tilde{\varphi}_d, \; \tilde{\mathbf{R}}_d)$ are deformational maps of displacements and rotations, and $(\varphi_r, \; \mathbf{R}_r)$ are mappings of the rigid-body displacements and rotations. The key element here is the

multiplicative decomposition of rotations. This allows us to continue with $\mathbf{R}_r$ as the state of identity, and thus either work in the tangent space of $\mathbf{R}_r$ (a function of $\mathbf{R}_d$ only), or in the tangent space of $\tilde{\mathbf{R}}_d$. As the physical forces and moments in the intermediate co-rotational basis can be established based on the first variation of Equation (5.37), we obtain:

$$\delta U_e = \delta(\tilde{\mathbf{v}})_{CR} \cdot \tilde{\mathbf{f}}_e^{CR} \tag{5.38}$$

$$\tilde{\mathbf{f}}_e^{CR} = \frac{\partial U_e}{\partial(\tilde{\mathbf{v}})_{CR}} \tag{5.39}$$

In these relations we tacitly assumed that the moments are derived as moments conjugate to an incremental rotation field, superimposed by a multiplicative update. We are thus working in the tangent space at $\tilde{\mathbf{R}}_d$. As noted in the introduction, the element can be formulated in any other way without invalidating the subsequent derivations. All we have to do is to map the forces to the correct tangent space, and include the derivative of this map in the internal tangent stiffness of the element.

The next step in the formulation is to separate the deformational nodal parameters from the rigid-body motion by the use of projectors. Projectors are idempotent matrices (usually given the symbol $\mathbf{P}$) thereby having the beneficial property of separating vectors into two disjoint subspaces $\mathbb{P}_{\|}$ and $\mathbb{P}_{\perp}$.

$$\mathbb{P}_{\|}(\mathbf{P} \in \mathbb{R}^{n\times n}) = \{\mathbf{x} \in \mathbb{R}^n | \mathbf{P}\mathbf{x} = \mathbf{x}\} \tag{5.40}$$

$$\mathbb{P}_{\perp}(\mathbf{P} \in \mathbb{R}^{n\times n}) = \{\mathbf{x} \in \mathbb{R}^n | (\mathbb{1} - \mathbf{P})\mathbf{x} = \mathbf{x}\} \tag{5.41}$$

and

$$\mathbb{P}_{\|} = \text{range}(\mathbf{P}) = \text{null}(\mathbb{1} - \mathbf{P}), \quad \mathbb{P}_{\perp} = \text{range}(\mathbb{1} - \mathbf{P}) = \text{null}(\mathbf{P}) \tag{5.42}$$

Thus we have $\mathbb{P}_{\perp} \cup \mathbb{P}_{\|} = \mathbb{R}^n$ and $\mathbb{P}_{\perp} \cap \mathbb{P}_{\|} = \varnothing$. The symbols $\perp$ and $\|$ are not to be taken literally, as for arbitrary $\mathbf{x}$, $\mathbf{P}\mathbf{x} \cdot (\mathbb{1} - \mathbf{P})\mathbf{x} = \mathbf{x} \cdot \mathbf{P}^{\mathsf{T}}(\mathbb{1} - \mathbf{P})\mathbf{x} = 0$ only in the special case of $\mathbf{P}$ being an orthogonal (symmetric) projector.

If we assume that there exist a projector $\mathbf{P}$, that separates differentials of motion into rigid-body motion and co-rotated deformational motion, we get a relation similar to Equation (5.35).

$$\delta(\tilde{\mathbf{v}})_{CR} = \mathbf{P}\delta(\tilde{\mathbf{v}})_{CR} = \mathbf{P}\delta\tilde{\mathbf{v}} \tag{5.43}$$

$$\delta\tilde{\mathbf{v}} = \mathbf{P}\delta\tilde{\mathbf{v}} + (\mathbb{1} - \mathbf{P})\delta\tilde{\mathbf{v}} = \delta(\tilde{\mathbf{v}})_{CR} + \delta(\tilde{\mathbf{v}})_{Rig} \tag{5.44}$$

By inserting this into the variation of the internal strain energy, we can rewrite the internal virtual work in terms of the variations of the visible system level dof's $\tilde{\mathbf{v}}$. As the co-rotated variations lie in tangent-spaces particular for each individual element, the variation of the visible dof's are needed to connect the dof's of neighboring elements.

$$\begin{aligned} \delta U_e &= \delta(\tilde{\mathbf{v}})_{CR} \cdot \tilde{\mathbf{f}}_e^{CR} \\ &= \mathbf{P}\delta(\tilde{\mathbf{v}})_{CR} \cdot \tilde{\mathbf{f}}_e^{CR} \\ &= \delta(\tilde{\mathbf{v}})_{CR} \cdot \mathbf{P}^{\mathsf{T}}\tilde{\mathbf{f}}_e^{CR} \\ &= \mathbf{P}\delta\tilde{\mathbf{v}} \cdot \mathbf{P}^{\mathsf{T}}\tilde{\mathbf{f}}_e^{CR} = \delta\tilde{\mathbf{v}} \cdot \mathbf{P}^{\mathsf{T}}\tilde{\mathbf{f}}_e^{CR} \end{aligned} \tag{5.45}$$

Since $\delta(\tilde{\mathbf{v}})_{CR} \cdot \tilde{\mathbf{f}}_e = \delta(\tilde{\mathbf{v}})_{CR} \cdot \mathbf{P}^{\mathsf{T}}\tilde{\mathbf{f}}_e$, we get the condition $\tilde{\mathbf{f}}_e = \mathbf{P}^{\mathsf{T}}\tilde{\mathbf{f}}_e$ for consistently evaluated forces that are conjugate to both the rigid body free, co-rotated variation and the variation of the total displacements. It can be shown that this projection brings the nodal forces (and moments) of the element into a state of external self-equilibrium. Subsequently we will denote a force vector satisfying $\tilde{\mathbf{f}}_e = \mathbf{P}^{\mathsf{T}}\tilde{\mathbf{f}}_e$ with the subscript b ($\tilde{\mathbf{f}}_b$), i.e. a *balanced* force vector.

The last step in establishing the expression of the internal virtual work is to express the vectors in a common basis for all elements, i.e. the global basis (or local nodal coordinates):

$$\begin{aligned} \delta U_e &= \delta\tilde{\mathbf{v}} \cdot \mathbf{P}^{\mathsf{T}}\tilde{\mathbf{f}}_e^{CR} \\ &= \mathbf{T}_{ne}^{\mathsf{T}}\delta\tilde{\mathbf{v}} \cdot \mathbf{T}_{ne}^{\mathsf{T}}\mathbf{P}^{\mathsf{T}}\tilde{\mathbf{f}}_e^{CR} \\ &= \delta\mathbf{v} \cdot \mathbf{T}_{ne}^{\mathsf{T}}\mathbf{P}^{\mathsf{T}}\tilde{\mathbf{f}}_e^{CR} \end{aligned} \tag{5.46}$$

$$\mathbf{f}_e = \mathbf{T}_{ne}^{\mathsf{T}}\mathbf{P}^{\mathsf{T}}\mathbf{T}_{0e}\mathbf{f}_e^{CR} = \mathbf{P}_n^{\mathsf{T}}\mathbf{R}_{re}\mathbf{f}_e^{CR} = \mathbf{R}_{re}\mathbf{P}_0^{\mathsf{T}}\mathbf{f}_e^{CR} \tag{5.47}$$

$$\mathbf{P}_0 = \mathbf{T}_{0e}^{\mathsf{T}}\mathbf{P}\mathbf{T}_{0e}, \quad \mathbf{P}_n = \mathbf{T}_{ne}^{\mathsf{T}}\mathbf{P}\mathbf{T}_{ne} \tag{5.48}$$

In the previous derivation we were relying on the existence of a stored energy function for the element. This would limit the use of the formulation to non-dissipative systems such as hyperelastic material behavior. It might be more pertinent to start the derivation by postu-

lating that the variation in the strains should vanish during rigid-body motion, an assumption that is well founded as then the strains are a function of either the left or the right stretch tensor only. By applying the projector, we then enforce this *a priori*, without any knowledge about the internal formulation of the element. Looking at the projector as a method of separating the variations gives a different perspective on the formulation: In the same sense that the Galerkin approximation is a projection from an infinite dimensional space to a finite dimensional one, EICR is a projection of the problem in finite dimensional space onto two separate finite dimensional subspaces. The imposition of vanishing virtual strains during rigid body motion results in zero virtual work of 'invisible' nodes. This point of view also brings forth an aspect worth noting about elements containing internally condensed nodes:

Internal nodes with non-zero residuals will invalidate the formulation.

Obviously, a system floating in space will only do so in a rigid manner if the system is in internal equilibrium. All is not lost, however, as all that is needed is a local equilibrium iteration on the condensed nodes. In certain situations this might be cumbersome, and the system of internal nodes may even become singular. The question that naturally arises is: What is the effect of neglecting the lack of internal equilibrium? As so often is the case in discussions about consistently or inconsistently derived tangent operators, the effect is not detrimental, and may even aid convergence in some instances. What is also noteworthy, is that the tangent stiffness becomes consistent (or at least not less consistent) on the equilibrium path.

Finally, the relationship of (5.46) with the co-rotational formulation of Bergan et al. [18] should be noted. In their formulation, the forces are not projected onto the subspace of balanced forces, leading to the following expression for the virtual work:

$$\delta U_e = \delta \mathbf{v} \cdot \mathbf{T}_{ne}^{\mathsf{T}} \tilde{\mathbf{f}}_e \tag{5.49}$$

This is equivalent to using the pull-back/push-forward operator $\mathbf{T}_{ne}^{\mathsf{T}} \mathbf{T}_{0e}$. In the formulation by Bergan et al., the tangent operator is obtained as the derivative with respect to the co-rotational dof's in a manner similar to the EICR. As the forces are not projected onto the space of balanced forces, the formulation results in an unsymmetrical stiffness-matrix

for elements that are not in self-equilibrium. In contrast, EICR yields symmetry on the equilibrium-path[1].

5.2.2 Assessing the projector

As will be shown later, the crucial component that makes EICR a method of improving the invariant properties of *any element*, is the action of the projection. It is then essential that the matrix $\mathbf{P}$ is indeed a projector. Combining and reorganizing Equations (5.25) and (5.34), give:

$$(\delta\tilde{\mathbf{v}})_{CR} = \begin{bmatrix} \delta\tilde{\mathbf{u}}_{d1} \\ \delta\tilde{\boldsymbol{\omega}}^{CR}_{d1} \\ \vdots \\ \delta\tilde{\mathbf{u}}_{dN} \\ \delta\tilde{\boldsymbol{\omega}}^{CR}_{dN} \end{bmatrix} = \left(\mathbf{1} - \frac{1}{N} \begin{bmatrix} 1 & 0 & \cdots & 1 & 0 \\ 0 & 0 & \cdots & 0 & 0 \\ \vdots & \vdots & \ddots & \vdots & \vdots \\ 1 & 0 & \cdots & 1 & 0 \\ 0 & 0 & \cdots & 0 & 0 \end{bmatrix} - \begin{bmatrix} \tilde{\mathbf{S}}_1 \\ \mathbf{1} \\ \vdots \\ \tilde{\mathbf{S}}_N \\ \mathbf{1} \end{bmatrix} \tilde{\mathbf{G}} \right) \delta\tilde{\mathbf{v}} = (\mathbf{1} - \mathbf{P}_T - \mathbf{P}_R)\delta\tilde{\mathbf{v}}, \quad (5.50)$$

where

$$\mathbf{P}_T = \frac{1}{N} \begin{bmatrix} 1 & 0 & \cdots & 1 & 0 \\ 0 & 0 & \cdots & 0 & 0 \\ \vdots & \vdots & \ddots & \vdots & \vdots \\ 1 & 0 & \cdots & 1 & 0 \\ 0 & 0 & \cdots & 0 & 0 \end{bmatrix} \quad (5.51)$$

and

$$\mathbf{P}_R = \begin{bmatrix} \tilde{\mathbf{S}}_1 \\ \mathbf{1} \\ \vdots \\ \tilde{\mathbf{S}}_N \\ \mathbf{1} \end{bmatrix} \tilde{\mathbf{G}} = \tilde{\mathbf{S}}\tilde{\mathbf{G}}, \quad \tilde{\mathbf{S}} = \begin{bmatrix} \tilde{\mathbf{S}}_1 \\ \mathbf{1} \\ \vdots \\ \tilde{\mathbf{S}}_N \\ \mathbf{1} \end{bmatrix} \quad (5.52)$$

1. Since symmetry is also determined by loading and boundary-conditions, this claim is not always valid.

It is easily verified that $\mathbf{P}_T$ is an orthogonal projector for any element. If the bi-orthonormality relation

$$\tilde{\mathbf{G}}\tilde{\mathbf{S}} = \tilde{\mathbf{S}}^{\mathsf{T}}\tilde{\mathbf{G}}^{\mathsf{T}} = \mathbb{1} \tag{5.53}$$

is satisfied, $\mathbf{P}_R$ is also guaranteed to be a (oblique) projector.

At the outset we wanted to find a relation such that

$$(\delta\mathbf{v})_{CR} = (\mathbb{1} - \mathbf{P}_T - \mathbf{P}_R)\delta\mathbf{v} = \mathbf{P}\delta\mathbf{v} \tag{5.54}$$

Where $\mathbf{P} = (\mathbb{1} - \mathbf{P}_T - \mathbf{P}_R)$ is a projector. This leads to the following sufficient and necessary condition:

$$\mathbf{P}_R\mathbf{P}_T + \mathbf{P}_T\mathbf{P}_R = \tilde{\mathbf{S}}\tilde{\mathbf{G}}\mathbf{P}_T + \mathbf{P}_T\tilde{\mathbf{S}}\tilde{\mathbf{G}} = \mathbb{O} \tag{5.55}$$

By observing that $\mathbf{P}_T\tilde{\mathbf{S}} = \mathbb{O}$ for all elements with a local coordinate system positioned at the element's nodal centroid, condition (5.55) reduces to:

$$\tilde{\mathbf{S}}\tilde{\mathbf{G}}\mathbf{P}_T = \mathbb{O} \tag{5.56}$$

As shown by Haugen [16] this is automatically satisfied as the stronger requirement

$$\tilde{\mathbf{G}}\mathbf{P}_T = \mathbb{O} \tag{5.57}$$

necessarily holds for a correctly developed $\tilde{\mathbf{G}}$-matrix. The significance of (5.57) can be realized by noting that any vector pre-multiplied by $\mathbf{P}_T$ contains rigid body translation only, thus $\tilde{\mathbf{G}}\mathbf{P}_T \neq \mathbb{O}$ if and only if this translation also leads to a rigid-body rotation.

5.3 Derivation of the tangent stiffness

The consistent element tangent stiffness is found as the variation of the balanced internal forces of the element.

$$\begin{aligned} \mathbf{k}\delta\mathbf{v} = \delta\mathbf{f}_b &= \delta\mathbf{T}_{ne}^{\mathsf{T}}\,\mathbf{P}^{\mathsf{T}}\tilde{\mathbf{f}}_e + \mathbf{T}_{ne}^{\mathsf{T}}\delta\mathbf{P}^{\mathsf{T}}\tilde{\mathbf{f}}_e + \mathbf{T}_{ne}^{\mathsf{T}}\mathbf{P}^{\mathsf{T}}\delta\tilde{\mathbf{f}}_e \\ &= \mathbf{k}_{GR}\delta\mathbf{v} + \mathbf{k}_{GP}\delta\mathbf{v} + \mathbf{k}_m\delta\mathbf{v} \end{aligned} \tag{5.58}$$

5.3.1 Variation of the internal force vector ($\mathbf{k}_m$)

Frequently, the internal force-displacement relation of the element is assumed to be linear within EICR. Generally, this assumption is unwarranted, but often useful as it allows us to re-use existing elements within the framework. The critical issue is not whether the element formulation is linear or not, but rather to what tangent-space the incremental rotations are referred to. Linear elements generally use additive rotations, as if we are operating in the tangent-space of the identity. The following derivations are then the same as if we are using an element that is formulated accordingly, examples of which are the beam elements developed by Cardona and Géradin [8]. If we denote $\tilde{\mathbf{k}}_e$ as the (consistently derived) stiffness matrix of the element, we have in most cases one of the following two situations:

Elements formulated at $T_{\mathbf{R}_{d1}^{CR}}\mathbf{R}$:

$$\mathbf{k}_m\delta\mathbf{v} = \mathbf{T}_{n\mathrm{e}}^{\mathsf{T}}\mathbf{P}^{\mathsf{T}}\delta\tilde{\mathbf{f}}_e = \mathbf{T}_{n\mathrm{e}}^{\mathsf{T}}\mathbf{P}^{\mathsf{T}}\tilde{\mathbf{k}}_e\mathbf{P}\mathbf{T}_{n\mathrm{e}}\delta\mathbf{v} \tag{5.59}$$

Elements formulated at $T_1\mathbf{R}$:

The moments are now no longer conjugate to the instantaneous rotations, and a transformation of the form $\delta\boldsymbol{\theta}_I = \mathbf{H}(\boldsymbol{\theta}_I)\delta\tilde{\boldsymbol{\omega}}_{d1}^{CR} = \mathbf{H}_I\delta\tilde{\boldsymbol{\omega}}_{d1}^{CR}$ is required in order to transform the internal virtual work. If the internal force vector of these elements is denoted $\tilde{\mathbf{f}}_e^a$, we get through the equivalence of virtual work, the expression:

$$\tilde{\mathbf{f}}_e = \mathbf{H}^{\mathsf{T}}\tilde{\mathbf{f}}_e^a, \text{ where } \mathbf{H} = \begin{bmatrix} \mathbf{1} & \mathbf{0} & \cdots & \mathbf{0} & \mathbf{0} \\ \mathbf{0} & \mathbf{H}_1 & \cdots & \mathbf{0} & \mathbf{0} \\ \vdots & \vdots & \ddots & \vdots & \vdots \\ \mathbf{0} & \mathbf{0} & \cdots & \mathbf{1} & \mathbf{0} \\ \mathbf{0} & \mathbf{0} & \cdots & \mathbf{0} & \mathbf{H}_N \end{bmatrix} \tag{5.60}$$

It is important that the transformation (5.60) is performed before using the internal force-vector in the stiffness terms in the following sections. Using Equation (5.60) in the variation of the forces, we get:

$$\begin{aligned}\mathbf{k}_m\delta\mathbf{v} &= \mathbf{T}_{ne}^{\mathsf{T}}\mathbf{P}^{\mathsf{T}}\delta\tilde{\mathbf{f}}_e = \mathbf{T}_{ne}^{\mathsf{T}}\mathbf{P}^{\mathsf{T}}\delta\mathbf{H}^{\mathsf{T}}\tilde{\mathbf{f}}_e^a + \mathbf{T}_{ne}^{\mathsf{T}}\mathbf{P}^{\mathsf{T}}\mathbf{H}^{\mathsf{T}}\delta\tilde{\mathbf{f}}_e^a \\ &= \mathbf{k}_{GM}\delta\mathbf{v} + \mathbf{T}_{ne}^{\mathsf{T}}\mathbf{P}^{\mathsf{T}}\mathbf{H}^{\mathsf{T}}\tilde{\mathbf{k}}_e^a\mathbf{H}\mathbf{P}\mathbf{T}_{ne}\delta\mathbf{v}\end{aligned} \tag{5.61}$$

$$\mathbf{k}_{GM} = \mathbf{T}_{ne}^{\mathsf{T}}\mathbf{P}^{\mathsf{T}}\tilde{\mathbf{M}}\mathbf{P}\mathbf{T}_{ne} \tag{5.62}$$

$$\tilde{\mathbf{M}} = \begin{bmatrix} \mathbb{1} & \mathbf{0} & \cdots & \mathbf{0} & \mathbf{0} \\ \mathbf{0} & \tilde{\mathbf{M}}_1 & \cdots & \mathbf{0} & \mathbf{0} \\ \vdots & \vdots & \ddots & \vdots & \vdots \\ \mathbf{0} & \mathbf{0} & \cdots & \mathbb{1} & \mathbf{0} \\ \mathbf{0} & \mathbf{0} & \cdots & \mathbf{0} & \tilde{\mathbf{M}}_N \end{bmatrix} \tag{5.63}$$

According to Nour-Omid and Rankin [26], the matrix $\tilde{\mathbf{M}}_I$ is given as:

$$\tilde{\mathbf{M}}_I = \left(-\frac{1}{2}\tilde{\widehat{\mathbf{m}}}_I + \eta((\tilde{\mathbf{m}}_I \cdot \tilde{\boldsymbol{\theta}}_I)\mathbb{1} + \tilde{\boldsymbol{\theta}}_I \otimes \tilde{\mathbf{m}}_I - 2(\tilde{\mathbf{m}}_I \otimes \tilde{\boldsymbol{\theta}}_I)) + \nu\left(\tilde{\widehat{\boldsymbol{\theta}}}_I\right)^2(\tilde{\mathbf{m}}_I \otimes \tilde{\boldsymbol{\theta}}_I)\right)\mathbf{H}_I \tag{5.64}$$

$$\nu = \frac{\theta_I(\theta_I + \sin(\theta_I)) - 8\sin^2(\frac{1}{2}\theta_I)}{4\theta_I^4\sin^2(\frac{1}{2}\theta_I)} \tag{5.65}$$

$$\eta = \frac{\sin(\frac{1}{2}\theta_I) - \frac{1}{2}\theta_I\cos(\frac{1}{2}\theta_I)}{\theta_I^2\sin^2(\frac{1}{2}\theta_I)} \tag{5.66}$$

$$\theta_I = \|\tilde{\boldsymbol{\theta}}_I\| \tag{5.67}$$

As noted by several authors, the expressions for η and ν are ill conditioned for small angles, and a truncated power series should be used for $\theta_I < 0{,}05$ radians.

$$\nu \approx \frac{1}{360} + \frac{1}{7560}\theta_I^2 + \frac{1}{201600}\theta_I^4 \tag{5.68}$$

$$\eta \approx \frac{1}{12} + \frac{1}{720}\theta_I^2 + \frac{1}{30240}\theta_I^4 \tag{5.69}$$

5.3.2 Variation of the base-vector matrix ($\mathbf{k}_{GR}$)

In the co-rotational procedure, the geometric contribution to the stiffness matrix obtained from the variation of the transformation-matrix $\mathbf{T}_{ne}$ is the most significant. It represents the change in moments and forces during an infinitesimal rigid body motion.

$$\delta\mathbf{T}_{ne} = \begin{bmatrix} \delta\mathbf{T}_n & \mathbf{0} & \cdots & \mathbf{0} & \mathbf{0} \\ \mathbf{0} & \delta\mathbf{T}_n & & \mathbf{0} & \mathbf{0} \\ \vdots & & \ddots & & \vdots \\ \mathbf{0} & \mathbf{0} & & \delta\mathbf{T}_n & \mathbf{0} \\ \mathbf{0} & \mathbf{0} & \cdots & \mathbf{0} & \delta\mathbf{T}_n \end{bmatrix} \tag{5.70}$$

From Equation (5.22) we have:

$$\delta\mathbf{T}_{ne} = -\mathrm{Spin}(\delta\tilde{\boldsymbol{\omega}}_{re})\mathbf{T}_{ne} \tag{5.71}$$

$$\begin{aligned} \mathbf{k}_{GR}\delta\mathbf{v} &= \delta\mathbf{T}_{ne}^{\mathsf{T}}\mathbf{P}^{\mathsf{T}}\tilde{\mathbf{f}}_{\mathbf{e}} = \delta\mathbf{T}_{ne}^{\mathsf{T}}\tilde{\mathbf{f}}_{\mathbf{b}} \\ &= \mathbf{T}_{ne}^{\mathsf{T}}\mathrm{Diag}\left[\mathrm{Spin}(\delta\tilde{\boldsymbol{\omega}}_{re}) \cdots \mathrm{Spin}(\delta\tilde{\boldsymbol{\omega}}_{re})\right]\tilde{\mathbf{f}}_{\mathbf{b}} \\ &= -\mathbf{T}_{ne}^{\mathsf{T}}\tilde{\mathbf{F}}_{nm}\delta\tilde{\boldsymbol{\omega}}_{re} = -\mathbf{T}_{ne}^{\mathsf{T}}\tilde{\mathbf{F}}_{nm}\tilde{\mathbf{G}}\delta\tilde{\mathbf{v}} \\ &= -\mathbf{T}_{ne}^{\mathsf{T}}\tilde{\mathbf{F}}_{nm}\tilde{\mathbf{G}}\mathbf{T}_{ne}\delta\mathbf{v} \end{aligned} \tag{5.72}$$

where

$$\tilde{\mathbf{F}}_{nm} = \begin{bmatrix} \mathrm{Spin}(\tilde{\mathbf{n}}_1) \\ \mathrm{Spin}(\tilde{\mathbf{m}}_1) \\ \vdots \\ \mathrm{Spin}(\tilde{\mathbf{n}}_N) \\ \mathrm{Spin}(\tilde{\mathbf{m}}_N) \end{bmatrix}, \qquad \tilde{\mathbf{f}}_b = \begin{bmatrix} \tilde{\mathbf{n}}_1 \\ \tilde{\mathbf{m}}_1 \\ \vdots \\ \tilde{\mathbf{n}}_N \\ \tilde{\mathbf{m}}_N \end{bmatrix} = \mathbf{P}^{\mathsf{T}}\tilde{\mathbf{f}}_e \tag{5.73}$$

5.3.3 Variation of the projector ($\mathbf{k}_{GP}$)

First we start by establishing some fundamental relations. The fact that $\mathbf{P}$ is a projector reveals some useful and important properties. Using the fact that $\mathbf{P} = \mathbf{P}^2$ we get

$$\delta\mathbf{P} = \delta\mathbf{P}\mathbf{P} + \mathbf{P}\delta\mathbf{P} \tag{5.74}$$

Also, by premultiplying (5.74) with $\mathbf{P}$ and rearranging we get

$$\mathbf{P}\delta\mathbf{P}\mathbf{P} = \mathbb{O} \tag{5.75}$$

These relations will prove essential in the proof that the variation of the projector can be split into two parts, where $\mathbf{P}\delta\mathbf{P}$ is independent of the variation of $\tilde{\mathbf{G}}$ and with $range(\mathbf{P}\delta\mathbf{P}) \subseteq range(\mathbf{P})$, and $\delta\mathbf{P}\mathbf{P}$ depends solely on the variation of $\tilde{\mathbf{G}}$ with $range(\delta\mathbf{P}\mathbf{P}) \subseteq null(\mathbf{P})$. In Equation (5.50), the only configuration dependent matrix is $\mathbf{P}_R$, so the variation of $\mathbf{P}$ then evaluates to:

$$\delta\mathbf{P} = \delta\mathbf{P}_R = -\tilde{\mathbf{S}}\delta\tilde{\mathbf{G}} - \delta\tilde{\mathbf{S}}\tilde{\mathbf{G}} \tag{5.76}$$

$$\begin{aligned}
\mathbf{P}\delta\mathbf{P} &= (\mathbf{1} - \mathbf{P}_T - \tilde{\mathbf{S}}\tilde{\mathbf{G}})(-\tilde{\mathbf{S}}\delta\tilde{\mathbf{G}} - \delta\tilde{\mathbf{S}}\tilde{\mathbf{G}}) \\
&= \tilde{\mathbf{S}}\tilde{\mathbf{G}}\tilde{\mathbf{S}}\delta\tilde{\mathbf{G}} + \mathbf{P}_T\tilde{\mathbf{S}}\delta\tilde{\mathbf{G}} - \tilde{\mathbf{S}}\delta\tilde{\mathbf{G}} - \mathbf{P}\delta\tilde{\mathbf{S}}\tilde{\mathbf{G}} \\
&= \tilde{\mathbf{S}}\delta\tilde{\mathbf{G}} - \tilde{\mathbf{S}}\delta\tilde{\mathbf{G}} - \mathbf{P}\delta\tilde{\mathbf{S}}\tilde{\mathbf{G}} \\
&= -\mathbf{P}\delta\tilde{\mathbf{S}}\tilde{\mathbf{G}}
\end{aligned} \tag{5.77}$$

This proves that the first term on the right-hand side of (5.74) is independent of $\delta\tilde{\mathbf{G}}$.

$$\begin{aligned}
\delta\mathbf{P}\mathbf{P} &= (-\tilde{\mathbf{S}}\delta\tilde{\mathbf{G}} - \delta\tilde{\mathbf{S}}\tilde{\mathbf{G}})(\mathbf{1} - \mathbf{P}_T - \tilde{\mathbf{S}}\tilde{\mathbf{G}}) \\
&= -\tilde{\mathbf{S}}\delta\tilde{\mathbf{G}}\mathbf{P} - \delta\tilde{\mathbf{S}}\tilde{\mathbf{G}} + \delta\tilde{\mathbf{S}}\tilde{\mathbf{G}}\mathbf{P}_T + \delta\tilde{\mathbf{S}}\tilde{\mathbf{G}}\tilde{\mathbf{S}}\tilde{\mathbf{G}} \\
&= -\tilde{\mathbf{S}}\delta\tilde{\mathbf{G}}\mathbf{P} - \delta\tilde{\mathbf{S}}\tilde{\mathbf{G}} + \delta\tilde{\mathbf{S}}\tilde{\mathbf{G}} \\
&= -\tilde{\mathbf{S}}\delta\tilde{\mathbf{G}}\mathbf{P} = -\mathbf{P}_R\tilde{\mathbf{S}}\delta\tilde{\mathbf{G}}\mathbf{P}
\end{aligned} \tag{5.78}$$

However, since $\mathbf{P}\delta\mathbf{P}\mathbf{P} = \mathbf{0}$, then $\delta\mathbf{P}\mathbf{P} = (\mathbf{1} - \mathbf{P})\delta\mathbf{P}\mathbf{P}$, which completes the proof. Furthermore, if $\tilde{\mathbf{G}}$ can be split into a 3x3 matrix $\mathbf{A}$ with full rank and a 3x(6*N*) constant matrix $\mathbf{B}$, then (5.78) evaluates to zero. This is easily shown by observing that

$$\mathbf{A}\mathbf{A}^{-1} = \mathbb{1} \Rightarrow \delta\mathbf{A}\mathbf{A}^{-1} + \mathbf{A}\delta\mathbf{A}^{-1} = \mathbb{0} \tag{5.79}$$

Thus the variation of any nonsingular matrix can be written as

$$\delta\mathbf{A} = -\mathbf{A}\delta\mathbf{A}^{-1}\mathbf{A} \tag{5.80}$$

By applying this to the matrix $\tilde{\mathbf{G}}$, we get

$$\delta\tilde{\mathbf{G}} = \delta(\mathbf{AB}) = (-\mathbf{A}\delta\mathbf{A}^{-1}\mathbf{A})\mathbf{B} = -\mathbf{A}\delta\mathbf{A}^{-1}\tilde{\mathbf{G}}\,, \tag{5.81}$$

Since $\tilde{\mathbf{G}}\mathbf{P} = \tilde{\mathbf{G}} - \tilde{\mathbf{G}}\mathbf{P}_T - \tilde{\mathbf{G}}\tilde{\mathbf{S}}\tilde{\mathbf{G}} = \tilde{\mathbf{G}} - \tilde{\mathbf{G}} = \mathbf{0}$, then

$$\delta\mathbf{P}\mathbf{P} \equiv \mathbf{0} \tag{5.82}$$

This relaxes the condition reported in [16] and [13], as the forces does not factor into the condition in order to satisfy relation (5.82). If one cannot factorize $\tilde{\mathbf{G}}$ in such a way, then $\tilde{\mathbf{f}}_e^{\mathsf{T}}\delta\mathbf{P}\mathbf{P}$ evaluates to zero if $\tilde{\mathbf{f}}_e = (\mathbf{1} - \mathbf{P}_R^{\mathsf{T}})\tilde{\mathbf{f}}_e$, i.e. if the element forces are in rotational equilibrium.

In order to find the geometric contribution to the tangent stiffness, we need to find the variation of the transpose of the projector contracted with the unprojected element forces. Using (5.74), (5.77) and (5.78) we obtain:

$$\begin{aligned}
\tilde{\mathbf{k}}_{GP}\delta\tilde{\mathbf{v}} = \delta\mathbf{P}^{\mathsf{T}}\tilde{\mathbf{f}}_e &= \mathbf{P}^{\mathsf{T}}\delta\mathbf{P}^{\mathsf{T}}\tilde{\mathbf{f}}_e + \delta\mathbf{P}^{\mathsf{T}}\mathbf{P}^{\mathsf{T}}\tilde{\mathbf{f}}_e \\
&= -\mathbf{P}^{\mathsf{T}}\delta\tilde{\mathbf{G}}^{\mathsf{T}}\tilde{\mathbf{S}}^{\mathsf{T}}\mathbf{P}_R^{\mathsf{T}}(\mathbf{1} - \mathbf{P}^{\mathsf{T}})\tilde{\mathbf{f}}_e - \tilde{\mathbf{G}}^{\mathsf{T}}\delta\tilde{\mathbf{S}}^{\mathsf{T}}\mathbf{P}^{\mathsf{T}}\tilde{\mathbf{f}}_e \\
&= -\mathbf{P}^{\mathsf{T}}\delta\tilde{\mathbf{G}}^{\mathsf{T}}\tilde{\mathbf{S}}^{\mathsf{T}}\mathbf{P}_R^{\mathsf{T}}\tilde{\mathbf{f}}_u - \tilde{\mathbf{G}}^{\mathsf{T}}\delta\tilde{\mathbf{S}}^{\mathsf{T}}\tilde{\mathbf{f}}_b \\
&= \tilde{\mathbf{k}}_{GPG}\delta\tilde{\mathbf{v}} + \tilde{\mathbf{k}}_{GPS}\delta\tilde{\mathbf{v}}
\end{aligned} \tag{5.83}$$

Here $\tilde{\mathbf{f}}_b = \mathbf{P}^{\mathsf{T}}\tilde{\mathbf{f}}_e$ is the balanced (projected) forces and $\tilde{\mathbf{f}}_u = (\mathbf{1} - \mathbf{P}^{\mathsf{T}})\tilde{\mathbf{f}}_e$ is the unbalanced forces (null-space of $\mathbf{P}^{\mathsf{T}}$). The term $\tilde{\mathbf{k}}_{GPG}\delta\tilde{\mathbf{v}} = -\mathbf{P}^{T}\delta\tilde{\mathbf{G}}^{\mathsf{T}}\tilde{\mathbf{S}}^{\mathsf{T}}\mathbf{P}_R^{\mathsf{T}}\tilde{\mathbf{f}}_u$ will be neglected in the following, because it will either be exactly zero, or it will vanish, based on the assumption that the (rotationally) unbalanced forces are small. This assumption is justified if the element in question is capable of describing the current state of deformation. If, however, the unbalanced forces are large, thereby making the contribution from $\mathbf{k}_{GPG}$ significant, the internal description of the element itself will be questionable. For linear elements, where the deformations are measured in a co-rotating "best fit" frame, the unbalanced forces will be significant only when the deformations are large.

The term $\tilde{\mathbf{k}}_{GPS}\delta\tilde{\mathbf{v}} = -\tilde{\mathbf{G}}^{\mathsf{T}}\delta\tilde{\mathbf{S}}^{\mathsf{T}}\tilde{\mathbf{f}}_b$ is the usual term denoted $\tilde{\mathbf{k}}_{GP}$ in [10, 13, 16, 26]. Performing the variation and contraction of forces, we obtain the explicit expression:

$$\begin{aligned}
\tilde{\mathbf{k}}_{GPS}\delta\tilde{\mathbf{v}} &= -\tilde{\mathbf{G}}^{\mathsf{T}}\delta\tilde{\mathbf{S}}^{\mathsf{T}}\mathbf{f}_b = -\tilde{\mathbf{G}}^{\mathsf{T}}\sum_I \begin{bmatrix}\delta\tilde{\mathbf{S}}_I^{\mathsf{T}} & \mathbf{0}\end{bmatrix}\mathbf{f}_{bI} \\
&= -\tilde{\mathbf{G}}^{\mathsf{T}}\sum_I \begin{bmatrix}\mathrm{Spin}(\delta\tilde{\mathbf{u}}_{dI}^{CR}) & \mathbf{0}\end{bmatrix}\begin{bmatrix}\tilde{\mathbf{n}}_I^{\mathsf{T}} & \tilde{\mathbf{m}}_I^{\mathsf{T}}\end{bmatrix}^{\mathsf{T}} \\
&= -\tilde{\mathbf{G}}^{\mathsf{T}}\sum_I \begin{bmatrix}-\mathrm{Spin}(\tilde{\mathbf{n}}_I) & \mathbf{0}\end{bmatrix}\begin{bmatrix}(\delta\tilde{\mathbf{u}}_{dI}^{CR})^{\mathsf{T}} & (\delta\tilde{\boldsymbol{\omega}}_{d1}^{CR})^{\mathsf{T}}\end{bmatrix}^{\mathsf{T}} \\
&= -\tilde{\mathbf{G}}^{\mathsf{T}}\begin{bmatrix}\mathrm{Spin}(\tilde{\mathbf{n}}_1)^{\mathsf{T}} & \mathbf{0} & \cdots & \mathrm{Spin}(\tilde{\mathbf{n}}_N)^{\mathsf{T}} & \mathbf{0}\end{bmatrix}(\delta\mathbf{v})_{CR} \\
&= -\tilde{\mathbf{G}}^{\mathsf{T}}\tilde{\mathbf{F}}_n^{\mathsf{T}}(\delta\mathbf{v})_{CR} = -\tilde{\mathbf{G}}^{\mathsf{T}}\tilde{\mathbf{F}}_n^{\mathsf{T}}\mathbf{P}\delta\tilde{\mathbf{v}}
\end{aligned} \tag{5.84}$$

$$\tilde{\mathbf{F}}_n = \begin{bmatrix}\mathrm{Spin}(\tilde{\mathbf{n}}_1) \\ \mathbf{0} \\ \vdots \\ \mathrm{Spin}(\tilde{\mathbf{n}}_N) \\ \mathbf{0}\end{bmatrix} \tag{5.85}$$

Again, by observing that $\mathbf{P}\delta\mathbf{P} = \mathbf{P}\delta\mathbf{P}(\mathbf{1}-\mathbf{P})$, and thus $\tilde{\mathbf{k}}_{GPS} = (\mathbf{1}-\mathbf{P}^{\mathsf{T}})\tilde{\mathbf{k}}_{GPS}$, we see the interesting fact that an infinitesimal deformational motion produces unbalanced forces from balanced forces through $\mathbf{k}_{GPS}$, whereas $\mathbf{k}_{GPG}$ produces balanced forces from unbalanced forces.

Box 5.2 EICR-framework

Given : $\tilde{\mathbf{f}}_e$, $\tilde{\mathbf{k}}_e$, $\mathbf{T}_{ne}$, $\tilde{\theta}_{dI}^{CR}$, $\tilde{\mathbf{u}}_{dI}^{CR}$ **and** $\tilde{\mathbf{G}}$, **determine** $\mathbf{f}$ **and** $\mathbf{k}$

- If the element is based on additive rotations, transform and add moment correction stiffness:

$$\tilde{\mathbf{f}}_e = \mathbf{H}^{\mathsf{T}}\tilde{\mathbf{f}}_e$$

$$\tilde{\mathbf{k}}_e = \mathbf{H}^{\mathsf{T}}\tilde{\mathbf{k}}_e\mathbf{H} + \tilde{\mathbf{M}}$$

- Construct projector:

$$\tilde{\mathbf{S}}_I = \mathrm{Spin}(\tilde{\mathbf{X}}_I + \tilde{\mathbf{u}}_{dI}^{CR})$$

$$\mathbf{P} = \mathbb{1} - \mathbf{P}_T - \tilde{\mathbf{S}}\tilde{\mathbf{G}}$$

- Project forces and stiffness:

$$\tilde{\mathbf{f}} = \mathbf{P}^{\mathsf{T}}\tilde{\mathbf{f}}_e$$

$$\tilde{\mathbf{k}} = \mathbf{P}^{\mathsf{T}}\tilde{\mathbf{k}}_e\mathbf{P}$$

- Add rigid rotation contribution:

$$\tilde{\mathbf{k}} = \tilde{\mathbf{k}} - \tilde{\mathbf{F}}_{nm}\tilde{\mathbf{G}}$$

- Add contribution from projector:

$$\tilde{\mathbf{k}} = \tilde{\mathbf{k}} - \tilde{\mathbf{G}}^{\mathsf{T}}\tilde{\mathbf{F}}_n^{\mathsf{T}}\mathbf{P}$$

- Transform to global coordinates:

$$\mathbf{k} = \mathbf{T}_{ne}^{\mathsf{T}}\tilde{\mathbf{k}}\mathbf{T}_{ne}$$

$$\mathbf{f} = \mathbf{T}_{ne}^{\mathsf{T}}\tilde{\mathbf{f}}$$

5.4 Element independence and the projector

The key to element independence actually lie in Equations (5.74) and (5.75). Without this property, the procedure described earlier reduces to a general procedure for generating non-linear terms associated with rigid body motion.

If the element produces forces that are conjugate to the co-rotated dof's, then the procedure requires no justification. If, on the other hand, relation (5.54) is not given as a projection, the element forces must be conjugate to the co-rotated dof's, and the consistent element stiffness matrix must be derived as the derivative with respect to the co-rotated dof's. This can be illustrated as follows:

$$(\delta\tilde{\mathbf{v}})_{CR} = \mathbf{Q}\delta\mathbf{v} \tag{5.86}$$

$$\frac{\partial(\tilde{\mathbf{v}})_{CR}}{\partial\mathbf{v}} = \mathbf{Q} \quad (= \mathbf{P}\mathbf{T}_{ne}) \tag{5.87}$$

Where $\mathbf{Q}$ is not necessarily given as a combination of a projector and an orthogonal matrix. The principle of virtual work now dictates that

$$\delta U = (\delta\tilde{\mathbf{v}})_{CR} \cdot \frac{\partial U_i}{\partial\tilde{\mathbf{v}}_{CR}} = (\delta\tilde{\mathbf{v}})_{CR} \cdot \tilde{\mathbf{f}}_e \tag{5.88}$$

where δU is the variation of the strain energy (internal virtual work). This simply states that the forces are correctly evaluated and free of spurious self-straining due to rigid body motion. By inserting (5.86) into (5.88) and performing a truncated Taylor-series expansion we get:

$$\begin{aligned}
\delta U|_{C_n^i} &= \mathbf{Q}\delta\mathbf{v} \cdot \tilde{\mathbf{f}}_e\,|_{C_n^i} = \delta\mathbf{v} \cdot \mathbf{Q}^T\tilde{\mathbf{f}}_e|_{C_n^i} \\
&\cong \delta\mathbf{v} \cdot \mathbf{Q}^T\tilde{\mathbf{f}}_e\,|_{C_n^{i-1}} + \delta\mathbf{v} \cdot \left(\frac{\partial\mathbf{Q}^T}{\partial\mathbf{v}}\tilde{\mathbf{f}}_e + \mathbf{Q}^T\frac{\partial\tilde{\mathbf{f}}_e}{\partial\tilde{\mathbf{v}}_{CR}}\frac{\partial\tilde{\mathbf{v}}_{CR}}{\partial\mathbf{v}}\right)\Bigg|_{C_n^{i-1}}\Delta\mathbf{v} \\
&= \delta U|_{C_n^{i-1}} + \delta\mathbf{v} \cdot \left(\frac{\partial\mathbf{Q}^T}{\partial\mathbf{v}}\tilde{\mathbf{f}}_e + \mathbf{Q}^T\tilde{\mathbf{k}}_m\mathbf{Q}\right)\Bigg|_{C_n^{i-1}}\Delta\mathbf{v} \\
&= \delta U|_{C_n^{i-1}} + \delta\mathbf{v} \cdot (\mathbf{k}_{GH} + \mathbf{Q}^T\tilde{\mathbf{k}}_m\mathbf{Q})\,|_{C_n^{i-1}}\Delta\mathbf{v}
\end{aligned} \tag{5.89}$$

where

$$\mathbf{k}_{GH} = \frac{\partial \mathbf{Q}^{\mathsf{T}}}{\partial \mathbf{v}} \tilde{\mathbf{f}}_e \quad (= \mathbf{k}_{GR} + \mathbf{k}_{GP}) \tag{5.90}$$

In Equation (5.89), $\mathbb{C}_n^i$ is the configuration at state n and iteration i and $\mathbb{C}_n^0 = \mathbb{C}_{n-1}$, i.e. the initial configuration at state n is the configuration at the previously converged solution. The term $\tilde{\mathbf{k}}_m$ includes both material terms and internal geometric effects. This equation relies crucially on consistently evaluated internal forces and internal stiffness, and albeit correct, the procedure is not completely element independent. Now, provided we have $\mathbf{Q} = \tilde{\mathbf{P}}\mathbf{T}_{ne}$, we can investigate the effect of (5.89) on a generic element. We can write the stiffness matrix of any element as:

$$\tilde{\mathbf{k}}_e = \mathbf{P}^{\mathsf{T}}\tilde{\mathbf{k}}_m\mathbf{P} + \tilde{\mathbf{k}}_{GR} + \tilde{\mathbf{k}}_{GP} + \tilde{\mathbf{k}}_{inc}, \tag{5.91}$$

where $\tilde{\mathbf{k}}_{inc}$ is the part not complying with a consistently derived tangent stiffness. Substituting $\tilde{\mathbf{k}}_e$ for $\tilde{\mathbf{k}}_m$ in (5.89) we obtain:

$$\begin{aligned}\mathbf{Q}^{\mathsf{T}}\tilde{\mathbf{k}}_e\mathbf{Q} &= \mathbf{T}_{ne}^{\mathsf{T}}\mathbf{P}^{\mathsf{T}}(\mathbf{P}^{\mathsf{T}}\tilde{\mathbf{k}}_m\mathbf{P} + \tilde{\mathbf{k}}_{GR} + \tilde{\mathbf{k}}_{GP} + \tilde{\mathbf{k}}_{inc})\mathbf{P}\mathbf{T}_{ne} \\ &= \mathbf{Q}^{\mathsf{T}}\tilde{\mathbf{k}}_m\mathbf{Q} - \mathbf{T}_{ne}^{\mathsf{T}}\mathbf{P}^{\mathsf{T}}\tilde{\mathbf{F}}_{nm}\mathbf{G}\mathbf{P}\mathbf{T}_{ne} - \mathbf{T}_{ne}^{\mathsf{T}}\mathbf{P}^{\mathsf{T}}\mathbf{G}^{\mathsf{T}}\tilde{\mathbf{F}}_n^{\mathsf{T}}\mathbf{P}\mathbf{P}\mathbf{T}_{ne} + \mathbf{T}_{ne}^{\mathsf{T}}\mathbf{P}^{\mathsf{T}}\tilde{\mathbf{k}}_{inc}\mathbf{P}\mathbf{T}_{ne}\end{aligned} \tag{5.92}$$

As $\mathbf{G}\mathbf{P} = \mathbf{P}^{\mathsf{T}}\mathbf{G}^{\mathsf{T}} = \mathbb{0}$ we get:

$$\begin{aligned}\mathbf{Q}^{\mathsf{T}}\tilde{\mathbf{k}}_e\mathbf{Q} &= \mathbf{Q}^{\mathsf{T}}\mathbf{P}^{\mathsf{T}}\tilde{\mathbf{k}}_m\mathbf{P}\mathbf{Q} + \mathbf{T}_{ne}^{\mathsf{T}}\mathbf{P}^{\mathsf{T}}\tilde{\mathbf{k}}_{inc}\mathbf{P}\mathbf{T}_{ne} \\ &= \mathbf{Q}^{\mathsf{T}}\tilde{\mathbf{k}}_m\mathbf{Q} + \mathbf{Q}^{\mathsf{T}}\mathbf{P}^{\mathsf{T}}\tilde{\mathbf{k}}_{inc}\mathbf{P}\mathbf{Q}\end{aligned} \tag{5.93}$$

$$\begin{aligned}\tilde{\mathbf{k}}_{inc} &= \mathbf{P}^{\mathsf{T}}\tilde{\mathbf{k}}_{inc}\mathbf{P} + (\mathbf{1} - \mathbf{P}^{\mathsf{T}})\tilde{\mathbf{k}}_{inc}\mathbf{P} + \tilde{\mathbf{k}}_{inc}(\mathbf{1} - \mathbf{P}) \\ &= \tilde{\mathbf{k}}_{inc}^{\text{def, b}} + \tilde{\mathbf{k}}_{inc}^{\text{def, u}} + \tilde{\mathbf{k}}_{inc}^{\text{rig}}\end{aligned} \tag{5.94}$$

$$\tilde{\mathbf{k}}_{inc}^{\text{def, b}} = \mathbf{P}^T\tilde{\mathbf{k}}_{inc}\mathbf{P}, \qquad \tilde{\mathbf{k}}_{inc}^{\text{def, u}} = (\mathbf{1} - \mathbf{P}^T)\tilde{\mathbf{k}}_{inc}\mathbf{P}, \qquad \tilde{\mathbf{k}}_{inc}^{\text{rig}} = \tilde{\mathbf{k}}_{inc}(\mathbf{1} - \mathbf{P}) \tag{5.95}$$

The term $\tilde{\mathbf{k}}_{inc}^{\text{def, b}}$ produces balanced forces from deformational motion, $\tilde{\mathbf{k}}_{inc}^{\text{def, u}}$ produces unbalanced forces from deformational motion, and $\tilde{\mathbf{k}}_{inc}^{\text{rig}}$ produces forces from rigid body motion (self straining and geometric effects). Thus as long as the inconsistent term $\tilde{\mathbf{k}}_{inc}^{\text{def, b}}$ vanishes, the correct form is reproduced. It is apparent that both consistent and inconsistent stiffness-terms associated with rigid body motion are purged from the matrix. Furthermore, the consistent and only some inconsistent terms from deformational motion are

retained. This effectively means that EICR has a slight influence on the internal force-displacement relation of an element. Haugen [16] has likened this to the effect of projecting the stiffness matrix onto the deformed configuration, which then corresponds to the elimination of the term $\tilde{\mathbf{k}}_{inc}^{\text{def, u}}$. What is certain is that the consistency of the element stiffness does not deteriorate on account of the transformation. Comparing this to the formulation by Bergan et al. [18], we can see some fundamental differences.

$$\mathbf{k} = \mathbf{T}_{ne}^{\mathsf{T}} \tilde{\mathbf{k}}_m \mathbf{Q} + \mathbf{T}_{ne}^{\mathsf{T}} \tilde{\mathbf{k}}_{GR} \mathbf{T}_{ne} \tag{5.96}$$

$$\begin{aligned} \mathbf{T}_{ne}^{\mathsf{T}} \tilde{\mathbf{k}}_e \mathbf{Q} &= \mathbf{T}_{ne}^{\mathsf{T}} (\mathbf{P}^{\mathsf{T}} \tilde{\mathbf{k}}_m \mathbf{P} + \tilde{\mathbf{k}}_{GR} + \tilde{\mathbf{k}}_{GP} + \tilde{\mathbf{k}}_{inc}) \mathbf{Q} \\ &= \mathbf{Q}^{\mathsf{T}} \tilde{\mathbf{k}}_m \mathbf{Q} + \mathbf{T}_{ne}^{\mathsf{T}} \tilde{\mathbf{k}}_{GP} \mathbf{T}_{ne} + \mathbf{T}_{ne}^{\mathsf{T}} (\tilde{\mathbf{k}}_{inc}^{\text{def, b}} + \tilde{\mathbf{k}}_{inc}^{\text{def, u}}) \mathbf{T}_{ne} \end{aligned} \tag{5.97}$$

The most striking difference is that the term relating to the variation of the projector will remain after the transformation of the element stiffness. This is not unreasonable, since this term is not included in the resulting geometric terms. In this formulation, the matrix $\mathbf{F}_{nm}$ used in $\tilde{\mathbf{k}}_{GR}$ is based on the unprojected forces. When linear elements are used internally, EICR will have the further advantage of being free of the term $\tilde{\mathbf{k}}_{inc}^{\text{def, u}}$.

5.5 Notes on implementation

In the preceding, the EICR was presented in a general form, without explicitly establishing the matrix $\mathbf{G}$, which depends, not only on geometric considerations, but the personal choices of the developer as well. From the perspective of a computer implementation this is also the most versatile and most easily implementable form, primarily because it requires little effort to implement a new ‘geometry’; just add the corresponding $\mathbf{G}$-matrix. With this said, it should be noted that this versatility comes at great costs in CPU-time, originating from both unnecessary memory requirements and floating point operations (flops). As flops are the most tangible problem[1] the following illustrates the potential savings in tailoring the procedure to a specific geometry. The approximate number of flops needed to calculate the necessary matrices are collected in Table 5.1 In the columns under the heading ‘Generic’, the only optimization of the ‘naive’ implementation has been that

1. Memory management may vary, and the memory-requirement will not exceed capacity.

of spin-matrix multiplication, taking the number of zeros in the $\mathbf{F}_n$-matrix into account, and in the ordering of the multiplications in $\mathbf{K}_{GPS}$. By comparing the columns representing the 2-node element, both the generic implementation and the optimized version, we see that the optimized implementation require only approximately 11% of the flops needed in the generic code. In addition to the flops in Table 5.1 comes the cost of $120N^2$ flops to transform the stiffness-matrix into the global basis.

Table 5.1 Flop-count of operations

	Generic (*N* nodes)	**Generic (2 nodes)**	**Specific (2 nodes)**
$\mathbf{P}$-matrix	$72N^2$	288	0
$\mathbf{P}^\mathsf{T}\tilde{\mathbf{f}}$	$72N^2 - 6N$	276	27
$\mathbf{P}^\mathsf{T}\tilde{\mathbf{k}}_m\mathbf{P}$	$864N^3 - 72N^2$	6624	792
$\tilde{\mathbf{k}}_{GPS} = -\tilde{\mathbf{G}}^\mathsf{T}\tilde{\mathbf{F}}_n^\mathsf{T}\mathbf{P}$	$288N^2 - 18N$	1116	16[a]
$\tilde{\mathbf{k}}_{GR} = -\tilde{\mathbf{F}}_{nm}\tilde{\mathbf{G}}$	$144N^2$	576	168[a]
Sum		8880	1003

a. Addition to the stiffness matrix is counted for all non-zero elements

The table shows that greatest cost actually lies in the application of the projector to the stiffness matrix. It should be noted, though, that there may be significant improvement by performing the operation with an implicitly formed projector.

5.6 Final remarks on the EICR and the internal element formulation

In the previous sections, we have presented the formulation arguing that the formulation is valid even for states of finite deformation. This is of course subject to the condition that the element can handle such deformations, and herein lies the challenge for the aspiring developer: How to produce an element that handles finite (or moderate) deformations correctly, whilst retaining efficiency. Much work has been done in the field of finite deforma-

tion elements and for beam-type elements specifically; the family of elements described by Simo et al. [35, 36, 37] and others has an excellent performance in large deformation problems. However, using these elements within the EICR framework does not produce an improvement in the originally developed element, as they are already invariant to rigid-body motion. The key concept to keep in mind is that EICR assures that spurious self-straining modes are purged from the element stiffness matrix. In conjunction with a co-rotated measure of deformation, the EICR offers a different set of challenges as frame invariance is handled by the framework. At present, the bulk of the work done on this formulation has been in the very successful re-use of existing linear elements, significantly extending their domain of validity. As they are generally computationally inexpensive, they are attractive and well suited candidates in most applications. By the use of very refined meshes, these elements can even handle large or moderate deformation problems, provided the stress-strain relation remains valid. In fact, as the mesh is refined, the element deformations may be smaller than the strains. However, these very refined meshes runs the risk of numerical instability, as well as being prohibitively costly in both memory requirement and floating point operations. A different approach is illustrated in Table 5.2,

Table 5.2 Conceptual performance of elements

	Geometrically exact	**EICR-tailored**	**EICR-linear**	**linear**
Comp. cost	High	Medium	Medium/Low	Low
Accuracy	High	High	Medium	Low

where the column *EICR-tailored* is used to describe elements specifically formulated so that they would display spurious self-straining when taken out of the EICR framework. This would allow for gain in accuracy in the deformational modes, at a small computational cost compared to the basic linear elements. At present, not much work has been done in pursuing and documenting this latter approach, with the notable exception of the work by Eggen [10] on a beam-type element. While higher order effects were effectively captured with a low number of elements, this came at a relatively high computational cost, not realizing the predicted small increase in flops, compared to the linear elements.

The final approach is particularly attractive for small deformation problems where the primary interest is to either:

- predict critical points by linearized buckling, or

- detect critical points in the solution without path following of post-critical range.

In most practical problems, the importance of a consistent tangent stiffness is not paramount as convergence is nearly always guaranteed, even if internal geometrically nonlinear terms are neglected in the element force vector. By simply adding internal geometric terms based on e.g. stability functions, more accurate prediction of critical points is obtained. These contributions are generally extremely simple and cost effective. The main objection to this approach lies in the fact that these terms will not be reflected in the force recovery process, thereby polluting path following and bifurcation analyses.

While it might seem extravagant to use a co-rotational procedure in connection with elements based on a Total Lagrangian formulation, there are advantages. As reported by Cardona and Géradin [8], when developing an element based on interpolation of rotations, difficulties arose when rotations at one node exceeded π, while the others did not. It should be noted that this might occur even for infinitesimal deformational rotations. To correct the problem, they recommended a UL-formulation if rotations of this magnitude were to be expected. This came, however, with the added cost of storing the previously converged state in the iteration process. While not eliminating the problem, applying the co-rotational procedure in the update would greatly reduce the probability of such an occurrence.

5.7 Implemented elements and internal nodes

In the implemented code, several beam formulations can be used in conjunction with the EICR framework, and a short summary of these is presented. All elements are reduced to the system with two visible nodes depicted in Figure 5.4 through simple static condensation of internal nodes.

- **Euler-Bernoulli small strain (EB)**
  This is the classical small strain formulation based on cubic Hermite interpolation of displacements normal to the beam axis. Axial deformation and torsional rotations are linearly interpolated. Planes normal to the beam-axis are assumed to be plane and normal to the deformed axis after deformation. Shear deformations can be included in an

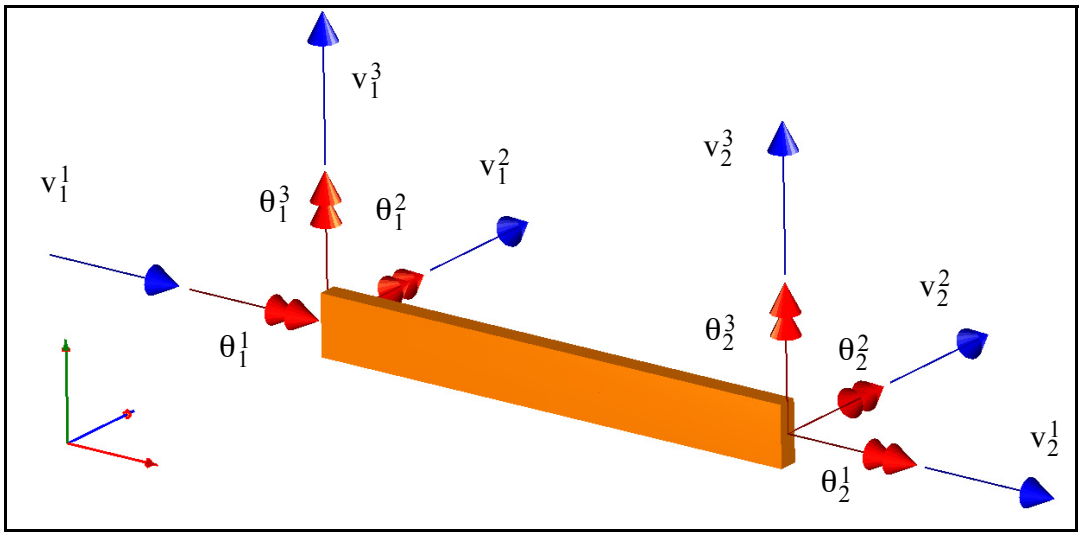

Figure 5.4 Element degrees of freedom

average sense, resulting in the Timoshenko beam formulation (EBT). Deformations are measured in the co-rotating frame.

- **Linear, small strain Mindlin-element (C^0)**
  Classic C^0 small strain beam element with linear interpolation of displacements and rotations. Integration is performed with a one-point integration scheme. Deformations are measured in the co-rotating frame.

- **Simplified UL-formulation**
  This is an adaptation of a simple UL beam element described by McGuire et al. [25]. The principal difference between this formulation and the EB-beam is the inclusion of some geometric terms. Deformations are measured in the co-rotating frame. The implementation results in an inconsistent stiffness matrix as the geometric terms are not mirrored in the force vector. A fully consistent formulation could be obtained at the cost of maintaining information of the deformations at the previous converged state.

- **Linear, reduced Cosserat rod (LRC)**
  The details of the Cosserat theory are presented in the previous chapter. This version of the element is based on linear interpolation of incremental rotations and displacements, and a one-point integration scheme. After each increment, the previous deformations are discarded and the incremental deformations are obtained as the deformations measured in a co-rotating frame.

- **General polynomial Cosserat rod (**COPO_N^{gp}**)**

  This formulation is the full Cosserat rod theory, generalized for any *N*-node element of polynomial order $d = N-1$ and a *gp* -point numerical integration scheme. In this version, only Gauss-Legendre integration is implemented. Deformations are measured as the total deformations. Internal nodes are statically condensed either directly or after a state of internal equilibrium is obtained.

- **General B-spline Cosserat rod (**$\mathrm{COSP}_N^{d,gp}$**)**

  Same as the general polynomial Cosserat rod, with the Lagrange-polynomial basis replaced with a B-spline basis with a uniform knot sequence. The degree *d* of the spline can be at most *N-1*, where *N* is the number of nodes. Integration is performed with a *gp*-point integration scheme over each knot interval, resulting in $(N-d)n$ numerical integration points.

To verify both the implemented code and the contention that EICR does not introduce any additional source of error, even for arbitrary deformations, the problem in Figure 5.5 was analyzed with high order COSP elements. These elements are properly invariant to rigid-body motion and should therefore be unaffected by the transformation. The analyses were performed with ten equal load increments with a simple load correction, i.e. the load increment was recursively halved if the solution did not converge or an indefinite stiffness matrix was detected.

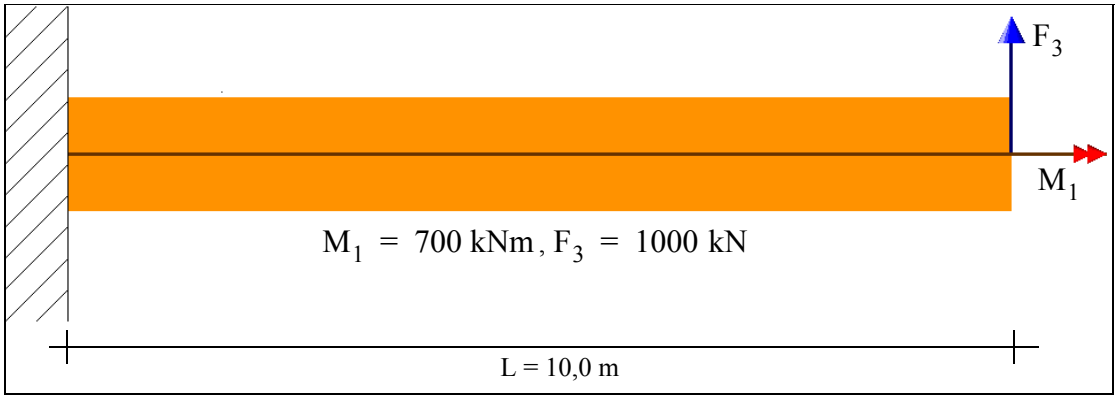

Figure 5.5 Model problem 1

Figure 5.6 shows the deformed state at 0%, 33%, 66% and 100% of the final load-level. The beam clearly experiences a high degree of localization of strain at the base, with coupled twisting and bending. In this situation, the linear, uncoupled assumption of the small strain beams is unjustified.

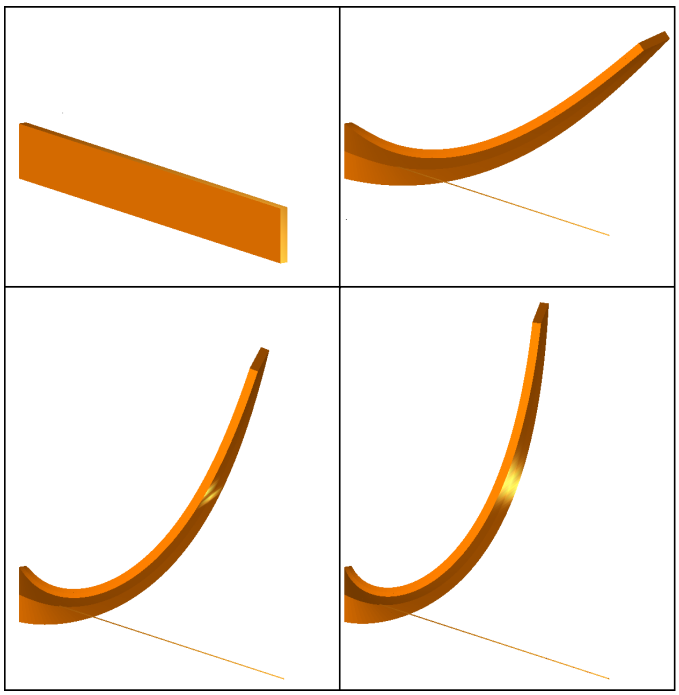

Figure 5.6 Deformed state

As it is difficult to obtain a quantitative measure of the effect of EICR on the stiffness matrix, the following procedure was adopted: The beam was analyzed with a single element of the $\mathrm{COSP}_{15}^{3,3}$ type. The internal nodes were statically condensed, leaving only the dof's at the two end nodes. The condensation was preceded by a) no internal equilibrium considerations, and b) internal equilibrium iterations. During the analysis, the error-estimate $e = \max_{ij} \left| \mathbf{k}_{ij} - \mathbf{k}_{ij}^{EICR} \right|$ was monitored for every instance of the stiffness matrix, where $\mathbf{k}^{EICR}$ is the EICR transformed stiffness, and $\mathbf{k}$ is the unchanged stiffness. Similarly, the measure $m = \max_{ij} \left| \mathbf{k}_{ij}^{EICR} \right|$ was monitored. The problem was subsequently solved using the transformed $\mathbf{k}^{EICR}$.

The error-measure e seems almost randomly distributed when the element is not brought into a state of internal equilibrium. As internal equilibrium is reached at the end of an iteration-cycle, and destroyed after the first increment, the graphs actually display a kind of 'shark-tooth' pattern.

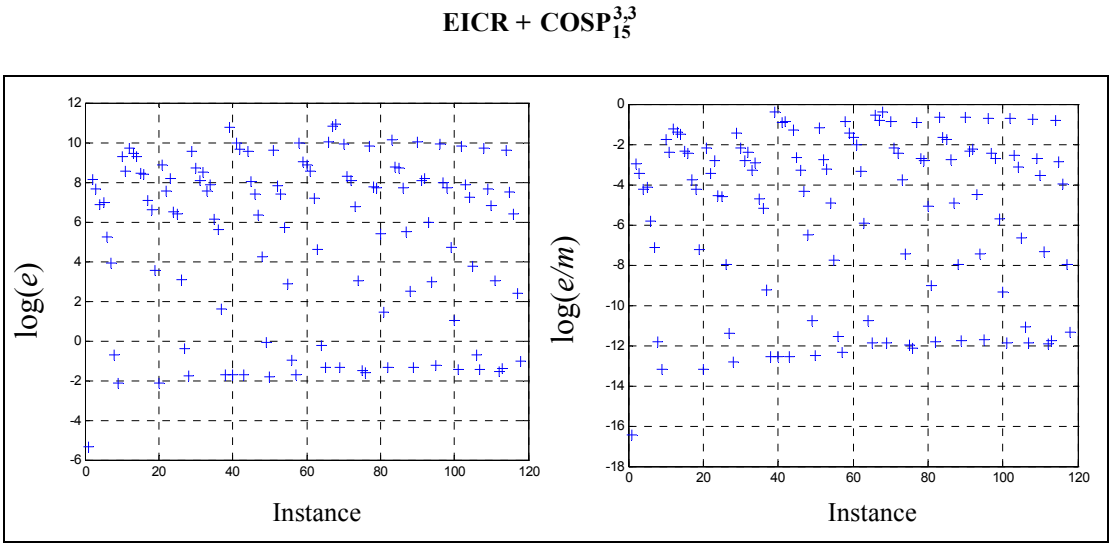

Figure 5.7 Error measures case a) (not in internal equilibrium)

Due to both numerical noise introduced by the transformation, and the fact that the internal nodes did not exactly satisfy equilibrium, *e* did not completely attain the desired value of zero in the case b). The critical factor seemed to be the unbalanced internal nodes, and *e* was consistently in the order of the norm of the internal unbalanced force vector. In Figure 5.8, instance #40 can be seen to deviate significantly. At this point, the beam had problems attaining equilibrium, resulting in a procedure similar to case a). The general conclusion

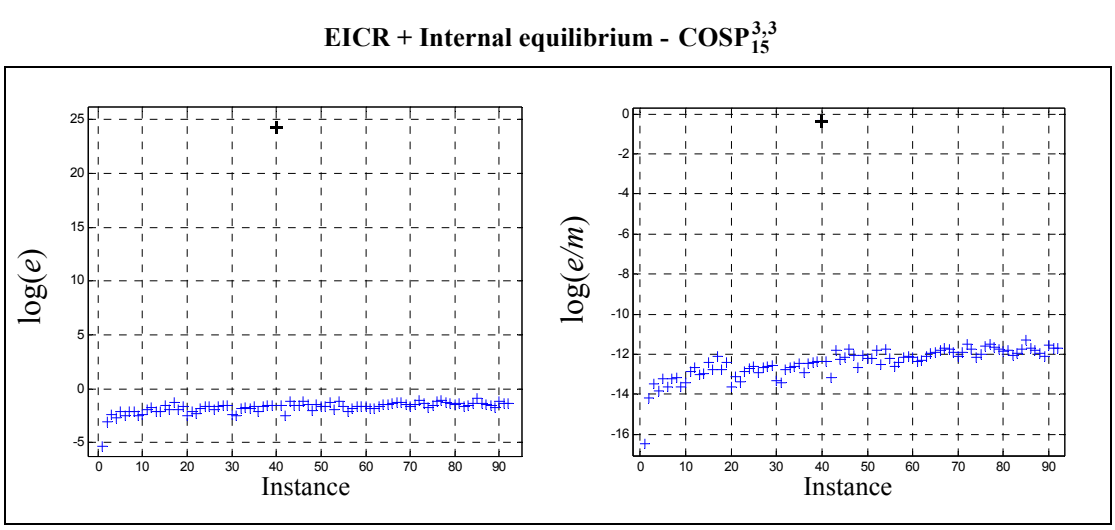

Figure 5.8 Error measures case b) (with internal equilibrium iterations)

that can be drawn, is that the transformation primarily introduce noise in the stiffness matrix of the $\mathrm{COSP}_N^{d,n}$ -elements.

To some extent, the results presented here contradicts a statement made by Crisfield [9]. He claims, without making any reservations, that internal nodes can simply be statically condensed when using this formulation. Although his discussion is limited to linear elements, the problem of nonzero residuals will also appear for linear elements when boundary conditions are imposed on internal nodes.

Chapter 6
Verification of code

6.1 Introduction

In beam type analyses, most parameters in the cross section elasticity tensor is readily available from closed form solutions. This is not, however, generally the case for stiffness parameters associated with shear-deformation, GA_α and GI_t specifically. Although simplified expressions (and sometimes closed form solutions) exist for some cross sections, these parameters must generally be obtained by numeric analysis if accurate results are needed for most geometries. In the following, stiffness parameters are obtained from finite element analyses using the cross section analysis tool CrossX^{TM} [2]. For rectangular cross sections, the following formula is sometimes used for the St. Venant torsion constant I_t:

$$I_t \cong \frac{1}{3}b^3h\left[1-0.63\frac{b}{h}\left(1-\frac{1}{12}\left(\frac{b}{h}\right)^4\right)\right] \cong \frac{1}{3}b^3h\left[1-0.63\frac{b}{h}\right] \qquad \text{(6.1 a and b)}$$

In Figure 6.1a, results obtained by these two approximate formulas are compared with finite element results, for different height to width ratios. Figure 6.1b shows how the shear

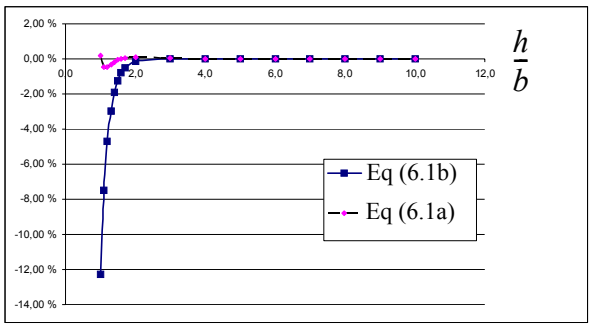

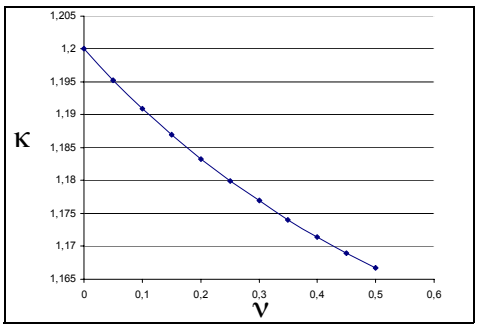

Figure 6.1a) Deviation of I_t for varying h/b **b) κ as a function of ν (isotropic material)**

area modification factor κ ($A_\alpha = A/\kappa_\alpha$) varies with the value of Poisson's ratio ν for a rectangular cross section. CrossX^{TM} was developed to handle isotropic materials only, and the results obtained by the program can be regarded as "exact" for reasonably fine element meshes. In the case of orthotropic materials, CrossX^{TM} will produce stresses that violate the boundary conditions (traction free perimeter). To circumvent this problem, $\nu = 0$ is used when modelling glue laminated timber (glulam). With this modification, reasonably accurate results are obtained, yielding for instance the well known value of $\kappa = 1.2$ for rectangular cross sections.

In the following, all elements based on linear theory are denoted by abbreviations related to the element only. The use of co-rotated deformational measures and EICR transformation are implicitly implied.

6.2 Elastica

In the original paper of Simo and Vu-Qouc [36], the following example of the elastica problem (Figure 6.2) was presented with the data $EA = GA = 1$, $EI = 2$, $L = 1$ and $M = 8\pi$. For this load, the beam curls around itself twice. This result was achieved in

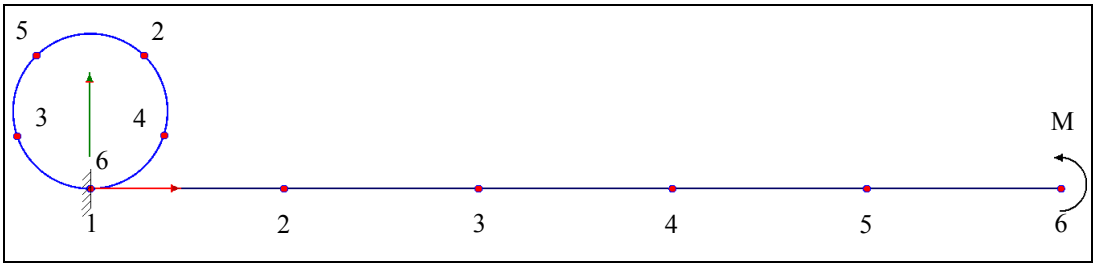

Figure 6.2 Elastica

only two iterations, using elements with linear interpolation functions and one-point integration. Figure 6.2 actually misrepresents slightly the results from this analysis. The actual final configuration of the beam looks like Figure 6.3a, where the real solution is drawn as a thin shell, intersecting the results from the analysis. Looking at Figure 6.3b, one might think that the two-point integration scheme is more appropriate since the nodal points

(nearly) coincide with the circle. However, the results obtained here are actually due to serendipity. They are highly dependant on the value of EA, as both axial and shear forces are introduced in the two-point integrated element.

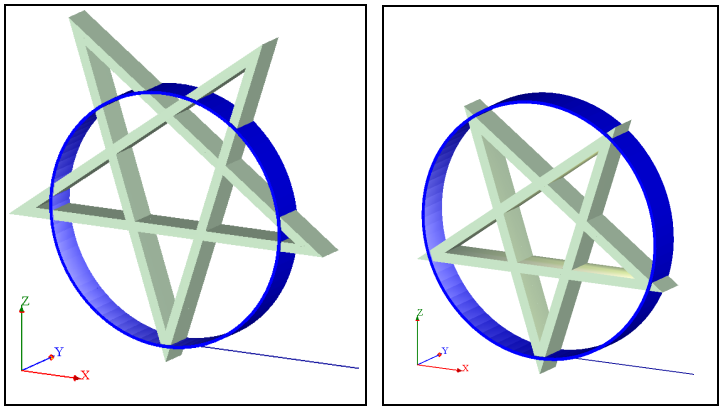

1 point integration 2 point integration

Figure 6.3 Results obtained with 5 Cosserat elements with linear basis

This result is by no means surprising, and in full accordance with the equivalence of the reduced integrated element and mixed methods in the *linear* domain. Under normal circumstances, the fully integrated element will be hopelessly stiff due to the well documented shear-locking phenomenon of C^0 beam elements. This shear-locking is a direct consequence of the elements inability to account for bending in any other way than as shear deformation.

The co-rotated elements are not able to reproduce the astonishing convergence rate of the finite strain elements. In fact, the rapid convergence of these elements is due to both the internal storage of curvatures, and the equality of EA and GA. For values other than $EA/GA = 1$, more modest convergence rates are observed. In the case of the co-rotated elements, the deformational rotations are extracted from a rotation matrix whenever curvatures and deformations are calculated. The predictor step in this analysis will yield incremental rotations exceeding 180º if no form of archlenght or displacement control is employed. Thus, the extracted deformational rotations will be erroneous in the first iteration. A simple form of displacement control is to monitor the maximum incremental nodal rotation, and scale the increment in the full solution if it exceeds a predefined value. Using this strategy, the EBT and RM elements converged in 14 iterations when the maximum

incremental nodal rotation was restricted to 70º. The LRC element was able to handle larger incremental rotations (180º), and converged in 7 iterations.

6.3 45º cantilever bend with transverse point load

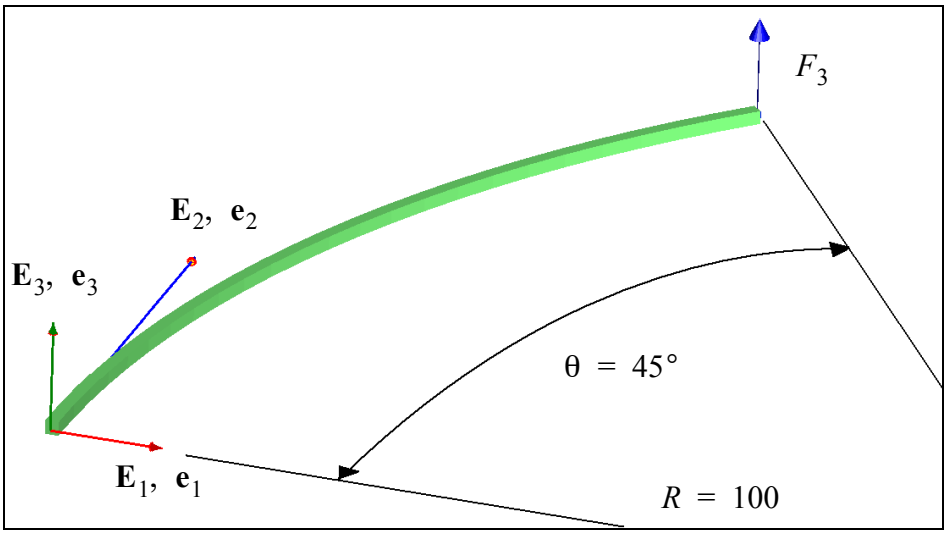

Figure 6.4 45º bend

.

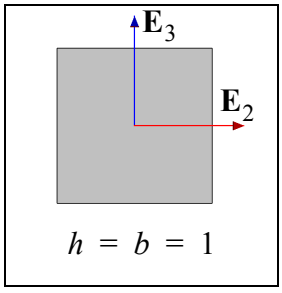

Square 1×1

E [MPa]	ν	A [mm²]	$I_2 = I_3$ [mm⁴]	I_t [mm⁴]	κ_α
1.0e7	0	1	8.333333e-2	1.40577e-1	1.2

An example, studied by several authors, is the 45º degree cantilever beam with transverse point load (see Figure 6.4). An attempt to replicate the results obtained by Simo and Vu-Quoc [36], using 8 linear elements, failed when "exact" cross section parameters obtained by CrossX were used. It appears that [36] uses $I_t = I_p = I_2 + I_3$ and $\kappa = 1$, and the following comparisons are therefore based on these parameters.

First, the beam is loaded in five steps of equal magnitude (75 N). In Table 6.1 the residual norm in the fifth load increment is compared with the results presented by Simo and Vu-

Quoc using both a non symmetric and a symmetrized stiffness matrix. The results from the current implementation hardly deviates from the results of Simo and Vu-Quoc. In addition to using 8 linear Cosserat elements, the problem is analyzed using 8 LRC elements. As expected, the LRC element does not perform quite as well as the fully consistent element:

Table 6.1 Residual norm of step 5 ($I_t = I_p$ and $A_\alpha = A$)

	Non symmetric			Symmetric		
Iter.	**Current**	**Simo et. al.**	**LRC**	**Current**	**Simo et. al.**	**LRC**
0	0.7500E+02	0.750E+02	0.7500E+02	0.7500E+02	0.750E+02	0.7500E+02
1	0.1465E+06	0.147E+06	0.1464E+06	0.1469E+06	0.147E+06	0.1468E+06
2	0.4264E+03	0.426E+03	0.5101E+03	0.4232E+03	0.423E+03	0.4492E+03
3	0.1736E+04	0.173E+04	0.1696E+04	0.1401E+04	0.140E+04	0.1429E+04
4	0.2991E+01	0.299E+01	0.1733E+03	0.8441E+00	0.844E+00	0.1270E+03
5	0.1766E+00	0.177E+00	0.9425E+01	0.6613E-01	0.661E-01	0.7200E+01
6	0.2217E-07	0.230E-07	0.2380E+00	0.1898E-04	0.190E-04	0.5733E-01

It is worth noting that, although only slightly, the symmetrized stiffness matrix actually improves the convergence properties of LRC for this particular case. This is probably due to chance, and should not be attributed to any intrinsic property of the element. In [36], the energy norm was also presented for the symmetrized stiffness matrix. As seen in Table 6.2, the present analysis corresponds well with the analysis by Simo and Vu-Quoc:

Table 6.2 Energy norm of step 5 using symmetrized matrix ($I_t = I_p$ and $A_\alpha = A$)

Iter.	**Current**	**Simo et. al.**	**LRC**
0	0.4100E+03	0.410E+03	0.4100E+03
1	0.2283E+05	0.228E+05	0.2283E+05
2	0.4535E+01	0.453E+01	0.4535E+01
3	0.2580E+01	0.258E+01	0.2583E+01
4	0.9498E-04	0.950E-04	0.5181E-03
5	0.2691E-08	0.269E-08	0.1508E-05
6	0.2746E-13	0.275E-13	0.8784E-10

The beam was also analyzed for a load history of 300 N, 450 N, and 600 N. As in the analysis reported by Simo and Vu-Quoc, convergence was attained in 13, 8 and 6 iterations respectively. Table 6.3 presents the final position of the tip for the various load levels.

Table 6.3 Tip position ($I_t = I_p$ and $A_\alpha = A$)

	Current			Simo et. al.		
Load [N]	**x [mm]**	**y [mm]**	**z [mm]**	**x [mm]**	**y [mm]**	**z [mm]**
300	22.3288	58.8447	40.0756	22.33	58.84	40.08
450	18.6152	52.3159	48.3939	18.62	52.32	48.39
600	15.8018	47.2328	53.3695	15.79	47.23	53.37

In closing, attention should be paid to the difference in torsional rigidity. When comparing I_t and I_p, we get the ratio $I_p / I_t = 1.19$. Although this is not a significant difference, it will noticeably affect the results with respect to convergence. The results obtained when using the parameters from CrossX, are presented in Table 6.4.

Table 6.4 Tip position ($I_t \neq I_p$ and $A_\alpha = A/1{,}2$)

	COPO_2^1 (Current)			LRC			EBT		
Load [N]	**x [mm]**	**y [mm]**	**z [mm]**	**x [mm]**	**y [mm]**	**z [mm]**	**x [mm]**	**y [mm]**	**z [mm]**
300	22.20	58.60	40.36	22.21	58.61	40.36	22.14	58.57	40.48
450	18.48	52.05	48.59	18.49	52.05	48.59	18.40	52.01	48.73
600	15.68	46.98	53.50	15.69	46.98	53.50	15.59	46.93	53.65

For the purpose of comparing the values of Table 6.4 with the values when a refined mesh is used, 80 COPO_2^1 elements resulted in the final tip position (15.56, 46.89, 53.61). As expected, the COPO_2^1 and LRC elements are quite similar. The results from the EBT element, however, are somewhat better than those of the others. The underlying formulation of the linear Cosserat rod is not too different from that of the RM element. Accordingly, the results are not significantly better than the results from the RM element (not presented here). Results that are closer to EBT would be obtained if higher order COPO elements are used. This is a natural consequence of the polynomial order of the interpolation function of the displacements. Even though this is a large part of the difference in the solutions, there are also some more subtle differences that will be discussed in the following section.

6.4 Combined torsion and bending

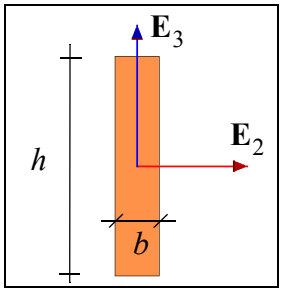

Rectangle 200×1200

E [MPa]	G [MPa]	A [mm^2]	I_t [mm^4]	κ
14500	830	240000	286.3897e+8	1.2

The example described in Section 4.7 serves as a good test of the elements and their performance. The combination of torsion and bending serves as the most severe and necessary component in the verification of 3D beam element behavior in static analyses. If the deformations are restricted to planar motion only, the discussions in the previous chapters are for the most part rendered mute, since rotations are reduced to scalar quantities. For this particular case, a minute difference in formulation will produce a relatively large difference in the tip displacements due to the large deformations at the base of the beam (see Figure 5.6). In Table 6.5, the tip displacements from a variety of elements and meshes, are presented, where the numbers in parentheses are the number of elements used in the analysis. The model is loaded in 100 equal load increments.

Table 6.5 Tip displacement

Element	v_x [mm]	v_y [mm]	v_z [mm]	θ_x [deg]	θ_y [deg]	θ_z [deg]
EICR - EBT (19)	-4564.60	1436.66	6945.01	-109.170	38.6652	-91.0047
EICR - EBT (200)	-4583.22	1417.97	6968.38	-108.939	38.8310	-90.9413
EICR - EB (200)	-4560.66	1440.44	6931.22	-108.924	38.8857	-90.8928
EICR- RM (19)	-4560.16	1443.18	6938.76	-109.193	38.6572	-91.0291
EICR- RM (200)	-4583.18	1418.03	6968.33	-108.939	38.8310	-90.9415
$COSP_{15}^{1,1}$ (1)	-4547.63	1508.22	6911.93	-109.593	38.1792	-91.3541
$COSP_{15}^{3,3}$ (1)	-4563.24	1438.58	6945.43	-109.072	38.7488	-90.8543
$COSP_{20}^{3,3}$ (1)	-4566.26	1437.25	6949.01	-109.058	38.7631	-90.8610
LRC (200)	-4566.57	1437.35	6949.30	-109.057	38.7632	-90.8635

The results obtained with 200 LRC elements are accurate to 5 digits when compared to a reference solution from 200 $COSP_4^{3,3}$ elements. Surprisingly, the linear elements are accurate to approximately 3 digits when 19 elements are used, but only accurate to 2 digits for

the refined mesh. Limited testing has revealed that the critical difference is the pre multiplication of $\mathbf{f}_e$ with the moment correction matrix, $\mathbf{H}^T$, thereby softening the element. If the first 2 m are modeled with 500 RM elements, while the last 8 m are modeled with 100 elements, the vertical displacement become 6968.63 mm, while it is reduced to 6952.05 mm if pre multiplication is omitted. However, excluding this term would adversely affect convergence for coarse meshes. Furthermore, the situation is not quite so simple as this test may indicate. In the finite strain formulation, stretching of the beam and shear forces will influence the moments, while this is only accounted for in the small strain elements by the EICR transformation. Without resolving this issue, it is still appropriate to note that there is a difference in the obtained results that is not solved by further mesh refinement. In Figure 6.5 the relative deviation in displacements are plotted as a function of load for some of the elements in Table 6.5 Clearly, the EBT element corresponds quite well with the finite strain elements.

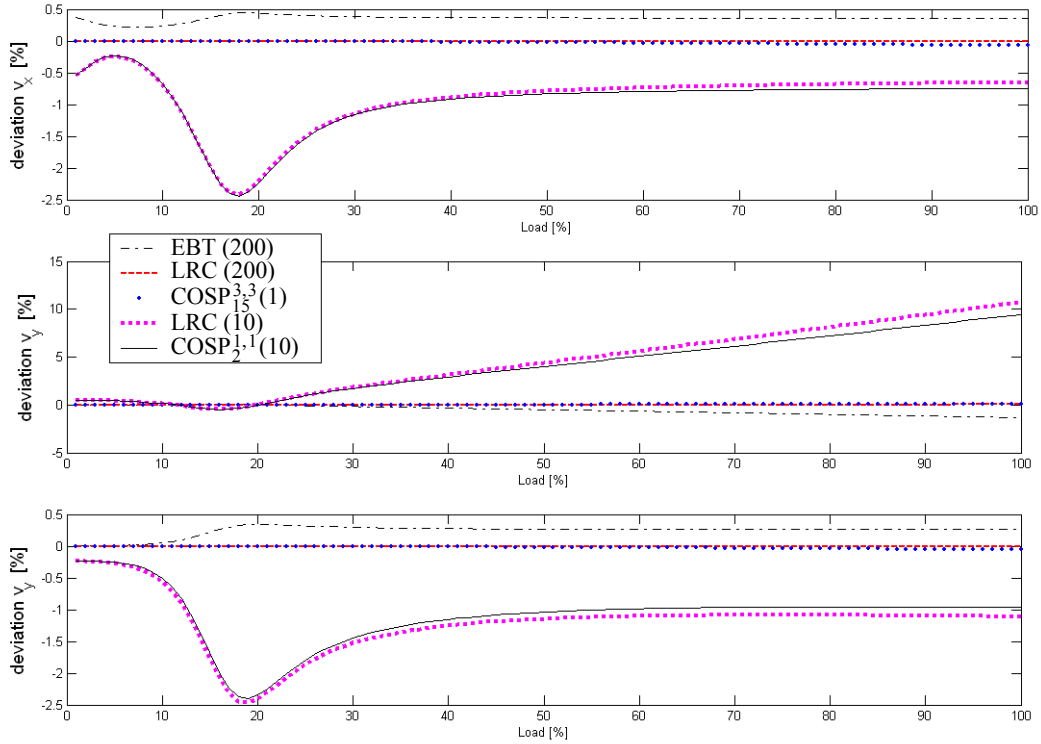

Figure 6.5 Deviation in displacements vs. load

This problem is also a good test for the simplified implementation of the finite strain formulation. When 10 LRC elements are used, the results are almost identical to those of the fully implemented version, although somewhat poorer when the deformations are very

large. Figure 6.6 shows the deviations when more moderate deformations are considered. Although modest compared to the deformations in Figure 6.5, the twist of the beam is approximately 20º when the load is 10% of that in the original problem.

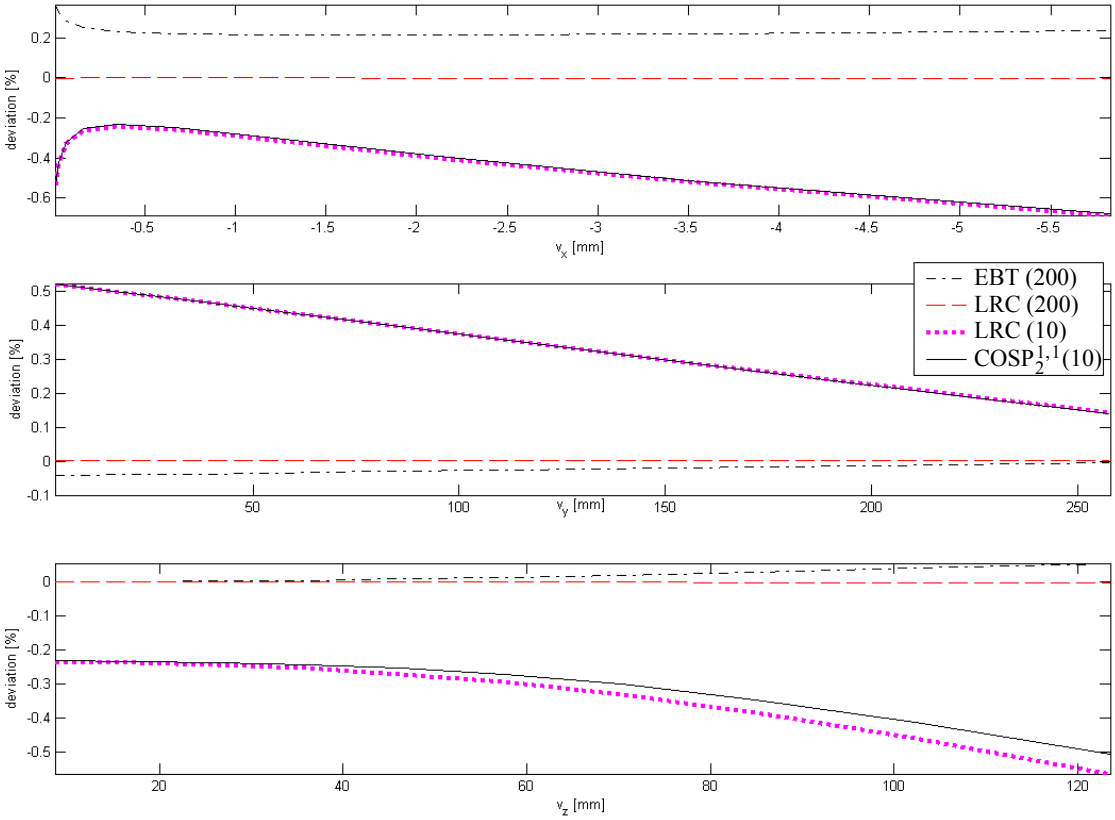

Figure 6.6 Deviation in displacements vs. displacements (load ≤ 10%)

Finally, the beam was subjected to four equal load increments from 0 to 10% of the original load(100 kN and 70 kNm), using 10 C^0 elements only. Convergence (in energy norm) was attained in 4, 5, 5, and 6 iterations for the LRC element, while the full element formulation converged in 4, 4, 5 and 5 iterations. The RM element also converged in 4, 4, 5 and 5 iterations with only slightly poorer results than the LRC as seen in Table 6.6.

Table 6.6 Tip displacement

Element	v_x [mm]	v_y [mm]	v_z [mm]	θ_x [deg]	θ_y [deg]	θ_z [deg]
EICR- RM (10)	-5.7241	256.02	122.68	-19.235	0.70735	-3.0300
LRC (10)	-5.7884	258.14	122.87	-19.231	0.70778	-3.0466
COPO$_2^1$ (10)	-5.7889	258.13	122.95	-19.231	0.70778	-3.0466
COPO$_2^1$ (200)	-5.8283	257.78	123.57	-19.270	0.70866	-3.0439

6.5 Flexural buckling

The properties of slender beams and columns with respect to elastic stability has been thoroughly studied throughout the past 150 years, primarily based on analytic solutions of the differential equation of the beam. Accordingly, closed form solutions of varying degree of complexity exist for many simple systems. Just as the complexity of the underlying differential equation influences the closed form solution, the formulation of an element will determine the effects that are captured in a linearized buckling analysis. Thus, the following sections are dedicated to the study of the analytical solution to which the element converges, as well as the accuracy of the described elements.

6.5.1 Rate of convergence and accuracy

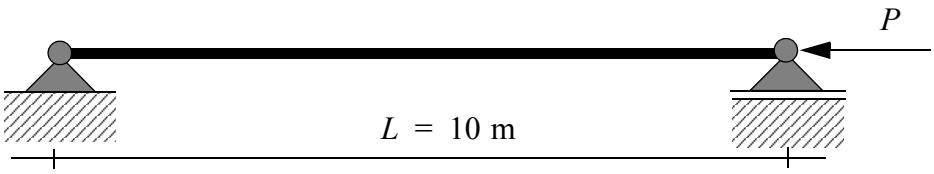

Figure 6.7 Euler beam

To investigate and verify the accuracy of the implemented elements, we proceed with a simply supported beam with a compressive end-load as depicted in Figure 6.7. The classical solution to this problem, commonly known as the Euler load, is given by

$$\mathrm{P}_E = \left(\frac{n\pi}{L}\right)^2 EI_3, \quad n = 1,\ 2,\ 3,\ \ldots \tag{6.2}$$

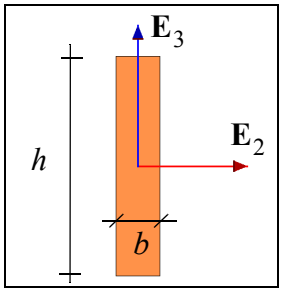

Rectangle 200×1000

E [MPa]	G [MPa]	A [mm²]	I_3 [mm⁴]	κ
6250	390	200000	6.666667e+8	1.2

For this problem, the cross section and material properties are taken to coincide with the parameters used by Eggen [10]. In his thesis, a consistent C^1 element with internal geometric stiffness was developed. It is of interest to see how this element compares with val-

ues obtained by simply including internal geometric stiffness based on simplified assumptions. These internal geometric stiffness terms are merely based on the interaction of bending of the beam and axial forces, subsequently denoted Pδ-effects.

The Euler-Bernoulli element and the element developed by Eggen [10] do not account for shear deformation; the other elements do. How shear will influence the "exact" solution will be discussed in the next section. For the moment it suffices to categorize the elements in shear elements and no shear elements. The reference value for the non shear elements is given by Equation (6.2) (411.2335 kN), while an analysis with 200 $COPO_5$-elements form the basis for the shear elements (408.645 kN).

Observing the convergence of the standard Euler-Bernoulli element in Table 6.7, it is clear that the EICR-procedure only contribute with terms equivalent to PΔ-effects (rigid body geometric stiffness). In flexural buckling, this element will therefore, in general, be considered too stiff and it will require a significant number of elements to converge. By simply including internal geometric stiffness terms based on the Pδ-effect, a far better element is obtained. Figure 6.8 shows that this element is virtually indistinguishable from the element developed by Eggen. It should be noted that this result is applicable in the context of flexural buckling analyses only. For nonlinear analyses the added terms may affect convergence rates, and the nonlinear internal behavior of the element will not be reflected in the final results.

Table 6.7 Buckling load of Euler beam-column

Nodes	EB [kN]	EB+Pδ [kN]	Eggen [kN]
2	-	500.0000	500.0000
3	500.0000	414.3269	414.3270
4	450.0000	411.8838	411.8825
5	432.7768	411.4441	411.4441
6	424.9329	411.3207	411.2470

While the comparisons of the no shear elements are rather straight forward, the situation is more complex for the shear elements. When comparing solutions with equal number of *dofs* one should keep in mind that the C^0 elements have to describe two fields (rotations and displacements are independent) while the C^1 EBT is based on Hermitian polynomials, thus using all *dofs* in describing the transverse displacement field. Therefore, one

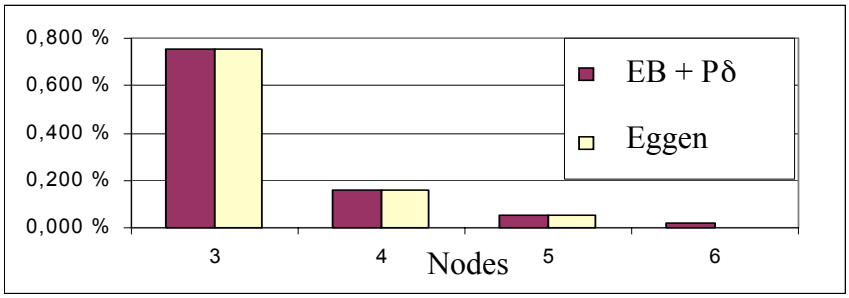

Figure 6.8 Deviation, no shear elements

would expect these elements to be more accurate when shear deformations are of less importance. In Figure 6.9 the relative error from a series of analyses is shown using

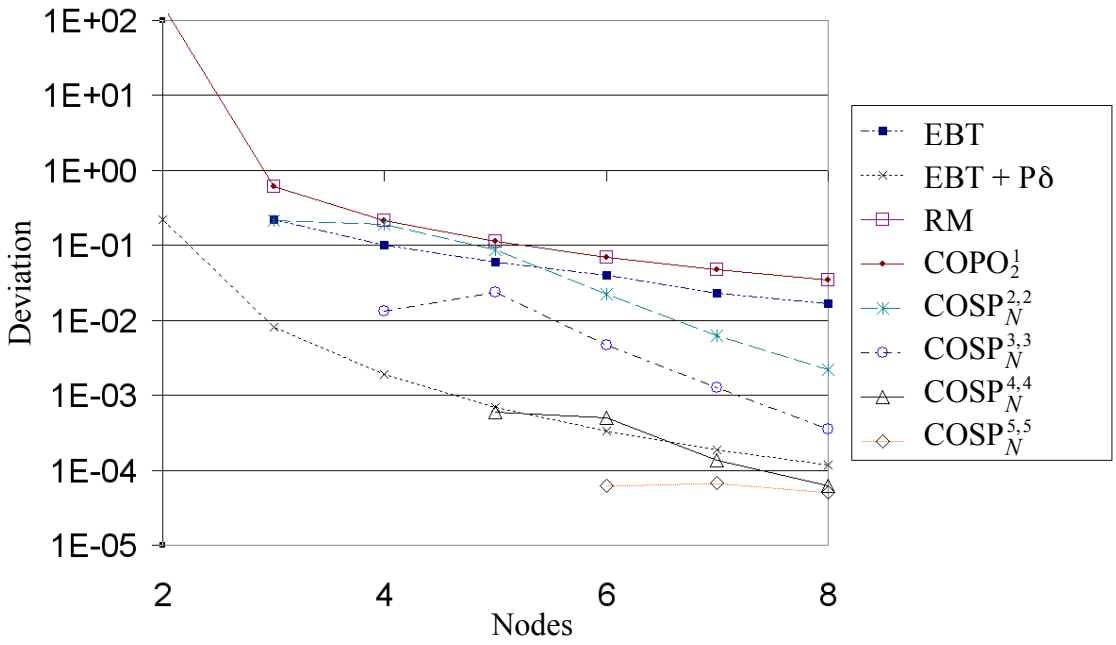

Figure 6.9 Deviation, shear elements

meshes ranging from 2 to 8 nodes. For low number of nodes the EBT element with Pδ-effect included is clearly the most accurate. When 5 and 6 nodes are used, however, the high order COSP elements are as good and even better with respect to accuracy.

The COSP elements in Figure 6.9 all employ uniformly reduced integration to avoid shear locking. Full integration would significantly stiffen the low order elements. For instance, using a COSP$_5^{2,8}$ element (8pt. integration) would result in an error of 14.23%

(466.805 kN) while the $\mathrm{COSP}_5^{2,2}$, presented in the graph, only deviates by 8.61% (443.811 kN). This effect is even more noticeable for the COPO elements; using two COPO_3^3 elements, thus having the same number of *dofs* as one COSP_5^2 (and polynomial order), the error becomes 18.48% (484.1784 kN). This is somewhat surprising since the continuity within the COSP element is higher (C^1) than between the two COPO elements (C^0), and also because the reduced integrated $2\times\mathrm{COPO}_3^2$ solution is significantly closer to the reference value than that of the $\mathrm{COSP}_5^{2,2}$ (1.50%).

6.5.2 Effect of shear on the lateral buckling load (cantilever beam-column)

Having verified that the elements behave appropriately for coarse meshes, we can proceed to investigate the effect of shear in more detail. For this purpose, we use a selection of axially end loaded cantilever beams. The equivalent to Equation (6.2), for a beam-column restricted to buckle in the 1-2 plane (X-Z plane in Figure 6.10), is:

$$\mathrm{P}_E = \left(\frac{n\pi}{2L}\right)^2 EI_3,\ n = 1,\ 3,\ 5,\ \ldots \tag{6.3}$$

Where the three first buckling modes are shown in Figure 6.10.

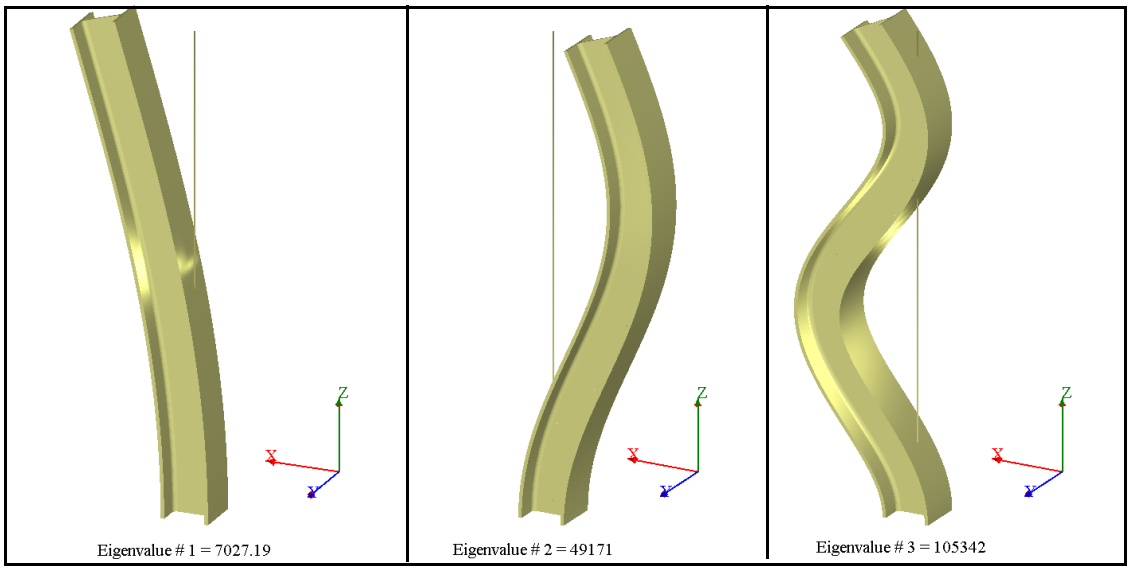

Figure 6.10 Lateral buckling of HEB200 ($L = 2000$ mm)

Equation (6.3) is based on the assumption of no shear deformation. According to Timoshenko and Gere [39], Engesser [11] later developed the following solution, incorporating the effect of shear:

$$P_{Eng} = \frac{GA_s P_E}{GA_s + P_E} \tag{6.4}$$

This solution is takes into account the appearance of shearing forces, normal to the deformed beam axis in the buckled state. Timoshenko and Gere [39] extended Equation (6.4) by also accounting for the shear deformation of the beam (cross sections which are not necessarily normal to the beam axis). In so doing, they obtained the following result:

$$P_{TG} = \frac{GA_s}{2}\left(\sqrt{1 + 4P_E / GA_s} - 1\right) \tag{6.5}$$

In the following analyses, 100 elements are used for each element type. This eliminates convergence issues, while not causing numerical difficulties. Three types of cross sections are used, two of which are assumed to be sensitive to shear (case 1 and 3). In all analyses, buckling is restricted to occur in the plane normal to the strong axis.

Case 1: HEB200

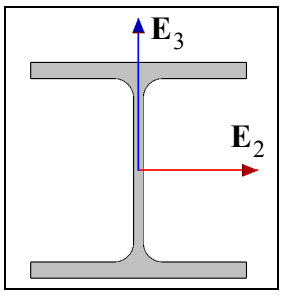

HEB200 (steel)

E [MPa]	ν	A [mm^2]	I_2 [mm^4]	κ_3
210000	0.3	7808.9	5.6967e+7	4.49824

The first series of analyses are designed to verify that the shear elements behave appropriately if the beam is infinitely stiff in shear. This is achieved by setting the shear stiffness to 1000 times the actual value. The results from these analyses are summarized in tables 5.6.8 and 5.6.9 for beams of length 4 and 2 m respectively.

Table 6.8 Buckling loads of 4m HEB200 (excluding effect of shear)

Element	Buckling load #1 [1000 kN]	Buckling load #2 [1000 kN]	Buckling load #3 [1000 kN]
Euler	1.844843	16.60359	46.12108
EB +EICR[a]	1.844843	16.60359	46.12108
EBT + EICR [ab]	1.844819	16.60162	46.10592
RM+EICR[b]	1.844895	16.60777	46.15334
LRC	1.844895	16.60777	46.15334
COPO$_4^3$ [b]	1.844818	16.60162	46.10592

a. $P\delta$-effect included

b. $GA_{eff} = 1000GA$

Table 6.9 Buckling loads of 2m HEB200 (excluding effect of shear)

Element	Buckling load #1 [1000 kN]	Buckling load #2 [1000 kN]	Buckling load #3 [1000 kN]
Euler	7.379373	66.41435	184.4843
EB +EICR[a]	7.379372	66.41435	184.4843
EBT + EICR [ab]	7.378984	66.38291	184.2419
RM+EICR[b]	7.379288	66.40747	184.4312
LRC	7.379288	66.40749	184.4316
COPO$_4^3$ [b]	7.378984	66.38292	184.2422

a. $P\delta$-effect included

b. $GA_{eff} = 1000GA$

The results seem to indicate that the elements behave appropriately. The slight deviation from the Euler load in the shear elements is most likely due to the crude method employed to exclude shear deformation.

The next set of analyses are performed in order to compare the solutions of Engesser and Timoshenko and Gere with the finite element solutions. Three different lengths are used;

4, 2 and 1 m. It should be mentioned that the beam hypothesis of Navier is maintained, and effects such as localized buckling of the web or flanges are not accounted for in this description. The results of these analyses are summarized in Tables 5.6.10, 5.6.11 and 5.6.12.

Table 6.10 Buckling loads 4m HEB200 (including effect of shear)

Element	Buckling load #1 [1000 kN]	Buckling load #2 [1000 kN]	Buckling load #3 [1000 kN]
Engesser	1.82096	14.84619	34.70646
Timoshenko and Gere	1.82126	14.99967	36.57987
EBT + EICR[a]	1.820824	14.81195	34.27144
RM +EICR	1.820959	14.85056	34.73227
LRC	1.821263	15.00417	36.60981
COPO$_4^3$	1.821189	14.99910	36.57863

a. $P\delta$-effect included

Table 6.11 Buckling loads 2m HEB200 (including effect of shear)

Element	Buckling load #1 [1000 kN]	Buckling load #2 [1000 kN]	Buckling load #3 [1000 kN]
Engesser	7.010700	45.06884	79.66722
Timoshenko and Gere	7.027470	49.17256	105.3450
EBT + EICR[a]	7.006889	44.11650	74.62140
RM +EICR	7.010696	45.07894	79.70137
LRC	7.027465	49.18542	105.4179
COPO$_4^3$	7.027190	49.17097	105.3421

a. $P\delta$-effect included

Table 6.12 Buckling loads 1m HEB200 (including effect of shear)

Element	Buckling load #1 [1000 kN]	Buckling load #2 [1000 kN]	Buckling load #3 [1000 kN]
Engesser	24.38506	91.77668	117.8273
Timoshenko and Gere	25.04516	135.2354	259.1175
EBT + EICR[a]	24.23339	84.24643	102.9547
RM +EICR	24.38506	91.78736	117.8907
LRC	25.04515	135.2654	259.2730 (-165.2604)
COPO$_4^3$	25.04426	135.2318	259.1113 (-165.2595)

a. $P\delta$-effect included

In all analyses, the linear elements converged towards the solution of Engesser, while the Cosserat rod theory elements all converged towards the solution of Timoshenko and Gere. The RM element produces results that are equivalent to the solution of Engesser, while the EBT element actually displayed a slightly softer behavior. This observation is also found in Figure 6.11, where the lowest curve is that of the EBT element. This figure is a compilation of results from buckling analyses of beam-columns with lengths ranging from 0.5 to 5 m in increments of 90 mm. The abscissa in the figure is the dimensionless slenderness ratio

$$\lambda = 2L\sqrt{\frac{A}{I_2}}. \tag{6.6}$$

The only difference between the geometrically exact finite strain element and the linear Reissner-Mindlin element is, in this case, the geometric stiffness matrix. For instance, the initial (undeformed) material stiffness of the LRC element is identical to the stiffness matrix of the RM element. Thus, the coalescence of the results from the linear Reissner-Mindlin element and the solution of Engesser is a natural consequence of the lack of internal geometric stiffness. The geometric stiffness matrix derived in Section 3.6, however, contains both internal geometric effects and rigid body terms. These elements are therefore able to account for shear deformations more accurately. For the very short beam-column, however, a peculiar result was observed; the third buckling load is tensile (reported in parenthesis in Table 6.12). To rule out error in the derivation of the geometric stiffness,

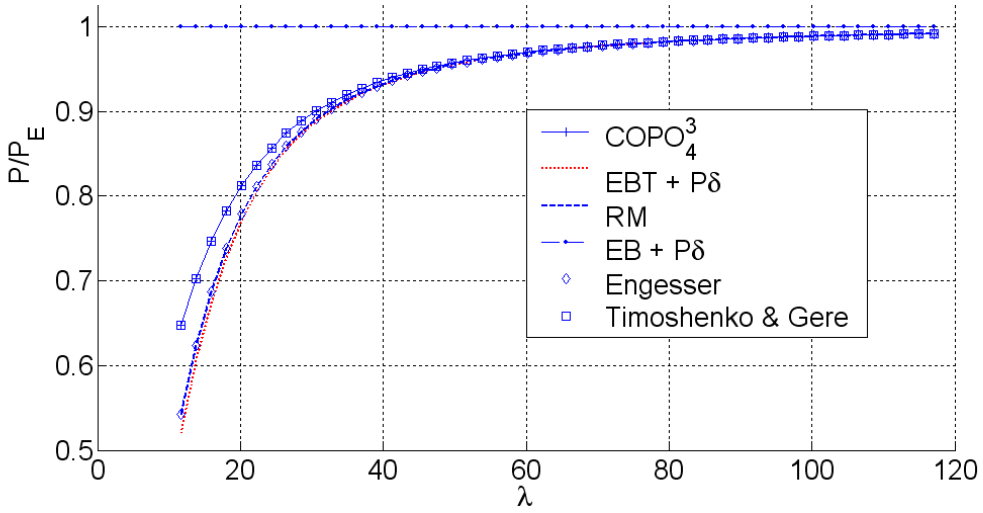

Figure 6.11 Buckling of cantilever column HEB200 L = 500...5000 mm (1st mode)

a nonlinear analysis using these elements was performed. The analysis revealed that the predicted singularity is present, and the beam buckles in a purely shear deformation mode. The forces at this stage is, however, unrealistically high, resulting in stresses of magnitude in the order of the modulus of shear. Attempts of finding a good explanation of this effect has not been pursued.

Case 2: Square 100×100

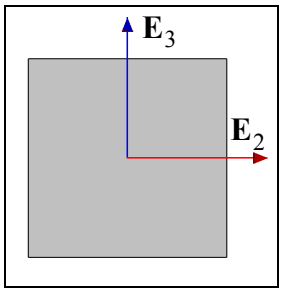

Square 100×100 (steel)

E [MPa]	ν	A [mm²]	I_2 [mm⁴]	κ_3
210000	0.3	10000	8.333333e+6	1.1769

For a square cross sections of isotropic material, the effects of shear are marginal for reasonably slender beams, but the same tendencies as in the previous case are observed: The Cosserat rods replicate the solution of Timoshenko and Gere within numerical accuracy, while the linear elements are close to the solution of Engesser.

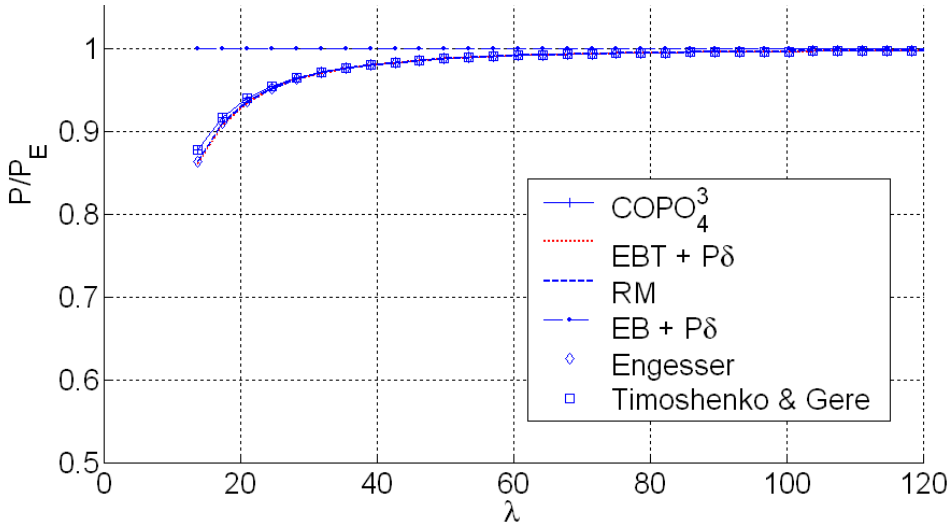

Figure 6.12 1st buckling mode of cantilever beam-column with square cross-section (100×100 mm) L = 500...5000 mm

Case 3: Glulam beam

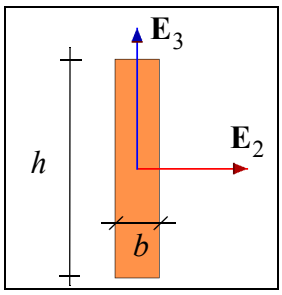

Rectangle 100×500 (glulam GL36c)

E [MPa]	G [MPa]	A [mm²]	I_2 [mm⁴]	κ_3
10062.5	632.5	50000	1.0417e+9	1.2

In all previous cases, isotropic material behavior was used and the shear parameter κ is a good indicator for the effect of shear on the buckling load. For non-isotropic modulus of shear, an equivalent κ value can be determined. Equating the shear stiffness of a given cross section with isotropic material properties with that of a similar cross-section with the actual non-isotropic stiffness, we get:

$$GA_s = \frac{E_0}{2(1+\nu)\kappa_{eq}}\frac{A}{}, \qquad \kappa_{eq} = \frac{E_0}{2(1+\nu)G}\kappa \tag{6.7}$$

Assuming ν is in the range 0 to 0.5, κ_{eq} is bounded by:

$$5.3 \le \kappa_{eq} \le 9.55 \tag{6.8}$$

Thus it is reasonable to assume that the shear effect on rectangular timber beams is even greater than the effect on the HEB200 steel cross section. This assumption is verified by

Figure 6.13, where the relative buckling load is plotted for beams of lengths varying from 0.6 m to 8 m.

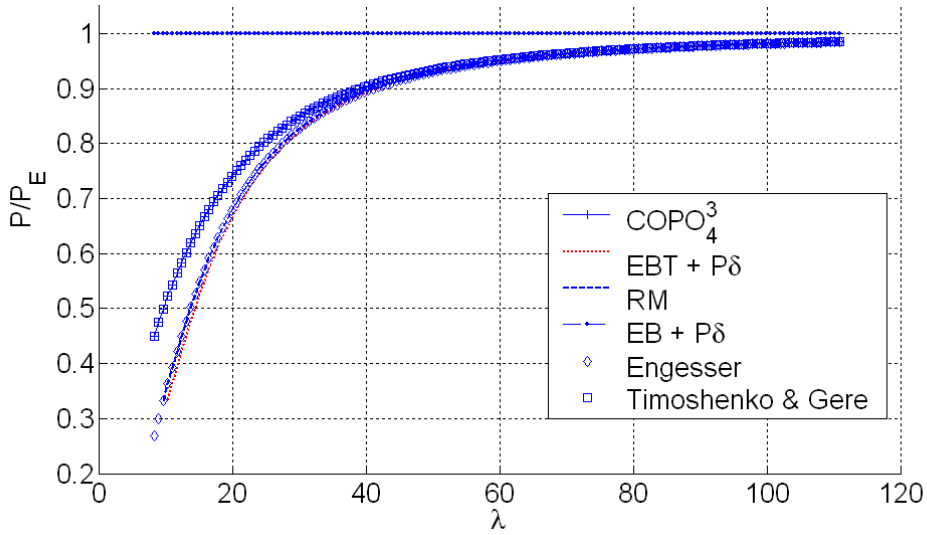

Figure 6.13 Buckling of cantilever glulam beam-column T30 h×b = 500×100 mm (1st mode)

From a practical point of view, the effect of shear does not seem critical for rectangular cross sections. In Figure 6.14, the critical stresses from the buckling analyses are plotted, as well as the characteristic allowable stresses in stability problems, f_{cud}, according to NS 3470-1, the Norwegian code of practice for timber structures. The allowable stresses in NS 3470-1 are based on critical loads obtained without shear effects (Euler load). If values obtained with the solution of Engesser were used in stead, the allowable stresses, plotted as f'_{cud}, would be affected, but not much. For composite timber cross sections, however, the effect may be more noticeable.

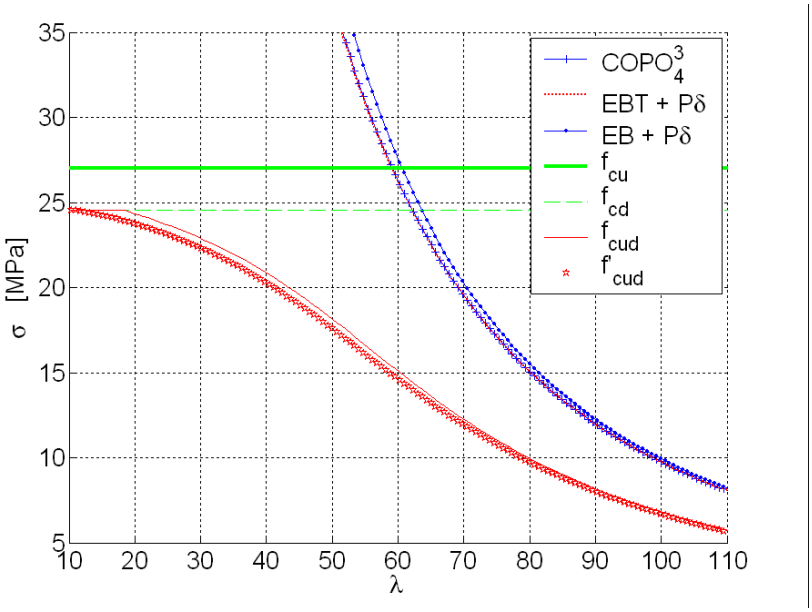

Figure 6.14 Critical stress

6.6 Lateral torsional buckling

6.6.1 Preliminary comments

In order to investigate the effects of orthotropy in a subsequent chapter, plate buckling analyses are carried out by FEMplate [4]. FEMplate uses high order thin plate bending elements (T18/T21) in combination with the in-plane stresses obtained by a linear solution of the membrane problem, using Linear Strain Triangles (LST). The stresses at corner nodes are provided as input for the geometric stiffness in the subsequent eigenvalue analysis.

$$(\mathbf{K}_M - \lambda \mathbf{K}_G)\mathbf{x} = 0 \tag{6.9}$$

To verify the accuracy of the model, a series of analyses using linear elastic, isotropic materials were performed. The results for a simply supported beam, prevented from rotation about its own axis, and subjected to a constant bending moment about the strong axis (M_y) are presented here. Assuming $I_y \ll I_z$ (no preceding deformation about strong axis), the classical solution to the differential equation of the beam is (Timoshenko [39])[1]:

1. All closed form solutions reported here apply to warping free conditions only

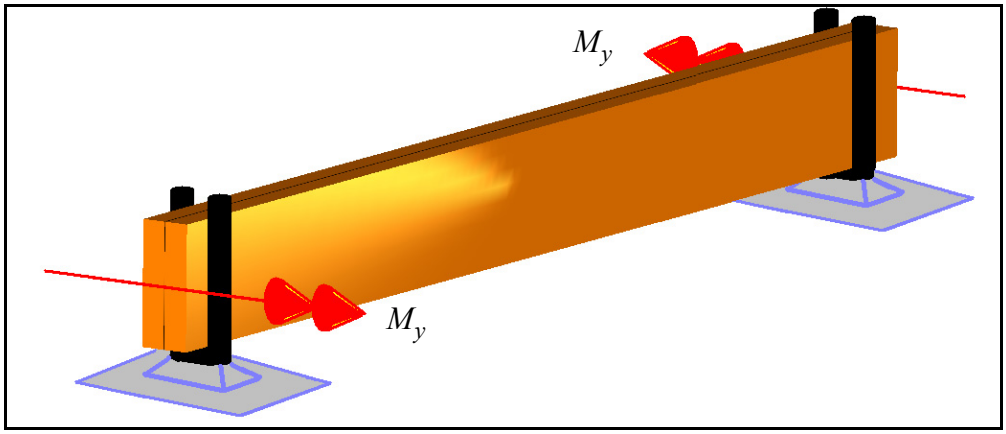

Figure 6.15 Simply supported beam subjected to constant bending moment

$$M_{v0} = \frac{\pi}{L}\sqrt{GI_t\, EI_z} \tag{6.10}$$

Hence, the critical moment depends strongly on the torsional stiffness of the beam. In a plate analysis, the stress/strain assumption in pure torsion is as shown in Figure 6.16a, yielding when integrated the moment of twist. This coincide with the assumption made in

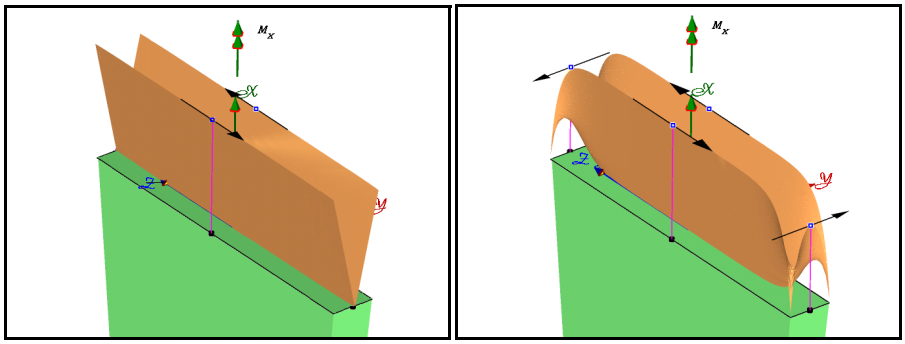

Figure 6.16 Stress distribution in torsionally loaded beam
a) as described by thin plate theory b) as obtained by solving the warping function

thin walled theory for cross sections [2]. It therefore seems reasonable to expect that Equation (6.10), with thin walled parameters, should yield the same result as a plate buckling analysis. A more accurate stress distribution, shown in Figure 6.16b, is obtained by CrossX [4] through a numerical solution of the warping function [2] as it occurs in St. Venant-theory (subsequently denoted “massive theory”). The resulting torsional stiffness obtained in these two cases will deviate as the width to height ratio increases. Based on

Equation (6.10) it seems reasonable to expect that scaling the plate buckling results by a modification factor

$$f_m = \sqrt{\frac{GI_t^m}{GI_t^t}} \tag{6.11}$$

should yield comparative results. Superscripts t and m indicate parameters found by thin walled and massive theory, respectively. Alternatively, for the purpose of comparing values only, the torsional rigidity of the beam model should be based on thin walled theory. This is a more general approach that does not rely on the simple form of Equation (6.10). The values obtained, however, will not be accurate if the effect of the torsional stiffness is significant.

6.6.2 Convergence and accuracy

Similarly to the case of flexural buckling, Eggen [10] performed lateral torsional buckling analyses in order to illustrate the performance of his element. Using this example, we can illustrate the difference between his element and the result of simply including the geometric terms of the element described by McGuire [25]. This is analogous to the inclusion of Pδ effects in the case of flexural buckling. The problem at hand is the lateral torsional buckling of a simply supported beam of height = 1 m, width = 200 mm and length = 10 m. The material properties are E = 6250 MPa and G = 390 MPa, and the loading is as shown in Figure 6.15.

Figure 6.17 tells a similar story to Figures 6.8 and 6.9, with the exception of the similarities in the elements of Eggen and McGuire. In this case, the element developed by Eggen is clearly the more accurate. Another difference is the improvement in performance of the COSP element relative to the C^1 elements. Because the angle of twist is interpolated by functions of the same order as the displacements, the accuracy of these elements is of the same order for torsional buckling as for flexural buckling. The C^1 elements has linear interpolants for the angle of twist, and the accuracy is degraded.

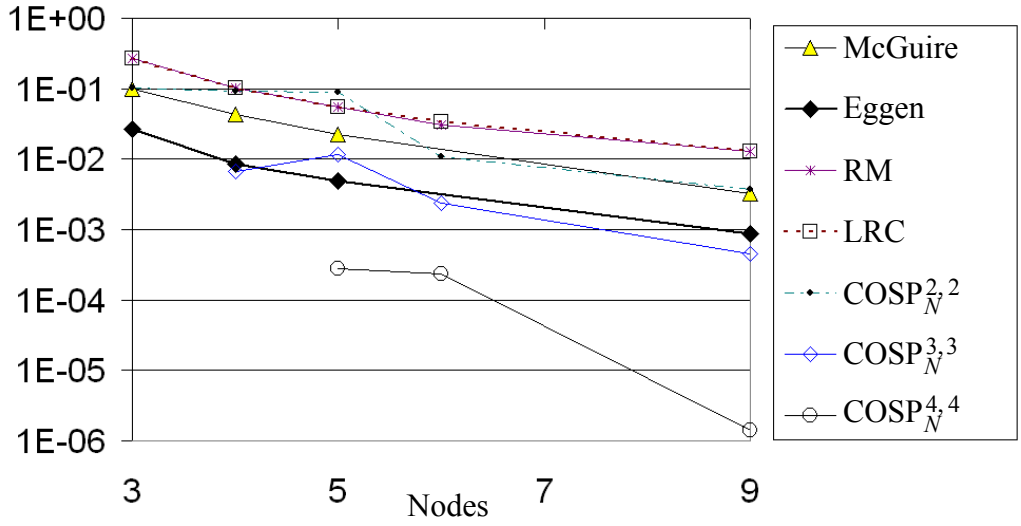

Figure 6.17 Relative error compared to Equation (6.10)

6.6.3 Effect of boundary conditions

If bending deformation, about the strong axis, preceding buckling is accounted for, a frequently quoted value for the critical moment is (Trahair [40]):

$$M_{\mathrm{v,\,def}} = \frac{\pi}{L}\frac{\sqrt{GI_t\,EI_z}}{\sqrt{1-EI_z/EI_y}\,\sqrt{1-GI_t/EI_y}} \tag{6.12}$$

When the beam was assumed to be undeformed up to the point of buckling, the boundary conditions did not pose a problem. When deformations are accounted for, however, the way boundary conditions are imposed is critical. When using the Euler angle parametrization, two fundamentally different ways of applying the load exists for this particular problem. The first alternative is to apply the load in such a way that all rotation axes remain orthogonal (e.g. let the beam axis follow $\mathbf{E}_1$, and apply the moment as a moment in the direction of $\mathbf{E}_3$ (M_z)). Alternatively, one can let two axes approach each other during deformation (e.g. let the beam axis follow $\mathbf{E}_1$ and apply the moment as a moment in the direction of $\mathbf{E}_2$ (M_y)). Similarly, the static boundary condition can either be imposed on a moving or a fixed axis. The numerical tests indicate that the solutions can be grouped into two categories depending on the value of some variable *a* and *b,* given by the following rule: *a* is assigned a positive value when the axis remain orthogonal, *b* is positive for fixed axis boundary conditions, *a* and/or *b* is negative otherwise. Investigation of the expres-

sions in the stiffness matrix verifies that the product of a and b can be used to categorize the problem into the following two alternative descriptions:

- Alternative 1:

  If $a \cdot b < 0$, the active part of the geometric stiffness is locally transformed according to Equation (3.45).

- Alternative 2:

  If $a \cdot b > 0$, the transformation in Equation (3.45) leave the active rows and columns of the stiffness matrix unchanged.

In Figure 6.18, the lateral torsional buckling moment versus width to height ratio is plotted for the different boundary conditions, scaled to the value given by Equation (6.11). The model used in these analyses is a 10.0 m long structural steel beam, with rectangular cross section of height 1.0 m and varying width. The beam solutions are based on 100 elements, while the FEMplate analysis is based on approximately 1300 shell elements. Each marker

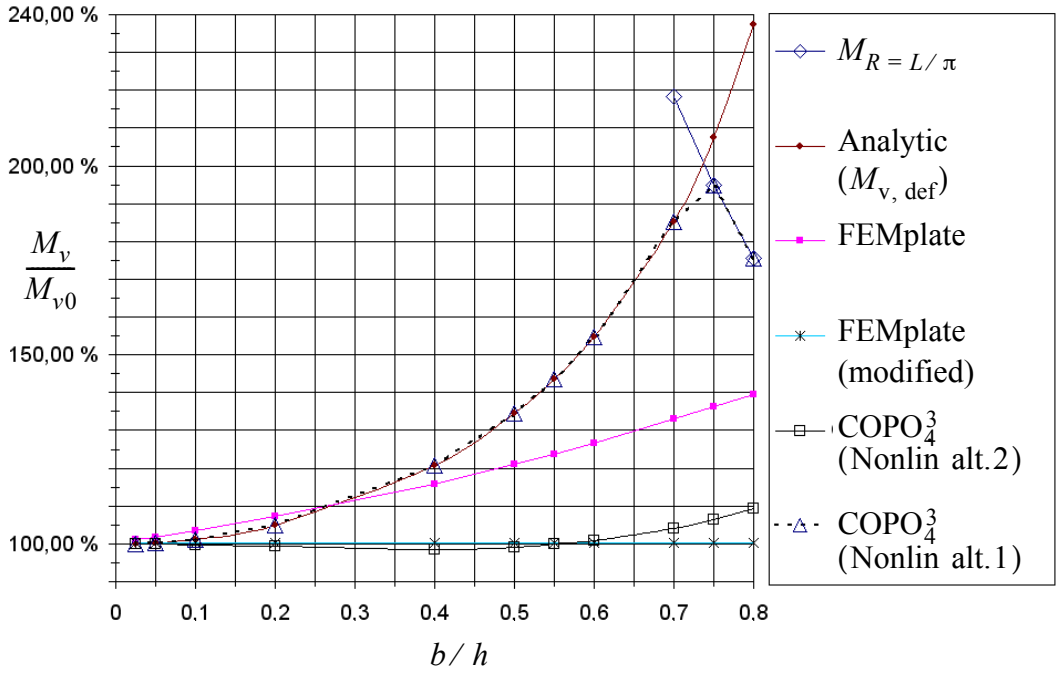

Figure 6.18 Lateral torsional buckling moment for simply supported beam

in the figure represents a value obtained from an analysis. To preserve clarity, the values obtained for linearized buckling analysis with beam elements are not included as they are

virtually coincident with the results obtained with the modified FEMplate model for all elements (using very fine meshes). Naturally, the linearized buckling analyses are not able to account for initial deformation, and the results are therefore comparable with Equation (6.11).

The nonlinear solutions split into two different solution according to the previously mentioned categories:

- Alternative 1 closely follows the solution of Equation (6.12) with a relative difference in the order of 10^{-4} %. In Figure 6.18, the result obtained for the Euler-Bernoulli element are not included as they are practically indistinguishable from the results obtained with COPO_4^3. The line $M_{R=L/\pi}$ is the value of the moment that bend the beam into a semicircle. When the critical moment exceed this value, the beam does not buckle, but rather the model becomes statically under determinate. This can bee seen by the 'kink' in the solution when using the boundary conditions of Alternative 1. To verify the correctness of the implementation, the Frobenius norm of both the symmetric and skew symmetric matrices at the point of singularity was monitored at b/h = 0.4. For the Euler-Bernoulli element the norm of the symmetric matrix was
  $\left\|\frac{1}{2}(\mathbf{K}+\mathbf{K}^{\mathsf{T}})\right\|_{\mathrm{F}} = 5.87 \cdot 10^{14}$, while the skew symmetric norm was
  $\left\|\frac{1}{2}(\mathbf{K}-\mathbf{K}^{\mathsf{T}})\right\|_{\mathrm{F}} = 8.58 \cdot 10^{-3}$.
  For the COPO_4^3 element the norms were of similar magnitude.
- Alternative 2 leads to a far softer behavior, with a difference compared to Alternative 1 of approximately 15% for b/h = 0.3. It should be noted that this is exactly the same solution that would be obtained if the rotations were parametrized with the pseudovector representation. Surprisingly, these results are quite similar to the linearized buckling analyses. In the range where lateral torsional buckling is of practical interest, the linearized buckling analyses yield only marginally stiffer values.

6.7 Conclusions and recommendations for further work

The results presented for the Cosserat rod formulation in combination with the B-spline interpolants are quite encouraging. Highly accurate and with fast convergence rates, these elements have capabilities far beyond the requirements of typical civil engineering structures. For an individual element, the use of B-splines represents a kind of "pseudo-discretization", resulting in a C^n two-field theory. It has been demonstrated that this may be less prone to shear locking than a C^0 formulation with equal number of *dof*'s, while avoiding unnatural "kinks" in the displaced shape, when full integration of the strain energy is used. However, one of the most interesting aspects of this formulation, namely the use of an isoparametric formulation to model complex shapes and varying cross sectional parameters, has not been pursued here. For problems where this is a necessary capability, it is believed that this formulation may become competitive with respect to both accuracy and efficiency, when compared to the use of many simple elements. Tests for efficiency have not been performed, partly due to the fact that these elements have not been "optimally" implemented with respect to efficiency. However, it is assumed that these elements are somewhat more costly, compared to the EICR with linear elements, for two reasons: They are based on a two-field theory, while the C^1 theory uses displacements only and this is in fact quite accurate. The additional accuracy is therefore "redundant", only adding to the cost of the element. Also, the need for numerical integration of some rather costly expressions will adversely contribute to the CPU cost. In order to get an accurate account, comparisons with other C^0 elements (e.g. RM with EICR) should be performed. The most significant drawback of the formulation, however, is the need for temporary storage of rotations and curvatures at the integration points. Although it has been shown that this may be replaced by a co-rotational measure of deformation, this comes with the added costs of extracting the deformational measures and possible decrease in the rate of convergence.

The capabilities of the EICR formulation with only internally linear elements are impressive. The principal advantage of the formulation is the "once off" implementation of the EICR framework. When this is done, a finite element program is easily extended to handle nonlinearity using only linear and well proven elements. Furthermore, elements based on small or moderate deformations, but nonlinear material models, can be used in geometri-

cally nonlinear analyses without modification. When the method is “customized” for a particular element geometry, the efficiency is also quite good. However, further improvement is possible by assuming that only very small deformations are present. A significant part of the computational cost of this formulation lies in the projection of the element stiffness matrix. In many practical situations, with small deformations at the element level, linear elements are sufficiently accurate. A significant decrease in CPU-costs can therefore be obtained by omitting this operation. This “optimized” version is even competitive compared to the simple UL element of McGuire et al. [25], while avoiding the need for storing the previously converged state. If high levels of accuracy are needed, though, internal nonlinearity must be accounted for if not very fine meshes are used. For most structural problems, where displacements and strains are small, this is particularly true in the prediction and detection of instabilities. Consistently developed elements, akin to that developed by Eggen in [10], are clearly the most stable and robust in this regard. A less computationally expensive option, though, is to use simple geometric terms such as those of the element of McGuire et al. in the stiffness matrix only. Although not shown here (except for the case of the LRC element), this will have a negative effect on convergence properties in a nonlinear analysis. However, if this effect is significant, one may have to reconsider the mesh size used, since internally linear elements may not be applicable for this mesh.

Cross sections in timber structures are often quite high, compared to the length, and the low modulus of shear makes even rectangular cross sections prone to shear deformations. However, the results show that shear is not of great importance in the evaluation of applicability of elements for most practical cases[1]. In spite of this, the C^1 element developed by Eggen should be extended to account for shear deformation. This is primarily due to the computational costs already involved in establishing the stiffness matrix and force vector of this element. The extension, by for instance a Timoshenko type shear assumption, is believed to only marginally increase the computational costs, while giving the element a higher degree of accuracy.

From a programming point of view, the EICR also have some additional positive aspects. The method is well suited for object oriented programming. If the general formulation is

1. Composite timber cross sections, however, are in use, and shear deformation may be important for even slender beams of this type.

implemented, the only specialization needed to include more element geometries is the implementation of a **G**-matrix[1]. Optimization for a particular geometry can be implemented at a later stage. Another useful property is that EICR can be used in combination with new, frame invariant elements as a "debugging device".

In this chapter, a number of elements have been compared in both nonlinear and linearized buckling analyses. In the case of nonlinear analyses, all elements are reasonably accurate. The poorest performance is that of the low order C^0 elements (in particular those with linear interpolation). A similar conclusion can be drawn from the linearized buckling analyses. However, this can in both cases be remedied by a modest increase in the number of elements. The best overall results are obtained with the high order Cosserat elements (polynomial order of 3 and higher). The computational costs are, however, significantly higher for these elements, compared to the 2-node elements. This is primarily due to the increase in the bandwidth of the stiffness matrix. The principal advantage of the Cosserat elements are that they are well balanced with respect to the most prevalent instability phenomenon in beam type analyses: flexural- and lateral torsional buckling. Of the other elements, the consistent element due to Eggen is the better choice with respect to accuracy compared to the simple EBT element with inconsistent geometric terms. In our view, the latter represents a minimum of what is required for the prediction of singularities. Since buckling may be local, using the EBT in conjunction with EICR only (no internal geometric terms), may require a very fine mesh for complex models. Provided individual members in the model are discretized by a sufficient number of elements, this element may still be used. In the examples that follow, which are concerned with problems having curved members, where many elements are needed to represent the initial geometry, this is the procedure adopted.

Finally, the use of rotational parametrizations in connection with boundary conditions should be commented. The results of Section 6.6 present strong arguments for the use of Euler angles when a single rotational degree of freedom at a node is constrained, and arguments in Chapter 3 to the same effect are even stronger. Any incremental-iterative finite

1. Note that elements with different configurations of "visible" nodes (nodes with *dofs* that affect continuity across elements) have different "geometrical properties" and must be handled independently.

element program should therefore treat boundary conditions of this type as Euler angles or another suitable parametrization.

Part II
Numerical studies

Chapter 7
Buckling of timber arches

Lateral buckling of beams is a problem that is well understood, and closed form solutions to numerous loading conditions exist. This is, however, not the case for buckling of arches, where analytical solutions focus primarily on arches in uniform compression. Not only is closed form solutions unavailable, but current codes of practice offer little help in assisting engineers in the treatment of stability of arches. The following section aims to shed some light on the subject of buckling of timber arches through numerical analyses. The results presented in this section are indicative (in a qualitative sense) of arch behavior. In order to draw conclusions for practical design, more results, for different geometries, loading and boundary conditions need to be considered. The results presented are therefore not immediately applicable to design, but hopefully able to spur the development of design guidelines, and design software.

Compared to other structural materials, timber structures are special in two respects: The material is highly orthotropic, and it is difficult to provide moment resisting joints and supports. In order to study orthotropy, the shell model discussed in Section 6.6 is used, while linear springs are used to simulate semi-rigid supports.

In all cases that follow, the loading condition is a negative vertical load, q, uniformly distributed per arch length (e.g. self weight). Note also that the bending stiffness EI_z is associated with out-of-plane bending (which is not necessarily the weak axis). The in-plane stiffness is denoted EI_y.

7.1 General behavior

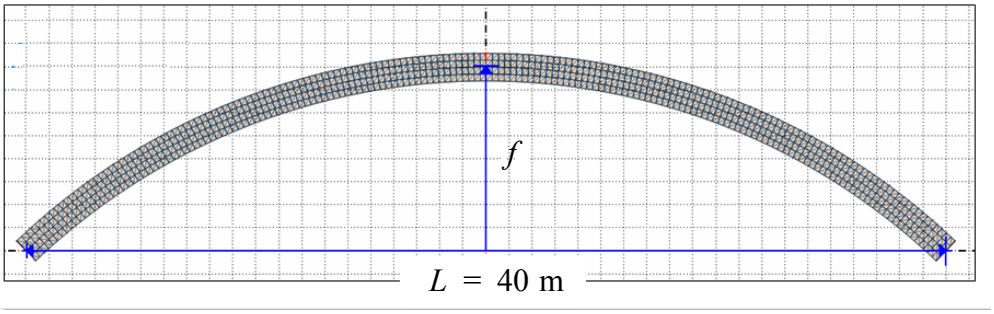

Figure 7.1 Shell element configuration of glulam arch

We consider a typical glulam[1] arch with a span of 40 m and a fairly deep rectangular cross section with $b \times h = 200 \times 1200$ mm as shown in Figure 7.1. The first analyses apply to a 2-hinge arch with no other out-of-plane support than that provided by the end supports. At these points the arch is free to rotate about an axis normal to the plane of the arch, but it cannot rotate about any axes in its own plane and displacements are prevented in all three directions. The only loading is the self weight of the beam. Material properties are assumed to be: $E_0 = 14500$ N/mm^2 (parallel to grain), $E_{90} = 960$ N/mm^2 (perpendicular to grain), $G = 830$ N/mm^2 and $q = 1.06$ kN/m ($\rho = 450$ kg/m^3). A series of plate buckling analyses, similar to those reported in Section 6.6, are carried out for different radius of curvature, parametrized by the ratio f/L, ranging from 0 (straight beam) to 0.5 (semicircle). A mesh as shown in Figure 7.1, with a total of 1344 triangular shell elements are used; each rectangle represents the position of two triangular elements.

For a straight beam, the lateral torsional buckling load, reported by Timoshenko and Gere [39], is given by:

$$q_{v0} = \frac{\gamma}{L^3}\sqrt{EI_z GI_t} \tag{7.1}$$

where γ is a scaling factor dependent on loading and boundary conditions. For uniformly distributed load applied at the center line and for simply supported end conditions with lateral constraints, the value $\gamma \cong 47.6$ corresponds well with the finite element solution. In

1. Short for glue laminated timber.

Figure 7.2, the buckling loads for both the shell and beam element analyses are plotted for various values of f/L. The results are scaled by the reference load $q_{v0} = 3.959\,q$. This is the buckling load of the straight beam obtained with the shell elements, or equivalently from Equation 7.1 when thin-walled cross section parameters are used. It should be noted that the load is distributed along the *arch length*, and the total load will thus increase with *f*.

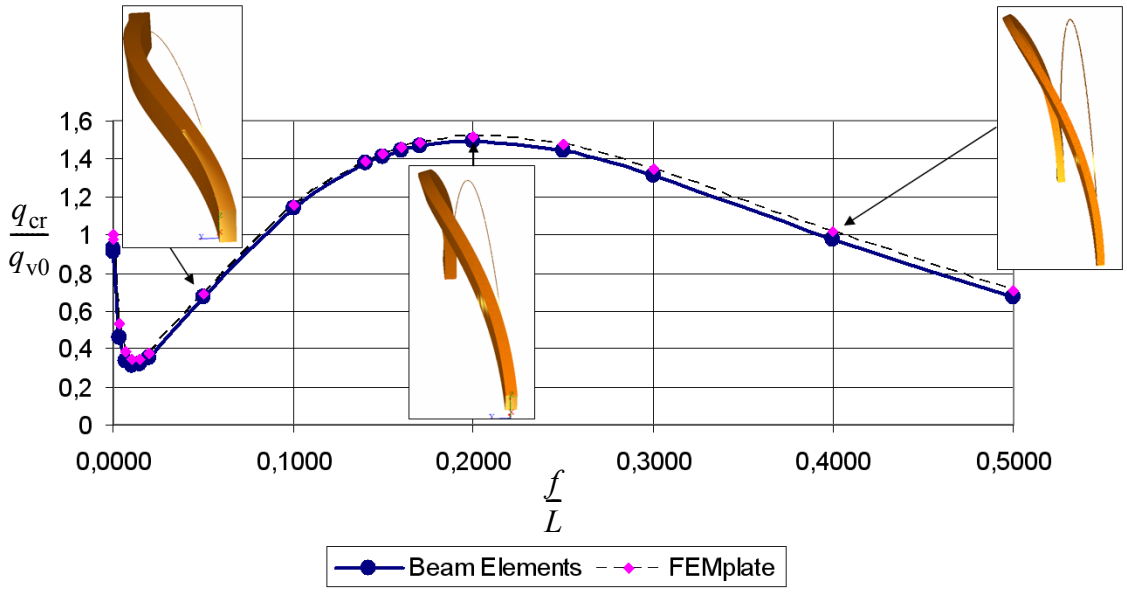

Figure 7.2 Lateral buckling load for a glulam arch with *b*×*h* = 200×1200 and *L* = 40m

Figure 7.2 illustrates a few key features of the problem. Firstly, the load carrying capacity diminishes rapidly for the low f/L ratios ($0 \le f/L \le 0.01$). In this range, the arch behave like a beam in compression due to the large axial forces induced by the shallow arch effect. In this range, the buckling analyses are somewhat suspect due to the underlying assumption of linear behavior. As is commonly known, shallow three-hinge arches normally display instabilities as a limit point connected with the snap-through phenomenon, not as a bifurcation point. Past this limit point, the arch regain stability due to what is sometimes referred to as a 'hammock-effect'. While the two hinge arch does not, in general, display a limit point, the stiffening effect due to the reversal of axial forces is present (see Section 6.6). If the arch is made into a 'negative' arch before buckling takes place, the predicted value may grossly underestimate the lateral buckling load. After this initial transitional phase, two noteworthy things start to happen: a) the axial forces become less dom-

inant, and b) the distribution of both axial forces and bending moments change. Up until $f/L \cong 0.03$, the drop in the axial force explains the change in the system. At this point, the arch is in a state of near uniform compression. The moment distribution is almost identical to that of a simply supported beam with uniformly distributed load. This leads to an increase in compressive stresses at the outer edge along the entire arch. With the decrease in compressive forces, the buckling mode becomes a combination of lateral torsional buckling and flexural buckling of the mid section. For $f/L \geq 0.03$, the principal effect is due to b) above. In Figure 7.3 the moment distribution for $f/L = 0.2$ is depicted. Note that the moment is drawn on the side having tensile stresses. When f/L increase, the points where $M_y = 0$ move towards the middle, and the compressive axial forces become more localized at the ends. Subsequently, the buckling mode becomes combined lateral torsional and flexural buckling.

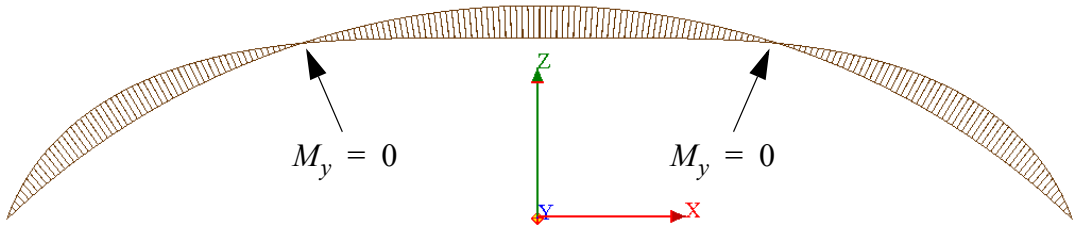

Figure 7.3 Moment distribution of a two-hinge circular arch (f / L = 0.2), subjected to self weight

7.2 Material properties

In the previous section, material properties akin to those of structural timber were used. Clearly these material properties are far from isotropic. In fact timber is one of the most severely orthotropic materials known to man[1]. Because of the one-dimensional discretization used in the beam element analyses, this property is only captured through the modulus of shear. By using shell elements, the additional effect of the cross grain modulus of elasticity (E_{90}) can be monitored. To this purpose, the analyses of Section 7.1 is replicated using three different values for E_{90}. The results, presented in Figure 7.4, clearly indicate

1. Strictly speaking, the material assumption used in the shell analysis is actually that of *plane isotropy*. The assumption of plane isotropy holds especially well for glulam members but is also applicable to structural timber. On account of this and common practice, no distinction will be made between plane isotropy and orthotropy.

that the effect is marginal at best. If we consider the "optimal" h/L ratio (= 0.2), the buckling load is about 6 times the weight of the beam, for the assumed material properties. What is the effect of orthotropic material properties on the buckling load? If we set E_{90}= E_0 the buckling load coefficient becomes 6.038, and if we set $E_{90} = E_0/14500 = 1$ N/mm^2, we find a buckling load coefficient of 6.006. The slight deviation between the results in Figure 7.2, obtained using beam elements and shell elements, respectively, must therefore be explained by other phenomenon.

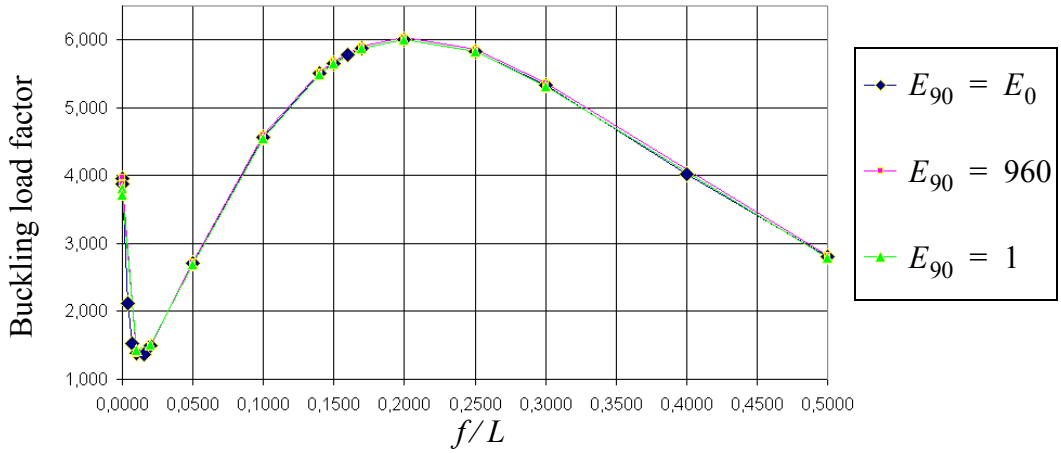

Figure 7.4 Effect of E_{90} on lateral buckling load, determined by shell elements

Another free parameter not present in isotropic materials is the modulus of shear. A second series of analyses were performed, using three different values for G. Two of these are strictly orthotropic (G = 850 MPa and G = 100 MPa) while one (G = 7250 MPa) can be interpreted as isotropic with $\nu = 0$. The shell elements used do not account for transverse shear (out-of-plane), and the results are assumed to be too stiff. This assumption is verified by the graph in Figure 7.5, where the results are compared to those obtained with beam elements. To exaggerate the problem, a fairly thick cross section is used ($b \times h$ = 600× 1200 mm).

For "normal" timber values of G (850 MPa), the results are quite similar for beam and shell analyses. The difference is slightly less than that observed for the straight beam. For the extreme value of G = 100 MPa, the difference become significant and actually exceeds the difference observed for the straight beam. The explanation for this is twofold; firstly, the effect of transverse shear is no longer negligible, and secondly, the torsional rigidity becomes more important. While the beam elements used are able to describe the effect of

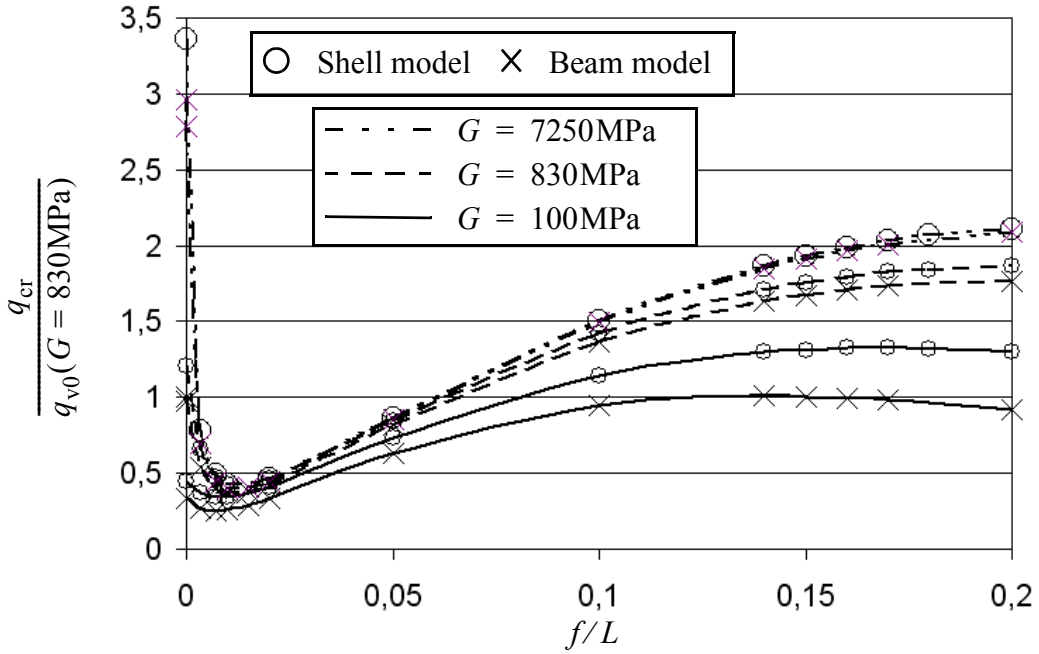

Figure 7.5 Effect of G on lateral buckling load (scaled to q_{v0} for G = 830 MPa)

transverse shear, the shell elements are not. However, using beam elements that does not account for transverse shear, produce buckling loads that is only a few percent higher. This indicates that the relationship between the buckling load and the torsional rigidity, GI_t, is not of the same form as for the lateral torsional buckling of beams. The dependence on GI_t also seems to vary with the ratio f/L. When the torsional rigidity decreases, the arch tends to twist, and the buckled shape starts to resemble that of f/L = 0.5 in Figure 7.2. This is shown in Figure 7.6, where the buckling modes for G = 830 MPa and G = 100 MPa are depicted for f/L = 0.15. When examining Figure 7.5, this also explains the shift in the 'optimal' ratio of f/L. For G = 830 MPa, this ratio was approximately 0.2, while it is approximately 0.13 for G = 100 MPa.

In structural timber, the value of E_0/G is approximately 16 for all strength classes. From a practical point of view, the ratio E_0/G can therefore be considered to be constant. Consequently, the graph in Figure 7.5, depicting the buckling load for G = 830 MPa is indicative of the behavior of this particular geometric configuration. It should be noted that E_0/G = 17.5 in this case, and the presented ratio q_{cr}/q_{v0} will therefore be a lower limit when using timber commonly produced in Norway.

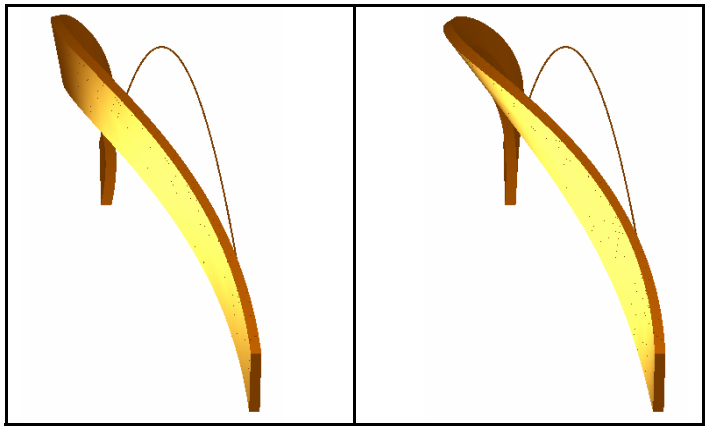

a) G = 830 MPa **b)** G = 100 MPa

Figure 7.6 Shear modulus effect on buckling mode for f / L = 0.15

For a complete picture of the effect of G, a solid model or a shell formulation that incorporates transverse shear should be used. Shear deformation of the cross section in its own plane is, however, assumed to be of less importance and is therefore not investigated. The presented results are therefore assumed to be adequate for the description of the problem. The principal result is that the beam elements are able to represent the material orthotropy, since the effect of E_0 is insignificant. Furthermore, the beam elements display softer (and more appropriate) behavior than the shell elements, particularly for high b / h ratios[1].

7.3 Effect of geometry

7.3.1 Width to height ratio

In the previous section, it was seen that the modulus of shear, G, has a noticeable effect on the buckling load. The principal reason for this is the change in the ratio GI_t / EI_z. Another way of changing GI_t / EI_z, that has practical importance, is to vary the width to height ratio. In Figure 7.7, results are presented for the arch configuration of Section 7.1, except that widths are now ranging from 12 to 1800 mm (height to width = 1/100 to 1½). In this plot, each series is scaled to q_{v0} (for a straight beam) evaluated for each individual width. This plot is actually quite similar to Figure 7.5, and the "optimal" ratio of f / L decreases

1. This is not surprising as the shell formulation relies on a thin-plate assumption.

slightly for decreasing values of GI_t / EI_z. Also, the relative value of q_{cr} versus q_{v0} increases for decreasing values of GI_t / EI_z. The principal difference, however, is the decrease in actual buckling load in Figure 7.5. The buckling loads of Figure 7.7 increase, both relative to the lateral torsional buckling load of the straight beam and in absolute value, for decreasing ratios of GI_t / EI_z. The latter can be observed in Figure 7.8, where the scaling factor $q_{v0}(b)$ is plotted against widths (b) ranging from 12 to 1200 mm. It should be emphasized that these values are strictly theoretical for the larger values of b / h.

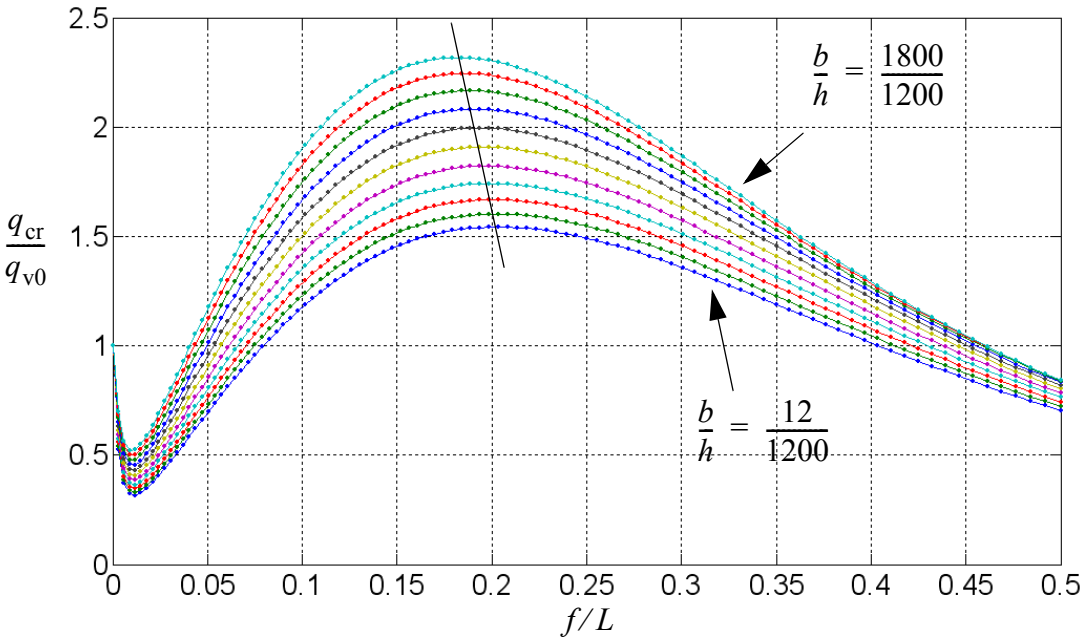

Figure 7.7 Lateral buckling load relative to lateral torsional buckling load for varying width of arch cross section (beam elements)

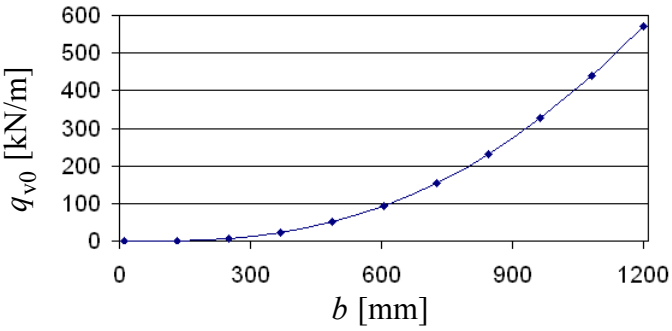

Figure 7.8 Lateral torsional buckling load for straight beam

The results in Figure 7.7 (and Figure 7.8) indicate that timber arches may have a significant potential for resisting lateral buckling, particularly for the massive cross sections which are typical for bridge arches. This can be demonstrated through the buckling of an arch of square cross section ($h \times b$ = 800×800 mm). The arch spans L = 40 m with a radius of 30 m ($f = 0.191L$). Loading and the boundary conditions are those of Section 7.1. If we consider both a 2- and a 3-hinge design, the three lowest buckling modes are presented in Table 7.1. For lateral buckling, the three-hinge design does not significantly alter the buckling load. For comparison, the second lateral buckling mode for the 3-hinge design (which is the fourth eigenmode) has a buckling load of 545.3 kN/m. This is only about 3% higher than the corresponding second lateral buckling load for the 2-hinge design.

Table 7.1 Buckling loads for a timber arch with f / L = 0.191 and $h \times b$ = 800×800 mm

	Mode 1 [kN/m]	Mode 2 [kN/m]	Mode 3 [kN/m]
2-hinge design	234.1 (lateral)	323.1 (in-plane)	531.7 (lateral)
3-hinge design	236.3 (lateral)	266.3 (in-plane)	319.1 (in-plane)

The two lowest lateral buckling modes are shown in Figure 7.9 for the 2-hinge design.

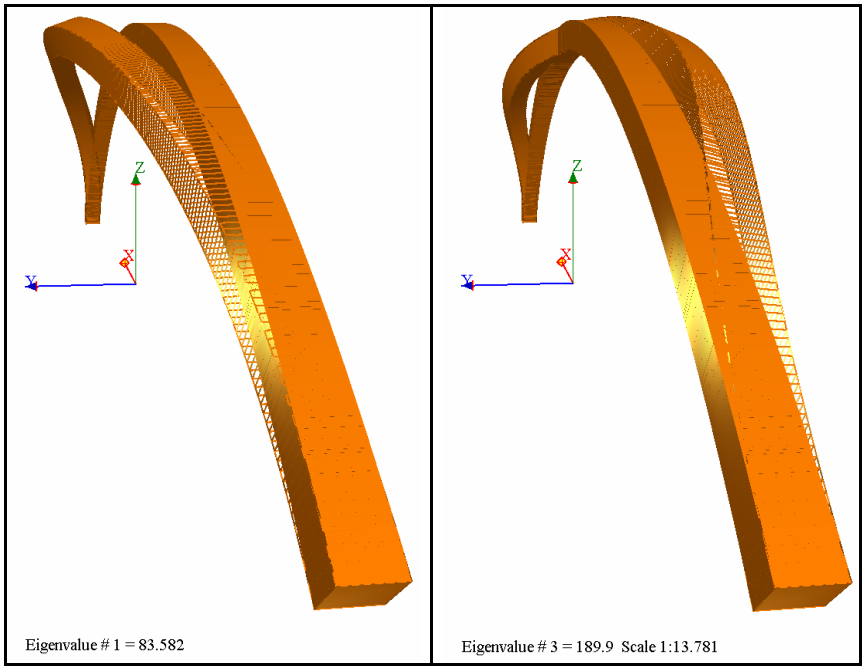

Figure 7.9 Lateral buckling modes for 2-hinge timber arch

The relationship between the lowest lateral buckling load versus the lowest in-plane buckling load for the 2-hinge design is investigated further in Figure 7.10. Here, the lateral buckling load is scaled by the lowest in-plane buckling load for different height to width ratios. The model characteristics used in this series of analyses are $h = 1.0$ m, $E_0 = 10062.5$ N/mm^2 and $G = 632.5$ N/mm^2. Loading and boundary conditions are still the same as in Section 7.1. The analyses are repeated for f/L-ratios ranging from 0.1 to 0.4. In all graphs, the thick line in the middle represents $f/L = 0.2$. In Figure 7.11, similar results for the 3-hinge design are presented. The difference in the plots are due to the combined effect of higher lateral buckling load and (primarily) lower in-plane buckling load for the 3-hinge compared to the 2-hinge design as shown in Figure 7.12.

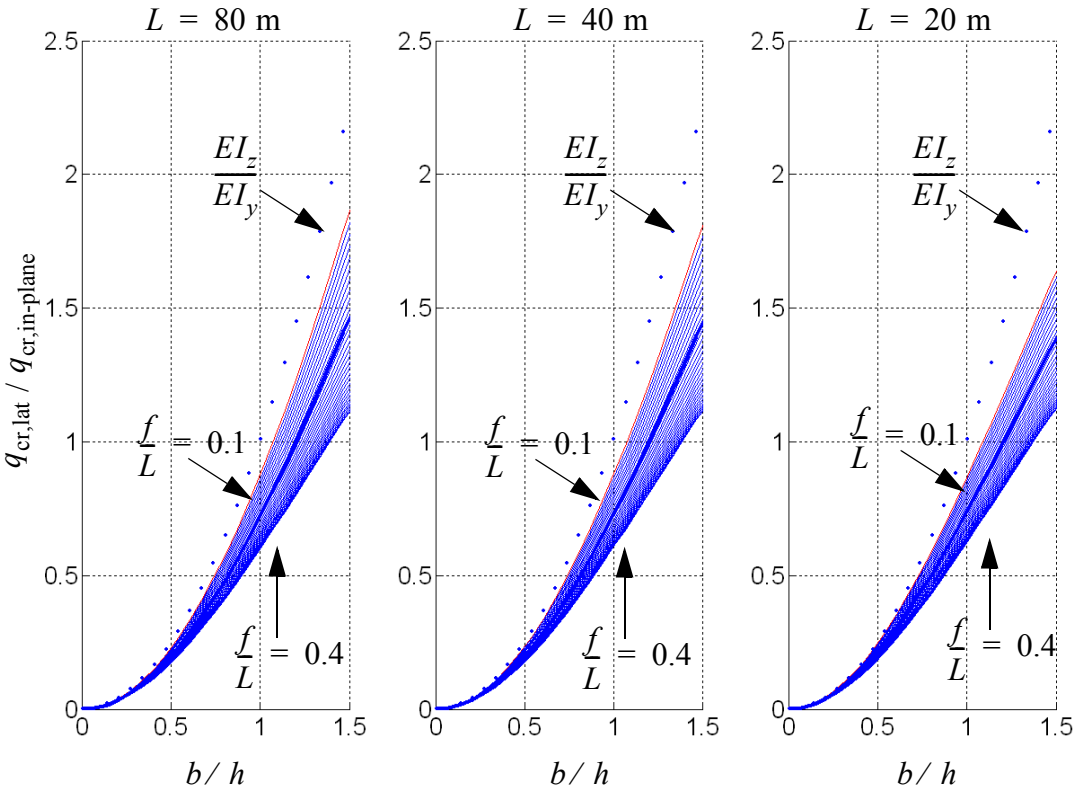

Figure 7.10 Lateral buckling load, relative to in-plane buckling (2-hinge)

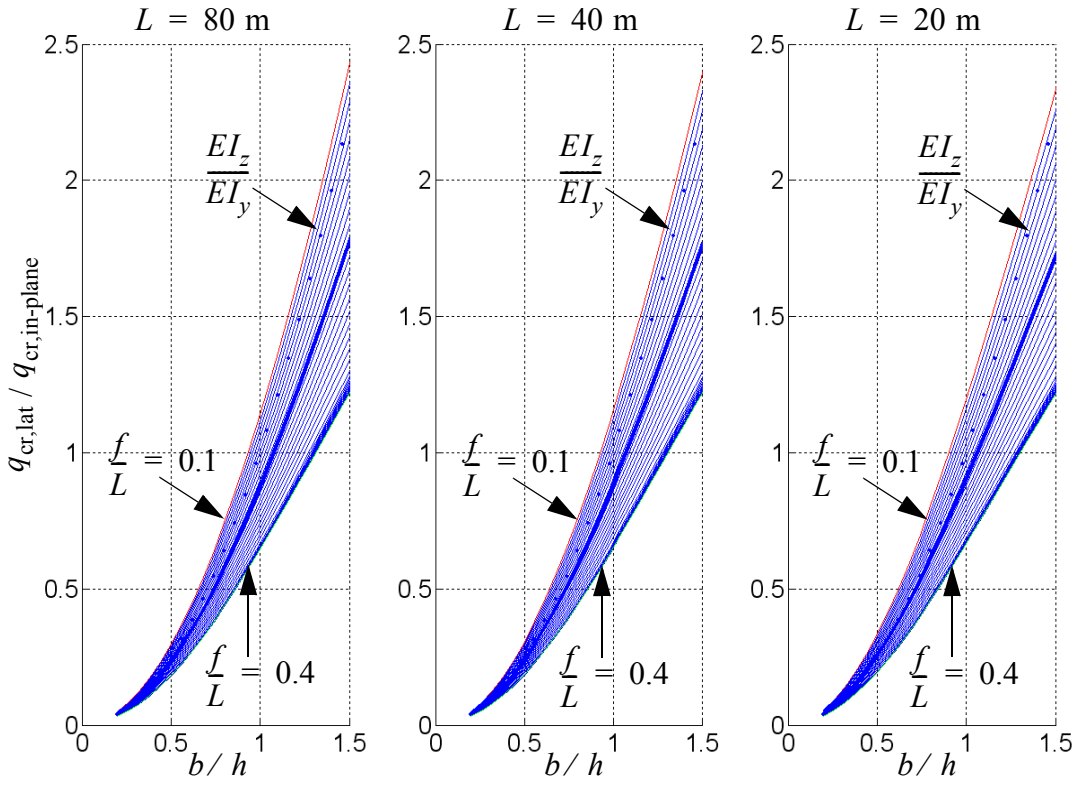

Figure 7.11 Lateral buckling load, relative to in-plane buckling (3-hinge)

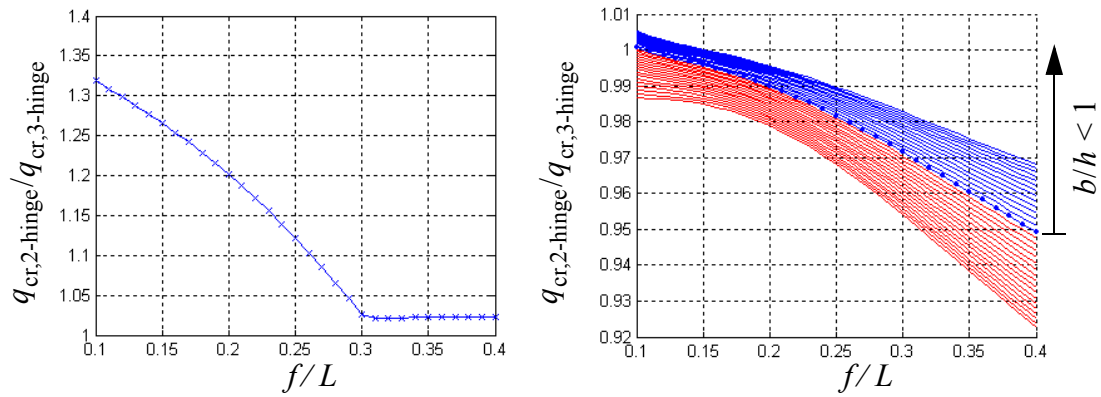

a) In-plane buckling b) Lateral buckling

Figure 7.12 Buckling loads for 2-hinge design relative to 3-hinge design (L = 40 m)

Obviously, a cross section with low width to height ratio will be significantly softer in lateral buckling than in in-plane buckling, primarily due to the difference in bending stiffness. It should be noted that for the assumed boundary conditions the out-of-plane buckling load equals the in-plane buckling load for a cross section with b in the range h to 1.35h, for all arch configurations. As seen in the figures, the span of the arch has some affect the ratio $q_{\text{cr, lat}} / q_{\text{cr, in-plane}}$. This is further investigated in the next section.

7.3.2 Effect of span length

Analyses in the previous section indicate that the lateral buckling load does not depend on length in the same manner as the in-plane buckling load. We see similar pictures in Figure 7.13, in which the lateral buckling loads of Figure 7.10 are scaled by the lateral buckling loads of a straight beam (q_{v0}) with the same b and h. It should be noted that Figure 7.13 shows similar curves as Figure 7.7 (but for a more narrow range of f / L), and we see that Figure 7.7 is somewhat dependent on L (notably at the low end of the range).

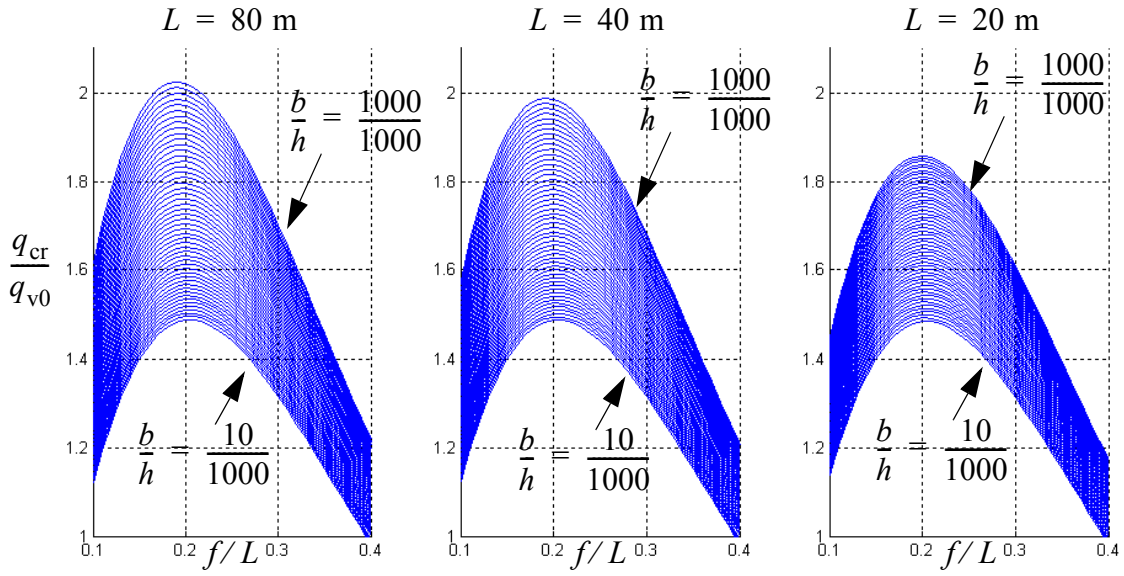

Figure 7.13 Lateral buckling load for varying *f/L* ratios

Figure 7.13 clearly indicate that q_{cr} / q_{vo} for arches with high GI_t / EI_z ratios are less sensitive to span length than those with low GI_t / EI_z ratios. For lateral torsional buckling of beams with uniformly distributed load, the critical load is a simple expression that is proportional with the cube of the length. A similar relation is given by Timoshenko and Gere [39] for an arch in uniform compression (simply supported laterally):

$$q_{cr} = \frac{EI_z}{R^3} \frac{(\pi^2 - \alpha^2)^2}{\alpha^2[\pi^2 + \alpha^2(EI_z / GI_t)]} \tag{7.2}$$

where α is the opening angle of the arch ($L = 2R\sin(\alpha/2)$). For buckling of arches with more general loading, the relation is not of this type, at least not for small values of L / h. Figure 7.14 is a compilation of 500 buckling analyses for varying lengths and 5 different

cross sections. In all cases, the ratio $f/L = 0.15$ and the material properties are $E_0 = 10062.5$ MPa and $G = 632.5$ MPa.

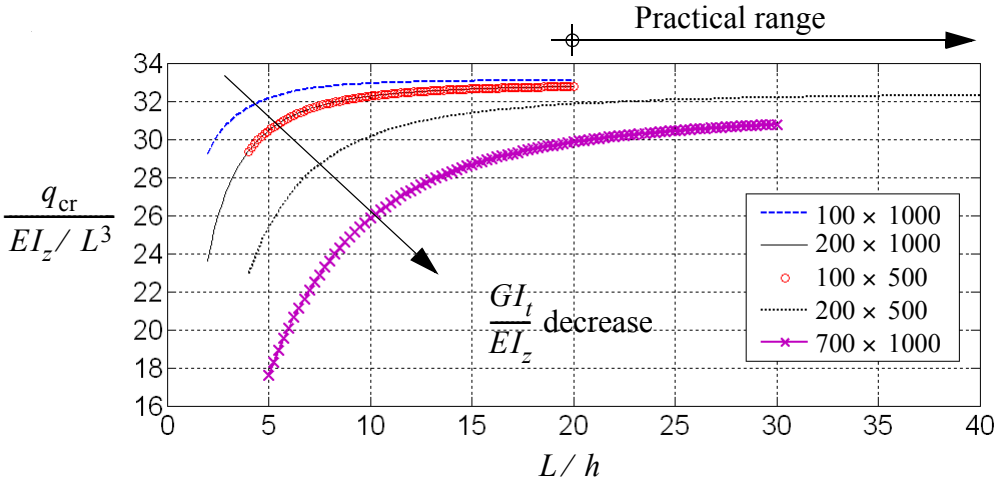

Figure 7.14 Lateral buckling load for *f*/*L* = 0.15

In the practical range, the ratio GI_t/EI_z has a moderate effect on the buckling load for the cross sections considered. Not surprisingly, the buckling of slender arches is primarily governed by the out of plane bending stiffness EI_z, while the torsional rigidity is the more limiting factor for massive arches. For comparison, the arch in Section 7.3 with $b = 250$ mm and $f/L = 0.152$, the ratio $(q_{cr}L^3)/EI_z$ is 32.73 and L/h is 33.33, which fits neatly in between the results for $b \times h = 100 \times 500$ and $b \times h = 200 \times 500$. This suggests that buckling of arches may be safely approximated by the use of 2D models if a reduction factor for EI_z similar to Equation (7.2), depending on both f/L and GI_t/EI_z, is introduced. However, as shown in Table 7.2 this is not the case for massive arches, where the curved part of Figure 7.14 will extend well into the practical range.

Table 7.2 The ratio $q_{cr}L^3/EI_z$ for different arches with $f/L = 0.15$

$b \times h$ [mm]	$L/h = 20$	$L/h = 33.33$	$L/h = 66.67$	$L/h = 100$
250×1200	32.59	32.73	32.79	32.80
1800×1200	22.30	25.55	27.25	27.59

In all cases presented here, the ratio GI_t/EI_z is strictly a function of the cross section width. If the cross section is not of rectangular shape and for mechanically joined cross sections with only partial bonding, significantly lower values of GI_t/EI_z are to be expected.

7.4 Effect of boundary conditions

In the previous analyses, the arch was assumed to be fully restrained with respect to out-of-plane rotations. For timber structures, this is difficult to achieve. On this note, the following section is dedicated to the study of boundary conditions.

The first case study is a fairly massive arch of dimensions $L = 40$ m, $b \times h = 700 \times 1000$ and $f / L = 0.15$. The arch is analyzed for three different boundary conditions for the rotational *dof's* in the arch plane (θ_x and θ_z):

a) Both *dof's* are supported by linear rotational springs

b) θ_x is fixed and θ_z is supported by a linear rotational spring

c) θ_z is fixed and θ_x is supported by a linear rotational spring.

In Figure 7.15 the buckling load, scaled to the buckling load obtained with both θ_x and θ_z fixed, is plotted versus the spring stiffnesses k_θ. The graph on the right is the same as the first part of the one on the left (the scale of k_θ is reduced by a factor of 10).

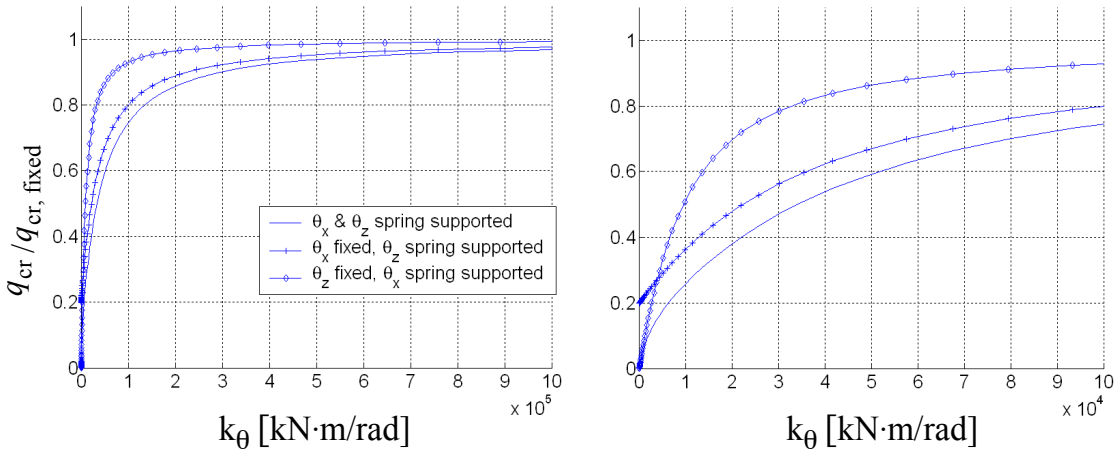

Figure 7.15 q_{cr} vs. spring stiffness (global supports) ($f / L = 0.15$)

As expected, all curves approach asymptotically the buckling value obtained for fixed θ_x and θ_z at the ends ($q_{cr,fixed}$). If θ_z is free (unconstrained) and θ_x is supported by a rotational spring, a similar asymptotic convergence is observed. The converged value is the same as the starting value of $0.202 \cdot q_{cr,fixed}$ obtained for case b. In order to relate the value

of the spring stiffness to a physical quantity of the arch, it may be mentioned that the bending stiffness about weak axis is $EI_z/1\text{m} = 2.88\times10^5$ kN·m/rad.

The results of Figure 7.15 apply to boundary conditions enforced in global axes. In many applications it is more appropriate to use boundary conditions in a radial-tangential coordinate frame (*t, y, r*). For the configuration considered ($f/L = 0.15$), the tangent to the curve at the end points intersect the horizontal line at an angle of ±33.40º. The graphs in Figure 7.16 shows the results using springs oriented along these axes. In addition to the three sets of boundary conditions described previously, the arch is also analyzed when two of the rotational *dof's* are completely free.

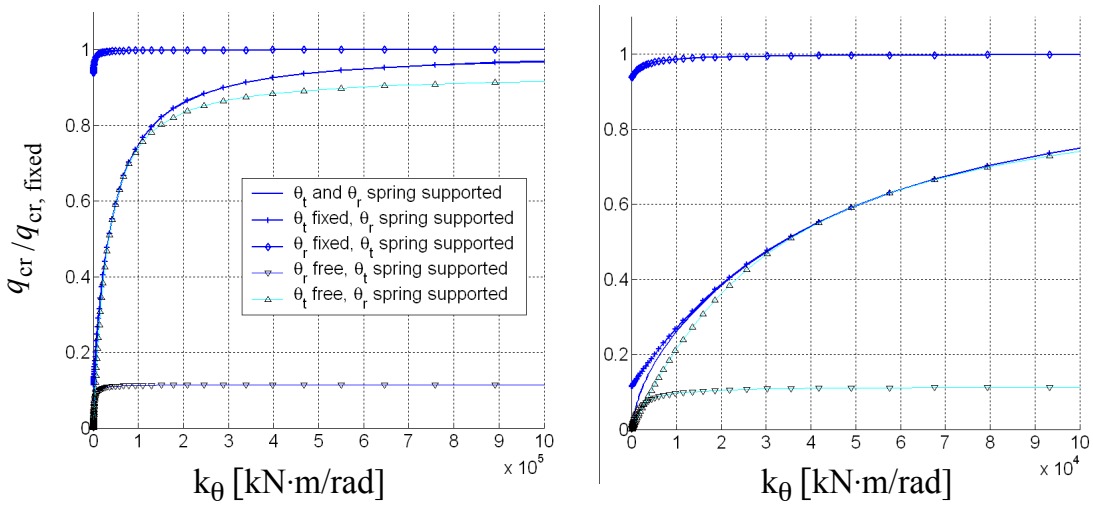

Figure 7.16 $q_{cr}/q_{cr,fixed}$ vs. spring stiffness (local supports)

The most notable feature of Figure 7.16 is the effect of restraining θ_r. With $\theta_r = 0$ and θ_t completely free, the buckling load is in fact 93.6% of $q_{cr,fixed}$. A similar plate buckling analysis with FEMplate (using 6400 triangular elements) yielded 98.4% of $q_{cr,fixed}$, a difference of approximately 5%. Again, this deviation is explained by the difference in torsional rigidity in the two models and not by effects due to orthotropy. This claim is substantiated by the effect of restraining the arch from twisting at the end points. The critical load obtained with the beam model was 11.4% of $q_{cr,fixed}$ when θ_r is free and θ_t is fixed. In comparison, the result obtained with FEMplate was 14.0% of $q_{cr,fixed}$, a relative difference of approximately 20%.

For arches with slender cross sections (small b / h ratios), restraining the radial rotation at the ends will not be sufficient, and other methods of stiffening the structure is required. In the following, a short study of the effects of supporting the arch with lateral springs (emulating transverse bracing) is presented. For this purpose, an arch of length 40 m and $b \times h$ = 200×1200 mm is chosen, the radius of the arch is R = 30 m leading to a near optimal ratio of f/L = 0,191. The material properties are E_0 = 14500 N/mm^2, E_{90} = 960 N/mm^2, G = 830 N/mm^2 and ν = 0.37, and the load density is γ = 4.4 kN/m^3. We first use a single lateral spring, positioned at mid span at three different heights; at the upper edge, at mid height and at the lower edge. The results from these analyses are summarized in Figure 7.17 for varying spring stiffness. All configurations result in a bilinear curve for the buck-

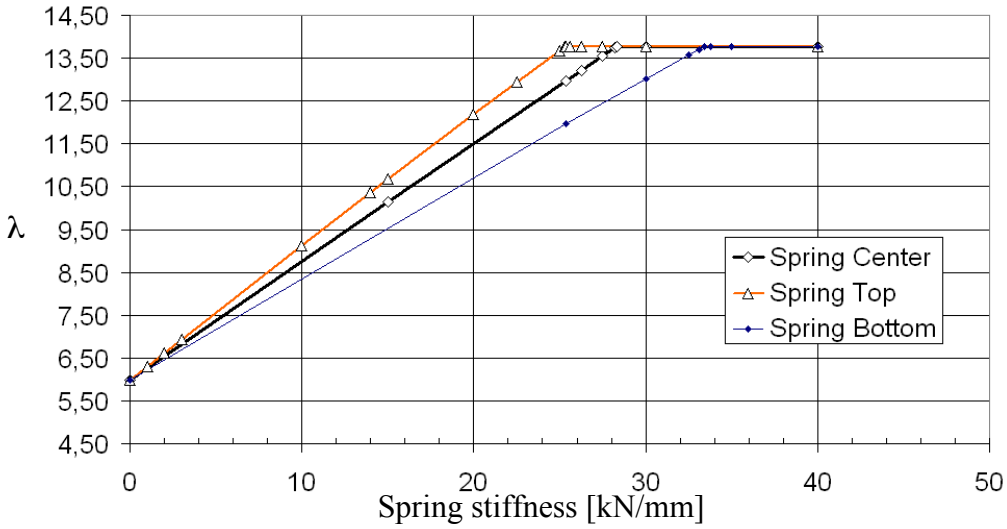

Figure 7.17 Buckling load coefficient with lateral spring at mid span

ling factor. The buckling loads increase linearly until the arch is forced into mode 2, which has a buckling load coefficient of 13.77. This compares to the buckling load coefficient of 5.91 for mode 1. Beyond this point, the spring acts as a rigid support and no further increase in buckling load is observed. This is attained for spring stiffnesses of 25.35, 28.35 and 33.45 kN/mm, respectively. When the spring is positioned at the bottom fibers, the stiffness required to force the arch into the second buckling mode is about 30% higher than for a spring placed at the top fibers. For an indication of the physical interpretation of the spring stiffness, consider a 5 m long transversal bracing member with a cross section

of 98×98 mm. This member has an axial stiffness of about 23kN/mm (for E_0 = 12000 N/mm^2).

The simple bilinear relationship of Figure 7.17 is not to be expected for other spring configurations. To illustrate this point, two different configurations of three linear lateral springs, positioned at the cross section centroid, are investigated. In the first case, the springs are placed at the inflection points of the 4th buckling mode, while in the second case, the springs are placed at the quarter points along the length of the arch. The rationale behind this positioning is illustrated in Figure 7.18. Since the inflection points of mode 3 are so closely spaced, the effect of reinforcing them with springs, would only marginally differ from using a single spring at mid span. The results from these analyses are shown in

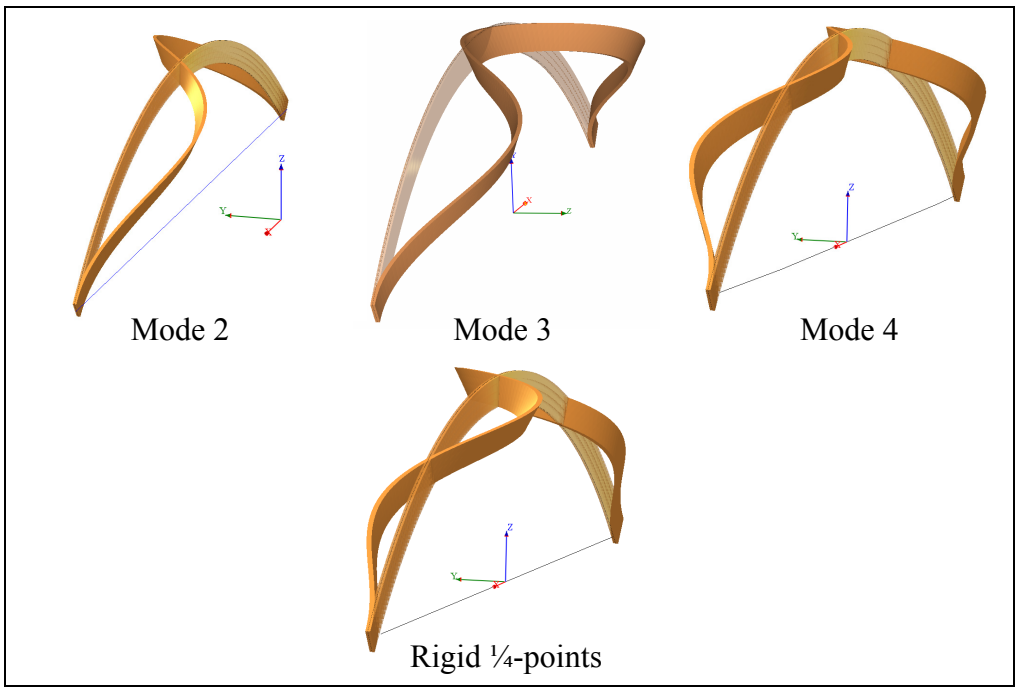

Figure 7.18 Various buckling modes for slender arch

Figure 7.19, and clearly a more complex picture is now drawn. Although both configurations results in an increase in the buckling load, very stiff springs are required to produce the buckling modes corresponding to laterally fixed conditions.

In summing up, we see that even moderately stiff lateral bracing will increase the buckling load considerably, regardless of where the bracing is applied over the cross section depth.

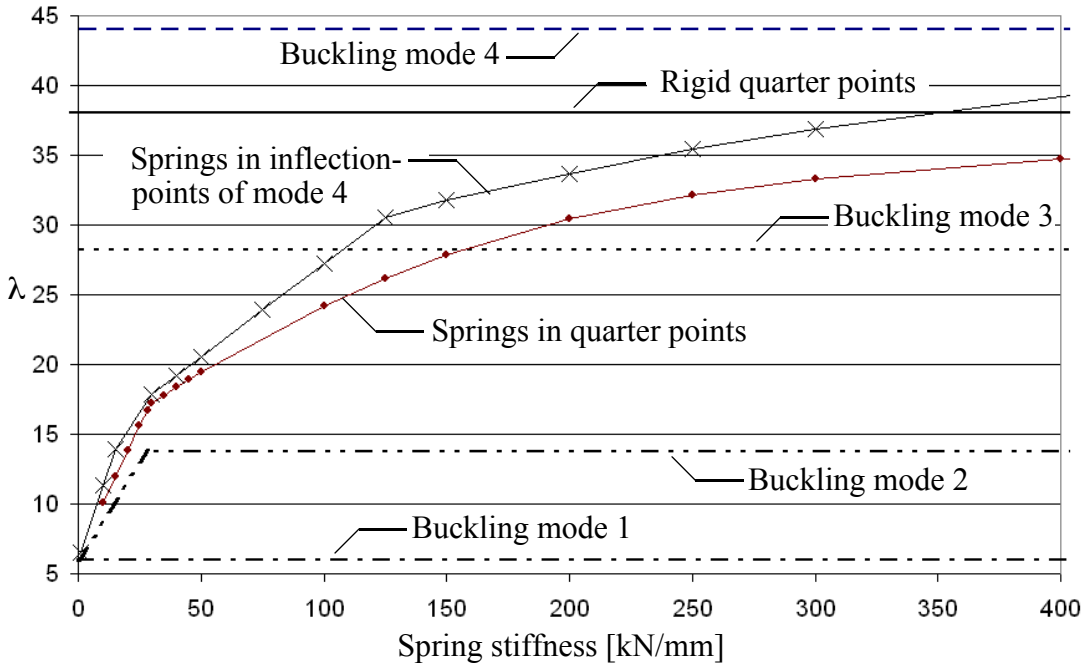

Figure 7.19 Buckling load coefficient for various lateral spring configurations

For the loading considered here, the bracing is clearly more effective when applied at the top fibers, but for practical purposes there is not much in it. The results (Figure 7.19) also suggest that the bracing is more effective if concentrated at the upper part of the arch, rather than distributed evenly along the arch.

7.5 Concluding remarks

The analyses of this chapter are limited with respect to both geometry and particularly loading, and conclusive statements cannot therefore be made. However, the results suggest the following tentative statements:

1) The computational model of timber arches need not consider the highly orthotropic nature of structural timber. The modulus of shear (G) is, however, an important parameter.

2) The 'optimal' height to span ratio (f / L) for 2- and 3-hinge arches, with respect to sideways stability, seems to be about 0.2.

3) Massive arches (with cross sections of nearly square shape) have a surprisingly good sideway stability, providing rotation about axes in the plane of the arch can be prevented at the supports.

Denoting the tangential and radial axes in the plane of the arch at the end supports with *t* and *r*, respectively, it is particularly important to control the rotation about the *r* axis.

4) For slender arches (with cross sections having low *b* / *h* ratio), transverse bracing will improve sideway stability dramatically. Even a moderately stiff, single bracing at the top of the arch will have a significant effect, regardless of where it is applied over the depth. If bracing is applied at several points along the arch, a concentration at the upper part of the arch improves their effectiveness.

Chapter 8
Design of real-world structures

At the outset of this study, the ambition was to provide some useful insight into the use of advanced, state-of-the-art, nonlinear 3D analysis as a basis for practical design of advanced timber structures. For reasons explained in the introduction, this ambition had to yield to other issues. Nevertheless, we include two case studies which indicate some of the challenges in practical design. Both examples are concerned with timber bridges.

8.1 Key features of a typical code based design

In order to set the scene, we first present a very brief description of a typical code based design in the ultimate limit state. Our example is the latest version of Eurocode 5 [12], which qualify as a "state-of-the-art" code of practice in this area. The description is not intended to be "in-depth", but rather to introduce some key features as well as indicate some problem areas.

The code suggests a design procedure in which the structural response to the ultimate load is determined by a linear (1st order) analysis. In order to account for nonlinear (2nd order) effects, the linear response is "corrected" by various (*k*-) factors. As an example, consider design of a beam-column (combined bending and compression) by Eurocode 5 [12]. This is acheived by the satisfaction of the following two requirements (stated in *Section 6.3.2* of the code):

$$\frac{\sigma_{c,0,d}}{k_{c,y} f_{c,0,d}} + \frac{\sigma_{m,y,d}}{f_{m,y,d}} + k_m \frac{\sigma_{m,z,d}}{f_{m,z,d}} \le 1 \tag{7.3}$$

$$\frac{\sigma_{c,0,d}}{k_{c,z} f_{c,0,d}} + k_m \frac{\sigma_{m,y,d}}{f_{m,y,d}} + \frac{\sigma_{m,z,d}}{f_{m,z,d}} \le 1 \tag{7.4}$$

σ denotes computed (1st order) stresses and f denotes corresponding material strength. Indices c and m denote compression and bending, respectively, 0 indicates the grain direction and d designate design stresses/strengths (as opposed to characteristic quantities). The k_m factor is of little consern for this current discussion (it has to do with the statistical distribution of material defects). The factors of interest for our discussion are $k_{c,y}$ and $k_{c,z}$, both of which depend in some rather obscure way on slenderness ratios (which in turn depend on buckling lengths), geometrical imperfections (shape errors), and to some (minor) extent on material properties. $k_{c,y}$ and $k_{c,z}$ account for all nonlinear effects. For simple structural members they can be determined in a fairly straightforward manner, but for more complex structures they represents a real hazzle that most design engineers would like to get rid of.

Another example is beams subjected to either bending or combined bending and compression. Here Eurocode 5 (in *Section 6.3.3*) states that two requirements need to be met, one of which applies to beams subjected to bending (about the strong axis) only:

$$\sigma_{m,d} \le k_{crit} f_{m,d} \tag{7.5}$$

and the other to a beam subjected to both bending (about the strong axis) and axial compression:

$$\left(\frac{\sigma_{m,d}}{k_{crit} f_{m,d}}\right)^2 + \frac{\sigma_{c,d}}{k_{c,x} f_{c,0,d}} \le 1 \tag{8.1}$$

In these two requirements, k_{crit} is a factor which takes into account the reduced bending strength ($f_{m,d}$) due to lateral buckling. Although the code does provide some guidelines for its determination, k_{crit} is a difficult quantity at the best of times, and very often it is quite unlikely that independent efforts would end up with the same values for a given (slightly complex) case. As a result one is often forced to make conservative assumptions. It should also be mentioned that all four requirements quoted do imbed some fairly crude (stress based) failure criteria.

In the above design requirements all nonlinear effects are disregarded in the static analysis of the structural assembly, and then accounted for, in an approximate manner, in the strength verification of the individual members. While Eurocode 5 does not encourage nonlinear analysis (or 2nd order analysis which is the term used by the code) as basis for

design, it does not exclude it. However, if used it must include the effects of "induced deflection" (geometrical imperfections or shape errors). In order to take fully advantage of the potential capabilities of current nonlinear finite element analysis tools, procedures must be developed to automatically or semi-automatically include these effects, and thus making the rather cumbersome *k*-factors superfluous. For simple struts and beams, this is easily solved by superimposing for instance the lowest buckling mode as the initial shape imperfection, scaled to within a specified tolerance. The gometrically modified problem is then solved by nonlinear static analysis. In the case of plane frames and arches, guidelines are given in *Section 5.4.4* of the code along with an example of assumed initial deviations in geometry for two simple cases reproduced in Figure 8.1. Since the most difficult (and often critical) issues related to structural instabilities are associated with out-of-plane buckling (e.g. lateral torsional buckling), 3D models are essential. Hence, Figure 8.1 needs to be extended to three dimensions. Currently, the following four options are readily available for implementation.

1. Direct modeling of imperfections for individual members (and/or full assembly).
2. Imperfections based on deformed shape, obtained by applying a perturbation load.
3. Imperfections based on one or more buckling modes.
4. Combination of 1, 2 and 3.

All of these methods rely on some user input and sound engineering judgement to assure reasonable estimates. The finite element program developed in connection with this work accomodates the first three methods. Due to the time constraints, testing has not been extensive and cannot support strong conclusions. However, the case study in the next section is hopefully able to illustrate some of the issues that need to be addressed in more detail.

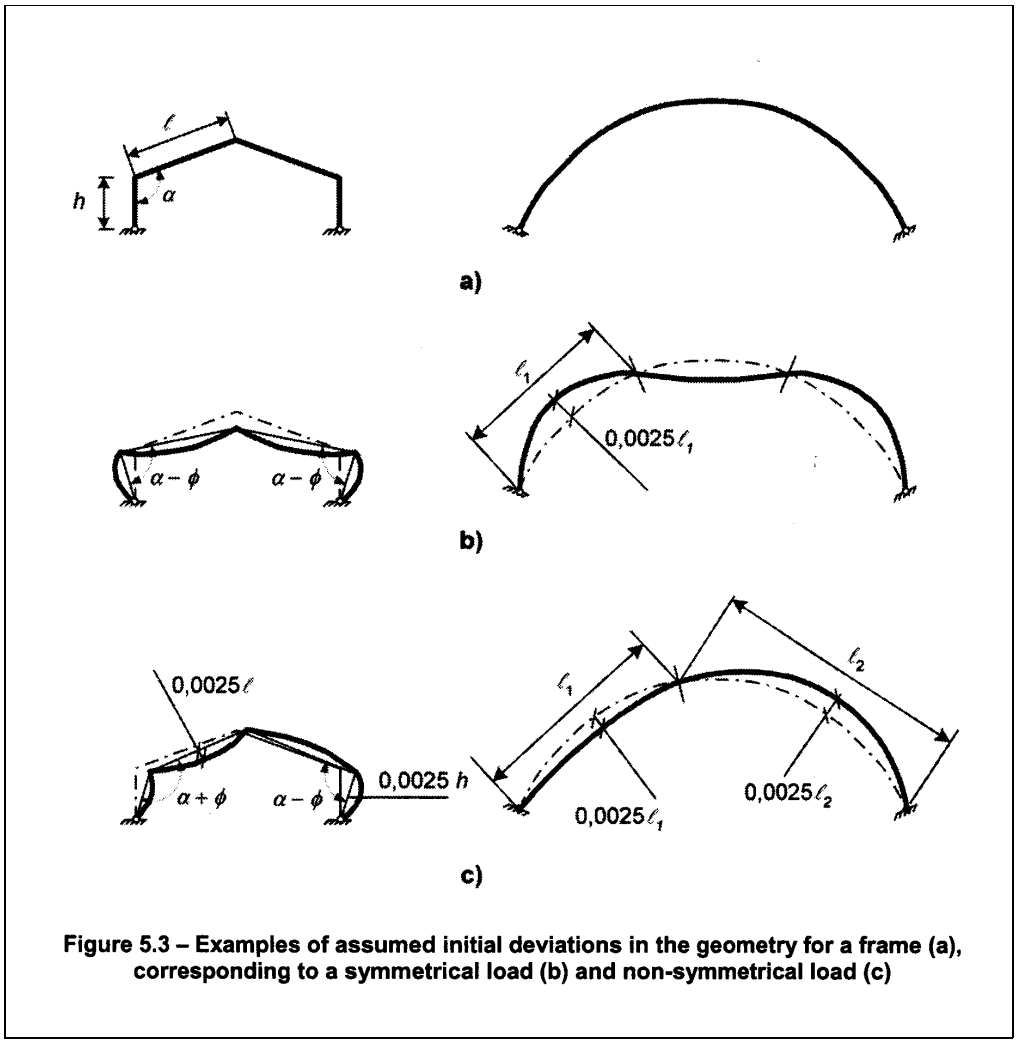

Figure 5.3 – Examples of assumed initial deviations in the geometry for a frame (a), corresponding to a symmetrical load (b) and non-symmetrical load (c)

Figure 8.1 Reprint of Figure 5.3 of Eurocode 5 EN 1995-1-1:2004 (E)

8.2 Mechanically joined network arch bridge

The design of timber structures has traditionally been based on plane models, which is also reflected in many of the guidelines in the current European codes of practice. These plane models require that the load carrying capacity of a structure can be adequately represented in isolated planes. This will inevitably introduce assumptions which, based on engineering judgement,and in view of the uncertainties should result in conservative estimates with respect to capacity. In many cases the degree of conservativeness is difficult to judge. Although 3D models will eliminate many of these assumptions, other modelling challenges arise. Particularly for beam type analyses, some of these challenges, which are by no means trivial, require good graphical representation for visual control. Some of the modeling challenges that arise when using a versatile 3D analysis tool in the design of timber structures are illustrated by the two case studies presented in this and the following section.

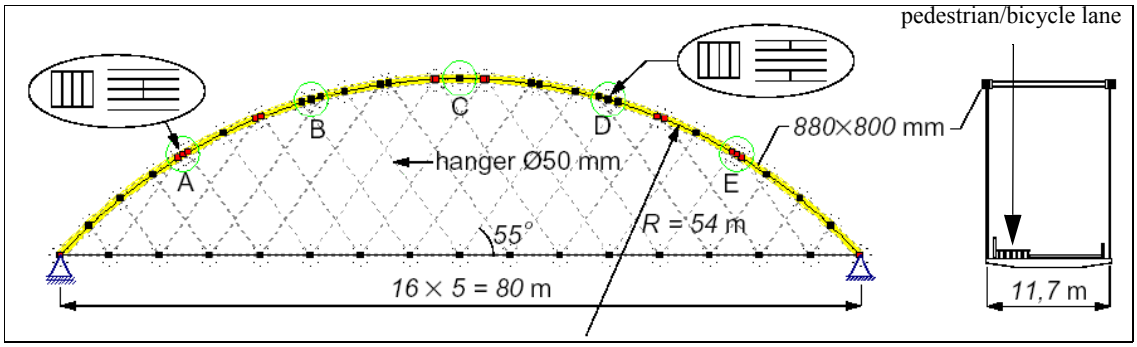

Figure 8.2 Network arch bridge (plane view)

Figure 8.2 shows a plane view of a network arch bridge for which a feasibility study has been carried out. Analyses performed by Bell et. al. with plane models in [5], indicated that if the overall stability of the system can be demonstrated, the design may be a viable one. The bridge adopts the deck solution used at the newly built timber bridge at Tynset [3] (which has two truss arches and vertical hangers). A 7 m wide stress laminated timber deck with asphalt constitute the two road traffic lanes. The bridge also has a 3 m wide pedestrian/bicycle lane. The deck rests on steel cross beams which are here spaced at an equal distance of 5 m (slightly shorter than at Tynset). Each cross beam is supported by two inclined steel hangers at each end. The two parallel arches are modified 2-hinge arches, each made up of four 220×800 mm glulam arches mechanically joined at five

points, A, B, C, D and E, in such a way that the two inner arches are joined at A, C and E, while the two outer arches are joined at B and D. The longest part of an arch is thus about 30 m, and its total height is under 3 m. Production and transportation should therefore not present any problems. Between the individual arches are placed 8 mm steel plates, on to which the hangers are fastened. The steel plates are fastened to the glulam arches by a system of bolts and shear plates (see Figure 8.4)..Figure 8.3 shows a 3D model of the entire bridge. It contains about 3500 beam elements and 60 bar elements, and a total of about 20000 degrees of freedom. With reference to Figure 8.2 each arch in Figure 8.3 is modelled as four individual arches next to each other. All 4 "sub-arches" (lamellas) are forced to have the same displacements (including rotations) at every point where a hanger is fastened to the arch. Between these points, however, they are completely unconnected. At points A, B, C, D and E the two joined sub-arches are connected by "hinges" that cannot transmit moments about any axes. The hanger force is assumed to be equally distributed between the 4 sub-arches. The hangers can only take tension. Hence, a hanger that for a given load condition, will be in compression, is removed from the model. Each cross beam is modelled with its appropriate stiffness, and the deck is modelled by four longitudinal (timber) beams, rigidly connected to the cross beams. Two of the longitudinal beams, each with a fictitious cross section of 1000×250 mm, are placed in connection with the fastening of the hangers to the cross beams, and the other two beams, with cross section 2000×250 mm, are placed such as to be in the correct position for traffic loading in each lane, assuming the loads to be as far over to the most loaded arch as possible. Each of the 4 longitudinal beams is rigidly connected to all cross beams. The deck model is clearly an approximate one, but it is believed to represent the deck stiffness with adequate accuracy, particularly with respect to the load distribution. Details of the load distribution and material properties are presented in Appendix I.

The horizontal thrust from the arches are taken by the end supports, at which the only degree of freedom that is not fully constrained is the rotation about an axis normal to the arch plane, which is unconstrained. This is perhaps optimistic, particularly for the two in-plane rotations. Two load conditions are considered: The dead or self load of the entire system, and the self load in combination with traffic load, both distributed and concentrated, at the middle of the bridge (see Figure 8.5). The same traffic load is placed in both lanes.

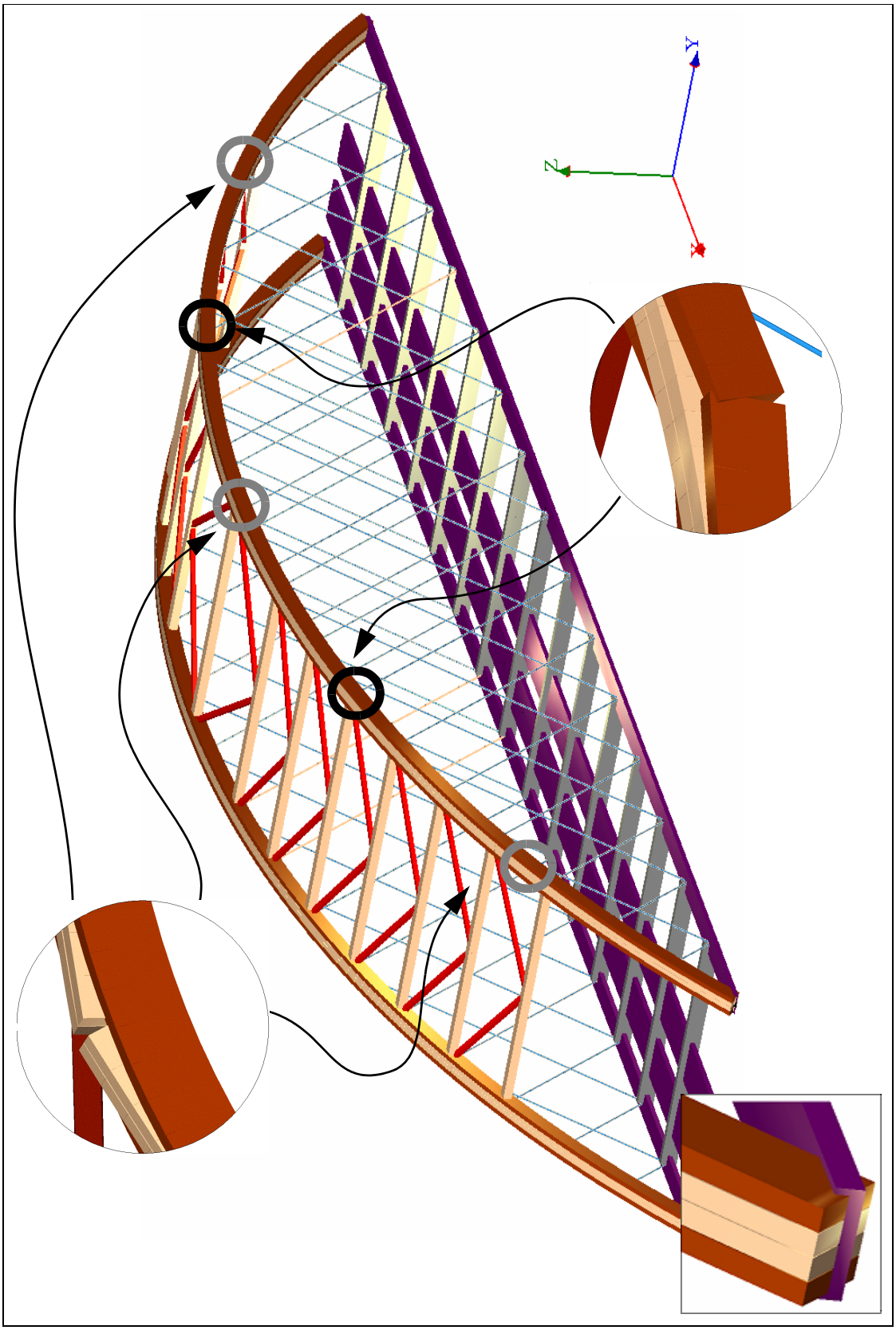

Figure 8.3 Network arch bridge (3D model)

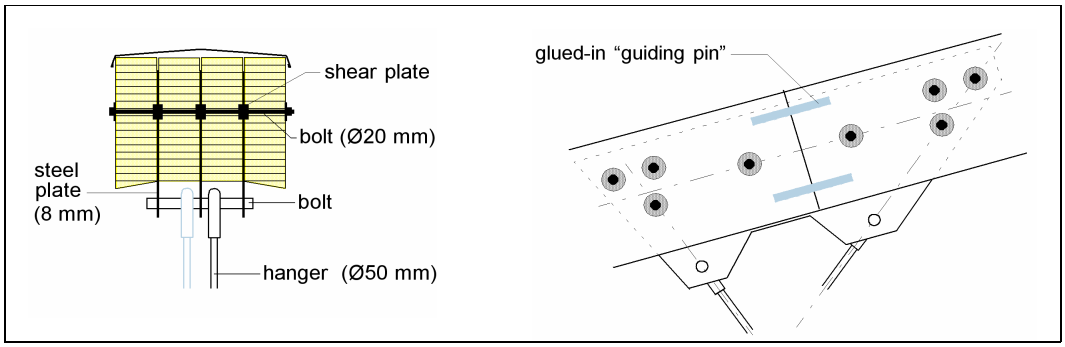

Figure 8.4 Joint with hangers (joint B in Figure 8.2)

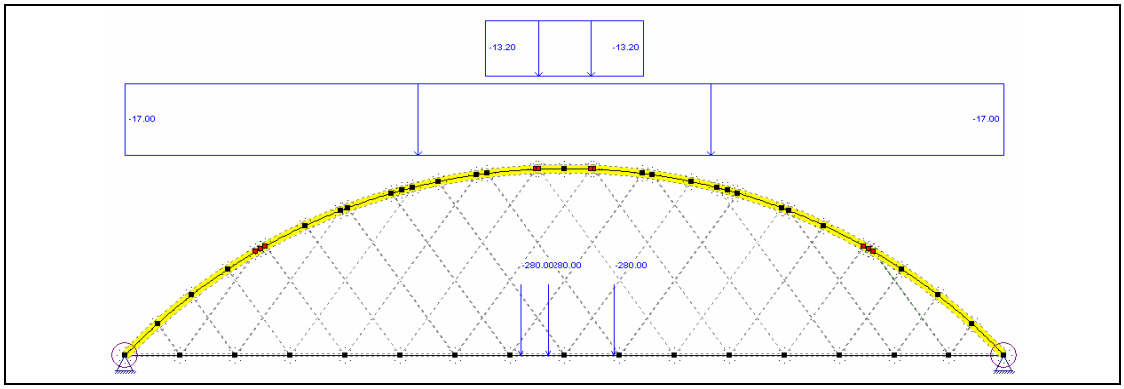

Figure 8.5 Applied traffic- and deck dead loads

In the plane model, the joints at A, B, C, D and E were modeled as hinges, reinforced with rotational springs. The arch (one side) is modeled as a single arch with a rectangular, massive 880×800 mm cross section.

Nonlinear static analyses are carried out for both models and results for bending moments and axial forces are compared in Figures 8.6 and 8.7, for the most loaded arch. The rotational spring stiffnesses for the 2D model is set to k_θ = 50000 kNm/rad at all hinges. Keeping in mind that the results in the 3D case apply to individual lamellas, whereas the 2D results apply to the total cross section (all four lamellas combined), the results are quite similar. The difference is, however, large enough to indicate that the 3D model capture effects not present in the 2D model. This may be due to the difference in the modeling of the hinges, but possible redistribution of load from the least loaded bridge arch cannot be excluded as a source of the deviation.

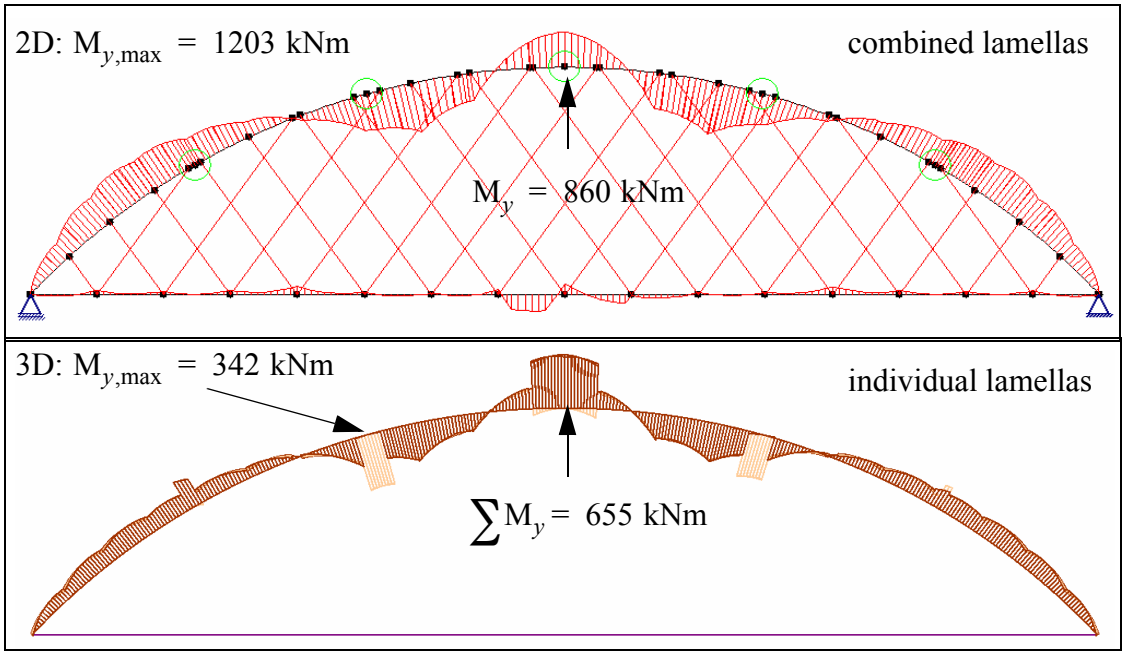

Figure 8.6 Arch-plane bending moment (M_y) distribution for self weight and traffic load for 2D and 3D model (not drawn to scale)

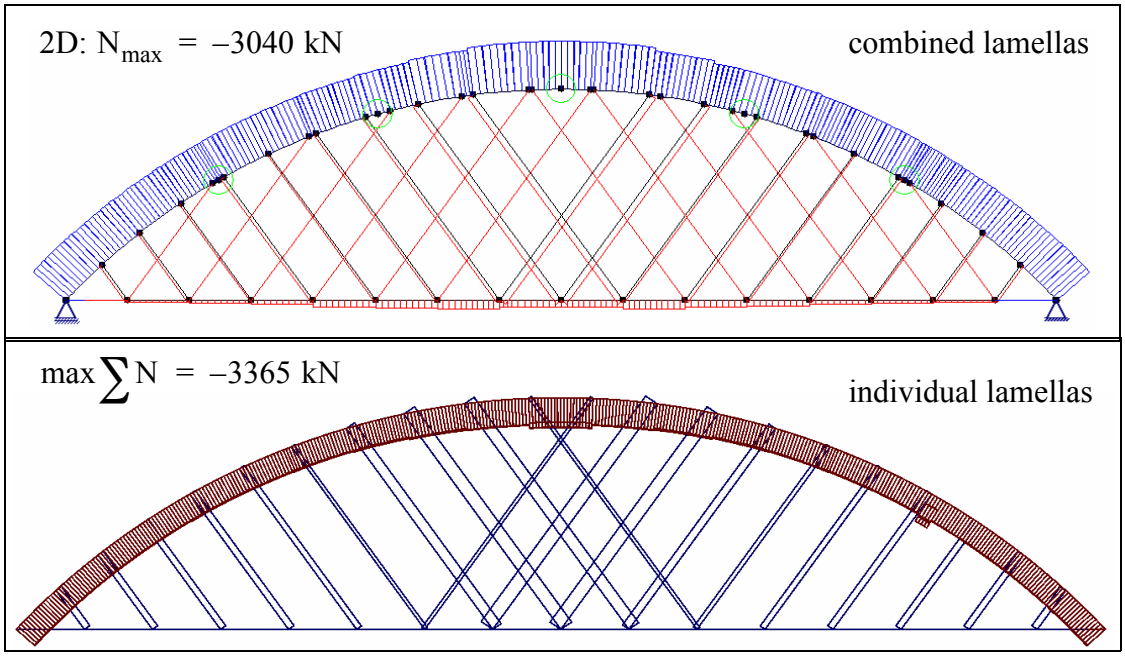

Figure 8.7 Axial force distribution for self weight and traffic load for 2D and 3D model (not drawn to scale)

Linearized buckling analyses are carried out for two load combinations. For self load only, a buckling coefficient of 19.24 is found for the lowest in-plane buckling mode (No. 14) shown in Figure 8.8 for the 3D model. This corresponds quite well with the buckling factor of 20.10 found for the plane model in [5]. The lowest (lateral) buckling mode of the 3D model has a buckling factor of 7.83[1]. For combined dead load and traffic load we find a buckling factor (corresponding to the total loading) of 4.28[2] for the buckling mode shown in Figure 8.9. This is somewhat higher than the 3.21 predicted by the 2D model with spring reinforced hinges at the joints (k_θ = 50000 kNm/rad). Since the 3D model exhibits a mode of buckling with both in-plane and out-of-plane components, it would be reasonable to expect a lower buckling load than that predicted by the 2D model, which is forced to in-plane buckling only. We will return to this discrepancy shortly, but first we mention that if we perform a linearized buckling analysis in which the geometric stiffness due to self load is included in the material stiffness and the geometric stiffness matrix in the eigenproblem only accounts for the stiffness resulting from the axial forces caused by traffic alone, we find (for the 3D model) that we need to multiply the traffic load by 8.15 in order for the system to buckle.

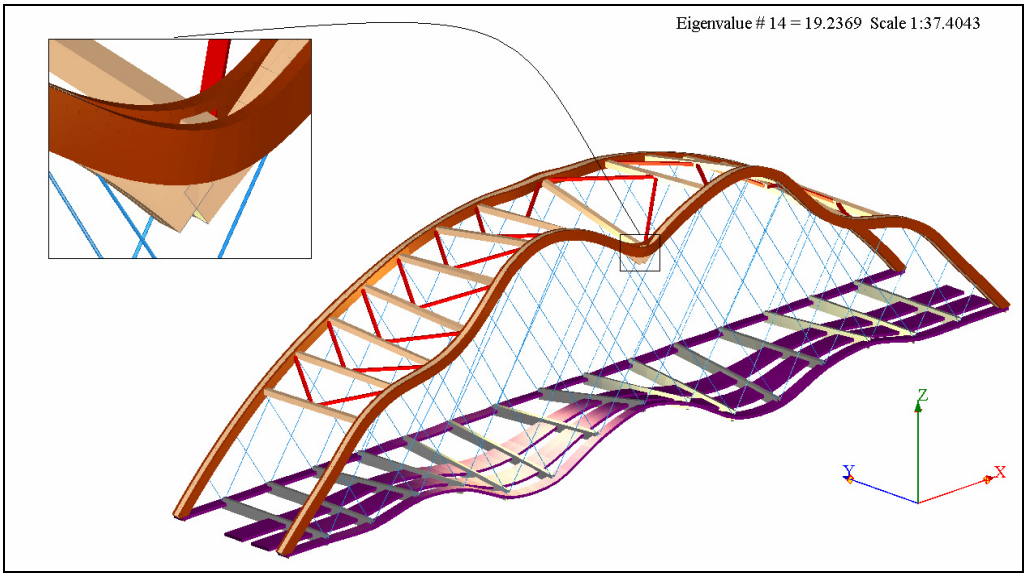

Figure 8.8 In-plane buckling mode of network arch, dead load only (2D model 18.66)

1. This prediction compares well with a nonlinear analysis, yielding a buckling load factor of 7.67.
2. The buckling load factor predicted by a nonlinear analysis is 3.95. The difference is primarily because additional hangers in compression are detected in the nonlinear analysis, compared to what is predicted in the linearized buckling analysis.

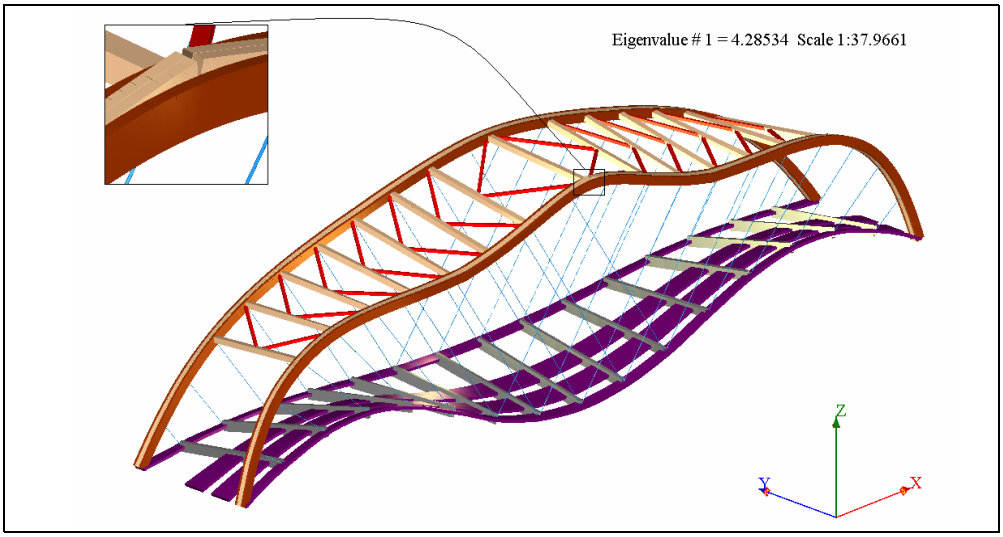

Figure 8.9 In-plane buckling mode of network arch, dead load and traffic (2D model: 2.49)

We modify the model in Figure 8.3 by replacing the mechanically joined arches by two identical, fictitious glulam arches made of a massive 880×800 mm cross section, that is two continuous and perfect 2-hinge arches. For this model the lowest buckling coefficient

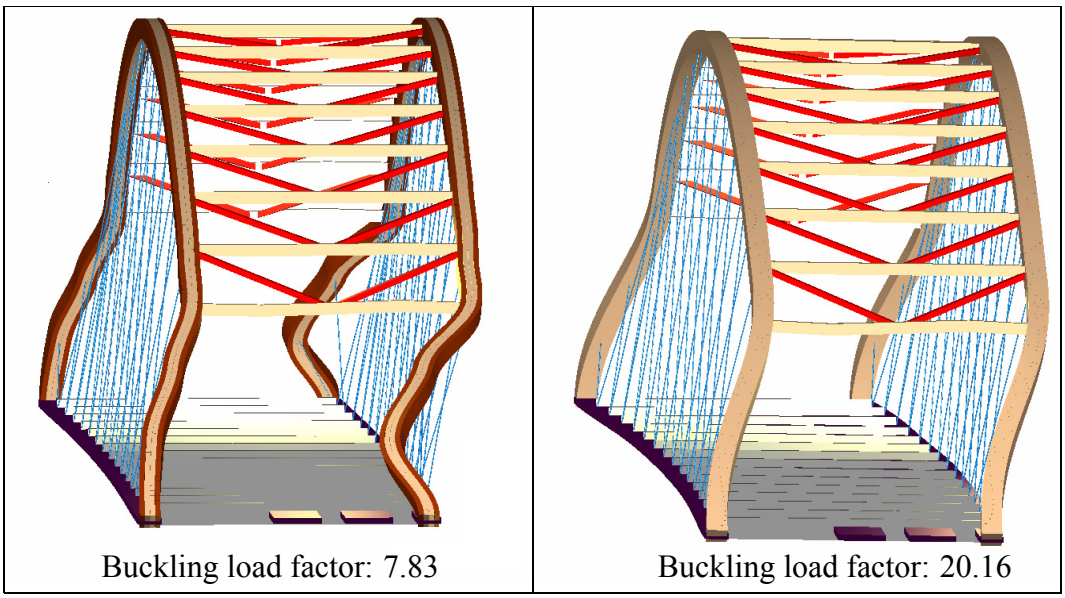

Figure 8.10 Lowest buckling mode for mechanically joined and massive arches, dead load only

for the bridge, subjected to self load only, is 20.16, and when subjected to combined self load and traffic the coefficient is 4.92. These numbers compare to 7.83 and 4.28, respectively, for the case of joined arches. Figure 8.10 compares the lowest buckling modes for

the two different arch designs, when the bridge is subjected to self load only. It seems clear that much of the difference in buckling load is due to the inability of the mechanically joined arches to transmit shear between the sub-arches except at discrete points. The relatively moderate difference between the two models, for self load plus traffic (4.28 compared to 4.92), seems to indicate that the 2D model in [5] may have a conservative estimate of the stiffness (k_θ) assumed for the rotational springs that reinforce the joint hinges. On the other hand it may be optimistic to assume that the four "sub-arches", in Figure 8.3, are completely and rigidly joined at each point of hanger fastening. Some movement in these joints is inevitable, the question is how much this will influence the results. This problem should be looked into more closely, by relaxing some of the constraints in the present model for joined arches. However, the analyses presented in this section seem to indicate that the suggested network arch design for an 80 m span bridge has sufficient stability properties. However, other problems need to be looked into more carefully before the design can be given a clean bill of health.

Finally, the use of buckling modes as a basis for shape imperfection is investigated briefly. A slightly different design, proposed by Gjessing [15], is now used. The principal differences, compared to the previously described network arch bridge, are the dimensions and the angle of the inclined hangers. A plane view of the bridge and loading in the arch-plane is shown in Figure 8.11. In addition to these vertical loads, both arches are subjected to an evenly distributed horizontal wind load of 0.63 kN/m.

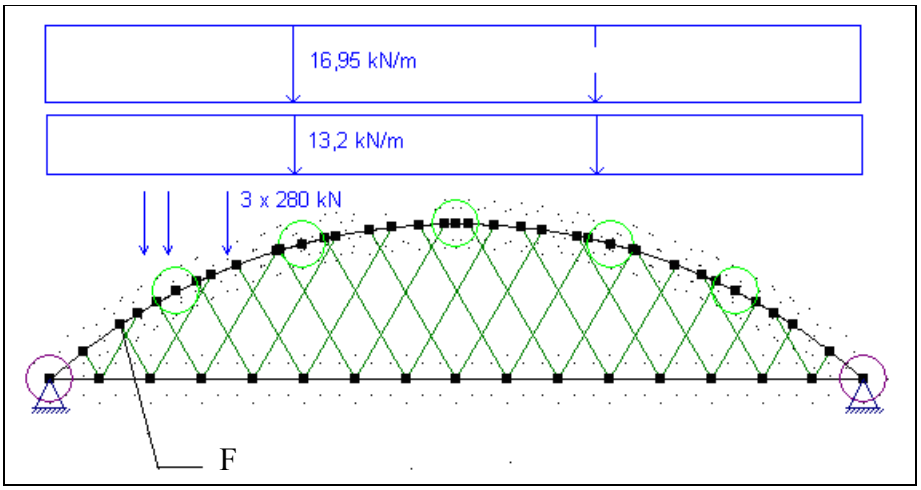

Figure 8.11 In-plane loads

The lowest buckling mode for this configuration, with the associated buckling load factor of 3.19, is depicted in Figure 8.12. The shape of this buckling mode differs significantly

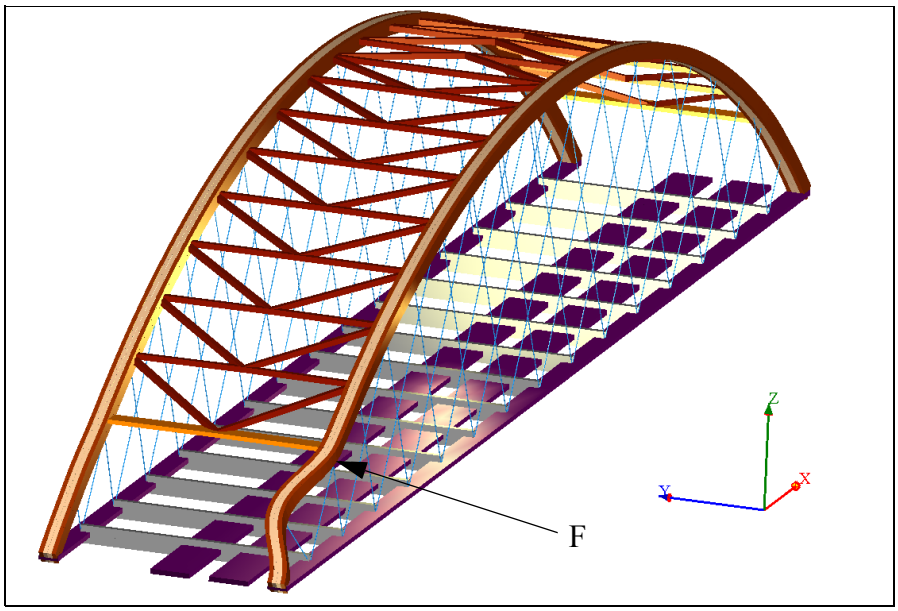

Figure 8.12 Lowest buckling mode for loading of Figure 8.11 plus wind load (buckling load factor 3.19)

from what a traditional (and simplified) plane model will predict, see Figure 8.13. The rea-

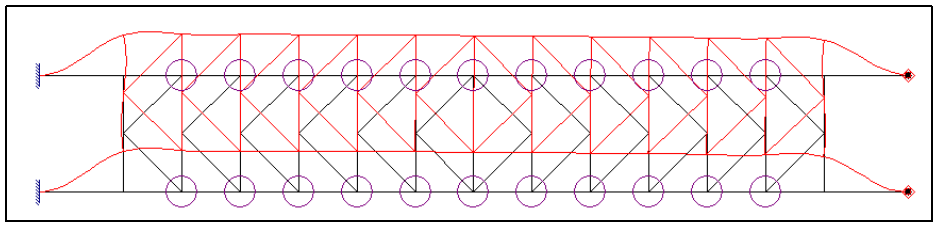

Figure 8.13 Typical buckling mode for 2D model

son for this is twofold: Firstly, in the 3D case the vertical hangers contribute lateral stiffness from the tensile axial forces. Secondly, all effects of bending about the strong lamella axes and torsional rigidity are absent in the 2D model.

Eurocode 5 suggests a sinusoidal shape imperfection, superimposed on the undeformed configuration, as the basis for a nonlinear static analysis. Even though a similar effect is obtained by the displacements due to the wind load, the effect of an additional shape imperfection is investigated. The forces and moments at point F in Figures 8.11 and 8.12

are monitored for each of the four lamellas 1 to 4, where 1 is the outer and 4 is the inner lamella. In the case of no shape imperfection, the largest bending moment M_Z (about a radial axis) occur at this point. In this study, four different 'horizontal' shape imperfections are used:

- Sinusoidal shape imperfection, with amplitudes of 100 and 50 mm, respectively, at mid span
- Shape imperfection based on buckling mode 1, with an amplitude of 50 and 25 mm, respectively

The local character of the buckling mode is why a smaller amplitude is used, since tolerance limits are stricter for shorter spans. In addition to these, a skew symmetric sinusoidal shape imperfection with an amplitude of 50 mm was also considered. This resulted, however, in lower forces and moments than what was obtained with no shape imperfection. The results from this analysis are therefore not included. The results from the other analyses are presented in Tables 6.3 to 6.9.

Table 8.1 Axial force (N)

Assumed imperfection	lamella 1	lamella 2	lamella 3	lamella 4
None	-1158.43	-1163.70	-1195.55	-1257.01
Sin (100)	-1162.00	-1166.45	-1197.57	-1258.32
Sin (50)	-1160.22	-1165.07	-1196.56	-1257.66
Mode 1 (50)	-1218.73	-1181.43	-1172.90	-1192.36
Mode 1 (25)	-1188.48	-1173.04	-1185.22	-1226.17

Table 8.2 Radial shear force (V_y)

Assumed imperfection	lamella 1	lamella 2	lamella 3	lamella 4
None	6.6413	6.0466	5.9875	6.4592
Sin (100)	6.9856	6.3578	6.2958	6.7946
Sin (50)	6.8136	6.2023	6.1417	6.6269
Mode 1 (50)	12.6609	10.8821	10.9824	12.9715
Mode 1 (25)	9.9794	8.6096	8.4614	9.5246

Table 8.3 Horizontal shear force (V_z)

Assumed imperfection	lamella 1	lamella 2	lamella 3	lamella 4
None	-46.732	-46.095	-46.543	-48.118
Sin (100)	-47.129	-46.351	-46.668	-48.111
Sin (50)	-46.929	-46.222	-46.604	
Mode 1 (50)	-55.862	-48.175	-41.873	-36.352
Mode 1 (25)	-51.613	-47.523	-44.675	-42.797

Table 8.4 Torsional moment (M_x)

Assumed imperfection	lamella 1	lamella 2	lamella 3	lamella 4
None	0.2392	0.2274	-0.2262	-0.2355
Sin (100)	0.2410	0.2291	-0.2274	-0.2360
Sin (50)	0.2401	0.2282	-0.2268	-0.2358
Mode 1 (50)	1.1767	0.9767	-0.7895	-0.6019
Mode 1 (25)	0.6657	0.6015	-0.5485	-0.5029

Table 8.5 Horizontal moment (M_y)

Assumed imperfection	lamella 1	lamella 2	lamella 3	lamella 4
None	103.53	100.63	-100.14	-102.03
Sin (100)	103.96	100.79	-100.05	-101.67
Sin (50)	103.74	100.71	-100.10	-101.85
Mode 1 (50)	123.53	106.64	-92.83	-80.79
Mode 1 (25)	113.48	103.74	-96.75	-91.83

Table 8.6 Radial moment (M_z)

Assumed imperfection	lamella 1	lamella 2	lamella 3	lamella 4
None	18.592	17.287	17.260	18.507
Sin (100)	19.595	18.218	18.189	19.505
Sin (50)	19.093	17.753	17.724	19.006
Mode 1 (50)	65.774	60.976	60.999	65.844
Mode 1 (25)	42.515	39.377	39.308	42.301

The most noticeable result from these analyses, is the increase in bending moment M_z due to a shape imperfection based on the first buckling mode. Even the smaller amplitude of 25 mm still produce bending moment more than twice that of the 100 mm sinusoidal shape imperfection. The question remains as to wether this is a reasonable amplitude. However, comparing the results to a plane model, with a shape imperfection based on Figure 8.13 with an amplitude of 25 mm results in a bending moment M_z more than 150% that of Mode 1 (25). This is primarily due to the stabilizing effects of the vertical hangers, reducing the need for the arches to transmit vertical moments.

While not in any way conclusive, these results indicate the importance of geometrical imperfections in nonlinear analyses. In order to be a viable tool for design engineers, nonlinear static analyses must include these imperfections, and the tools need to do so in a semi-automatic, but user controlled manner. The lowest buckling modes present themselves as obvious candidates for the definition of the shape of the imperfections. They are

also easily implemented. However, the user should also have other options at his or her disposal, such as (sinusoidal) imperfections for individual compression members, and probably also deformations due to prescribed loads. It should also be mentioned that for more complex structures, linearized buckling analyses, as such, may provide useful information for the determination of the code defined correction (or *k*-) factors. However, the ultimate goal must be to make these factors superfluous,through nonlinear 3D analysis of the structural system, including viable geometrical imperfections.

The network arch bridge example also highlights a major problem with timber structures, which is independent of 2D/3D and linear/nonlinear, namely the modelling of the joints/ supports, which invariably are semi-rigid.

8.3 Lardal pedestrian bridge

Figure 8.14 Lardal pedestrian bridge

The next case concerns the dynamic behavior of a footbridge, erected in Lardal, Norway in 2001 (see Figure 8.14). Being a “small-scale” and low budget project, the study of the dynamic behavior of the bridge prior to construction was limited. In preliminary analyses of the eigenfrequencies, using a level of detailing appropriate to the scale of the project, the lowest eigenfrequency, corresponding to an in-plane mode, was found to be quite close to 1.3 Hz. In a resent study, in connection with the resonance problems of the Millennium Bridge in London, a threshold value of 1.3 Hz was recommended. Lower values for the eigenfrequencies were considered unsafe, while 1.3 Hz and higher were considered safe. However, soon after completion of the Lardal bridge, unacceptable dynamic response due to pedestrian loads, similar to the Millennium Bridge, was observed.

In a Ph.D. project, carried out in parallel with this one, a detailed study of both the dynamics of pedestrian loads and structural response, as well as full scale measurements on the bridge, has been performed by Rönnquist [34]. In connection with the measurements, a more detailed model than the pre-construction model was established and analyzed, using the commercial software package ANSYS^{TM}. Although more plausible results than the preliminary ones were obtained, a significant deviation was still observed between calculated and measured results. This was particularly evident in that the eigenmodes did not match the measured modes when ordered with respect to increasing eigenfrequencies. Furthermore, the measurements revealed serious horizontal vibrations imposed by pedestrians crossing the bridge. In this mode, the bridge deck moved laterally, with the trusses and cables trailing in an “inverted pendulum” motion. This was not detected at all in the

ANSYS^{TM} model, where the first horizontal mode was an ordinary pendulum ("hammock type") motion of the bridge cross section. Even though the calculated eigenfrequency was well below the threshold value of 1.3 Hz, this calculated behavior would have been far less severe than what was actually observed.

This problem presented itself as a challenging test bed for the program developed as part of the present work. An even more detailed model was therefore created, including both railing and eccentric positioning of the mass of the bridge deck. Figure 8.15 shows a 3D and a plane view of the model to indicate geometry and level of detailing. The principal structural components of the bridge are the primary span and the two abutments (secondary spans). The abutments are anchored to the river banks on either side of the river, while the main span is supported by the cantilever part of the abutments. Vertical loads are carried by massive glulam bridge beams, hinged at mid span and supported by a system of steel cables and timber trusses. A separate horizontal steel truss, positioned between, and bolted to, the main glulam beams is designed to take the horizontal loads. For a more detailed account of both geometry and member dimensions, as well as material properties and detailing, the interested reader is referred to [34].

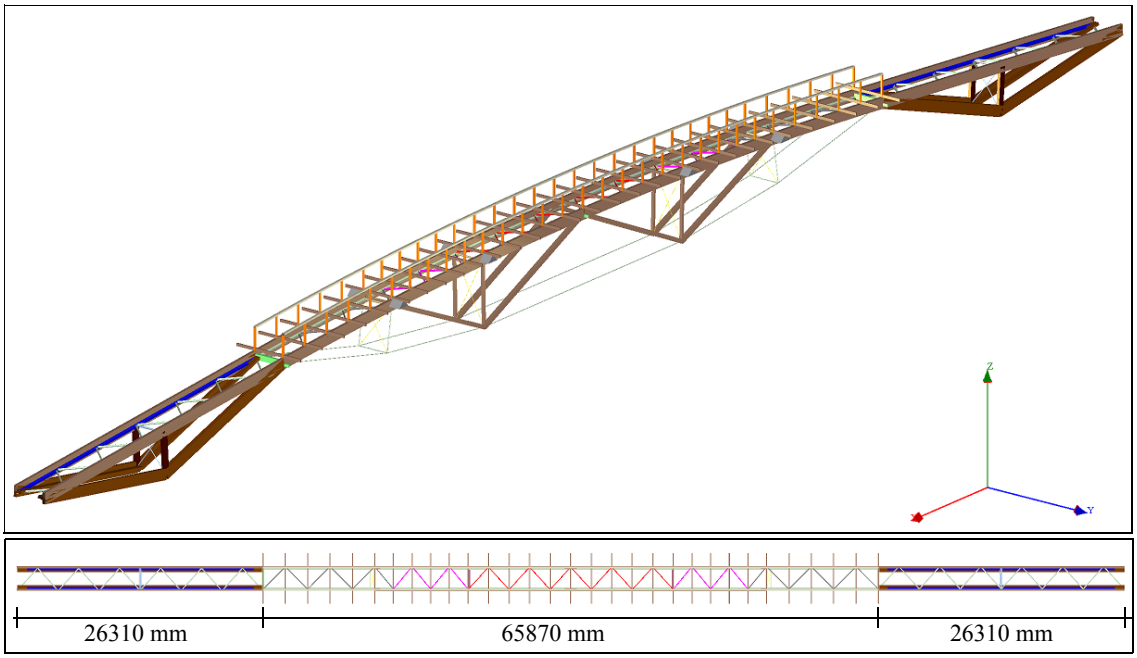

Figure 8.15 Computer model of Lardal Bridge

The bridge is quite slender, with slightly curved beams (radius of vurvature is approximately 400 m for a 66 m long beam). In a preliminary study, Rönnquist found that the dynamic behavior of the bridge was very sensitive to vertical displacements (primarily due to mass distribution). It was therefore critical to maintain correct vertical distribution of the mass, while also accounting for geometric effects due to initial deformation and forces. The adopted procedure was therefore to first apply a "negative" gravitational field (directed upwards) and performing a static analysis based on the self weight of the bridge. A new undeformed configuration of the bridge is subsequently obtained from this, deformed configuration. The static analysis is then repeated, but now in a "natural" gravitational field. The natural frequencies are obtained by solving the classical (free vibration) symmetric eigenproblem, evaluated at this final state of deformation:

$$(\mathbf{K}_T - \omega_i^2 \mathbf{M})\mathbf{x}_i = 0\,,\; i = 1, \ldots n \tag{8.2}$$

where ω_i is the circular frequency and $\mathbf{x}_i$ the corresponding free vibration mode. $\mathbf{M}$ is the consistent (or "lumped") mass matrix and $\mathbf{K}_T = (\mathbf{K}_m + \mathbf{K}_G)$ is the consistent tangent stiffness matrix. The use of the consistent tangent stiffness matrix assures that geometric effects are properly included. The natural frequency (in Hz), f_i, is obtained as:

$$f_i = \frac{\omega_i}{2\pi} \tag{8.3}$$

The natural frequencies from both the full scale measurements and the FEM-model are presented as the first two rows of Table 8.7. Although the numeric values of the natural frequencies are similar, the associated eigenmodes do not match. This is particularly obvious for the first two modes. The two lowest measured natural frequencies are associated with a horizontal and a torsional eigenmode, respectively, while the results from the FEM analysis are associated with a torsional and a horizontal eigenmode, respectively. The overall shapes of the calculated modes, however, are similar to the measured modes (also for the inverted pendulum motion). In order to obtain better agreement between measured and calculated values, some of the cross sectional parameters in the model were modified. Since it was assumed that the glulam beams were not rigidly connected to the horizontal wind truss, it was decided to weaken the diagonals in the truss by reducing their modulus of elasticity. A similar argument led to the reduction in stiffness for the secondary spans,

since the brackets "hinging" the primary span to the secondary will allow some movement. The results from this analysis is presented in Table 8.7 as FEM[b].

Table 8.7 Computed and measured natural frequencies f_i [Hz][a]

	f_1	f_2	f_3	f_4	f_5	f_6
Measured	0.83 (1st h)	1.12 (1st t)	1.45 (1st v)	2.10 (2nd h)	2.45 (2nd t)	2.85 (2nd v)
FEM	1.06 (1st t)	1.12 (1st h)	1.52 (1st v)	2.51 (2nd t)	3.11 (2nd h)	3.27 (2nd v)
FEM[b]	0.87 (1st h)	1.12 (1st t)	1.45 (1st v)	2.06 (2nd h)	2.63 (2nd t)	2.82 (2nd v)

a. h = horizontal, t = torsional and v = vertical

b. Modified cross section parameters

Even if the results from the modified model show very good agreement with the measured values, it should be kept in mind that they have been obtained through a trial and error process. However, the excellent agreement for even the 6th natural frequency, seems to indicate that the critical problem areas, with respect to modelling, have been identified. Interestingly, the modifications did not noticeably change the shape of the vibration modes (only their associated frequencies). The first three modes are depicted in figures 8.16 to 8.18. Finally, the primary displacement (or rotation) components in the bridge deck, obtained by the final modified analysis, are plotted in Figure 8.19 along with the (average) recorded values and equivalent sinusoidal mode shapes.

The main message from this example is the importance of the modelling process. In most practical cases correct answers (in the form of prototype measurements) are not available, and for complex structures it may therefore be appropriate to vary critical properties in order to map their influence on the final result.

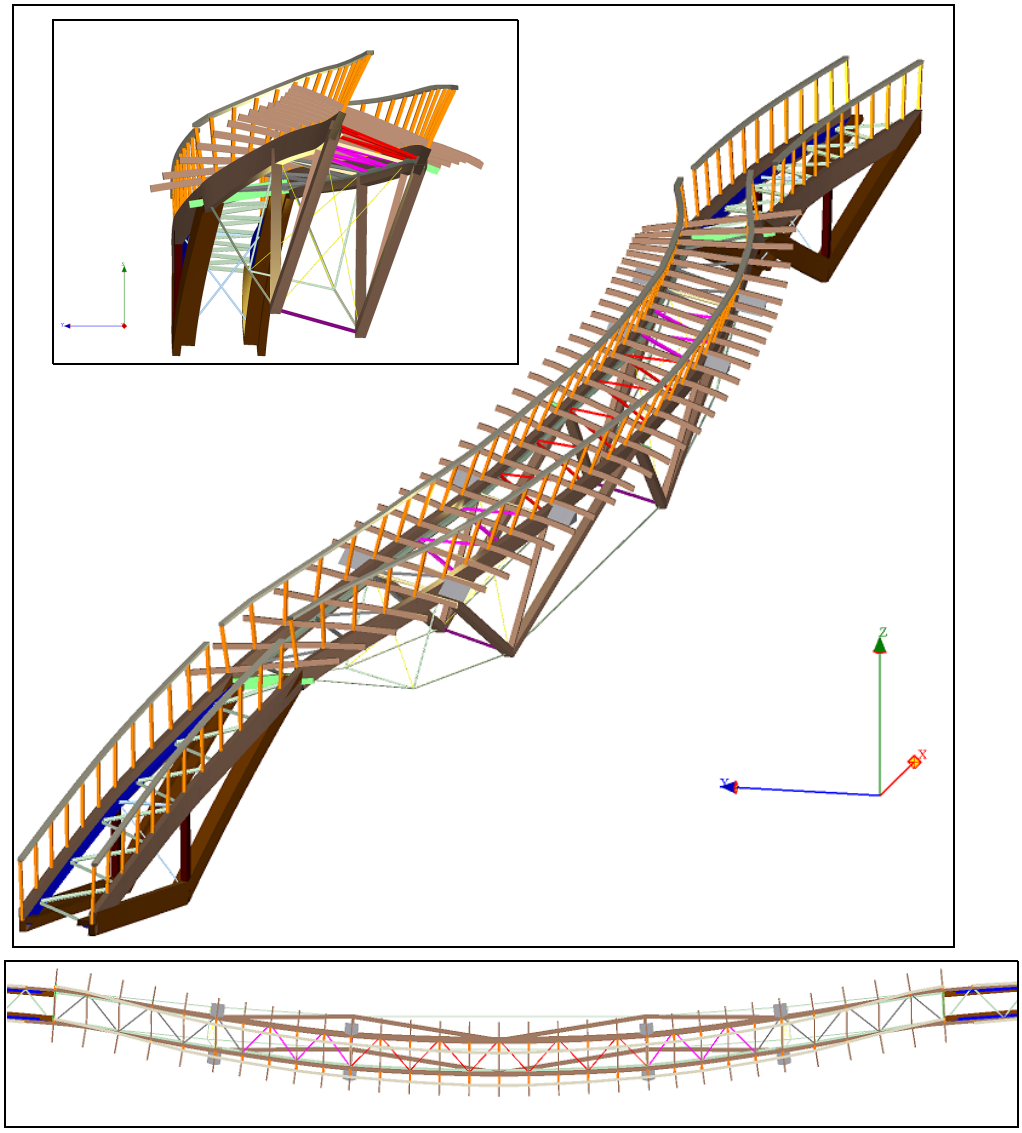

Figure 8.16 Lardal Bridge, eigenmode 1 (horizontal)

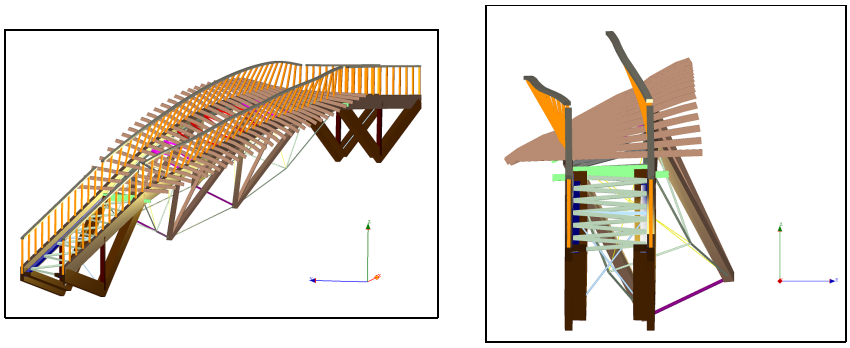

Figure 8.17 Lardal Bridge, eigenmode 2 (torsional)

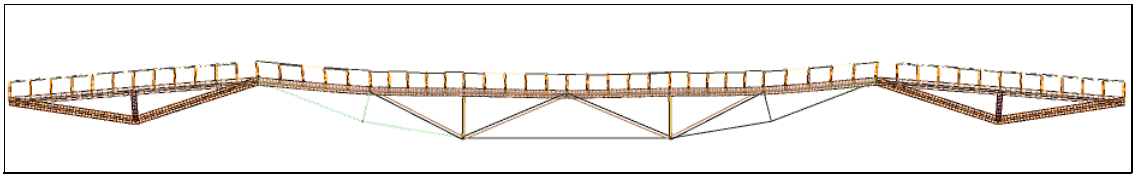

Figure 8.18 Lardal Bridge, eigenmode 3 (vertical)

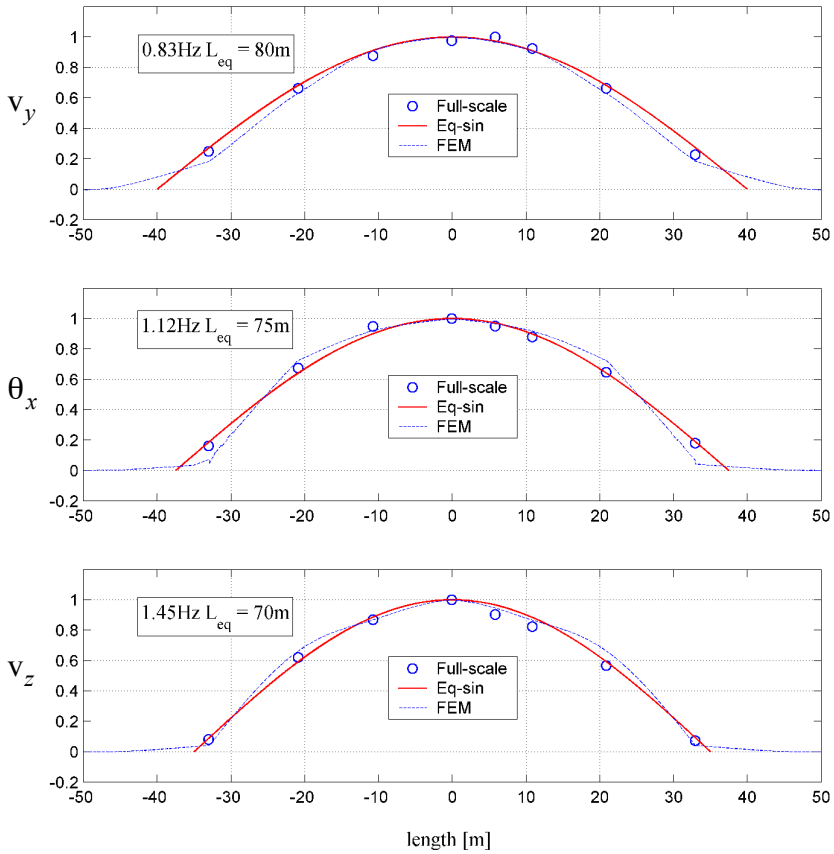

Figure 8.19 Full scale measurements, FEM-analysis and equivalent sinusoidal mode representation of principal displacements of the 3 first eigenmodes

8.4 Concluding remarks and suggestions for further work

The network arch bridge case presented indicates the potential of a flexible 3D analysis and design tool with graphical user interaction. However, as seen in the case of the Lardal pedestrian bridge, 3D modelling of real structures is not always a straightforward process. It will probably take some time before the powerful, state-of-the-art computational engines are developed into robust, easy to use and understand and, to some extent, fool-proof tools, for the ordinary practising engineer. Although the nonlinear behavior of timber members are at present adequately described by the use of nonlinear beam type elements, some problem areas still remain: How to model and analyze the semi-rigid connections, shape imperfections and the need for improved fracture models. In addition, the time-dependant behavior of wood (rheology) due to loading and transportation of moisture content should also be addressed. Connections and rheology can readily be modeled and analyzed with available software packages, using volume and contact elements and nonlinear material models. In a practical design context, however, this is still far too costly and cumbersome. Of the mentioned challenges, the most pressing are:

- Guidelines for shape imperfections for use in 3D nonlinear analyses
- Improved, discrete models for timber connections and supports

To facilitate safe and accurate design, the design software should offer flexible and comprehensive options for modelling shape imperfections. Furthermore, extensive libraries with accurate models of predefined joints and connections coupled with good visual user feedback are needed. This is primarily due to the semi-rigid properties present for all fasteners used in connection with timber. Also, since timber structures often base the transmission of axial forces on contact forces, discrete “contact-joints” would be useful.

In conclusion it seems fair to state that while some aspects of the stability of glulam arches have been demonstrated, a more comprehensive and systematic series of analyses is necessary in order to provide solid information and guidelines for practical design work. The aim is to include (code based) capacity controls of all members, coupled with full fledged nonlinear static analyses that account properly for the stiffness of the entire (3D) structural system, including all bracing and geometric imperfection, and thus eliminate the use of some rather cumbersome correction (k-) factors.

References

[1] Argyris, J.H. and Symeonidis, S., "Nonlinear Finite Element Analysis of Elastic Systems under Nonconservative Loading - Natural Formulation. Part I : Quasistatic Problems", *Comp. Meths. Appl. Mech. Engrg*. **vol. 26**, p. 75-123, 1981

[2] Bell, K., Bleie, O.V. and Wollebæk, L., "CrossX, A WINDOWS-based program for computation of parameters for, and stress distribution on, arbitrary beam cross sections. User's manual", Norwegian University of Science and Technology, Report No. R-13-00, Trondheim, Norway, 2000.

[3] Bell, K. and Karlsrud, E., "Large Glulam Arch Bridges - A Feasibility Study", Proceedings of the IABSE conf. on Innovative Wooden Structures and Bridges (pages 193-198), Lahti, Finland 2001. IABSE report, Volume 85.

[4] Bell, K. and Wollebæk, L., "Large, mechanically joined glulam arches" , Proceedings of the 8th World Conference on Timber Engineering (pages 55-60), Volume I, Lahti, Finland, 2004

[5] Bell, K. and Wollebæk, L., "FEMplate , A WINDOWS-based program for linear, static analysis of plates, considering both in-plane and transverse loading. User's manual" , Norwegian University of Science and Technology, Department of Structural engineering (59 pages), Norway, 2004.

[6] Belytschko, T., "*Nonlinear Finite Elements for Continua and Structures",* John Wiley & Sons Ltd, West Sussex, England, 2000, ISBN: 471-98774-3

[7] Bolotin, V.V., *"Nonconservative Problems of the Theory of Elastic Stability"*, Pergamon Press Ltd., 1963

[8] Cardona, A. and Géradin, M., "A beam finite element non-linear theory with finite rotations", *Int. J. Num. Meth. Eng.*, **vol. 26**, p. 2403-2438, 1988

[9] Crisfield, M.A., *"Non-Linear Finite Element Analysis of Solids and Structures*, *Volume 2, Advanced Topics",* John Wiley & Sons; 1st edition, 1997, ISBN: 047195649X

[10] Eggen, T.E., "*Buckling and geometrical nonlinear beam-type analyses of timber structures",* Department of Structural engineering, Norwegian University of Science and Technology. Trondheim, Norway, 2000

[11] Engesser, F., *Zentr. Bauvervaltung*, vol. 11, p. 483, 1891

[12] European committee for standardization, Eurocode 5: Design of timber structures - Part 1-1: General - Common rules and rules for buildings, Ref. No. EN1995-1-1:2004 (E), 2004

[13] Felippa, C.A. and Haugen, B., "A Unified Formulation of Small-Strain Corotational Finite Elements: I. Theory", to be published (2005)

[14] Géradin, M. and Rixen, D., *Parametrization of Finite Rotations in Computational Dynamics : a Review,* Revue europèenne des èlèments finis, Vol. 4, number 5/6, p. 497-553, 1995

[15] Gjessing, R.S., "Store, massive limtrebuer i bru med vegtrafikk. Mulighetsstudie". Masters thesis, Norwegian University od Science and Technology, Department of Structural engineering. Trondheim, Norway, 2004, (in Norwegian only)

[16] Haugen, B., "Buckling and stability problems for thin shell structures using high performance finite elements", PhD thesis, University of Colorado, 1994.

[17] Haugen, B. and Felippa, C.A., "Rigid eccentricities in geometric nonlinear analysis of elastic structures", Proceedings of the NSCM VIII conf., Gothenburg, Sweden. NoACM report, Department of Structural Mechanics, Chalmers University of Technology. Publication 95:15, 1995.

[18] Horringmoe, G. and Bergan, P.G., "Instability analysis of fre-form shells by flat finite elements". *Comp. Meths. Appl. Mech. Engrg*. **vol. 16**, p. 11-35, 1978

[19] Kouhia, R., "Techniques for the Analysis of Non-Linear Systems - With Applications to Solid and Structural Mechanics". Acta Polytechnica Scandinavica, Civil Engineering and Building Construction Series No. 116. Finnish Academy of Technology. Helsinki, Finland. ISBN 952-5148-92-0, 1999

[20] Lanczos, C., "*The Variational Principles of Mechanics"*, Dover Pubns; 4th edition (March 1, 1986), ISBN: 0486650677, 1986

[21] Lautersztajn-S, N. and Samuelsson, A*.,* "On application of differential geometry to computational mechanics"*, Comp. Meth. Appl. Mech.* **vol. 150**, p. 25-38, 1997.

[22] Lyche, T. and Mørken, K., "*Spline Methods Draft"*, Lecture notes, University of Oslo, Dept. of informatics, 2000

[23] Marsden, J.E. and Hughes, T.J.R., "*Mathematical foundations of elasticity"*, Prentice-Hall, Inc., Englewood Cliffs, N.J., USA, 1983, ISBN 0-13-561076-1

[24] Marsden, J.E and Ratiu, T.S., "*Introduction to mechanics and symmetry",* second edition, Springer-Verlag New York, Inc. USA, 1999, ISBN 0-387-98643-X

[25] McGuire, W. and Gallagher, R.H., Ziemian R.D., "*Matrix structural analysis"*, second edition, John Wiley & Sons, Inc., USA, 2000, ISBN 0-471-12918-6

[26] Nour-Omid, B. and Rankin, C.C., "Finite Rotation analysis and consistent linearization using projectors"*, Comp. Meth. Appl. Mech*. **vol. 93**, p. 353-384, 1991.

[27] Pacoste, C., *"Co-rotational flat facet triangular elements for shell instability analyses", Comp. Meth. Appl. Mech*. **vol. 156**, p. 75-110, 1998.

[28] Pacoste, C. and Eriksson A., "Element behavior in post-critical plane frame analysis"*,* Comp. Meth. Appl. Mech. **vol. 125**, p. 319-343, 1995.

[29] Pacoste, C. and Eriksson, A., "Beam elements in instability problems"*, Comp. Meth. Appl. Mech.* **vol. 144**, p. 163-197, 1997.

[30] Petrov, E. and Géradin, M., "Finite element theory for curved and twisted beams based on exact solutions for three-dimensional solids Part 1"*, Comp. Meth. Appl. Mech.* **vol. 165,** p. 43-92, 1998

[31] Petrov, E. and Géradin, M., "Finite element theory for curved and twisted beams based on exact solutions for three-dimensional solids Part 2"*, Comp. Meth. Appl. Mech.* **vol. 165**, p. 93-127, 1998.

[32] Rankin, C.C. and Brogan, F.A., "An Element-independent Co-Rotational procedure for the treatment of large rotations". *ASME J. Pressure Vessel Techn*., **vol 108**, p. 353-384, 1986.

[33] Rankin, C.C. and Nour-Omid, B., *"*The use of projectors to improve finite element performance"**,** *Computers & Structures,* **vol. 30***,* Issues 1-2, 1988, Pages 257-267, 1988.

[34] Rönnquist, A.N. . "Pedestrian induced lateral vibrations of slender footbridges"*,* Department of Structural engineering Norwegian University of Science and Technology. Trondheim, Norway, 2005 (to be published)

[35] Simo, J.C., "A finite strain beam formulation. The three dimensional dynamic problem. Part I", *Comp. Meth. Appl. Mech.* **vol.** 49, p. 55-70, 1985.

[36] Simo, J.C. and Vu-Quoc, L., "A finite strain beam formulation. The three dimensional dynamic problem. Part II"*, Comp. Meth. Appl. Mech.* **vol. 58**, p. 79-116, 1986.

[37] Simo, J.C. and Vu-Quoc, L., "A geometrically-exact rod model incorporating shear and torsion-warping deformation"*, Int. J. Solids Structures*, **vol. 27**, No 3, p. 371-393, 1991.

[38] Spurrier, R.A., "Comment on 'Singularity-Free Extraction of a Quaternion from a Direction-Cosine Matrix' ", *Journal of spacecraft and rockets.* **vol. 15**, p. 255, 1978.

[39] Timoshenko, S.P. and Gere J.M., "*Theory of elastic stability"*, McGraw-Hill book company, inc. 2nd edition, 1961.

[40] Trahair, N.S., "*Flexural-Torsional Buckling of Structures"*, E & F N Spoon, London, UK, 1993

Appendices

Appendix A

Some basic properties of the spin matrix

The skew symmetric 3×3 spin matrix (so(3)) of a vector is defined by:

$$\widehat{\mathbf{a}} = \mathrm{Spin}(\mathbf{a}) = \begin{bmatrix} 0 & -a_3 & a_2 \\ a_3 & 0 & -a_1 \\ -a_2 & a_1 & 0 \end{bmatrix} \in \mathrm{so}(3) \tag{A.1}$$

This can be deduced by the fact that pre-multiplication of the matrix has the same effect as the cross-product of its axial vector (Axial(Spin(**a**)) = **a**) and an arbitrary vector (**b**):

$$\mathbf{a} \times \mathbf{b} = \widehat{\mathbf{a}}\,\mathbf{b} = -\widehat{\mathbf{b}}\,\mathbf{a} \tag{A.2}$$

Elements of so(3) satisfy the *Lie bracket* $[\circ, \circ]$:

$$[\widehat{\mathbf{a}}, \widehat{\mathbf{b}}] = \widehat{\mathbf{a}}\,\widehat{\mathbf{b}} - \widehat{\mathbf{b}}\,\widehat{\mathbf{a}} \in \mathrm{so}(3) \tag{A.3}$$

$$[\widehat{\mathbf{a}}, \widehat{\mathbf{a}}] = \widehat{\mathbf{a}}\,\widehat{\mathbf{a}} - \widehat{\mathbf{a}}\,\widehat{\mathbf{a}} = \mathbf{0} \tag{A.4}$$

$$[\widehat{\mathbf{a}} + \widehat{\mathbf{c}}, \widehat{\mathbf{b}}] = \widehat{\mathbf{a}}\,\widehat{\mathbf{b}} - \widehat{\mathbf{b}}\,\widehat{\mathbf{a}} + \widehat{\mathbf{c}}\,\widehat{\mathbf{b}} - \widehat{\mathbf{b}}\,\widehat{\mathbf{c}} = [\widehat{\mathbf{a}}, \widehat{\mathbf{b}}] + [\widehat{\mathbf{c}}, \widehat{\mathbf{b}}] \tag{A.5}$$

By using the fact that

$$\widehat{\mathbf{a}}\,\widehat{\mathbf{b}} = \mathbf{b} \otimes \mathbf{a} - (\mathbf{a} \cdot \mathbf{b})\mathbf{1} \tag{A.6}$$

and

$$\mathrm{Spin}(\widehat{\mathbf{a}}\,\mathbf{b}) = \mathbf{b} \otimes \mathbf{a} - \mathbf{a} \otimes \mathbf{b} \tag{A.7}$$

the Lie bracket can be re expressed as:

$$[\widehat{\mathbf{a}},\ \widehat{\mathbf{b}}] = \widehat{\mathbf{a}}\widehat{\mathbf{b}} - \widehat{\mathbf{b}}\widehat{\mathbf{a}} = \mathbf{a}\otimes\mathbf{b} - \mathbf{b}\otimes\mathbf{a} = \mathrm{Spin}(\widehat{\mathbf{b}}\,\mathbf{a}) \tag{A.8}$$

It is sometimes useful to obtain the symmetric and skew symmetric parts of $\widehat{\mathbf{a}}\widehat{\mathbf{b}}$. By using equations (A.6) and (A.7) it is easily shown that:

$$\mathrm{Sym}(\widehat{\mathbf{a}}\widehat{\mathbf{b}}) = \frac{1}{2}(\mathbf{b}\otimes\mathbf{a} + \mathbf{a}\otimes\mathbf{b}) - (\mathbf{a}\cdot\mathbf{b})\mathbb{1} \tag{A.9}$$

$$\mathrm{Skew}(\widehat{\mathbf{a}}\widehat{\mathbf{b}}) = \frac{1}{2}[\widehat{\mathbf{a}},\ \widehat{\mathbf{b}}] = \frac{1}{2}(\mathbf{b}\otimes\mathbf{a} - \mathbf{a}\otimes\mathbf{b}) = \frac{1}{2}\mathrm{Spin}(\widehat{\mathbf{a}}\,\mathbf{b}) \tag{A.10}$$

Transformation of the spin matrix follow basic transformation laws of matrices. This can be observed since

$$(\mathbf{R}\mathbf{a})\times(\mathbf{R}\mathbf{b}) = \mathbf{R}(\mathbf{a}\times\mathbf{b}) \tag{A.11}$$

and

$$\begin{aligned}\mathrm{Spin}(\mathbf{R}\mathbf{a})\mathbf{b} &= (\mathbf{R}\mathbf{a})\times\mathbf{b} = (\mathbf{R}\mathbf{a})\times(\mathbf{R}\mathbf{R}^{\mathsf{T}}\mathbf{b}) \\ &= \mathbf{R}(\mathbf{a}\times(\mathbf{R}^{\mathsf{T}}\mathbf{b})) = \mathbf{R}\,\widehat{\mathbf{a}}\,\mathbf{R}^{\mathsf{T}}\mathbf{b}\end{aligned} \tag{A.12}$$

we get

$$\mathrm{Spin}(\mathbf{R}\mathbf{a}) = \mathbf{R}\,\mathrm{Spin}(\mathbf{a})\mathbf{R}^{\mathsf{T}} \ \forall\ \mathbf{R}\mathbf{R}^{\mathsf{T}} = \mathbb{1} \tag{A.13}$$

Furthermore, if the rotation, **R,** is a rotation about an axis parallel to **a**, then:

$$\mathbf{R}\,\mathrm{Spin}(\mathbf{a}) = \mathrm{Spin}(\mathbf{a})\mathbf{R} \ \forall\ \mathbf{R}\mathbf{R}^{\mathsf{T}} = \mathbb{1},\ |\mathbf{R}| = 1,\ \mathbf{R}\mathbf{a} = \mathbf{a} \tag{A.14}$$

Equation (A.6) can also be used to show that:

$$\widehat{\mathbf{b}}\,\widehat{\mathbf{a}}\,\widehat{\mathbf{b}} = -(\mathbf{a}\cdot\mathbf{b})\,\widehat{\mathbf{b}} \tag{A.15}$$

Appendix B
Derivation of H-matrix

This appendix deals with the derivation of the matrix, **H**, that relates additive differentials of the rotation at one rotational state to another. Derivation of this matrix is usually done by the use of the Rodriguez-parameters, primarily due to the simple form of the evaluation of compound rotations. In the following, no such shift in parametrization will be done.

We start by defining the current state of rotation:

$$\mathbf{R}(\theta_t) = \mathbf{R}(\theta)\mathbf{R}(\theta_0), \quad \theta = \|\theta\|\mathbf{n}, \quad \theta_0 = \|\theta_0\|\mathbf{n}_0 \tag{B.1}$$

where θ_t is the total rotation in the current state, θ_0 is an initial rotation and θ is the additional rotation. If the additional rotation is perturbed by the vector $\varepsilon\,\delta\theta$, where $\varepsilon > 0$ is a scalar, we get the perturbed rotational state:

$$\mathbf{R}(\theta_t^\varepsilon) = \mathbf{R}(\theta^\varepsilon)\mathbf{R}(\theta_0), \qquad \theta^\varepsilon = \theta + \varepsilon\,\delta\theta = \|\theta^\varepsilon\|\mathbf{n}^\varepsilon \tag{B.2}$$

The Frêchet derivative along $\delta\theta$ now evaluates to:

$$D\mathbf{R}(\theta_t)\cdot\delta\theta = D\mathbf{R}(\theta)\mathbf{R}(\theta_0)\cdot\delta\theta = (D\mathbf{R}(\theta)\cdot\delta\theta)\mathbf{R}(\theta_0) \tag{B.3}$$

where

$$D\mathbf{R}(\theta)\cdot\delta\theta = \frac{\partial}{\partial\varepsilon}\left[\mathbb{1}\cos(\|\theta^\varepsilon\|) + \frac{(1-\cos(\|\theta^\varepsilon\|))}{\|\theta^\varepsilon\|^2}\theta^\varepsilon\otimes\theta^\varepsilon + \frac{\sin(\|\theta^\varepsilon\|)}{\|\theta^\varepsilon\|}\widehat{\theta^\varepsilon}\right]\Bigg|_{\varepsilon=0} \tag{B.4}$$

Before proceeding, the following useful relations are noted:

$$D\theta\cdot\delta\theta = \delta\theta, \qquad D\|\theta\|\cdot\delta\theta = \frac{\theta\cdot\delta\theta}{\|\theta\|} = \mathbf{n}\cdot\delta\theta \tag{B.5}$$

$$D\mathbf{n}\cdot\delta\theta = D\frac{\theta}{\|\theta\|}\cdot\delta\theta = \frac{\delta\theta}{\|\theta\|} - \frac{\mathbf{n}\cdot\delta\theta}{\|\theta\|}\mathbf{n} = (\mathbb{1}-\mathbf{n}\otimes\mathbf{n})\frac{\delta\theta}{\|\theta\|} \tag{B.6}$$

Separating Equation (B.4) into the three terms **A**, **B** and **C** results in:

$$\mathbf{A} = \mathrm{D}[\mathbb{1}\cos(\|\boldsymbol{\theta}\|)]\cdot\delta\boldsymbol{\theta} = -\sin(\|\boldsymbol{\theta}\|)\,\mathbf{n}\cdot\delta\boldsymbol{\theta}\,\mathbb{1} \tag{B.7}$$

$$\begin{aligned}\mathbf{B} &= \mathrm{D}[(1-\cos(\|\boldsymbol{\theta}\|))\mathbf{n}\otimes\mathbf{n}]\cdot\delta\boldsymbol{\theta}\\ &= \sin(\|\boldsymbol{\theta}\|)\mathbf{n}\cdot\delta\boldsymbol{\theta}\;\;\mathbf{n}\otimes\mathbf{n}\\ &\quad+\frac{(1-\cos(\|\boldsymbol{\theta}\|))}{\|\boldsymbol{\theta}\|}[\delta\boldsymbol{\theta}\otimes\mathbf{n}+\mathbf{n}\otimes\delta\boldsymbol{\theta}-2\mathbf{n}\cdot\delta\boldsymbol{\theta}\;\;\mathbf{n}\otimes\mathbf{n}]\end{aligned} \tag{B.8}$$

$$\begin{aligned}\mathbf{C} &= \mathrm{D}[\sin(\|\boldsymbol{\theta}\|)\,\widehat{\mathbf{n}}]\cdot\delta\boldsymbol{\theta}\\ &= \cos(\|\boldsymbol{\theta}\|)\,\mathbf{n}\cdot\delta\boldsymbol{\theta}\;\widehat{\mathbf{n}}+\frac{\sin(\|\boldsymbol{\theta}\|)}{\|\boldsymbol{\theta}\|}[\widehat{\delta\boldsymbol{\theta}}-\;\mathbf{n}\cdot\delta\boldsymbol{\theta}\;\widehat{\mathbf{n}}]\\ &= \cos(\|\boldsymbol{\theta}\|)\,\mathbf{n}\cdot\delta\boldsymbol{\theta}\;\widehat{\mathbf{n}}+\frac{\sin(\|\boldsymbol{\theta}\|)}{\|\boldsymbol{\theta}\|}[\widehat{\delta\boldsymbol{\theta}}\mathbf{n}\otimes\mathbf{n}+\mathbf{n}\otimes\mathbf{n}\widehat{\delta\boldsymbol{\theta}}]\end{aligned} \tag{B.9}$$

Collecting terms, we get:

$$\begin{aligned}\mathrm{D}\mathbf{R}(\boldsymbol{\theta})\cdot\;\delta\boldsymbol{\theta} &= \mathbf{A}+\mathbf{B}+\mathbf{C}\\ &= -\sin(\|\boldsymbol{\theta}\|)\,\mathbf{n}\cdot\delta\boldsymbol{\theta}\,\mathbb{1}+\sin(\|\boldsymbol{\theta}\|)\,\mathbf{n}\cdot\delta\boldsymbol{\theta}\;\;\mathbf{n}\otimes\mathbf{n}\\ &\quad+\frac{(1-\cos(\|\boldsymbol{\theta}\|))}{\|\boldsymbol{\theta}\|}[\delta\boldsymbol{\theta}\otimes\mathbf{n}+\mathbf{n}\otimes\delta\boldsymbol{\theta}-2\,\mathbf{n}\cdot\delta\boldsymbol{\theta}\;\;\mathbf{n}\otimes\mathbf{n}]\\ &\quad+\cos(\|\boldsymbol{\theta}\|)\,\mathbf{n}\cdot\delta\boldsymbol{\theta}\;\widehat{\mathbf{n}}+\frac{\sin(\|\boldsymbol{\theta}\|)}{\|\boldsymbol{\theta}\|}[\widehat{\delta\boldsymbol{\theta}}\mathbf{n}\otimes\mathbf{n}+\mathbf{n}\otimes\mathbf{n}\widehat{\delta\boldsymbol{\theta}}]\\ &= \sin(\|\boldsymbol{\theta}\|)\,\mathbf{n}\cdot\delta\boldsymbol{\theta}\;\widehat{\mathbf{n}}^{2}+\cos(\|\boldsymbol{\theta}\|)\,\mathbf{n}\cdot\delta\boldsymbol{\theta}\;\widehat{\mathbf{n}}\\ &\quad+\frac{(1-\cos(\|\boldsymbol{\theta}\|))}{\|\boldsymbol{\theta}\|}[\delta\boldsymbol{\theta}\otimes\mathbf{n}+\mathbf{n}\otimes\delta\boldsymbol{\theta}-2\,\mathbf{n}\cdot\delta\boldsymbol{\theta}\;\;\mathbf{n}\otimes\mathbf{n}]\\ &\quad+\frac{\sin(\|\boldsymbol{\theta}\|)}{\|\boldsymbol{\theta}\|}[\widehat{\delta\boldsymbol{\theta}}\mathbf{n}\otimes\mathbf{n}+\mathbf{n}\otimes\mathbf{n}\widehat{\delta\boldsymbol{\theta}}]\end{aligned} \tag{B.10}$$

Post-multiplication of $\mathbf{R}^T$ results in:

$$\begin{aligned}
D\mathbf{R}(\theta)\cdot\delta\theta\ \mathbf{R}^T &= \sin(\|\theta\|)\cos(\|\theta\|)\ \mathbf{n}\cdot\delta\theta\ \widehat{\mathbf{n}}^2 + \sin^2(\|\theta\|)\ \mathbf{n}\cdot\delta\theta\ \widehat{\mathbf{n}} \\
&\quad + \cos^2(\|\theta\|)\ \mathbf{n}\cdot\delta\theta\ \widehat{\mathbf{n}} - \cos(\|\theta\|)\sin(\|\theta\|)\ \mathbf{n}\cdot\delta\theta\ \widehat{\mathbf{n}}^2 \\
&\quad + \frac{(1-\cos(\|\theta\|))\cos(\|\theta\|)}{\|\theta\|}[\delta\theta\otimes\mathbf{n} + \mathbf{n}\otimes\delta\theta - 2\,\mathbf{n}\cdot\delta\theta\ \mathbf{n}\otimes\mathbf{n}] \\
&\quad + \frac{(1-\cos(\|\theta\|))^2}{\|\theta\|}[\delta\theta\otimes\mathbf{n} - \mathbf{n}\cdot\delta\theta\ \mathbf{n}\otimes\mathbf{n}] \\
&\quad + \frac{(1-\cos(\|\theta\|))\sin(\|\theta\|)}{\|\theta\|}[\mathbf{n}\otimes\mathbf{n}\widehat{\delta\theta}] \\
&\quad + \frac{\sin(\|\theta\|)\cos(\|\theta\|)}{\|\theta\|}[\widehat{\delta\theta}\mathbf{n}\otimes\mathbf{n} + \mathbf{n}\otimes\mathbf{n}\widehat{\delta\theta}] \\
&\quad + \frac{(1-\cos(\|\theta\|))\sin(\|\theta\|)}{\|\theta\|}[\widehat{\delta\theta}\mathbf{n}\otimes\mathbf{n}] \\
&\quad - \frac{\sin^2(\|\theta\|)}{\|\theta\|}[\mathbf{n}\otimes\mathbf{n}\widehat{\delta\theta}\,\widehat{\mathbf{n}}] \\
&= \mathbf{n}\cdot\delta\theta\ \widehat{\mathbf{n}} + \frac{\sin(\|\theta\|)}{\|\theta\|}[\mathbf{n}\otimes\mathbf{n}\widehat{\delta\theta} + \widehat{\delta\theta}\mathbf{n}\otimes\mathbf{n}] \\
&\quad + \frac{(\cos(\|\theta\|)-1)}{\|\theta\|}[\mathbf{n}\otimes\delta\theta - \delta\theta\otimes\mathbf{n}]
\end{aligned} \tag{B.11}$$

By using the fact that

$$[\mathbf{n}\otimes\delta\theta - \delta\theta\otimes\mathbf{n}] = \mathrm{Spin}(\widehat{\delta\theta}\mathbf{n}) = -\mathrm{Spin}(\widehat{\mathbf{n}}\,\delta\theta) \tag{B.12}$$

and

$$\begin{aligned}
[\mathbf{n}\otimes\mathbf{n}\widehat{\delta\theta} + \widehat{\delta\theta}\mathbf{n}\otimes\mathbf{n}] &= [(\widehat{\delta\theta}\mathbf{n})\otimes\mathbf{n} - \mathbf{n}\otimes(\widehat{\delta\theta}\mathbf{n})] = \mathrm{Spin}(\widehat{\mathbf{n}}\,\widehat{\delta\theta}\mathbf{n}) \\
&= -\mathrm{Spin}(\widehat{\mathbf{n}}^2\delta\theta) = \mathrm{Spin}(\delta\theta - \mathbf{n}\otimes\mathbf{n}\delta\theta)
\end{aligned} \tag{B.13}$$

we get

$$
\begin{aligned}
\mathrm{D}\mathbf{R}(\boldsymbol{\theta})\cdot\delta\boldsymbol{\theta}\ \mathbf{R}^{\mathsf{T}} &= \mathbf{n}\cdot\delta\boldsymbol{\theta}\,\widehat{\mathbf{n}} + \frac{(1-\cos(\|\boldsymbol{\theta}\|))}{\|\boldsymbol{\theta}\|}\mathrm{Spin}(\widehat{\mathbf{n}}\,\delta\boldsymbol{\theta}) \\
&\quad + \frac{\sin(\|\boldsymbol{\theta}\|)}{\|\boldsymbol{\theta}\|}\mathrm{Spin}(\delta\boldsymbol{\theta} - \mathbf{n}\otimes\mathbf{n}\delta\boldsymbol{\theta}) \\
&= \mathrm{Spin}(\mathbf{n}\otimes\mathbf{n}\delta\boldsymbol{\theta}) + \frac{(1-\cos(\|\boldsymbol{\theta}\|))}{\|\boldsymbol{\theta}\|}\mathrm{Spin}(\widehat{\mathbf{n}}\,\delta\boldsymbol{\theta}) \\
&\quad + \frac{\sin(\|\boldsymbol{\theta}\|)}{\|\boldsymbol{\theta}\|}\mathrm{Spin}(\delta\boldsymbol{\theta} - \mathbf{n}\otimes\mathbf{n}\delta\boldsymbol{\theta}) \\
&= \mathrm{Spin}(\mathbf{H}^{-1}\delta\boldsymbol{\theta})
\end{aligned}
\tag{B.14}
$$

where

$$
\begin{aligned}
\mathbf{H}^{-1} &= \mathbf{n}\otimes\mathbf{n} + \frac{(1-\cos(\|\boldsymbol{\theta}\|))}{\|\boldsymbol{\theta}\|}\widehat{\mathbf{n}} + \frac{\sin(\|\boldsymbol{\theta}\|)}{\|\boldsymbol{\theta}\|}(\mathbb{1} - \mathbf{n}\otimes\mathbf{n}) \\
&= \mathbb{1} + \frac{2\sin^2(\|\boldsymbol{\theta}\|/2)}{\|\boldsymbol{\theta}\|}\widehat{\mathbf{n}} + \left(1 - \frac{\sin(\|\boldsymbol{\theta}\|)}{\|\boldsymbol{\theta}\|}\right)\widehat{\mathbf{n}}^2
\end{aligned}
\tag{B.15}
$$

It should be noted that $\mathbf{H}^{-1}$ is singular for $\|\boldsymbol{\theta}\| = 2n\pi$, $n = 1, 2, \ldots$.

For $\|\boldsymbol{\theta}\| = 0$, the total rotation is described by $\boldsymbol{\theta}_0 = \boldsymbol{\theta}_t$, and the multiplicative differential is obtained, $\delta\boldsymbol{\theta} = \delta\boldsymbol{\omega}$ ($\mathbf{H}^{-1} = \mathbb{1}$):

$$
\delta\mathbf{R} = \mathrm{D}\mathbf{R}(\boldsymbol{\theta} = \mathbb{0})\mathbf{R}(\boldsymbol{\theta}_t)\cdot\delta\boldsymbol{\omega} = \mathrm{Spin}(\mathbf{H}^{-1}\delta\boldsymbol{\omega})\mathbf{R} = \widehat{\delta\boldsymbol{\omega}}\mathbf{R} \tag{B.16}
$$

otherwise

$$
\delta\mathbf{R} = \mathrm{D}\mathbf{R}(\boldsymbol{\theta})\cdot\delta\boldsymbol{\theta} = \mathrm{Spin}(\mathbf{H}^{-1}\delta\boldsymbol{\theta})\mathbf{R} \tag{B.17}
$$

Since equations (B.16) and (B.17) should produce the same perturbed $\delta\mathbf{R}$, we get:

$$
\mathrm{Spin}(\mathbf{H}^{-1}\delta\boldsymbol{\theta}) = \widehat{\delta\boldsymbol{\omega}} \quad\Leftrightarrow\quad \mathbf{H}^{-1}\delta\boldsymbol{\theta} = \delta\boldsymbol{\omega} \tag{B.18}
$$

For nonsingular $\mathbf{H}^{-1}$, we have:

$$
\delta\boldsymbol{\theta} = \mathbf{H}\delta\boldsymbol{\omega} \tag{B.19}
$$

Appendix C
Geometric interpretation of the exponential map of rotations

"On a *Lie group*, exp is a map from the *Lie algebra* to its Lie group. If you think of the Lie algebra as the *tangent space* to the identity of the Lie group, exp(v) is defined to be *h(1)*, where *h* is the unique Lie group *homeomorphism* from the real numbers to the Lie group such that its velocity at time 0 is *v*."[1]

In this particular case, the Lie algebra is the set of all skew symmetric matrices, $\mathbf{so}(3) \subset \mathbb{R}^{3x3}$ with the commutator (Lie bracket) $[\widehat{\alpha}, \widehat{\beta}] = \widehat{\alpha}\widehat{\beta} - \widehat{\beta}\widehat{\alpha} \in \mathbf{so}(3)$, and the Lie group is the rotation group **SO**(3). The purpose of this appendix is not to delve into the intricacies of group-theory and abstract algebra, but rather to give an intuitive interpretation of the exponential map and how it relates the spins to the rotations. To do so, we

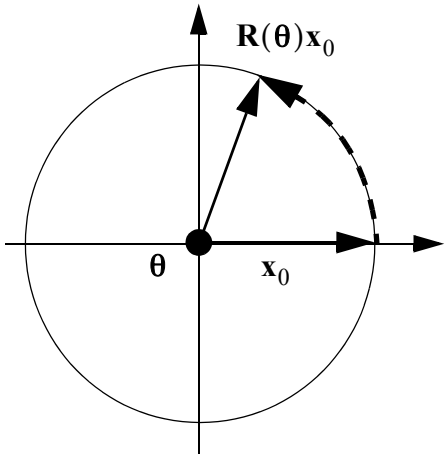

Figure C.1 Rotation of vector $\mathbf{x}_0$

1. Eric W. Weisstein. "Exponential Map." From *MathWorld*--A Wolfram Web Resource. http://mathworld.wolfram.com/ExponentialMap.html.

start by looking at the action of rotating a vector in space. As a rotation only affect the components of the vector projected onto the rotation plane, the motion will be illustrated in this plane.

Figure C.1 depicts two approximations of the rotation of the vector $\mathbf{x}_0$ from its state of identity to the final position $\mathbf{x}_1$ and $\mathbf{x}_2$, respectively. These approximations are obtained

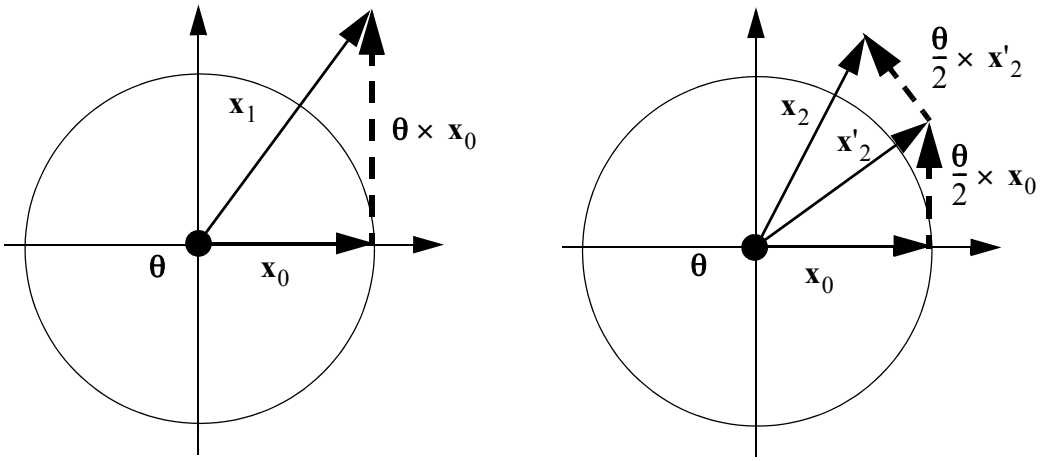

Figure C.1 Successive approximations

by adding the cross product with the pseudovector incrementally, written in matrix form as:

$$\mathbf{x}_1 = [\mathbb{1} + \text{Spin}(\theta)]\mathbf{x}_0 \tag{C.1}$$

$$\mathbf{x}_2 = \left[\mathbb{1} + \frac{1}{2}\text{Spin}(\theta)\right]\left[\mathbb{1} + \frac{1}{2}\text{Spin}(\theta)\right]\mathbf{x}_0 \tag{C.2}$$

Equation (C.2) is a second order approximation to the rotated vector, whereas (C.1) is only a first order approximation. Intuitively, as we proceed in smaller increments, the vector should trace the circular line. By defining the general form of this approximation, we get

$$\mathbf{x}_n = \left[\mathbb{1} + \frac{1}{n}\text{Spin}(\theta)\right]^n \mathbf{x}_0 \tag{C.3}$$

Taking the limit as n approaches infinity, we get the exponential map:

$$\mathbf{x} = \lim_{n\to\infty} \mathbf{x}_n = \lim_{n\to\infty}\left[\mathbb{1} + \frac{1}{n}\mathrm{Spin}(\boldsymbol{\theta})\right]^n \mathbf{x}_0 = \exp(\widehat{\boldsymbol{\theta}})\,\mathbf{x}_0 = \mathbf{R}(\boldsymbol{\theta})\mathbf{x}_0 \tag{C.4}$$

Where the definition $\exp(\widehat{\boldsymbol{\theta}}) = \lim_{n\to\infty}\left[\mathbb{1} + \frac{1}{n}\mathrm{Spin}(\boldsymbol{\theta})\right]^n$ is used in the last transition.

To obtain a closed-form solution of $\exp(\widehat{\boldsymbol{\theta}})$, we introduce the series-expansion of the exponential function:

$$\exp(\widehat{\boldsymbol{\theta}}) = \mathbb{1} + \sum_{k=1}^{\infty} \frac{1}{k!}\widehat{\boldsymbol{\theta}}^k \tag{C.5}$$

As it can be shown by simply performing the matrix multiplications, that

$$\widehat{\mathbf{a}}\,\widehat{\mathbf{b}}\,\widehat{\mathbf{a}} = -(\mathbf{a}\cdot\mathbf{b})\,\widehat{\mathbf{a}} \tag{C.6}$$

holds for arbitrary vectors $\mathbf{a}$ and $\mathbf{b}$. Applying this to Equation (C.5), and using $\boldsymbol{\theta} = \|\boldsymbol{\theta}\|\mathbf{n}$, for odd numbered k we get:

$$\frac{1}{k!}\widehat{\boldsymbol{\theta}}^k = \frac{(-\|\boldsymbol{\theta}\|^2)^{\frac{k-1}{2}}}{k!}\widehat{\boldsymbol{\theta}} = \frac{(-1)^{\frac{k-1}{2}}\|\boldsymbol{\theta}\|^{k-1}}{k!}\widehat{\boldsymbol{\theta}} = \frac{(-1)^{\frac{k-1}{2}}\|\boldsymbol{\theta}\|^{k}}{k!}\widehat{\mathbf{n}} \tag{C.7}$$

For even numbered terms, we have:

$$\frac{1}{k!}\widehat{\boldsymbol{\theta}}^k = \frac{(-\|\boldsymbol{\theta}\|^2)^{\frac{k-2}{2}}}{k!}\widehat{\boldsymbol{\theta}}^2 = \frac{(-1)^{\frac{k}{2}-1}\|\boldsymbol{\theta}\|^{k}}{k!}\widehat{\mathbf{n}}^2 \tag{C.8}$$

Organizing and collecting terms, we obtain the Rodriguez formula for rotations:

$$\begin{aligned}\mathbf{R}(\boldsymbol{\theta}) = \exp(\widehat{\boldsymbol{\theta}}) &= \mathbb{1} + \sum_{k=1,\,3,\,5,\,\ldots} \frac{(-1)^{\frac{k-1}{2}}\|\boldsymbol{\theta}\|^{k}}{k!}\widehat{\mathbf{n}} + \sum_{k=2,\,4,\,6,\,\ldots} \frac{(-1)^{\frac{k}{2}-1}\|\boldsymbol{\theta}\|^{k}}{k!}\widehat{\mathbf{n}}^2 \\ &= \mathbb{1} + \sum_{k=0}^{\infty} \frac{(-1)^k\|\boldsymbol{\theta}\|^{2k+1}}{(2k+1)!}\widehat{\mathbf{n}} - \sum_{k=1}^{\infty} \frac{(-1)^k\|\boldsymbol{\theta}\|^{2k}}{(2k)!}\widehat{\mathbf{n}}^2 \\ &= \mathbb{1} + \sin\|\boldsymbol{\theta}\|\,\widehat{\mathbf{n}} + (1-\cos\|\boldsymbol{\theta}\|)\,\widehat{\mathbf{n}}^2\end{aligned} \tag{C.9}$$

Appendix D
Extraction of rotational pseudovector and establishing the rotation matrix

The most reliable method of extracting the rotational pseudovector from the rotation matrix is to go via the *quaternion* representation. A quaternion represents a hypercomplex number $q = q_0 + \mathrm{i}q_1 + \mathrm{j}q_2 + \mathrm{k}q_3 = q_0 + \mathbf{q}$, where

$$q_0 = \cos(\theta/2) \tag{D.1}$$

$$\|\mathbf{q}\|^2 = q_1^2 + q_2^2 + q_3^2 = \sin^2(\theta/2) \tag{D.2}$$

$$\mathbf{n} = \frac{\mathbf{q}}{\|\mathbf{q}\|} \tag{D.3}$$

$$\|\mathbf{q}\|^2 + q_0^2 = 1 \tag{D.4}$$

For the extraction of the quaternions from a given rotation matrix **R**, Spurriers algorithm [38], presented on the next page, is fast and reportedly the most reliable, particularly for small rotations. When using this algorithm, it should be noted that the resulting rotations are in the range from 0 to 2π ($-1 \le q_0 \le 1$). Thus, for rotations exceeding π, a "corrected value of $\theta^* = \theta - 2\pi$ should be used.

The rotation matrix, based on the quaternions, is established as follows:

$$\mathbf{R} = 2\begin{bmatrix} q_1^2 + q_0^2 - \frac{1}{2} & q_1q_2 - q_0q_3 & q_1q_3 + q_0q_2 \\ q_1q_2 + q_0q_3 & q_2^2 + q_0^2 - \frac{1}{2} & q_2q_3 - q_0q_1 \\ q_1q_3 - q_0q_2 & q_2q_3 + q_0q_1 & q_3^2 + q_0^2 - \frac{1}{2} \end{bmatrix} \tag{D.5}$$

Spurrier's algorithm:

$M = max(trace(\mathbf{R}),\ R_{11},\ R_{22},\ R_{33})$

if ($M = trace(\mathbf{R})$) then

$q_0 = \frac{1}{2}\sqrt{1 + trace(\mathbf{R})}$

$q_i = \frac{1}{4}(R_{kj} - R_{jk}) / q_0$ for $i = 1, 2, 3$ and cyclic, even permutations of i, j, k

else

let i be such that $R_{ii} = M$

$q_i = \sqrt{\left(\frac{1}{2}R_{ii} + \frac{(1 - trace(\mathbf{R}))}{4}\right)}$

$q_0 = \frac{1}{4}(R_{kj} - R_{jk}) / q_i$

$q_j = \frac{1}{4}(R_{ji} - R_{ij}) / q_i$

$q_k = \frac{1}{4}(R_{ki} - R_{ik}) / q_i$

end

$p = \sqrt{q_0^2 + q_1^2 + q_2^2 + q_3^2}$

$q_0 = q_0 / p$

$\mathbf{q} = \mathbf{q} / p$

Appendix E
Variation of a co-rotating frame for an element with 2 nodes

In the following the derivation of the matrix $\mathbf{G}$ that links the variation in the visible degrees of freedom, $\delta\tilde{\mathbf{v}}$, to the variation of the rigid body rotations $\delta\tilde{\boldsymbol{\omega}}_r$ for a 2-node element will be presented. A similar derivation has been presented by several authors, among which Haugen [16] and Eggen [10] can be mentioned for a clear and concise presentation. In the derivation that follows, the definition of the base vectors will follow the same geometric considerations as in [10, 16]. The principal reason for including this appendix is to conform with the notation in the previous chapters. In [10] and [16] the derivation was based on geometric considerations, in the following a purely mathematical approach will be presented, starting with the general form of variations of an orthogonal co-rotating basis. As this mathematical approach may preclude intuitive understanding, the interested reader should confer with the referred work to get a more physical interpretation.

E.1 General relations

From previous derivations in Chapter 4, we have:

$$\mathbf{T}_r = \mathbf{E}_i^0 \otimes \mathbf{E}_i^n = \mathbf{R}_r^{\mathsf{T}} \tag{E.1}$$

Where each $\mathbf{E}_i^n$ and $\mathbf{E}_i^0$ must be uniquely defined. Leaving the actual definition of these base vectors to the next section, we proceed by taking the variation of the transpose of (E.1):

$$\begin{aligned} \delta\mathbf{T}_r^{\mathsf{T}} &= \delta\mathbf{E}_i^n \otimes \mathbf{E}_i^0 = \delta\widehat{\boldsymbol{\omega}}_r \mathbf{T}_r^{\mathsf{T}} \\ \Rightarrow \quad \delta\widehat{\boldsymbol{\omega}}_r &= \delta\mathbf{T}_r^{\mathsf{T}}\mathbf{T}_r = \delta\mathbf{E}_i^n \otimes \mathbf{E}_i^n \end{aligned} \tag{E.2}$$

As we are seeking a relation expressed in coordinates of $\mathbf{E}_i^n$, (E.2) is transformed to obtain the local form:

$$\delta\widehat{\tilde{\boldsymbol{\omega}}}_r = \mathbf{T}_n \delta\widehat{\boldsymbol{\omega}}_r \mathbf{T}_n^{\mathsf{T}} = \mathbf{T}_n \delta\mathbf{T}_r^{\mathsf{T}} \mathbf{T}_0 = (\mathbf{I}_i \otimes \mathbf{E}_i^n)(\delta\mathbf{E}_j^n \otimes \mathbf{I}_j) \tag{E.3}$$

In the following, superscripts indicating configuration will be omitted for the base vectors, assuming updated axes $\{\mathbf{E}_i^n\}$ are used. Because we know that $\delta\widehat{\tilde{\boldsymbol{\omega}}}_r$ is a skew symmetric matrix, we can extract the axial vector by means of the alternator e_{ijk}, defined in (E.5).

$$\delta\tilde{\omega}_r^i = -\frac{1}{2} e_{ijk} \delta_{jl} \mathrm{E}_l^m \delta\mathrm{E}_n^m \delta_{kn} \tag{E.4}$$

where the alternator is defined as

$$e_{ijk} = \begin{cases} 0, & \text{repeated indices} \\ 1, & \text{even permutations of } (i,\ j,\ k) \\ -1, & \text{odd permutations of } (i,\ j,\ k) \end{cases} \tag{E.5}$$

and also, by definition

$$[\mathrm{Axial}(\mathbf{W})]_i = -\frac{1}{2} e_{ijk} \mathbf{W}_{jk}, \quad [\mathrm{Spin}(\mathbf{w})]_{ik} = e_{ijk} \mathrm{w}_j \tag{E.6}$$

For each component $\delta\tilde{\omega}_r^i$ of $\delta\tilde{\boldsymbol{\omega}}_r$ we get:

$$\delta\tilde{\omega}_r^1 = -\frac{1}{2} e_{123} \mathrm{E}_2^m \delta\mathrm{E}_3^m - \frac{1}{2} e_{132} \mathrm{E}_3^m \delta\mathrm{E}_2^m = \frac{1}{2}(\mathbf{E}_3 \cdot \delta\mathbf{E}_2 - \mathbf{E}_2 \cdot \delta\mathbf{E}_3) \tag{E.7}$$

$$\delta\tilde{\omega}_r^2 = -\frac{1}{2} e_{231} \mathrm{E}_3^m \delta\mathrm{E}_1^m - \frac{1}{2} e_{213} \mathrm{E}_1^m \delta\mathrm{E}_3^m = \frac{1}{2}(\mathbf{E}_1 \cdot \delta\mathbf{E}_3 - \mathbf{E}_3 \cdot \delta\mathbf{E}_1) \tag{E.8}$$

$$\delta\tilde{\omega}_r^3 = -\frac{1}{2} e_{312} \mathrm{E}_1^m \delta\mathrm{E}_2^m - \frac{1}{2} e_{321} \mathrm{E}_2^m \delta\mathrm{E}_1^m = \frac{1}{2}(\mathbf{E}_2 \cdot \delta\mathbf{E}_1 - \mathbf{E}_1 \cdot \delta\mathbf{E}_2) \tag{E.9}$$

The basis $\{\mathbf{E}_i\}$, is by definition an orthonormal right-handed system, yielding the following useful expressions:

$$\mathbf{E}_1 = \mathbf{E}_2 \times \mathbf{E}_3, \quad \mathbf{E}_2 = \mathbf{E}_3 \times \mathbf{E}_1, \quad \mathbf{E}_3 = \mathbf{E}_1 \times \mathbf{E}_2 \tag{E.10}$$

$$\delta\mathbf{E}_2 = \widehat{\mathbf{E}}_3 \delta\mathbf{E}_1 - \widehat{\mathbf{E}}_1 \delta\mathbf{E}_3 \tag{E.11}$$

$$\mathbf{E}_1 \cdot \delta\mathbf{E}_2 = -\mathbf{E}_2 \cdot \delta\mathbf{E}_1, \quad \mathbf{E}_3 \cdot \delta\mathbf{E}_2 = -\mathbf{E}_2 \cdot \delta\mathbf{E}_3 \tag{E.12}$$

$$\delta\mathbf{E}_3 = \widehat{\mathbf{E}}_1 \delta\mathbf{E}_2 - \widehat{\mathbf{E}}_2 \delta\mathbf{E}_1 \tag{E.13}$$

$$\mathbf{E}_1 \cdot \delta\mathbf{E}_3 = -\mathbf{E}_3 \cdot \delta\mathbf{E}_1, \quad \mathbf{E}_2 \cdot \delta\mathbf{E}_3 = -\mathbf{E}_3 \cdot \delta\mathbf{E}_2 \tag{E.14}$$

Organizing and combining terms in Equations (E.7) through (E.14), result in:

$$\delta\tilde{\boldsymbol{\omega}}_r = \begin{bmatrix} \mathbf{E}_3 \cdot \delta\mathbf{E}_2 \\ -\mathbf{E}_3 \cdot \delta\mathbf{E}_1 \\ \mathbf{E}_2 \cdot \delta\mathbf{E}_1 \end{bmatrix} \tag{E.15}$$

Equation (E.15) is now a general form of the variation of the instantaneous axis of rigid body rotation, expressed by the variation of the co-rotating basis.

E.2 Axes, definitions and variations (2-node beam)

The position of the two nodes of the element are given by the vectors $\mathbf{x}_I = \mathbf{x}_I^0 + \mathbf{v}_I$, where the $\mathbf{v}_I$'s are vectors collecting the total displacements at the node. The two points cannot uniquely define a complete basis in 3D. We therefore introduce the following auxiliary vector:

$$\mathbf{d}_m = \mathbf{R}_1 \mathbf{E}_3^0 + \mathbf{R}_2 \mathbf{E}_3^0 = \mathbf{d}_1 + \mathbf{d}_2 \tag{E.16}$$

where $\mathbf{E}_3^0$ is the initial base vector $\mathbf{E}_3$, and $\mathbf{R}_I$ is the current rotation at node I. Defining $\mathbf{E}_1$ to be parallel to the straight line from node 1 to node 2, the following becomes a natural choice of basis:

$$\mathbf{E}_1 = \frac{\mathbf{x}_2 - \mathbf{x}_1}{\|\mathbf{x}_2 - \mathbf{x}_1\|} = \frac{\mathbf{x}_{12}}{\|\mathbf{x}_{12}\|}, \quad \mathbf{E}_2 = \frac{\mathbf{d}_m \times \mathbf{E}_1}{\|\mathbf{d}_m \times \mathbf{E}_1\|}, \quad \mathbf{E}_3 = \mathbf{E}_1 \times \mathbf{E}_2 \tag{E.17}$$

Note that $\mathbf{d}_m \perp \mathbf{E}_2$ yields the following relation:

$$\left\|\mathbf{d}_m \times \mathbf{E}_1\right\| = \left\|\mathbf{T}_n^{\mathrm{T}}\tilde{\mathbf{d}}_m \times \mathbf{T}_n^{\mathrm{T}}\mathbf{I}_1\right\| = \left\|\tilde{\mathbf{d}}_m \times \mathbf{I}_1\right\| = \left|\tilde{\mathrm{d}}_m^3\right| = \tilde{\mathrm{d}}_m^3 \tag{E.18}$$

Here we have taken advantage of the fact that $\tilde{\mathrm{d}}_m^3 \geq 0$. Next we get the variation of $\mathbf{E}_1$ and $\mathbf{E}_2$:

$$\delta\mathbf{E}_1 = \frac{1}{\left\|\mathbf{x}_{12}\right\|}(\mathbb{1} - \mathbf{E}_1 \otimes \mathbf{E}_1)(\delta\mathbf{v}_2 - \delta\mathbf{v}_1) \tag{E.19}$$

$$\begin{aligned}\delta\mathbf{E}_2 &= \frac{1}{\tilde{\mathrm{d}}_m^3}(\mathbb{1} - \mathbf{E}_2 \otimes \mathbf{E}_2)\delta(\widehat{\mathbf{d}}_m\mathbf{E}_1) \\ &= \frac{1}{\tilde{\mathrm{d}}_m^3}(\mathbb{1} - \mathbf{E}_2 \otimes \mathbf{E}_2)[\widehat{\mathbf{d}}_m\delta\mathbf{E}_1 - \widehat{\mathbf{E}}_1\delta\mathbf{d}_m]\end{aligned} \tag{E.20}$$

$$\begin{aligned}\delta\mathbf{d}_m &= \mathbf{R}_1\delta\mathbf{i}_3^0 + \delta\mathbf{R}_1\mathbf{i}_3^0 + \mathbf{R}_2\delta\mathbf{i}_3^0 + \delta\mathbf{R}_2\mathbf{i}_3^0 = \mathrm{Spin}(\delta\boldsymbol{\omega}_1)\mathbf{d}_1 + \mathrm{Spin}(\delta\boldsymbol{\omega}_2)\mathbf{d}_2 \\ &= (\mathbf{E}_i \otimes \mathbf{I}_i)\mathrm{Spin}(\delta\tilde{\boldsymbol{\omega}}_1)\tilde{\mathbf{d}}_1 + (\mathbf{E}_i \otimes \mathbf{I}_i)\mathrm{Spin}(\delta\tilde{\boldsymbol{\omega}}_2)\tilde{\mathbf{d}}_2\end{aligned} \tag{E.21}$$

We now need the contracted vectors $\mathbf{E}_2 \cdot \delta\mathbf{E}_1$, $\mathbf{E}_3 \cdot \delta\mathbf{E}_1$ and $\mathbf{E}_3 \cdot \delta\mathbf{E}_2$. The first two are rather straightforward:

$$\mathbf{E}_2 \cdot \delta\mathbf{E}_1 = \frac{(\delta\tilde{\mathbf{v}}_2^2 - \delta\tilde{\mathbf{v}}_1^2)}{\left\|\mathbf{x}_{12}\right\|}, \quad \mathbf{E}_3 \cdot \delta\mathbf{E}_1 = \frac{(\delta\tilde{\mathbf{v}}_2^3 - \delta\tilde{\mathbf{v}}_1^3)}{\left\|\mathbf{x}_{12}\right\|} \tag{E.22}$$

The derivation of the last expression, however, is a more lengthy affair:

$$\begin{aligned}\mathbf{E}_3 \cdot \delta\mathbf{E}_2 &= \frac{1}{\tilde{\mathrm{d}}_m^3}\mathbf{E}_3 \cdot (\mathbb{1} - \mathbf{E}_2 \otimes \mathbf{E}_2)[\widehat{\mathbf{d}}_m\delta\mathbf{E}_1 - \widehat{\mathbf{E}}_1\delta\mathbf{d}_m] \\ &= \frac{1}{\tilde{\mathrm{d}}_m^3}\mathbf{E}_3 \cdot [\widehat{\mathbf{d}}_m\delta\mathbf{E}_1 - \widehat{\mathbf{E}}_1\delta\mathbf{d}_m] \\ &= \frac{1}{\tilde{\mathrm{d}}_m^3}[\mathbf{E}_3 \cdot \widehat{\mathbf{d}}_m\delta\mathbf{E}_1 - (\mathbf{E}_2 \cdot \delta\mathbf{d}_m)]\end{aligned} \tag{E.23}$$

The expression (E.23) is divided into two parts, which are evaluated separately for convenience:

$$
\begin{aligned}
\frac{-1}{\tilde{d}_m^3}(\mathbf{E}_2 \cdot \ \delta\mathbf{d}_m) &= \frac{-1}{\tilde{d}_m^3}\mathbf{I}_2 \cdot \ [\mathrm{Spin}(\delta\tilde{\boldsymbol{\omega}}_1)\tilde{\mathbf{d}}_1 + \mathrm{Spin}(\delta\tilde{\boldsymbol{\omega}}_2)\tilde{\mathbf{d}}_2] \\
&= \frac{1}{\tilde{d}_m^3}\mathbf{I}_2 \cdot \ [\mathrm{Spin}(\tilde{\mathbf{d}}_1)\delta\tilde{\boldsymbol{\omega}}_1 + \mathrm{Spin}(\tilde{\mathbf{d}}_2)\delta\tilde{\boldsymbol{\omega}}_2] \\
&= \frac{-1}{\tilde{d}_m^3}[\mathrm{Spin}(\tilde{\mathbf{d}}_1)\mathbf{I}_2 \cdot \ \delta\tilde{\boldsymbol{\omega}}_1 + \mathrm{Spin}(\tilde{\mathbf{d}}_2)\mathbf{I}_2 \cdot \ \delta\tilde{\boldsymbol{\omega}}_2] \qquad \text{(E.24)} \\
&= \frac{1}{\tilde{d}_m^3}\left[\begin{bmatrix} \tilde{d}_1^3 \\ 0 \\ -\tilde{d}_1^1 \end{bmatrix} \cdot \ \delta\tilde{\boldsymbol{\omega}}_1 + \begin{bmatrix} \tilde{d}_2^3 \\ 0 \\ -\tilde{d}_2^1 \end{bmatrix} \cdot \ \delta\tilde{\boldsymbol{\omega}}_2\right]
\end{aligned}
$$

$$
\begin{aligned}
\frac{1}{\tilde{d}_m^3}[\mathbf{E}_3 \cdot \ \widehat{\mathbf{d}}_m\delta\mathbf{E}_1] &= \frac{1}{\tilde{d}_m^3\|\mathbf{x}_{12}\|}[\mathbf{E}_3 \cdot \ \widehat{\mathbf{d}}_m(\mathbb{1} - \mathbf{E}_1 \otimes \mathbf{E}_1)(\delta\mathbf{v}_2 - \delta\mathbf{v}_1)] \\
&= \frac{1}{\tilde{d}_m^3\|\mathbf{x}_{12}\|}[\mathbf{E}_3 \cdot \ (\widehat{\mathbf{d}}_m - \widehat{\mathbf{d}}_m\mathbf{E}_1 \otimes \mathbf{E}_1)(\delta\mathbf{v}_2 - \delta\mathbf{v}_1)] \\
&= \frac{1}{\tilde{d}_m^3\|\mathbf{x}_{12}\|}\mathbf{E}_3 \cdot \ \widehat{\mathbf{d}}_m(\delta\mathbf{v}_2 - \delta\mathbf{v}_1) \\
&\quad -\frac{1}{\|\mathbf{x}_{12}\|}\mathbf{E}_3 \cdot (\mathbf{E}_2 \otimes \mathbf{E}_1)(\delta\mathbf{v}_2 - \delta\mathbf{v}_1) \qquad \text{(E.25)} \\
&= \frac{1}{\tilde{d}_m^3\|\mathbf{x}_{12}\|}\mathbf{I}_3 \cdot \ \widetilde{\mathbf{d}}_m(\delta\tilde{\mathbf{v}}_2 - \delta\tilde{\mathbf{v}}_1) \\
&= \frac{1}{\tilde{d}_m^3\|\mathbf{x}_{12}\|}\begin{bmatrix} -\tilde{d}_m^2 & \tilde{d}_m^1 & 0 \end{bmatrix}(\delta\tilde{\mathbf{v}}_2 - \delta\tilde{\mathbf{v}}_1) \\
&= \frac{1}{\tilde{d}_m^3\|\mathbf{x}_{12}\|}\begin{bmatrix} 0 & \tilde{d}_m^1 & 0 \end{bmatrix}(\delta\tilde{\mathbf{v}}_2 - \delta\tilde{\mathbf{v}}_1)
\end{aligned}
$$

Collecting and organizing terms, we obtain the required relation:

$$\tilde{\delta\boldsymbol{\omega}}_r = \begin{bmatrix} \mathbf{E}_3 \cdot \delta\mathbf{E}_2 \\ -\mathbf{E}_3 \cdot \delta\mathbf{E}_1 \\ \mathbf{E}_2 \cdot \delta\mathbf{E}_1 \end{bmatrix}$$

$$= \frac{1}{\|\mathbf{x}_{12}\|} \begin{bmatrix} \frac{\tilde{d}_m^1}{\tilde{d}_m^3}(\tilde{\delta v}_2^2 - \tilde{\delta v}_1^2) \\ -(\tilde{\delta v}_2^3 - \tilde{\delta v}_1^3) \\ (\tilde{\delta v}_2^2 - \tilde{\delta v}_1^2) \end{bmatrix} + \frac{1}{\tilde{d}_m^3} \begin{bmatrix} \tilde{d}_1^3 \tilde{\delta\omega}_1^1 - \tilde{d}_1^1 \tilde{\delta\omega}_1^3 \\ 0 \\ 0 \end{bmatrix} + \frac{1}{\tilde{d}_m^3} \begin{bmatrix} \tilde{d}_2^3 \tilde{\delta\omega}_2^1 - \tilde{d}_2^1 \tilde{\delta\omega}_2^3 \\ 0 \\ 0 \end{bmatrix} \tag{E.26}$$

$$= \begin{bmatrix} \mathbf{G}_1 & \mathbf{G}_2 \end{bmatrix} \begin{bmatrix} \tilde{\delta\mathbf{v}}_1 \\ \tilde{\delta\boldsymbol{\omega}}_1 \\ \tilde{\delta\mathbf{v}}_2 \\ \tilde{\delta\boldsymbol{\omega}}_2 \end{bmatrix} = \mathbf{G}\tilde{\delta\mathbf{v}}$$

Where the matrices $\mathbf{G}_1$ and $\mathbf{G}_2$ are given by:

$$\mathbf{G}_1 = \begin{bmatrix} 0 & \frac{-1}{\|\mathbf{x}_{12}\|}\frac{\tilde{d}_m^1}{\tilde{d}_m^3} & 0 & \frac{\tilde{d}_1^3}{\tilde{d}_m^3} & 0 & \frac{-\tilde{d}_1^1}{\tilde{d}_m^3} \\ 0 & 0 & \frac{1}{\|\mathbf{x}_{12}\|} & 0 & 0 & 0 \\ 0 & \frac{-1}{\|\mathbf{x}_{12}\|} & 0 & 0 & 0 & 0 \end{bmatrix} \tag{E.27}$$

$$\mathbf{G}_2 = \begin{bmatrix} 0 & \frac{1}{\|\mathbf{x}_{12}\|}\frac{\tilde{d}_m^1}{\tilde{d}_m^3} & 0 & \frac{\tilde{d}_2^3}{\tilde{d}_m^3} & 0 & \frac{-\tilde{d}_2^1}{\tilde{d}_m^3} \\ 0 & 0 & \frac{-1}{\|\mathbf{x}_{12}\|} & 0 & 0 & 0 \\ 0 & \frac{1}{\|\mathbf{x}_{12}\|} & 0 & 0 & 0 & 0 \end{bmatrix} \tag{E.28}$$

Appendix F
Explicit expressions of EICR-matrices for a 2-node element

F.1 Projector

$$\mathbf{P} = \begin{bmatrix}
\frac{1}{2} & 0 & 0 & 0 & 0 & 0 & -\frac{1}{2} & 0 & 0 & 0 & 0 & 0 \\
0 & 0 & 0 & 0 & 0 & 0 & 0 & 0 & 0 & 0 & 0 & 0 \\
0 & 0 & 0 & 0 & 0 & 0 & 0 & 0 & 0 & 0 & 0 & 0 \\
0 & \frac{\tilde{d}^1_m}{L_n \tilde{d}^3_m} & 0 & 1-\frac{\tilde{d}^3_1}{\tilde{d}^3_m} & 0 & \frac{\tilde{d}^1_1}{\tilde{d}^3_m} & 0 & -\frac{\tilde{d}^1_m}{L_n \tilde{d}^3_m} & 0 & -\frac{\tilde{d}^3_2}{\tilde{d}^3_m} & 0 & \frac{\tilde{d}^1_2}{\tilde{d}^3_m} \\
0 & 0 & -\frac{1}{L_n} & 0 & 1 & 0 & 0 & 0 & \frac{1}{L_n} & 0 & 0 & 0 \\
0 & \frac{1}{L_n} & 0 & 0 & 0 & 1 & 0 & -\frac{1}{L_n} & 0 & 0 & 0 & 0 \\
-\frac{1}{2} & 0 & 0 & 0 & 0 & 0 & \frac{1}{2} & 0 & 0 & 0 & 0 & 0 \\
0 & 0 & 0 & 0 & 0 & 0 & 0 & 0 & 0 & 0 & 0 & 0 \\
0 & 0 & 0 & 0 & 0 & 0 & 0 & 0 & 0 & 0 & 0 & 0 \\
0 & \frac{\tilde{d}^1_m}{L_n \tilde{d}^3_m} & 0 & -\frac{\tilde{d}^3_1}{\tilde{d}^3_m} & 0 & \frac{\tilde{d}^1_1}{\tilde{d}^3_m} & 0 & -\frac{\tilde{d}^1_m}{L_n \tilde{d}^3_m} & 0 & 1-\frac{\tilde{d}^3_2}{\tilde{d}^3_m} & 0 & \frac{\tilde{d}^1_2}{\tilde{d}^3_m} \\
0 & 0 & -\frac{1}{L_n} & 0 & 0 & 0 & 0 & 0 & \frac{1}{L_n} & 0 & 1 & 0 \\
0 & \frac{1}{L_n} & 0 & 0 & 0 & 0 & 0 & \frac{1}{L_n} & 0 & 0 & 0 & 1
\end{bmatrix} \tag{F.1}$$

F.2 Projected forces

$$\tilde{\mathbf{f}}_b = \mathbf{P}^T\tilde{\mathbf{f}}_e = \begin{bmatrix} \frac{1}{2}(\tilde{n}_1^1 - \tilde{n}_2^1) \\ \frac{\tilde{d}_m^1(\tilde{m}_1^1 + \tilde{m}_{2x}) + \tilde{d}_m^3(\tilde{m}_1^3 + \tilde{m}_2^3)}{L_n\tilde{d}_m^3} \\ -\frac{\tilde{m}_1^2 + \tilde{m}_2^2}{L_n} \\ \tilde{m}_1^1 - \frac{\tilde{d}_1^3}{\tilde{d}_m^3}(\tilde{m}_1^1 + \tilde{m}_2^1) \\ \tilde{m}_1^2 \\ \frac{\tilde{d}_m^3\hat{m}_{1z} + \tilde{d}_1^1(\tilde{m}_1^1 + \tilde{m}_2^1)}{\tilde{d}_m^3} \\ \text{----------} \\ -\frac{1}{2}(\tilde{n}_1^1 - \tilde{n}_2^1) \\ -\frac{\tilde{d}_m^1(\tilde{m}_1^1 + \tilde{m}_2^1) + \tilde{d}_m^3(\tilde{m}_1^3 + \tilde{m}_2^3)}{L_n\tilde{d}_m^3} \\ \frac{\tilde{m}_1^2 + \tilde{m}_2^2}{L_n} \\ \tilde{m}_2^1 - \frac{\tilde{d}_2^3}{\tilde{d}_m^3}(\tilde{m}_1^1 + \tilde{m}_2^1) \\ \tilde{m}_2^2 \\ \frac{\tilde{d}_m^3\tilde{m}_2^3 + \tilde{d}_2^1(\tilde{m}_1^1 + \tilde{m}_2^1)}{\tilde{d}_m^3} \end{bmatrix} = \begin{bmatrix} \tilde{\mathbf{n}}_1 \\ \tilde{\mathbf{m}}_1 \\ \tilde{\mathbf{n}}_2 \\ \tilde{\mathbf{m}}_2 \end{bmatrix} \tag{F.2}$$

$$\tilde{\mathbf{n}}_1 = -\tilde{\mathbf{n}}_2 \tag{F.3}$$

F.3 Geometric stiffness

Projection geometric stiffness

$$\mathbf{K}_{GP} = \frac{1}{L_n}\begin{bmatrix} 0 & 0 & 0 & 0 & 0 & 0 & 0 & 0 & 0 & 0 & 0 & 0 \\ \tilde{n}_1^2 & 0 & 0 & 0 & 0 & 0 & -\tilde{n}_1^2 & 0 & 0 & 0 & 0 & 0 \\ \tilde{n}_1^3 & 0 & 0 & 0 & 0 & 0 & -\tilde{n}_1^3 & 0 & 0 & 0 & 0 & 0 \\ 0 & 0 & 0 & 0 & 0 & 0 & 0 & 0 & 0 & 0 & 0 & 0 \\ 0 & 0 & 0 & 0 & 0 & 0 & 0 & 0 & 0 & 0 & 0 & 0 \\ 0 & 0 & 0 & 0 & 0 & 0 & 0 & 0 & 0 & 0 & 0 & 0 \\ 0 & 0 & 0 & 0 & 0 & 0 & 0 & 0 & 0 & 0 & 0 & 0 \\ \tilde{n}_2^2 & 0 & 0 & 0 & 0 & 0 & -\tilde{n}_2^2 & 0 & 0 & 0 & 0 & 0 \\ \tilde{n}_2^3 & 0 & 0 & 0 & 0 & 0 & -\tilde{n}_2^3 & 0 & 0 & 0 & 0 & 0 \\ 0 & 0 & 0 & 0 & 0 & 0 & 0 & 0 & 0 & 0 & 0 & 0 \\ 0 & 0 & 0 & 0 & 0 & 0 & 0 & 0 & 0 & 0 & 0 & 0 \\ 0 & 0 & 0 & 0 & 0 & 0 & 0 & 0 & 0 & 0 & 0 & 0 \end{bmatrix} \tag{F.4}$$

Rotational geometric stiffness

The rotational geometric stiffness is divided into three parts for convenience:

$$\mathbf{K}_{GR1} = \frac{1}{L_n}\begin{bmatrix} 0 & \tilde{n}_1^2 & \tilde{n}_1^3 & 0 & 0 & 0 & 0 & -\tilde{n}_1^2 & -\tilde{n}_1^3 & 0 & 0 & 0 \\ 0 & -\tilde{n}_1^1 & 0 & 0 & 0 & 0 & 0 & \tilde{n}_1^1 & 0 & 0 & 0 & 0 \\ 0 & 0 & -\tilde{n}_1^1 & 0 & 0 & 0 & 0 & 0 & \tilde{n}_1^1 & 0 & 0 & 0 \\ 0 & 0 & 0 & 0 & 0 & 0 & 0 & 0 & 0 & 0 & 0 & 0 \\ 0 & 0 & 0 & 0 & 0 & 0 & 0 & 0 & 0 & 0 & 0 & 0 \\ 0 & 0 & 0 & 0 & 0 & 0 & 0 & 0 & 0 & 0 & 0 & 0 \\ 0 & \tilde{n}_2^2 & \tilde{n}_2^3 & 0 & 0 & 0 & 0 & -\tilde{n}_2^2 & -\tilde{n}_2^3 & 0 & 0 & 0 \\ 0 & -\tilde{n}_2^1 & 0 & 0 & 0 & 0 & 0 & \tilde{n}_2^1 & 0 & 0 & 0 & 0 \\ 0 & 0 & -\tilde{n}_2^1 & 0 & 0 & 0 & 0 & 0 & \tilde{n}_2^1 & 0 & 0 & 0 \\ 0 & 0 & 0 & 0 & 0 & 0 & 0 & 0 & 0 & 0 & 0 & 0 \\ 0 & 0 & 0 & 0 & 0 & 0 & 0 & 0 & 0 & 0 & 0 & 0 \\ 0 & 0 & 0 & 0 & 0 & 0 & 0 & 0 & 0 & 0 & 0 & 0 \end{bmatrix} \tag{F.5}$$

By defining the auxiliary vector:

$$\mathbf{g} = \begin{bmatrix} 0 & -\tilde{n}_1^3 & \tilde{n}_1^2 & 0 & -\tilde{m}_1^3 & \tilde{m}_1^2 & 0 & -\tilde{n}_2^3 & \tilde{n}_2^2 & 0 & -\tilde{m}_2^3 & \tilde{m}_2^2 \end{bmatrix}^T \tag{F.6}$$

the second part of the rotational geometric stiffness is defined as:

$$\begin{aligned} \mathbf{K}_{GR2} = & \frac{\tilde{d}_1^3}{\tilde{d}_m^3} \begin{bmatrix} 0 & 0 & 0 & \mathbf{g} & 0 & 0 & 0 & 0 & 0 & 0 & 0 & 0 \end{bmatrix} \\ & + \frac{\tilde{d}_2^3}{\tilde{d}_m^3} \begin{bmatrix} 0 & 0 & 0 & 0 & 0 & 0 & 0 & 0 & 0 & \mathbf{g} & 0 & 0 \end{bmatrix} \\ & - \frac{\tilde{d}_m^1}{\tilde{d}_m^3 L_n} \begin{bmatrix} 0 & \mathbf{g} & 0 & 0 & 0 & 0 & 0 & 0 & 0 & 0 & 0 & 0 \end{bmatrix} \\ & + \frac{\tilde{d}_m^1}{\tilde{d}_m^3 L_n} \begin{bmatrix} 0 & 0 & 0 & 0 & 0 & 0 & 0 & \mathbf{g} & 0 & 0 & 0 & 0 \end{bmatrix} \\ & - \frac{\tilde{d}_1^1}{\tilde{d}_m^3} \begin{bmatrix} 0 & 0 & 0 & 0 & 0 & \mathbf{g} & 0 & 0 & 0 & 0 & 0 & 0 \end{bmatrix} \\ & - \frac{\tilde{d}_2^1}{\tilde{d}_m^3} \begin{bmatrix} 0 & 0 & 0 & 0 & 0 & 0 & 0 & 0 & 0 & 0 & 0 & \mathbf{g} \end{bmatrix} \end{aligned} \tag{F.7}$$

The third part is defined as:

$$\mathbf{K}_{GR3} = \frac{1}{L_n} \begin{bmatrix} 0 & 0 & 0 & 0 & 0 & 0 & 0 & 0 & 0 & 0 & 0 & 0 \\ 0 & 0 & 0 & 0 & 0 & 0 & 0 & 0 & 0 & 0 & 0 & 0 \\ 0 & 0 & 0 & 0 & 0 & 0 & 0 & 0 & 0 & 0 & 0 & 0 \\ 0 & \tilde{m}_1^2 & \tilde{m}_1^3 & 0 & 0 & 0 & 0 & -\tilde{m}_1^2 & -\tilde{m}_1^3 & 0 & 0 & 0 \\ 0 & -\tilde{m}_1^1 & 0 & 0 & 0 & 0 & 0 & \tilde{m}_1^1 & 0 & 0 & 0 & 0 \\ 0 & 0 & -\tilde{m}_1^1 & 0 & 0 & 0 & 0 & 0 & \tilde{m}_1^1 & 0 & 0 & 0 \\ 0 & 0 & 0 & 0 & 0 & 0 & 0 & 0 & 0 & 0 & 0 & 0 \\ 0 & 0 & 0 & 0 & 0 & 0 & 0 & 0 & 0 & 0 & 0 & 0 \\ 0 & 0 & 0 & 0 & 0 & 0 & 0 & 0 & 0 & 0 & 0 & 0 \\ 0 & \tilde{m}_2^2 & \tilde{m}_2^3 & 0 & 0 & 0 & 0 & -\tilde{m}_2^2 & -\tilde{m}_2^3 & 0 & 0 & 0 \\ 0 & -\tilde{m}_2^1 & 0 & 0 & 0 & 0 & 0 & \tilde{m}_2^1 & 0 & 0 & 0 & 0 \\ 0 & 0 & -\tilde{m}_2^1 & 0 & 0 & 0 & 0 & 0 & \tilde{m}_2^1 & 0 & 0 & 0 \end{bmatrix} \tag{F.8}$$

It should be noted that the projection geometric stiffness and the first part of the rotational geometric stiffness form a symmetric matrix:

$$\mathbf{K}_{GR1} + \mathbf{K}_P = \frac{1}{L_n}\begin{bmatrix} 0 & \tilde{n}_1^2 & \tilde{n}_1^3 & 0 & 0 & 0 & 0 & -\tilde{n}_1^2 & -\tilde{n}_1^3 & 0 & 0 & 0 \\ \tilde{n}_1^2 & -\tilde{n}_1^1 & 0 & 0 & 0 & 0 & -\tilde{n}_1^2 & \tilde{n}_1^1 & 0 & 0 & 0 & 0 \\ \tilde{n}_1^3 & 0 & -\tilde{n}_1^1 & 0 & 0 & 0 & -\tilde{n}_1^3 & 0 & \tilde{n}_1^1 & 0 & 0 & 0 \\ 0 & 0 & 0 & 0 & 0 & 0 & 0 & 0 & 0 & 0 & 0 & 0 \\ 0 & 0 & 0 & 0 & 0 & 0 & 0 & 0 & 0 & 0 & 0 & 0 \\ 0 & 0 & 0 & 0 & 0 & 0 & 0 & 0 & 0 & 0 & 0 & 0 \\ 0 & -\tilde{n}_1^2 & -\tilde{n}_1^3 & 0 & 0 & 0 & 0 & \tilde{n}_1^2 & \tilde{n}_1^3 & 0 & 0 & 0 \\ -\tilde{n}_1^2 & \tilde{n}_1^1 & 0 & 0 & 0 & 0 & \tilde{n}_1^2 & -\tilde{n}_1^1 & 0 & 0 & 0 & 0 \\ -\tilde{n}_1^3 & 0 & \tilde{n}_1^1 & 0 & 0 & 0 & \tilde{n}_1^3 & 0 & -\tilde{n}_1^1 & 0 & 0 & 0 \\ 0 & 0 & 0 & 0 & 0 & 0 & 0 & 0 & 0 & 0 & 0 & 0 \\ 0 & 0 & 0 & 0 & 0 & 0 & 0 & 0 & 0 & 0 & 0 & 0 \\ 0 & 0 & 0 & 0 & 0 & 0 & 0 & 0 & 0 & 0 & 0 & 0 \end{bmatrix} \quad \text{(F.9)}$$

Appendix G

Contracted matrices for Cosserat elements

Material stiffness

$$\mathbf{S}_{IJ} = \int_{[0,\ L]} \hat{\boldsymbol{\Xi}}_{hI}\hat{\boldsymbol{\Pi}}\hat{\mathbf{C}}\hat{\boldsymbol{\Pi}}^{\mathsf{T}}\hat{\boldsymbol{\Xi}}_{hJ}^{\mathsf{T}}\,dS$$

$$\hat{\boldsymbol{\Xi}}_{hI}\hat{\boldsymbol{\Pi}}\hat{\mathbf{C}}\hat{\boldsymbol{\Pi}}^{\mathsf{T}}\hat{\boldsymbol{\Xi}}_{hJ}^{\mathsf{T}} = \begin{bmatrix} \mathbf{S}_{IJ}^{11} & \mathbf{S}_{IJ}^{12} \\ \mathbf{S}_{IJ}^{21} & \mathbf{S}_{IJ}^{22} \end{bmatrix} \tag{G.1}$$

$$\begin{aligned}
\mathbf{S}_{IJ}^{11} &= \mathrm{B}'_I\hat{\mathbf{c}}_{11}\mathrm{B}'_J \\
\mathbf{S}_{IJ}^{12} &= \mathrm{B}'_I\hat{\mathbf{c}}_{12}\mathrm{B}'_J + \mathrm{B}'_I\hat{\mathbf{c}}_{11}\,\widehat{\hat{\boldsymbol{\varphi}}_0'}\,\mathrm{B}_J \\
\mathbf{S}_{IJ}^{21} &= \mathrm{B}'_I\hat{\mathbf{c}}_{21}\mathrm{B}'_J - \mathrm{B}_I\,\widehat{\hat{\boldsymbol{\varphi}}_0'}\hat{\mathbf{c}}_{11}\,\mathrm{B}'_J \\
\mathbf{S}_{IJ}^{22} &= \mathrm{B}'_I\hat{\mathbf{c}}_{22}\mathrm{B}'_J - \mathrm{B}_I\,\widehat{\hat{\boldsymbol{\varphi}}_0'}\hat{\mathbf{c}}_{12}\mathrm{B}'_J + \mathrm{B}'_I\hat{\mathbf{c}}_{21}\,\widehat{\hat{\boldsymbol{\varphi}}_0'}\,\mathrm{B}_J - \mathrm{B}_I\,\widehat{\hat{\boldsymbol{\varphi}}_0'}\hat{\mathbf{c}}_{11}\,\widehat{\hat{\boldsymbol{\varphi}}_0'}\,\mathrm{B}_J
\end{aligned} \tag{G.2}$$

Geometric stiffness

$$\mathbf{T}_{IJ} = \int_{[0,\ L]} \boldsymbol{\Psi}_{hI}\hat{\mathbf{A}}\boldsymbol{\Psi}_{hJ}^{\mathsf{T}}\,dS$$

$$\boldsymbol{\Psi}_{hI}\hat{\mathbf{A}}\boldsymbol{\Psi}_{hJ}^{\mathsf{T}} = \begin{bmatrix} \mathbf{0} & -\mathrm{B}_I'\,\widehat{\mathbf{n}}\,\mathrm{B}_J \\ \mathrm{B}_I\,\widehat{\mathbf{n}}\,\mathrm{B}_J' & \mathrm{B}_I\mathbf{n}\otimes\boldsymbol{\varphi}_0'\mathrm{B}_J - \mathrm{B}_I(\mathbf{n}\cdot\boldsymbol{\varphi}_0')\mathbf{1}\mathrm{B}_J - \mathrm{B}_I'\,\widehat{\mathbf{m}}\,\mathrm{B}_J \end{bmatrix} \tag{G.3}$$

Appendix H
Spline functions

H.1 Definitions

Let $(\boldsymbol{c}_i)_{i=1}^{n}$ be a set of *control points* (weights) for a spline curve f of degree d, with nondecreasing knots $(\tau_i)_{i=1}^{n+d+1}$. f is then defined by:

$$f(\tau) = \sum_{i=d+1}^{n} p_{i,\,d}(\tau) B_{i,\,0}(\tau), \quad \tau \in [\tau_{d+1},\ \tau_{n+1}] \tag{H.1}$$

where $p_{i,\,d}(\tau)$ is given by the recurrence relation:

$$p_{i,\,d-r+1}(\tau) = \frac{\tau_{i+r} - \tau}{\tau_{i+r} - t_i} p_{i-1,\,d-r}(\tau) + \frac{\tau - \tau_i}{\tau_{i+r} - \tau_i} p_{i,\,d-r}(\tau) \tag{H.2}$$

for $i = d-r+1, \ldots, n$, and $r = d,\ d-1, \ldots, 1$, while $p_{i,\,0}(\tau) = \boldsymbol{c}_i$. Alternatively, Equation (H.2) can be written as

$$p_{i,\,d}(\tau) = \frac{\tau_{i+1} - \tau}{\tau_{i+1} - \tau_i} p_{i-1,\,d-1}(\tau) + \frac{\tau - \tau_i}{\tau_{i+1} - \tau_i} p_{i,\,d-1}(\tau) \tag{H.3}$$

The functions $\{B_{i,\,0}\}_{i=d+1}^{n}$ are given by

$$B_{i,\,0}(\tau) = \begin{cases} 1, & \tau_i \le \tau < \tau_{i+1} \\ 0, & \text{otherwise} \end{cases} \tag{H.4}$$

The spline can also be written in the *B-spline basis* $B_{i,\,d}$ as in Equation H.5

$$f(\tau) = \sum_{i=1}^{n} c_i B_{i,\,d}(\tau) \tag{H.5}$$

with the recursive definition of the basis functions $B_{i,\,d}$:

$$B_{i,\,d}(\tau) = \frac{\tau - \tau_i}{\tau_{i+d} - \tau_i} B_{i,\,d-1}(\tau) + \frac{\tau_{i+1+d} - \tau}{\tau_{i+1+d} - \tau_{i+1}} B_{i+1,\,d-1}(\tau) \tag{H.6}$$

In the previous equations, some of the relations might yield division by zero. This is resolved by the fact that if $\tau_{i+1} - \tau_i = 0$, then $B_{i,\,0} \equiv 0$. By carrying out the recurrences, we find that when division by zero is encountered, we will always get $0/0$, which will be defined to be zero. Although the evaluation of the recurrence relation (H.6) may seem cumbersome, it is actually quite computationally cheap to evaluate the nonzero terms. This is illustrated in Figure H.1 (reprint of figure in [22]), where all nonzero basis functions $B_{i,3}$ are calculated.

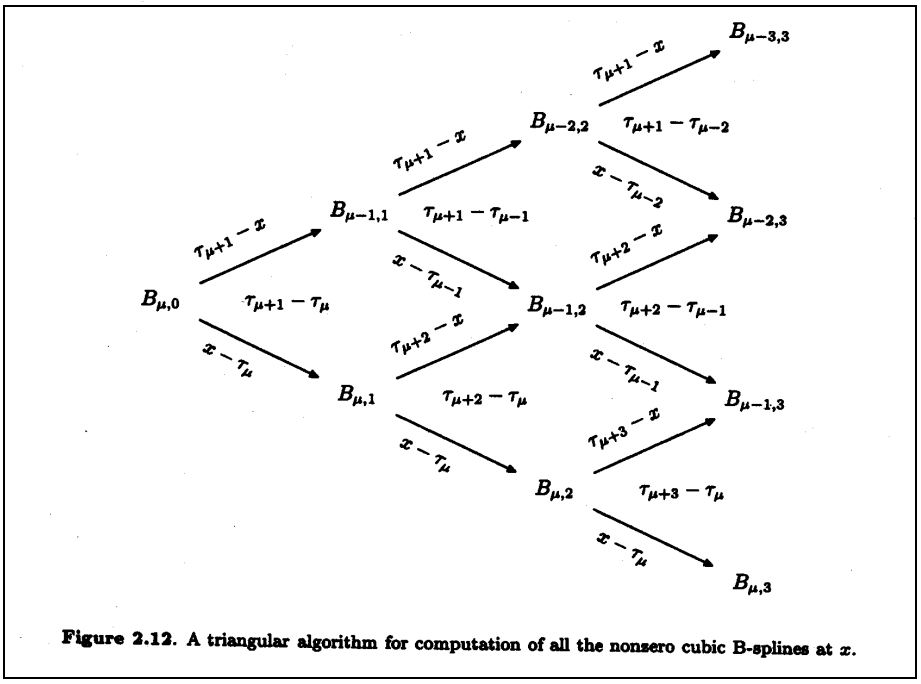

Figure 2.12. A triangular algorithm for computation of all the nonzero cubic B-splines at x.

Figure H.1 Evaluation of nonzero *B*-spline basis functions

Note that the spline is independent of the end knots τ_1 and τ_{n+d+1}, which are introduced to avoid exeption handling at the ends. Still, it is customary to demand that $\tau_1 \le \tau_2$ and $\tau_{n+d} \le \tau_{n+d+1}$, so the knot vector is a strictly non decreasing sequence.

H.2 Properties of splines and B-splines

- The B-spline $B_{j,\ d}$ depends only on the knots $(\tau_k)_{k=j}^{j+d+1}$.
- On each interval $\tau \in [\tau_j,\ \tau_{j+1})$, $f(\tau) = \sum c_i B_{i,\ d}(\tau)$ is a polynomial of degree *d*.
- $f(\tau)$ is C^{d-m}-continous at a point *z*, where *m* is the number of times *z* occur among $\tau_j,\ \ldots,\ \tau_{j+d+1}$.
- The *control polynomial* of a spline function, is defined as the points with coordinates $(\tau_j^*,\ c_j),\ j = 1,\ \ldots,\ n$ where $\tau_j^* = \frac{\tau_{j+1} + \cdots + \tau_{j+d}}{d}$
- If τ is outside the interval $[\tau_j,\ \tau_{j+d+1})$ then $B_{j,\ d} = 0$, so for $\tau \in [\tau_\mu,\ \tau_{\mu+1})$

$$f(\tau) = \sum_{i=\mu-d}^{\mu} c_i B_{i,\ d}(\tau)$$

The name “spline” comes from the “draftman’s spline”, a flexible rod used by ship builders to trace the contour of the hull of the ship by pinning it at predetermined points. The reason for using this name for the function comes from the following property of the cubic spline-function. We star by defining the space, $\mathbb{E}(f)$, that is the set of all functions with continous derivatives up to second order that interpolate *f* at given data points (in the range from *a* to *b*).

$$\mathbb{E}(f) = \{g \in C^2[a,\ b] \,|\, g(x_i) = f(x_i) \text{ for } i = 1,\ldots,\mathrm{m}\} \tag{H.7}$$

If we restrict the derivatives to coincide with the derivatives of *f* at the ends, we have:

$$\mathbb{E}_H(f) = \{g \in \mathbb{E}_H(f) \,|\, g'(a) = f'(a),\ g'(b) = f'(b)\} \tag{H.8}$$

Assume that *h* is a cubic spline interpolation with Hermite end conditions. It can then be shown that (see [22]):

$$\int_a^b (h''(x))^2 dx \leq \int_a^b (g''(x))^2 dx \text{ for all } g \text{ in } \mathbb{E}_H(f) \tag{H.9}$$

with equality if and only if $g = h$. This means that the cubic spline interpolation with Hermite end conditions minimizes the linearized bending energy in the given problem.

Appendix I

Additional geometric and material properties for network arch

The material properties for the glulam arches of Section 8.2 are:

E_0 = 12000 N/mm^2 , G = 700 N/mm^2 and ρ = 500 kg/m^3

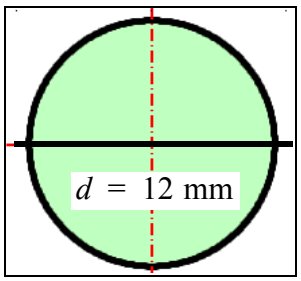

Steel hangers (d = 12 mm)

E = 210000 N/mm^2 , ν = 0.3 and ρ = 7850 kg/m^3

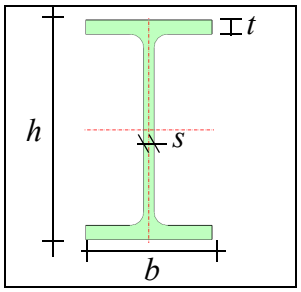

Steel cross beams

E = 210000 N/mm^2 , ν = 0.3 and ρ = 7850 kg/m^3

h = 900 mm, b = 300 mm, s = 18.5 mm and t = 35 mm

Longitudinal deck beams

E = 9000 N/mm^2 , G = 560 N/mm^2 and ρ = 2440 kg/m^3

A-beams: $b \times h$ = 1000×250 mm, B-beams: $b \times h$ = 2000×250 mm

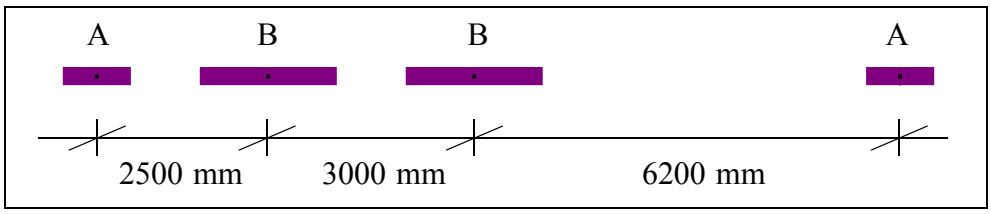

For self weight, a load amplification factor of 1.2 is used. For traffic loads, a load amplification factor of 1.3 is already included.

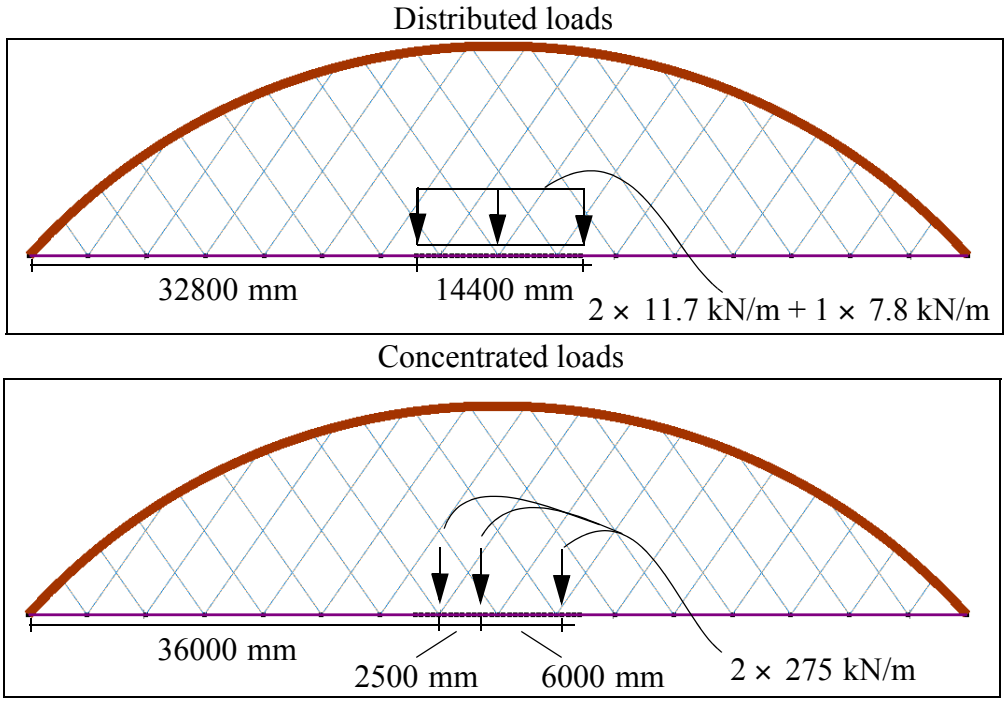

Figure I.1 Along span positioning of loads

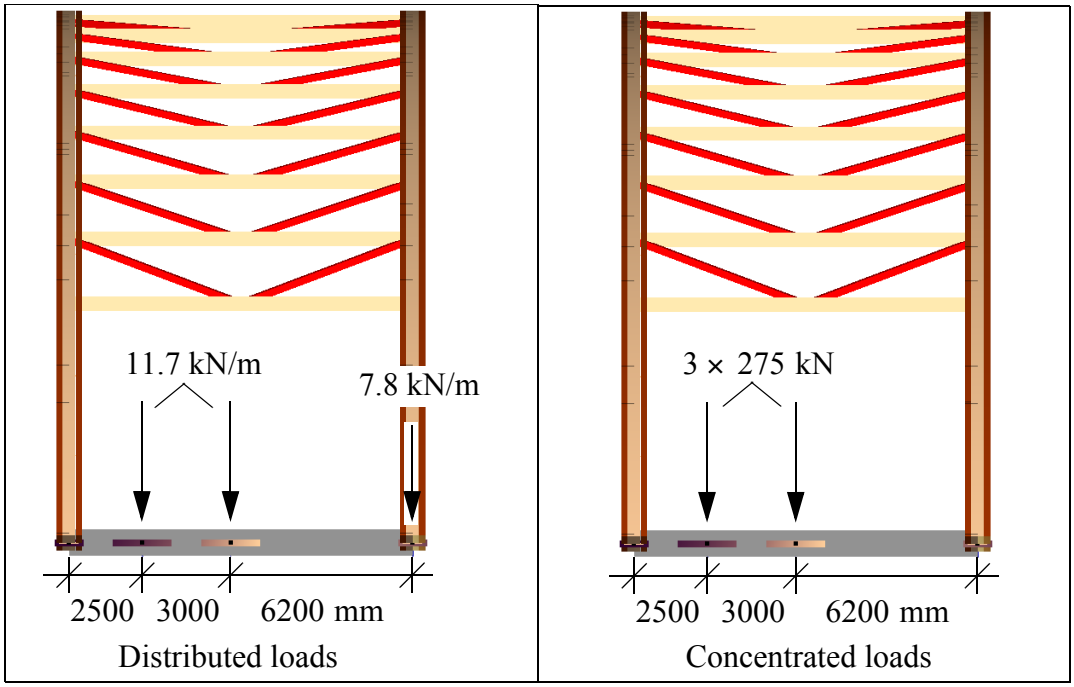

Figure I.2 Lateral positioning of loads

DEPARTMENT OF STRUCTURAL ENGINEERING

NORWEGIAN UNIVERSITY OF SCIENCE AND TECHNOLOGY

N–7491 TRONDHEIM, NORWAY

Telephone: +47 73 59 47 00 Telefax: +47 73 59 47 01

"Reliability Analysis of Structural Systems using Nonlinear Finite Element Methods",
C. A. Holm, 1990:23, ISBN 82-7119-178-0.

"Uniform Stratified Flow Interaction with a Submerged Horizontal Cylinder",
Ø. Arntsen, 1990:32, ISBN 82-7119-188-8.

"Large Displacement Analysis of Flexible and Rigid Systems Considering Displacement-Dependent Loads and Nonlinear Constraints", K. M. Mathisen, 1990:33, ISBN 82-7119-189-6.

"Solid Mechanics and Material Models including Large Deformations",
E. Levold, 1990:56, ISBN 82-7119-214-0, ISSN 0802-3271.

"Inelastic Deformation Capacity of Flexurally-Loaded Aluminium Alloy Structures",
T. Welo, 1990:62, ISBN 82-7119-220-5, ISSN 0802-3271.

"Visualization of Results from Mechanical Engineering Analysis",
K. Aamnes, 1990:63, ISBN 82-7119-221-3, ISSN 0802-3271.

"Object-Oriented Product Modeling for Structural Design",
S. I. Dale, 1991:6, ISBN 82-7119-258-2, ISSN 0802-3271.

"Parallel Techniques for Solving Finite Element Problems on Transputer Networks",
T. H. Hansen, 1991:19, ISBN 82-7119-273-6, ISSN 0802-3271.

"Statistical Description and Estimation of Ocean Drift Ice Environments",
R. Korsnes, 1991:24, ISBN 82-7119-278-7, ISSN 0802-3271.

“Properties of concrete related to fatigue damage: with emphasis on high strength concrete”,
G. Petkovic, 1991:35, ISBN 82-7119-290-6, ISSN 0802-3271.

"Turbidity Current Modelling",
B. Brørs, 1991:38, ISBN 82-7119-293-0, ISSN 0802-3271.

"Zero-Slump Concrete: Rheology, Degree of Compaction and Strength. Effects of Fillers as Part Cement-Replacement", C. Sørensen, 1992:8, ISBN 82-7119-357-0, ISSN 0802-3271.

"Nonlinear Analysis of Reinforced Concrete Structures Exposed to Transient Loading",
K. V. Høiseth, 1992:15, ISBN 82-7119-364-3, ISSN 0802-3271.

"Finite Element Formulations and Solution Algorithms for Buckling and Collapse Analysis of Thin Shells",
R. O. Bjærum, 1992:30, ISBN 82-7119-380-5, ISSN 0802-3271.

"Response Statistics of Nonlinear Dynamic Systems",
J. M. Johnsen, 1992:42, ISBN 82-7119-393-7, ISSN 0802-3271.

"Digital Models in Engineering. A Study on why and how engineers build and operate digital models for decisison support", J. Høyte, 1992:75, ISBN 82-7119-429-1, ISSN 0802-3271.

"Sparse Solution of Finite Element Equations",
A. C. Damhaug, 1992:76, ISBN 82-7119-430-5, ISSN 0802-3271.

"Some Aspects of Floating Ice Related to Sea Surface Operations in the Barents Sea",
S. Løset, 1992:95, ISBN 82-7119-452-6, ISSN 0802-3271.

"Modelling of Cyclic Plasticity with Application to Steel and Aluminium Structures",
O. S. Hopperstad, 1993:7, ISBN 82-7119-461-5, ISSN 0802-3271.

"The Free Formulation: Linear Theory and Extensions with Applications to Tetrahedral Elements with Rotational Freedoms", G. Skeie, 1993:17, ISBN 82-7119-472-0, ISSN 0802-3271.

"Høyfast betongs motstand mot piggdekkslitasje. Analyse av resultater fra prøving i Veisliter'n",
T. Tveter, 1993:62, ISBN 82-7119-522-0, ISSN 0802-3271.

"A Nonlinear Finite Element Based on Free Formulation Theory for Analysis of Sandwich Structures",
O. Aamlid, 1993:72, ISBN 82-7119-534-4, ISSN 0802-3271.

"The Effect of Curing Temperature and Silica Fume on Chloride Migration and Pore Structure of High Strength Concrete", C. J. Hauck, 1993:90, ISBN 82-7119-553-0, ISSN 0802-3271.

"Failure of Concrete under Compressive Strain Gradients",
G. Markeset, 1993:110, ISBN 82-7119-575-1, ISSN 0802-3271.

"An experimental study of internal tidal amphidromes in Vestfjorden",
J. H. Nilsen, 1994:39, ISBN 82-7119-640-5, ISSN 0802-3271.

"Structural analysis of oil wells with emphasis on conductor design",
H. Larsen, 1994:46, ISBN 82-7119-648-0, ISSN 0802-3271.

"Adaptive methods for non-linear finite element analysis of shell structures",
K. M. Okstad, 1994:66, ISBN 82-7119-670-7, ISSN 0802-3271.

"On constitutive modelling in nonlinear analysis of concrete structures",
O. Fyrileiv, 1994:115, ISBN 82-7119-725-8, ISSN 0802-3271.

"Fluctuating wind load and response of a line-like engineering structure with emphasis on motion-induced wind forces",
J. Bogunovic Jakobsen, 1995:62, ISBN 82-7119-809-2, ISSN 0802-3271.

"An experimental study of beam-columns subjected to combined torsion, bending and axial actions",
A. Aalberg, 1995:66, ISBN 82-7119-813-0, ISSN 0802-3271.

"Scaling and cracking in unsealed freeze/thaw testing of Portland cement and silica fume concretes",
S. Jacobsen, 1995:101, ISBN 82-7119-851-3, ISSN 0802-3271.

"Damping of water waves by submerged vegetation. A case study of laminaria hyperborea",
A. M. Dubi, 1995:108, ISBN 82-7119-859-9, ISSN 0802-3271.

"The dynamics of a slope current in the Barents Sea",
Sheng Li, 1995:109, ISBN 82-7119-860-2, ISSN 0802-3271.

"Modellering av delmaterialenes betydning for betongens konsistens",
Ernst Mørtsell, 1996:12, ISBN 82-7119-894-7, ISSN 0802-3271.

"Bending of thin-walled aluminium extrusions",
Birgit Søvik Opheim, 1996:60, ISBN 82-7119-947-1, ISSN 0802-3271.

"Material modelling of aluminium for crashworthiness analysis",
Torodd Berstad, 1996:89, ISBN 82-7119-980-3, ISSN 0802-3271.

"Estimation of structural parameters from response measurements on submerged floating tunnels",
Rolf Magne Larssen, 1996:119, ISBN 82-471-0014-2, ISSN 0802-3271.

“Numerical modelling of plain and reinforced concrete by damage mechanics”,
Mario A. Polanco-Loria, 1997:20, ISBN 82-471-0049-5, ISSN 0802-3271.

“Nonlinear random vibrations - numerical analysis by path integration methods”,
Vibeke Moe, 1997:26, ISBN 82-471-0056-8, ISSN 0802-3271.

“Numerical prediction of vortex-induced vibration by the finite element method”,
Joar Martin Dalheim, 1997:63, ISBN 82-471-0096-7, ISSN 0802-3271.

“Time domain calculations of buffeting response for wind sensitive structures”,
Ketil Aas-Jakobsen, 1997:148, ISBN 82-471-0189-0, ISSN 0802-3271.

"A numerical study of flow about fixed and flexibly mounted circular cylinders",
Trond Stokka Meling, 1998:48, ISBN 82-471-0244-7, ISSN 0802-3271.

“Estimation of chloride penetration into concrete bridges in coastal areas”,
Per Egil Steen, 1998:89, ISBN 82-471-0290-0, ISSN 0802-3271.

“Stress-resultant material models for reinforced concrete plates and shells”,
Jan Arve Øverli, 1998:95, ISBN 82-471-0297-8, ISSN 0802-3271.

“Chloride binding in concrete. Effect of surrounding environment and concrete composition”,
Claus Kenneth Larsen, 1998:101, ISBN 82-471-0337-0, ISSN 0802-3271.

“Rotational capacity of aluminium alloy beams”,
Lars A. Moen, 1999:1, ISBN 82-471-0365-6, ISSN 0802-3271.

“Stretch Bending of Aluminium Extrusions”,
Arild H. Clausen, 1999:29, ISBN 82-471-0396-6, ISSN 0802-3271.

“Aluminium and Steel Beams under Concentrated Loading”,
Tore Tryland, 1999:30, ISBN 82-471-0397-4, ISSN 0802-3271.

"Engineering Models of Elastoplasticity and Fracture for Aluminium Alloys",
Odd-Geir Lademo, 1999:39, ISBN 82-471-0406-7, ISSN 0802-3271.

"Kapasitet og duktilitet av dybelforbindelser i trekonstruksjoner",
Jan Siem, 1999:46, ISBN 82-471-0414-8, ISSN 0802-3271.

“Etablering av distribuert ingeniørarbeid; Teknologiske og organisatoriske erfaringer fra en norsk ingeniørbedrift”, Lars Line, 1999:52, ISBN 82-471-0420-2, ISSN 0802-3271.

“Estimation of Earthquake-Induced Response”,
Símon Ólafsson, 1999:73, ISBN 82-471-0443-1, ISSN 0802-3271.

“Coastal Concrete Bridges: Moisture State, Chloride Permeability and Aging Effects”
Ragnhild Holen Relling, 1999:74, ISBN 82-471-0445-8, ISSN 0802-3271.

”Capacity Assessment of Titanium Pipes Subjected to Bending and External Pressure”,
Arve Bjørset, 1999:100, ISBN 82-471-0473-3, ISSN 0802-3271.

“Validation of Numerical Collapse Behaviour of Thin-Walled Corrugated Panels”,
Håvar Ilstad, 1999:101, ISBN 82-471-0474-1, ISSN 0802-3271.

“Strength and Ductility of Welded Structures in Aluminium Alloys”,
Miroslaw Matusiak, 1999:113, ISBN 82-471-0487-3, ISSN 0802-3271.

“Thermal Dilation and Autogenous Deformation as Driving Forces to Self-Induced Stresses in High Performance Concrete”,
Øyvind Bjøntegaard, 1999:121, ISBN 82-7984-002-8, ISSN 0802-3271.

“Some Aspects of Ski Base Sliding Friction and Ski Base Structure”,
Dag Anders Moldestad, 1999:137, ISBN 82-7984-019-2, ISSN 0802-3271.

"Electrode reactions and corrosion resistance for steel in mortar and concrete",
Roy Antonsen, 2000:10, ISBN 82-7984-030-3, ISSN 0802-3271.

"Hydro-Physical Conditions in Kelp Forests and the Effect on Wave Damping and Dune Erosion. A case study on Laminaria Hyperborea",
Stig Magnar Løvås, 2000:28, ISBN 82-7984-050-8, ISSN 0802-3271.

"Random Vibration and the Path Integral Method",
Christian Skaug, 2000:39, ISBN 82-7984-061-3, ISSN 0802-3271.

"Buckling and geometrical nonlinear beam-type analyses of timber structures",
Trond Even Eggen, 2000:56, ISBN 82-7984-081-8, ISSN 0802-3271.

”Structural Crashworthiness of Aluminium Foam-Based Components”,
Arve Grønsund Hanssen, 2000:76, ISBN 82-7984-102-4, ISSN 0809-103X.

“Measurements and simulations of the consolidation in first-year sea ice ridges, and some aspects of mechanical behaviour”, Knut V. Høyland, 2000:94, ISBN 82-7984-121-0, ISSN 0809-103X.

”Kinematics in Regular and Irregular Waves based on a Lagrangian Formulation”,
Svein Helge Gjøsund, 2000-86, ISBN 82-7984-112-1, ISSN 0809-103X.

”Self-Induced Cracking Problems in Hardening Concrete Structures”,
Daniela Bosnjak, 2000-121, ISBN 82-7984-151-2, ISSN 0809-103X.

"Ballistic Penetration and Perforation of Steel Plates",
Tore Børvik, 2000:124, ISBN 82-7984-154-7, ISSN 0809-103X.

"Freeze-Thaw resistance of Concrete. Effect of: Curing Conditions, Moisture Exchange and Materials",
Terje Finnerup Rønning, 2001:14, ISBN 82-7984-165-2, ISSN 0809-103X

Structural behaviour of post tensioned concrete structures. Flat slab. Slabs on ground",
Steinar Trygstad, 2001:52, ISBN 82-471-5314-9, ISSN 0809-103X.

"Slipforming of Vertical Concrete Structures. Friction between concrete and slipform panel",
Kjell Tore Fosså, 2001:61, ISBN 82-471-5325-4, ISSN 0809-103X.

"Some numerical methods for the simulation of laminar and turbulent incompressible flows",
Jens Holmen, 2002:6, ISBN 82-471-5396-3, ISSN 0809-103X.

“Improved Fatigue Performance of Threaded Drillstring Connections by Cold Rolling”,
Steinar Kristoffersen, 2002:11, ISBN: 82-421-5402-1, ISSN 0809-103X.

"Deformations in Concrete Cantilever Bridges: Observations and Theoretical Modelling",
Peter F. Takâcs, 2002:23, ISBN 82-471-5415-3, ISSN 0809-103X.

"Stiffened aluminium plates subjected to impact loading",
Hilde Giæver Hildrum, 2002:69, ISBN 82-471-5467-6, ISSN 0809-103X.

"Full- and model scale study of wind effects on a medium-rise building in a built up area",
Jónas Thór Snæbjørnsson, 2002:95, ISBN82-471-5495-1, ISSN 0809-103X.

“Evaluation of Concepts for Loading of Hydrocarbons in Ice-infested water”,
Arnor Jensen, 2002:114, ISBN 82-417-5506-0, ISSN 0809-103X.

”Numerical and Physical Modelling of Oil Spreading in Broken Ice”,
Janne K. Økland Gjøsteen, 2002:130, ISBN 82-471-5523-0, ISSN 0809-103X.

”Diagnosis and protection of corroding steel in concrete”,
Franz Pruckner, 20002:140, ISBN 82-471-5555-4, ISSN 0809-103X.

“Tensile and Compressive Creep of Young Concrete: Testing and Modelling”,
Dawood Atrushi, 2003:17, ISBN 82-471-5565-6, ISSN 0809-103X.

“Rheology of Particle Suspensions. Fresh Concrete, Mortar and Cement Paste with Various Types of Lignosulfonates”,
Jon Elvar Wallevik, 2003:18, ISBN 82-471-5566-4, ISSN 0809-103X.

“Oblique Loading of Aluminium Crash Components”, Aase Reyes, 2003:15, ISBN 82-471-5562-1, ISSN 0809-103X.

“Utilization of Ethiopian Natural Pozzolans”, Surafel Ketema Desta, 2003:26,
ISSN 82-471-5574-5, ISSN:0809-103X.

“Behaviour and strength prediction of reinforced concrete structures with discontinuity regions”, Helge Brå, 2004:11, ISBN 82-471-6222-9, ISSN 1503-8181.

“High-strength steel plates subjected to projectile impact. An experimental and numerical study”, Sumita Dey, 2004:38, ISBN 82-471-6281-4 (elektr. Utg.), ISBN 82-471-6282-2 (trykt utg.), ISSN 1503-8181.

“Alkali-reactive and inert fillers in concrete. Rheology of fresh mixtures and expansive reactions.” Bård M. Pedersen, 2004:92, ISBN 82-471-6401-9 (trykt utg.), ISBN 82-471-6400-0 (elektr. utg.), ISSN 1503-8181.

“On the Shear Capacity of Steel Girders with Large Web Openings”. Nils Christian Hagen, 2005:9 ISBN 82-471-6878-2 (trykt utg.), ISBN 82-471-6877-4 (elektr. utg.), ISSN 1503-8181.

”Behaviour of aluminium extrusions subjected to axial loading”. Østen Jensen, 2005:7, ISBN 82-471-6872-3 (elektr. utg.) , ISBN 82-471-6873-1 (trykt utg.), ISSN 1503-8181.

”Thermal Aspects of corrosion of Steel in Concrete”. Jan-Magnus Østvik, 2005:5, ISBN 82-471-6869-3 (trykt utg.) ISBN 82-471-6868 (elektr.utg), ISSN 1503-8181.

”Mechanical and adaptive behaviour of bone in relation to hip replacement.” A study of bone remodelling and bone grafting. Sébastien Muller, 2005:34, ISBN 82-471-6933-9 (trykt utg.) (ISBN 82-471-6932-0 (elektr.utg), ISSN 1503-8181.